# Nanoparticles of antiferromagnetic materials

**Madsen, Daniel Esmarch; Mørup, Steen; Hansen, Mikkel Fougt**

*Publication date:*
2008

*Document Version*
Early version, also known as pre-print

# Nanoparticles of antiferromagnetic materials

Daniel Esmarch Madsen

Ph.D. Thesis

Department of Physics
Technical University of Denmark
DK-2800 Kgs. Lyngby Denmark

May 2008

# Contents

# Preface

This thesis is submitted in partial fulfilment of the requirements to obtain the Ph.D. degree from the Technical University of Denmark (DTU). This study has been carried out under the supervision of Professor Steen Mørup, Department of Physics, DTU, and Associate Professor Mikkel F. Hansen, Department of Micro- and Nanotechnology, DTU. The thesis covers most of the results obtained during my time at DTU (from March 2005 to May 2008).

## Layout

This thesis is in two parts. The first part summarizes the main results of my work and serves as an introduction to the second part, which contains the papers that have been written as part of my work at DTU. Chapter 2 of the introductory part reviews the methods used to obtain the bulk of the experimental results. In chapter 3, the methods used for the analysis of the results are discussed, while spin precession in nanoparticles of antiferromagnetic materials is considered in chapter 4. Finally, the Mössbauer spectra of nanoparticles of goethite are the topic of chapter 5. The conclusions of this thesis are summarized in chapter 6. Although three years are a long time, I did not manage to exhaust the topic of antiferromagnetic nanoparticles, hence included in chapter 6 are also some suggestions for further work. A summary of the work, in English as well as Danish, may be found at the end of the introductory part.

## About notation

When writing this thesis I became aware that certain symbols had different meanings in the various papers. To avoid unnecessary confusion, a consistent notation has therefore been introduced in part I of the thesis. It should also be noted that all units reported are S.I. $B$ is denoted the magnetic field. $H$ is in some sections used instead of $B$ due to notational convenience.

## Acknowledgements

The work presented here is the result of a collaboration with a number of people. First of all, I would like to thank my supervisors, Steen Mørup and Mikkel F. Hansen, for providing inspiring suggestions and motivation throughout the years. I would also like to thank Christian R. H. Bahl, Cathrine Frandsen, Davide Peddis, and Chen Wei, for fruitful discussions and enjoyable company. From a practical point of view, I owe, at DTU, my thanks to Lis Lilleballe for assisting me in the chemical laboratory, to Helge Rasmussen for always helping in the Mössbauer laboratory, and to Jacob Wagner from the Center for Electron Nanoscopy

for obtaining TEM images. From the University of Copenhagen, I would like to thank Christian B. Koch, Department of Natural Sciences, Faculty of Life Sciences, for providing me with numerous intriguing samples and to Jesper Bendix, Department of Chemistry, Faculty of Science, for helping me with the SQUID measurements. Bente Lebech from Risø, DTU, is also thanked for helping me performing the Rietveld analysis of the XRD data. Finally, the financial support from the Danish Research Council for Technology and Production Sciences, which made this project possible, is greatly acknowledged.

Daniel Esmarch Madsen
May 30, 2008

# Part I

# Introduction and summary

# Chapter 1

# Ouverture

Magnetic nanoparticles have been intensely studied for the past many years as they exhibit a number of properties that, from a fundamental as well as applied point of view, are most intriguing. Magnetism itself has found numerous uses in many aspects of everyday life, ranging from the generators in power plants to loudspeakers, to an extent that is probably not realized by most people. From an applied point of view, the interest in magnetic *nanoparticles* is a natural consequence of the, apparently, never-ending desire to decrease the size of magnetic devices. However, as the dimensions of such devices are decreased, regimes are approached where the "bulk" rules of physics may no longer be applicable. For example, quantum mechanical effects may start to play a role, or, as discussed below, the particles may start to exhibit superparamagnetic relaxation. Consequently, while this size regime is very exciting from a strictly scientific point of view, it introduces new challenges as well as possibilities in regards to possible applications.

## 1.1 Origins of magnetism

An electron carries a magnetic moment due to its spin and orbital magnetic moments. In an atom, where several electrons are typically present, these moments must be added up, the detailed mechanics of which is not of relevance to this study. It suffices to note that an atom in a crystal will have a resulting spin moment $S$ and a total orbital moment $L$, the magnitudes of which are determined by interactions between the individual electrons and between the electrons and the surrounding ligands. In the same way the atomic nucleus has a total spin $I$. An in-depth introduction to magnetism may be found in the book by Chikazumi [1].

The magnetic ordering observed in a number of materials is due to the interaction between spins on neighboring atoms in the lattice, which for a pair of ions, $i$ and $j$, takes the form

$$\hat{H}_{\text{ex}}^{ij} = -J_{ij}\hat{S}_i \cdot \hat{S}_j, \tag{1.1}$$

where $J_{ij}$ is the exchange coupling constant for that specific pair of ions. To work out the total exchange energy one simply sums over all magnetic ions, i.e.,

$$\hat{H}_{\text{ex}} = -\sum_{i,j} J_{ij}\hat{S}_i \cdot \hat{S}_j. \tag{1.2}$$

The ground state depends on the sign of $J_{ij}$. Fig. 1.1 shows the basic spin configurations. A positive $J_{ij}$ favors a parallel alignment of the moments (Fig. 1.1(a)) while a negative $J_{ij}$

results in an antiparallel ordering of the moments (Fig. 1.1(b)). This is known as *ferromagnetic* and *antiferromagnetic* ordering, respectively. A third possibility is the *ferrimagnetic* ordering shown in Fig. 1.1(c), which is similar to the antiferromagnetic ordering, but where the magnitude of the spins differ. Ferro- and ferrimagnetic orderings are easily recognized as they cause the material to have a magnetic moment, whereas antiferromagnetic ordering, due to the absence of an external moment of any significance, is more elusive and requires other techniques, such as neutron scattering, to be identified. It is also possible to have several

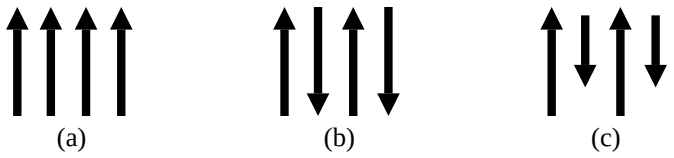


Figure 1.1: Types of magnetic ordering: (a) Ferromagnetic, (b) antiferromagnetic, (c) ferrimagnetic.

competing interactions, which may lead to spin frustration and/or an absence of long-range order (although a short-range order may still exist).

The topic of this thesis is antiferromagnetic nanoparticles, which until recently have been somewhat overlooked, since they are not as readily applicable as ferro- or ferrimagnetic nanoparticles. As the work presented here will show, there are certain aspects of antiferromagnetic nanoparticles that have generally been neglected. We will also be considering properties resulting from the antiferromagnetic ordering itself, and finally we will have a look at interactions between antiferromagnetic nanoparticles. A general review of the research on antiferromagnetic nanoparticles is presented in Paper I.

## 1.2 Magnetic nanoparticles

Fig. 1.2(a) illustrates a typical magnetic particle. We assume that this particle is so small that only a single magnetic domain is present. In the following we will consider some general properties of such a system.

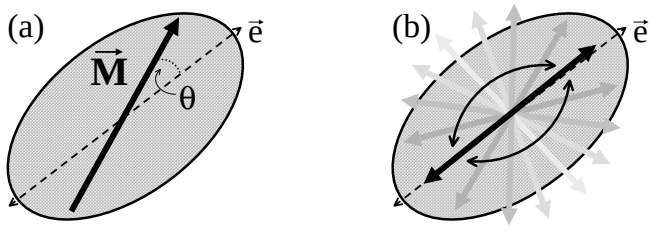


Figure 1.2: (a) A magnetic nanoparticle with magnetization $\vec{M}$ and uniaxial anisotropy axis $\vec{e}$. (b) Superparamagnetic relaxation in a magnetic particle.

### 1.2.1 Magnetic anisotropy

Consider the angular part of the free energy of a magnetic particle in zero external field, $F(\theta)$, where $\theta$ characterizes the direction of the magnetization $\vec{M}$ with respect to some reference orientation. The minima of $F(\theta)$ are known as "easy" directions, whereas the maxima are known as "hard" directions. Due to the dot product appearing in Eq. (1.2), the exchange energy is isotropic; its value is determined by the relative orientation of the moments with respect to each other, not by the absolute orientation with respect to the crystal axis, hence the exchange interaction does not play a role here. $F(\theta)$, which represents the magnetic anisotropy (free) energy, however, may contain contributions from several other sources such as

- *magnetocrystalline anisotropy*, which is due to the anisotropy of the crystal lattice. The symmetry of the lattice will be reflected in the orbital wave functions, which couple to the spins through the spin-orbit interaction.

- *shape anisotropy*, due to demagnetization effects. For a prolate ellipsoidal particle with semi-major axis $a$ and semi-minor axis $b$ this is given as

$$F_D = \frac{1}{2}\mu_0 M_\mathrm{s}^2 V(D_b - D_a)\sin^2\theta, \tag{1.3}$$

  where $M_\mathrm{s}$ is the saturation magnetization, $V$ is the volume of the particle, $\theta$ is the angle between $\vec{M}$ and $a$, and $D_a$ and $D_b$ are the demagnetization factors along $a$ and $b$, respectively.

- *strain anisotropy*, due to magnetostriction if the particle is subjected to strain.

- *surface anisotropy*, due to the reduced symmetry of the surface sites.

The resulting anisotropy is commonly assumed to be uniaxial, in which case the associated energy may be expanded as

$$E(\theta) = K_2 V \sin^2\theta + K_4 V \sin^4\theta + \ldots, \tag{1.4}$$

where $K_i$ is $i$'th order anisotropy energy constant and $\theta$ is the angle between the magnetization and the easy axis. Ordinarily, only the first term is considered, and the anisotropy energy is simply written

$$E_\mathrm{K}(\theta) = KV\sin^2\theta, \tag{1.5}$$

where $K$ is the effective anisotropy constant, containing contributions from all of the above mentioned sources. $K$ is typically on the order of $10^3 - 10^5\,\mathrm{J/m^3}$. The anisotropy constant is claimed to be dependent on temperature; however, this is usually ignored. For example, some authors have found that for cubic crystals the anisotropy constant depends on the magnetization to the power of 10 [2]. It has also been observed that the anisotropy constant increases with decreasing volume, presumably due to a larger contribution from surface anisotropy [3].

### 1.2.2 Superparamagnetism

The magnetic anisotropy energy as given by Eq. (1.5) contains two minima, at $\theta = 0$ and $\pi$, separated by a barrier, the height of which depends on the volume of the particle. At zero temperature the magnetization will be confined to one of these minima; however, as the temperature is increased and/or the size is decreased, the likelihood of a magnetization reversal (i.e., a jump of the magnetization from one minima to another as shown in Fig. 1.2(b)) increases. Néel [4] suggested that the average time between two successive *coherent* reversals is given by the Arrhenius-like expression

$$\tau = \tau_0 \exp\left(\frac{KV}{k_\mathrm{B}T}\right), \tag{1.6}$$

where $\tau_0$ may be considered an "attempt time". A particle is said to be superparamagnetic if the rate of magnetization reversals is such that the magnetization averages to zero during the measurement, i.e., if $\tau_\mathrm{m} \gg \tau$, where $\tau_\mathrm{m}$ is a typical time scale for the experimental method in question; the temperature at which $\tau_\mathrm{m} = \tau$ is denoted the (superparamagnetic) blocking temperature $T_\mathrm{B}$. A number of authors have subsequently refined the derivations and have found that the above expression is a valid approximation for $KV/k_\mathrm{B}T \geq 1$ [5, 6]. The various models (for both uniaxial and cubic anisotropy) have been reviewed by Jones and Srivastava [7]. It is often assumed that $\tau_0$ is independent of temperature; however, all of the models find that it does actually depend slightly on $T$ as well as $KV$. Nonetheless, this is often ignored as the dependence is much weaker than that originating from the exponential term.

From an application point of view, superparamagnetic relaxation poses a huge problem in the magnetic recording industry. In order to obtain increasingly higher data densities, smaller and smaller particles are used. However, below a certain size they may become superparamagnetic and hence may not be able to retain the information stored in them [8]. On the other hand, superparamagnetic particles may potentially be used in biomedicine, for hyperthermia treatment of, e.g., cancer cells or as an MRI (Magnetic Resonance Imaging) contrast enhancer (for a review of biomedical applications of magnetic nanoparticles, see Pankhurst et al. [9]).

### 1.2.3 Polydisperse samples

While it is possible to do measurements on single nanoparticles [10], in most cases, for practical reasons, a sample contains a large number of particles with different sizes. This must often be taken into account when analyzing experimental data by introducing some size (e.g., volume or diameter) distribution $p(x)\,\mathrm{d}x$. The size distribution is in the work presented here assumed to be log-normal [11]

$$p(x, x_\mathrm{m}, \sigma)\,\mathrm{d}x = \frac{1}{\sqrt{2\pi}\sigma x} \exp\left(-\frac{(\ln x - \ln x_\mathrm{m})^2}{2\sigma^2}\right) \mathrm{d}x, \tag{1.7}$$

where $x_\mathrm{m}$ and $\sigma$ are the median value and the width, respectively. In most cases we use the substitution $x \to yx_\mathrm{m}$, giving

$$p(y, \sigma)\,\mathrm{d}y = \frac{1}{\sqrt{2\pi}\sigma y} \exp\left(-\frac{\ln^2 y}{2\sigma^2}\right) \mathrm{d}y. \tag{1.8}$$

Some general properties of the log-normal distribution are reviewed in appendix A.1. Other distributions are often encountered in the literature, in particular the normalized $\Gamma$ distribution

[12],

$$p(y,a,b)\,\mathrm{d}y = \frac{b^{-1}}{\Gamma(1+a)}\left(\frac{y}{b}\right)^{a}\exp\left(-\frac{y}{b}\right)\,\mathrm{d}y, \tag{1.9}$$

where $\Gamma(1+a)$ is the $\Gamma$ function and the parameters $a$ and $b$ determine the shape of the distribution. The log-normal distribution and the $\Gamma$ distribution are very similar for small values of $\sigma$ and larger values of $a$. However, the $\Gamma$ distribution is not as straightforward to use as the log-normal distribution since there is no simple relationship between the median value and the width of the $\Gamma$ distribution and $a$ and $b$.

### 1.2.4 Inter-particle interactions

The systems discussed so far have all been assumed to be non-interacting, but while it is possible to obtain samples in which inter-particle interactions are negligible (as for example in ferritin which we will consider in section 3.3), in general, interactions are difficult to avoid, and their effects must in most cases be dealt with.

On important consequence of interactions is that the superparamagnetic relaxation time will be changed [13]. However, the direction and extent of this change has been a source of considerable debate over the years [14–17]. Interactions may also lead to the formation of a more or less ordered state. For example, in many magnetic samples, the magnetic moments of neighboring particles are coupled due to dipole interactions and it can be shown that an ordered state will be formed in such a system below a critical temperature $T_\mathrm{d}$ on the order of [16]

$$k_\mathrm{B}T_\mathrm{d} \simeq \frac{\mu_0}{4\pi}\frac{\langle\mu\rangle^2}{\langle r\rangle^3}, \tag{1.10}$$

where $\langle r\rangle$ is the average distance between the particles and $\langle\mu\rangle$ is the average magnetic moment. Inter-particle interactions between antiferromagnetic nanoparticles are not mediated by dipole interactions, but instead by direct exchange coupling between surface atoms of neighboring particles. Inter-particle interactions in goethite ($\alpha$-FeOOH) are the topic of chapter 5.

## 1.3 Antiferromagnetic nanoparticles

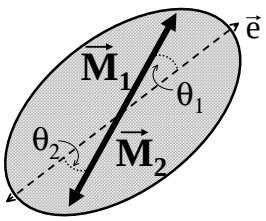


Figure 1.3: An antiferromagnetic nanoparticle with sublattice magnetizations $\vec{M}_1$ and $\vec{M}_2$ and uniaxial anisotropy axis $\vec{e}$.

If we consider, specifically, the properties of antiferromagnetic nanoparticles, the magnetic structure may, as indicated in Fig. 1.1(b), be described as a number of sublattices, where all spins within each sublattice have the same orientation. Fig. 1.3 shows the simplest case of two sublattices, with sublattice magnetizations $\vec{M}_1$ and $\vec{M}_2$, which will be the basis of the description of antiferromagnetic nanoparticles presented in this thesis.

### 1.3.1 Uncompensated moments

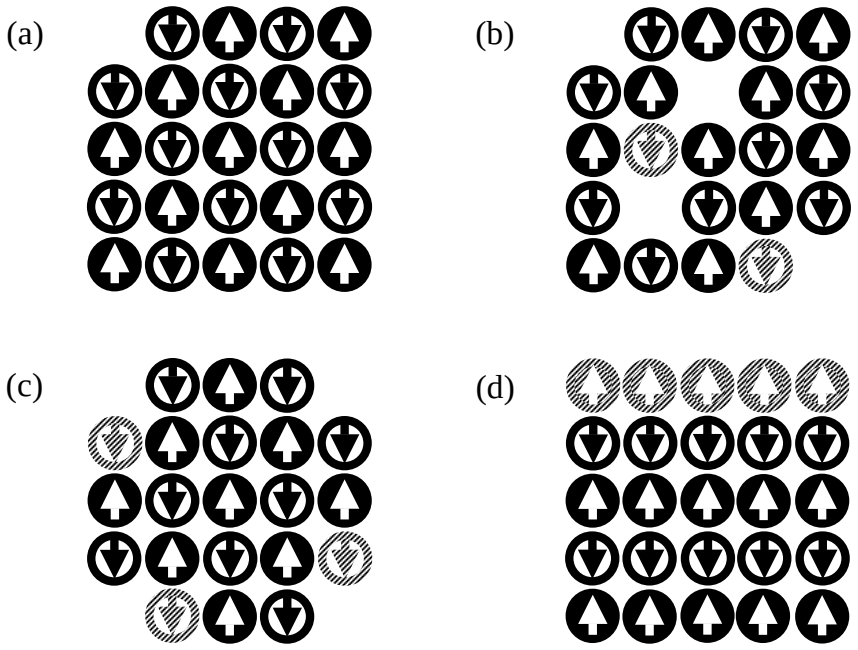


Figure 1.4: Uncompensated spins in antiferromagnetic nanoparticles. (a) a perfect antiferromagnet with no uncompensated spins, (b) uncompensated spins in the entire particle, (c) uncompensated spins confined to the surface, (d) uncompensated spins due to a missing layer. The shaded spins are uncompensated.

For a perfect antiferromagnet, $|\vec{M}_1| = |\vec{M}_2|$; however, perfect antiferromagnetic ordering (Fig. 1.4(a)) is not expected in very small particles due to various finite-size effects. Néel [18] originally suggested that in an antiferromagnetic particle containing $N$ spins, the average number of uncompensated spins $N_{\mathrm{u}}$ will equal $N^{\nu}$, where $\nu$ is a parameter ranging from $\frac{1}{3}$ to $\frac{2}{3}$, depending on the precise arrangement of the uncompensated spins in the crystal structure. Fig. 1.4 illustrates a number of possible configurations for the uncompensated spins. Néel [18] found that if the uncompensated spins are randomly distributed in the structure (Fig. 1.4(b)), their number will equal the square root of the total number of spins, i.e., $\nu = \frac{1}{2}$. On the other hand, if the uncompensated spins are confined to the surface of the particle (Fig. 1.4(c)),

their number will equal the square root of the number of surface spins, i.e. $\nu = \frac{1}{3}$. A third configuration was considered, namely that shown in Fig. 1.4(d) where the particles contain layers of alternating spin directions. In particles containing an even number of layers, the uncompensated moment will be zero, whereas a moment of considerable size is expected from particles with an odd number of layers. In total, Néel [18] estimated that in a sample containing an equal amount of particles with an even and odd number of layers, $\nu = \frac{2}{3}$. In any case, the resulting moment due to the uncompensated spins will be given by

$$\mu = \mu_{\mathrm{at}} N_{\mathrm{u}} \simeq \mu_{\mathrm{at}} N^{\nu}, \tag{1.11}$$

where $\mu_{\mathrm{at}}$ is the magnetic moment per magnetic atom. The importance of the uncompensated moment will be discussed in chapters 3 and 4; in chapter 3 from the perspective that it must be taken into account when analyzing experimental data, and in chapter 4 we will consider its influence on the spin precession states and the thermoinduced moment.

# Chapter 2

# Experimental methods

In this chapter, we will review the principles behind the experimental techniques (Mössbauer spectroscopy, SQUID magnetometry and X-ray diffraction) used to obtain the bulk of the experimental results presented in this work. A number of other techniques (e.g., Transmission Electron Microscopy (TEM)) have been used as well, however, to a limited extent only, and these will not be discussed here. The results presented in Paper V are, among other methods, obtained from Neutron Scattering experiments. However, this technique will not be discussed either as I have not been involved in the acquisition of these data.

## 2.1 Mössbauer spectroscopy

### 2.1.1 Introduction

Mössbauer spectroscopy is a powerful technique, which has found numerous applications within an impressive number of different scientific branches (as demonstrated by, e.g., the proceedings of the biennial International Conference on the Applications of the Mössbauer Effect (ICAME), published in Hyperfine Interactions). The technique is named after Rudolf Mössbauer who in 1958, while working on his Ph.D., discovered a recoilless nuclear resonance absorption of $\gamma$-radiation in $^{191}$Ir. For this he was awarded the 1961 Nobel prize in physics. An interesting account of this discovery can be found in his 1961 Nobel lecture [19]. In the following, the basic principles of Mössbauer spectroscopy will be reviewed. For a more extensive introduction the reader is referred to the books by Greenwood and Gibb [20] and Gütlich et al. [21].

Consider a system with an energy level spectrum consisting of a ground state, $|0\rangle$, and several excited states, $|1\rangle, |2\rangle \ldots$ If we want to figure out experimentally the separation between the levels, we could subject the system to something capable of exciting it, and monitor at which energies the excitations take places. This is the basic principle behind most spectroscopic techniques.

In Mössbauer spectroscopy, we study the absorption of $\gamma$-photons by certain atomic nuclei. The $\gamma$-photon, emitted by one nucleus as a result of a transition between two states is used to excite a similar transition in the absorbing nucleus. The energy distribution $I(E)$ of the emitted $\gamma$-radiation is given as

$$I(E) \propto \frac{1}{(E - E_\gamma)^2 + (\Gamma/2)^2}, \tag{2.1}$$

which is a Lorentzian line centered at $E_\gamma$ with a full-width-at-half-maximum (FWHM) $\Gamma = \hbar/\tau_\mathrm{n}$, where $\tau_\mathrm{n}$ is the mean lifetime of the excited state. This line shape is obtained by considering the emitting nucleus as a damped oscillator, in which case the resulting electromagnetic field is given as

$$\epsilon(t) = \epsilon_0 \exp\left(i\omega_\gamma t - \frac{t}{2\tau_\mathrm{n}}\right) \exp\left(-ik_\gamma x\right), \tag{2.2}$$

where $\omega_\gamma = E_\gamma/\hbar$. A Fourier transformation yields the spectral distribution of radiation $a(\omega)$ from which the intensity distribution is obtained (as it is proportional to $|a(\omega)|^2$).

For many isotopes the natural line width of the emitted $\gamma$-photons is extremely narrow, hence it is possible to resolve minute differences between the energy levels of the absorbing and emitting nuclei. However, Mössbauer spectroscopy is only possible since a certain fraction of the $\gamma$-photons can be emitted without a significant loss of energy due to recoil (the Mössbauer effect). Recoil would make the energy of the $\gamma$-photons $E_\gamma$ different from the transition energy $E_0$, and resonant absorption would become impossible. This is avoided as the recoil is taken up by the entire crystal, rendering the recoil energy (which is inversely proportional to the recoiling mass) negligible. The probability $f$ that a $\gamma$-photon is emitted without a loss of energy due to recoil is given by a quantity known as the $f$-factor. It can be shown that

$$f = \exp\left(-\frac{E_\gamma^2}{\hbar c}\langle x^2\rangle\right), \tag{2.3}$$

where $\langle x^2\rangle$ is the mean squared amplitude of the thermal vibrations of the emitting nucleus.

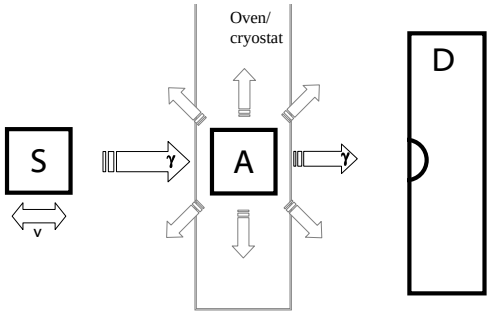


Figure 2.1: Typical transmission Mössbauer spectroscopy setup. (S) source, (A) absorber, (D) detector.

Fig. 2.1 shows a typical experimental setup. When performing a measurement, moving the source nuclei with a small velocity $v$ relative to the absorbing nuclei modifies the energy of the emitted photon through a small, but sufficient, Doppler shift of magnitude $\Delta E = E_0\,(v/c)$, where $c$ is the speed of light. Hence one may monitor the absorption as a function of the photon energy, and in that way probe the energy levels of the absorbing nuclei. As the induced Doppler shift in energy is very small ($\Delta E/E_0$ is typically on the order of $10^{-10}$) the energy difference between the two nuclei cannot be too big. As a consequence the two nuclei

must be of the same isotope. One of the most suitable isotopes is $^{57}$Fe, which constitutes approximately 2% of naturally occurring Fe. This is rather fortunate considering the role Fe plays in many systems. In $^{57}$Fe the transition takes place between the ground state $|0\rangle$, which has $I = 1/2$, and the first excited state $|1\rangle$, which has $I = 3/2$. The energy difference $E_0$ between these two levels is 14.4 keV. The mean life time of the excited state is $1.41 \cdot 10^{-7}$ s giving a line width of $4.7 \cdot 10^{-9}$ eV. The emitted photons are generated when $^{57}$Co decays to $^{57}$Fe.

### 2.1.2 Hyperfine interactions

Due to interactions between the nucleus and the surrounding electrons, the ground state and exciting states will be shifted and/or split according to the environment in which the nucleus is located. These interactions are either electrostatic or magnetic and will in the following be discussed.

#### Electrostatic interactions

The energy due to interactions between the nuclear charge distribution $\rho_{\mathrm{N}}(\vec{r})$ and the potential $V(\vec{r})$ due to the surrounding electrons may be written

$$E = \int \rho_{\mathrm{N}}(\vec{r}) V(\vec{r}) \, \mathrm{d}\tau, \tag{2.4}$$

where $\mathrm{d}\tau$ is a volume element. Through a Taylor expansion this may be reduced to

$$E \simeq \frac{1}{6} \sum_i V_{ii} \int \rho_{\mathrm{N}}(\vec{r}) r^2 \, \mathrm{d}\tau + \frac{1}{2} \sum_i V_{ii} \int \rho_{\mathrm{N}}(\vec{r}) \left( x_i^2 - \frac{r^2}{3} \right) \mathrm{d}\tau, \tag{2.5}$$

where the electric field gradient (EFG) tensor

$$V_{ij} = \left. \frac{\partial^2 V}{\partial x_i \partial x_j} \right|_0 \tag{2.6}$$

has been introduced and a coordinate system which diagonalizes the EFG has been chosen.

#### The isomer shift ($\delta$)

From the first term of Eq. (2.5) one may obtain

$$E = \frac{2}{3} \pi Z e^2 |\psi(0)|^2 \langle r^2 \rangle, \tag{2.7}$$

where $Ze$ is the nuclear change, $e|\psi(0)|^2$ is the charge density of the surrounding electrons (at the site of the nucleus), and $\langle r^2 \rangle$ is the expectation value of the square of the nuclear radius. As the nuclear radii in the ground and excited states differ, any transition between the two states is accompanied by a change in energy given as

$$\Delta E = \frac{2}{3} \pi Z e^2 |\psi(0)|^2 \left( \langle r^2 \rangle_{\mathrm{e}} - \langle r^2 \rangle_{\mathrm{g}} \right), \tag{2.8}$$

with e and g denoting the excited and ground states, respectively. If the electronic charge density in the emitting (S) and absorbing (A) nuclei differ, a shift in the energy

$$\delta = \frac{2}{3}\pi Z e^2 \left(|\psi(0)|^2_{\mathrm{A}} - |\psi(0)|^2_{\mathrm{S}}\right)\left(\langle r^2\rangle_{\mathrm{e}} - \langle r^2\rangle_{\mathrm{g}}\right) \tag{2.9}$$

will be observed. This is known as the isomer shift. It is important to note that the nuclear radii are constants of a given nuclei, hence differences in $\delta$ reflect different chemical environments and may be used, e.g., to distinguish between ions of different valency.

### The quadrupole splitting ($\Delta E_{\mathrm{Q}}$)

Defining the quadrupole tensor, $Q_{ii}$ as

$$Q_{ii} = \int \rho_N(\vec{r})(3x_i^2 - r^2)\,\mathrm{d}\tau, \tag{2.10}$$

the latter part of Eq. (2.5) may be written

$$E_{\mathrm{Q}} = \frac{1}{2}\sum_{i=1}^{3} V_{ii}\frac{Q_{ii}}{3}. \tag{2.11}$$

The potential $V(\vec{r})$ contains contributions from several sources, including the s-electrons, which have a finite charge density at the site of the nucleus, the surrounding electron cloud, and the neighboring ligands. However, since the s-electrons are distributed with spherical symmetry, the principal components ($V_{xx}^{(s)}, V_{yy}^{(s)}$, and $V_{zz}^{(s)}$) of the EFG due to these will be identical. As a consequence, we see from Eqs. (2.10) and (2.11) that the s-electrons do not contribute to $E_{\mathrm{Q}}$. Concerning the contribution from the remaining sources, which do not give rise to any charge at the site of the nucleus, we have from Laplace's equation that

$$\nabla^2 V = 0, \tag{2.12}$$

hence $V_{xx}+V_{yy}+V_{zz} = 0$. If we choose the principal axis of the EFG such that $V_{zz} \geq V_{xx} \geq V_{yy}$, the EFG is described by just two parameters, $V_{zz}$ and the asymmetry parameter $\eta$, defined as

$$\eta = \frac{V_{xx} - V_{yy}}{V_{zz}}. \tag{2.13}$$

As $Q_{\mathrm{g}} = 0$ only the excited levels are split; it can be shown that the energies of these levels depend on $|m_{\mathrm{I}}|$ (the $z-$component of the nuclear spin $I$) and are given as

$$E_{\mathrm{Q}} = \frac{eQV_{zz}}{4I(2I-1)}\left(3m_{\mathrm{I}}^2 - I(I+1)\right)\sqrt{1+\frac{\eta^2}{3}}, \tag{2.14}$$

where $Q \equiv Q_{zz}$. Fig. 2.2 shows the energy levels and the resulting Mössbauer spectrum. It may be noted that the quadrupole interaction gives rise to two lines in the $^{57}$Fe Mössbauer spectrum, where the splitting is given as

$$\Delta E_{\mathrm{Q}} = \frac{eQV_{\mathrm{zz}}}{2}\sqrt{1+\frac{\eta^2}{3}}. \tag{2.15}$$

It is again important to note that $Q$ is constant for a given nuclei, hence it is $V_{zz}$ and $\eta$, which differ in different compounds. Consequently, from the quadrupole splitting it is possible to obtain information about the local charge distribution of a given material.

*Quadrupole splitting*

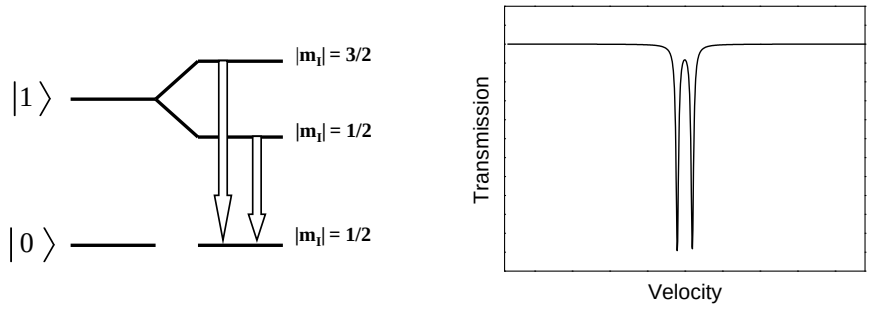


*Magnetic hyperfine splitting*

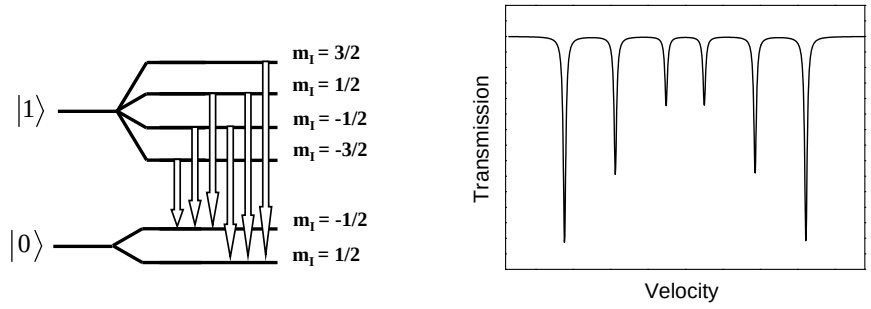


Figure 2.2: Quadrupole ($\Delta E_{\mathrm{Q}}$) and magnetic ($B_{\mathrm{hf}}$) splitting of the nuclear energy levels (left) and the resulting Mössbauer spectra (right). The arrows indicate the allowed transitions.

### Magnetic interactions ($B_{\mathrm{hf}}$)

The energy of a magnetic dipole moment $\vec{\mu}$ in a magnetic field $\vec{B}$ is given as

$$E_{\mathrm{B}} = -\vec{\mu} \cdot \vec{B}. \tag{2.16}$$

Similarly, the energy levels of the atomic orbitals are split due to their different magnetic moments (the Zeeman effect), and the same effect is observed for the nuclear energy states, the energies of which are given as

$$\Delta E_{m_{\mathrm{I}}} = -g_{\mathrm{n}} \mu_{\mathrm{n}} B m_{\mathrm{I}}, \tag{2.17}$$

where $g_{\mathrm{n}}$ is the nuclear Landé factor and $\mu_{\mathrm{n}}$ is the nuclear magneton. For the ground and excited states, the energy levels are split into 2 and 4, respectively. This gives rise to 8 possible transitions as shown in Fig. 2.2. However, due to the selection rules $\Delta m_{\mathrm{I}} = 0, \pm 1$ for magnetic dipole transitions only 6 of these are allowed; consequently, only six lines (a sextet) are observed in the Mössbauer spectrum. From the width of this sextet one may determine the magnitude of the magnetic field, termed the hyperfine field $B_{\mathrm{hf}}$, at the site of the nucleus.

The contributions to $B_{\mathrm{hf}}$ include the dipole field due to the spin of the surrounding electrons, the field induced by the orbital motion of the electrons, and a more direct contribution

| Line No. | $m_e$ | $m_g$ | Intensity ($\theta$) |
|---|---|---|---|
| 1 | $-3/2$ | $-1/2$ | $\frac{3}{12}(1+\cos^2\theta)$ |
| 2 | $-1/2$ | $-1/2$ | $\frac{4}{12}\sin^2\theta$ |
| 3 | $1/2$ | $-1/2$ | $\frac{1}{12}(1+\cos^2\theta)$ |
| 4 | $-1/2$ | $1/2$ | $\frac{1}{12}(1+\cos^2\theta)$ |
| 5 | $1/2$ | $1/2$ | $\frac{4}{12}\sin^2\theta$ |
| 6 | $3/2$ | $1/2$ | $\frac{3}{12}(1+\cos^2\theta)$ |

Table 2.1: Transition probabilities. $\theta$ is the angle between the emitted $\gamma$ photon and the $z$ direction. $m_g$ and $m_e$ denote the value of $m_I$ in the ground state and excited state, respectively.

(known as Fermi contact) from the spin of s-electrons having a finite charge density at the site of the nucleus. This latter one is the most important contribution for Fe compounds (in general for 3d transition element compounds). As a consequence, the internal magnetic field is coupled to the spin structure, and hence will reflect the magnetic ordering (if present).

The individual line intensities are determined by the corresponding transition probabilities $P(I_2m_2, I_1m_1)$. These are found to be products of a Clebsch-Gordan coefficient $\langle I_1m_1, Lm|I_2m_2\rangle$ and a part, which depends only on the direction of the emitted $\gamma$-rays relative to the $z$ axis as defined by, e.g., the hyperfine field. The transition probabilities in the presence of a magnetic hyperfine field are listed in Table 2.1. One may note that the intensities are pairwise identical. In the case of random orientations the relative intensities are 3:2:1; this is the ratio shown in Fig. 2.2.

#### Combined effects

In most cases, quadrupole and magnetic interactions are present at the same time. If the quadrupole interaction can be treated as a perturbation, it can be shown that it will lead to a shift of the inner four lines of the spectrum relative to the outer two as shown in Fig. 2.3. This shift is referred to as the quadrupole *shift* ($\varepsilon$) and its magnitude depends additionally on the angle between $B_{\rm hf}$ and the principal axes of the EFG. In the case where $\eta = 0$, this shift is given as

$$\varepsilon = \frac{eQV_{zz}}{8}(3\cos^2\theta - 1), \tag{2.18}$$

where $\theta$ is the angle between $B_{\rm hf}$ and $V_{zz}$.

### 2.1.3 Effects of superparamagnetic relaxation

As discussed in section 1.2.2, in a particle exhibiting fast superparamagnetic relaxation, the observed magnetization averages to zero; in Mössbauer spectroscopy this corresponds to a collapse of the sextet into a doublet or singlet. However, this collapse does not take place instantaneously. Fig. 2.4(a) shows a number of Mössbauer spectra simulated using the model of Blume and Tjon [22], which attempts to describe the dependence of the Mössbauer spectrum on the superparamagnetic relaxation time $\tau$. It is observed that the shape of the Mössbauer spectrum is gradually changed with $\tau$; as $\tau$ is decreased, the lines of the sextets become broadened to an extent where they are no longer Lorentzian in shape. Only when the relaxation

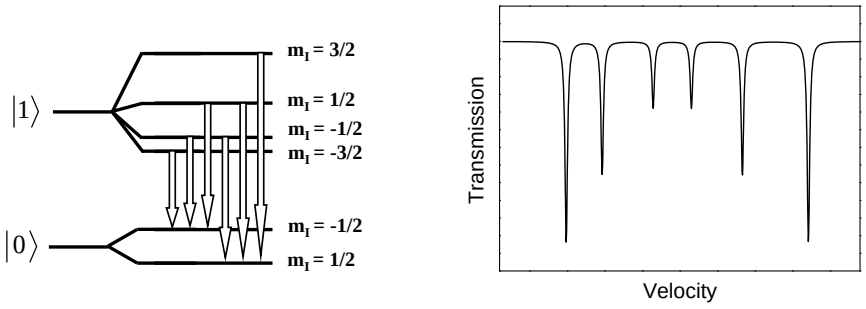


Figure 2.3: The combined effect of a magnetic hyperfine splitting and a quadrupole shift ($\varepsilon$) on the nuclear energy levels (left) and the resulting Mössbauer spectra (right). The arrows indicate the allowed transitions.

is very fast does the spectrum contain a single collapsed component, in this case a singlet (the spectra were simulated with zero quadrupole splitting).

A distribution of volumes will give rise to a certain spread in superparamagnetic relaxation times; however, due to the exponential dependence of $\tau$ on $V$ (Eq. (1.6)), at a given temperature, only a minor fraction of the particles will have relaxation times in the range where the broadened components are observed. This is illustrated in Fig. 2.4(b) and (c), which show spectra simulated with $\tau_0 = 2 \cdot 10^{-13}$ s and a log-normal distribution of volumes with width $\sigma_\mathrm{v}$ for different values of $\sigma_\mathrm{v}$ and $KV_\mathrm{m}/k_\mathrm{B}T$, where $V_\mathrm{m}$ is the median volume of the distribution. It is observed that these spectra are well described as superpositions of discrete components (sextets and singlets) exhibiting negligible line broadening.

Based on the above considerations, the shape of the Mössbauer spectrum as a function of temperature for an idealized sample may be determined: At zero temperature, the spectrum will contain only a sextet. As the temperature is increased, the hyperfine field will decrease due to the ordinary decrease of the magnetization. As the blocking temperature of the sample is approached, a doublet (or singlet) will appear in the spectrum. The area fraction of this doublet (or singlet) corresponds to the volume fraction of particles exhibiting superparamagnetic relaxation if we assume that the $f$-factor is the same as in the ordered state. Consequently, this fraction will continue to increase until the blocking temperature has been passed. The width of the temperature range for which the doublet (or singlet) and sextet coexist is determined by the width of the size distribution.

## 2.2 Magnetization measurements

The magnetization data presented in this thesis were obtained with a SQUID (Superconducting QUantum Interference Device) detector. The SQUID was conceived by R. Jaklevic and coworkers at the Ford Scientific Laboratories in 1964 [23, 24]. Fig. 2.5 shows their original setup. It consists of two coupled Josephson junctions and allows for a very accurate determination of the magnetic moment of a sample. In a Josephson junction, two superconductors are separated

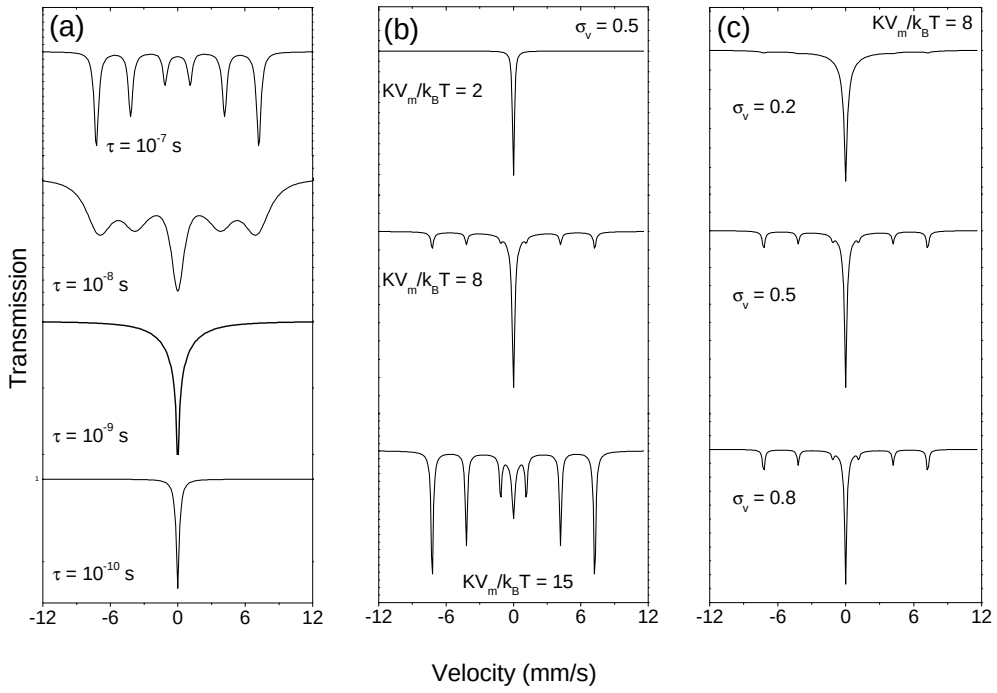


Figure 2.4: Simulated Mössbauer spectra. (a) Non-weighted spectra for different values of $\tau$ (b) Volume-weighted, for a log-normal distribution of volumes with $\sigma_{\mathrm{v}} = 0.5$ and different values of $KV_{\mathrm{m}}/k_{\mathrm{B}}T$, (c) Volume-weighted, for $KV_{\mathrm{m}}/k_{\mathrm{B}}T = 8$ and different values of $\sigma_{\mathrm{v}} = 0.5$. For all of the simulations, $B_{\mathrm{hf}} = 45$ T and $\tau_0 = 2 \cdot 10^{-13}$ s.

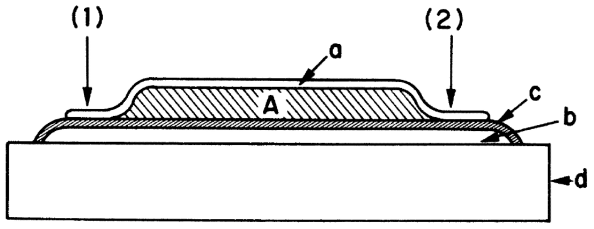


Figure 2.5: Cross section of the setup studied by Jaklevic et al. Josephson junctions are formed at (1) and (2) where two Sn films (a and b) are separated by a Sn oxide file (c). From Jaklevic et al. [23].

by a small insulating barrier. The maximum current $I_{\max}$ through such a junction is given by

$$I_{\max} = I_0 \left| \frac{\sin(\pi\Phi_j/\Phi_0)}{\pi\Phi_j/\Phi_0} \right|, \tag{2.19}$$

where $\Phi_j$ is the total flux enclosed in the junction and $\Phi_0 = h/2e$ is the magnetic flux quantum. Jaklevic et al. [23] showed that an additional interference effect is introduced if two identical junctions are connected in parallel by superconducting links. The resulting maximum current is in this case given by

$$I_{\max} = 2I_0 \left| \frac{\sin(\pi\Phi_j/\Phi_0)}{\pi\Phi_j/\Phi_0} \right| \left|\cos(\pi\Phi_T/\Phi_0)\right|, \tag{2.20}$$

where $\Phi_T$ is the total flux enclosed *between* the junctions. As the area between the junctions is typically much larger, this renders the current extremely sensitive to minute changes in the magnetic field (as produced, e.g, by a nearby magnetic dipole). Fig. 2.6 shows some early experimental results.

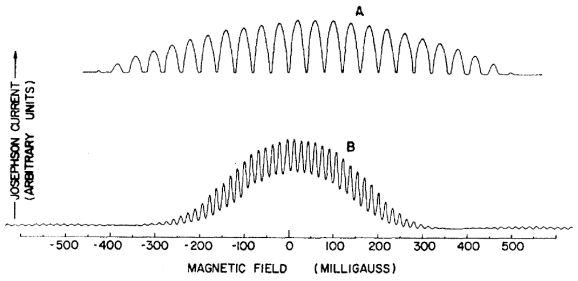


Figure 2.6: Observed current as a function of applied magnetic field. A and B refer to different experimental parameters. From Jaklevic et al. [25].

The instrument used for the measurements was a Quantum Design MPMS XL 5. In this particular instrument the superconducting pickup coils are in the form of a second order gradiometer as shown in Fig. 2.7. During a dc measurement the sample is moved through the coils (Fig. 2.7(a)) and the change in current is recorded. From this response, the moment $m$ of the sample is obtained. For the ac measurements (Fig. 2.7(b)), the sample is first positioned at the lower coil and a nullifying waveform is sent through the SQUID circuitry. The sample is then moved to the middle coils and the signal (now of threefold intensity, as the polarity of both the middle coils is opposite to that of the bottom coil) is recorded from which the moment is obtained.

## 2.3 Powder X-ray diffraction

From X-ray diffraction (XRD) one may obtain information about the crystal structure of a material. This information is obtained by irradiating a sample with X-rays of a given wavelength $\lambda$. The atoms of the sample will scatter the incoming X-rays, and X-rays scattered (elastically) by atoms forming a set of lattice planes $(hkl)$ will in certain directions interfere constructively and give rise to sharp diffraction peaks. In the following we will briefly review the principles behind this process. The reader is referred to the book by Als-Nielsen and McMorrow [26] for a more in-depth introduction to X-ray diffraction.

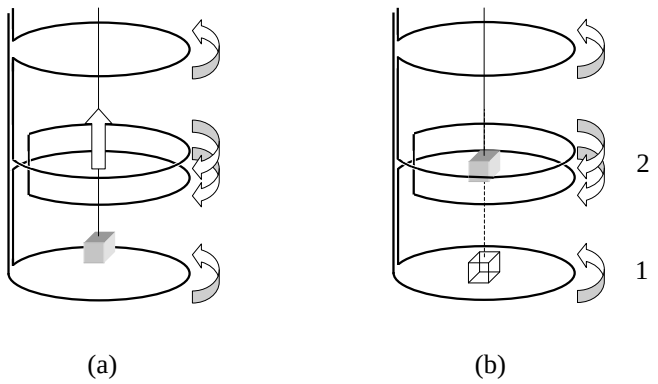


Figure 2.7: The superconducting pickup coils in the configuration of a second order gradiometer. The box represents the sample and the arrows indicate the direction of the current. (a) dc measurement (b) ac measurement. The numbers refer to the sequence of positions during the measurement.

### 2.3.1 Basic principles

Fig. 2.8 illustrates the scattering process. The two X-rays, going from a source (S) to the observer (O), are scattered by different atoms. From the figure, we see that the resulting path difference is given by $2c$, where $c = d\sin\theta$. For constructive interference to take place, this difference must equal an integer number of wavelength, i.e.,

$$2d_{hkl}\sin\theta = \lambda, \tag{2.21}$$

which is the well-known Bragg law. We may arrive at this result in a more general way by first considering, in three dimensions, scattering from a pair of scatterers. If one denotes the wave vectors of the incoming and scattered waves by $\vec{k}_0$ and $\vec{k}$, respectively, and two scatterers are separated by $\vec{r}$, the phase difference between the waves scattered at these two scatterers will be given by $(\vec{k}-\vec{k}_0)\cdot\vec{r}$. If we next consider an entire crystal, for constructive interference to take place, the overall phase factor $\exp[(\vec{k}-\vec{k}_0)\cdot\vec{r}]$ must equal unity. In a crystal, $\vec{r}$ will be a translational vector of the underlying Bravais lattice, hence the above statements result in the requirement that the momentum transfer $\vec{q}\equiv\vec{k}-\vec{k}_0$ must equal a reciprocal lattice vector $\vec{G}_{hkl}$. As we are dealing with elastic scattering, $|\vec{k}| = |\vec{k}_0| = 2\pi/\lambda$, hence $|\vec{q}| = 4\pi\sin\theta/\lambda$, where $2\theta$ is the angle between $\vec{k}$ and $\vec{k}_0$. We arrive at the Bragg law by using that $|\vec{G}_{hkl}| = 2\pi/d_{hkl}$, where $d_{hkl}$ is the lattice spacing for the $(hkl)$ lattice planes. As the positions of the diffraction peaks are determined by the reciprocal lattice vectors, we obtain from this information about the *unit cell* of the material in question.

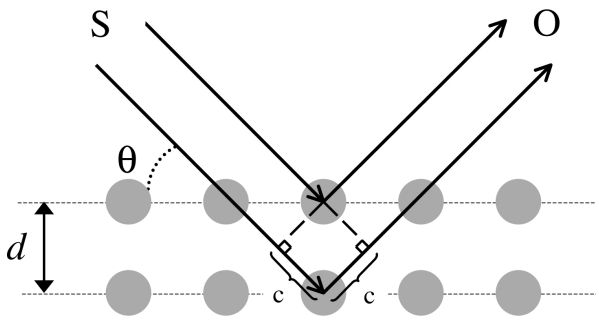


Figure 2.8: Two incident X-rays are scattered by two different scatterers.

The intensity $I_{hkl}$ of a $(hkl)$ diffraction peak depends on the structure factor

$$F_{hkl} = \sum_n f_n \exp[2\pi i(\vec{G}_{hkl} \cdot \vec{r}_n)] \tag{2.22}$$

as

$$I_{hkl} \propto |F_{hkl}|^2. \tag{2.23}$$

Here, $\vec{r}_n$ is the position of the $n$'th atom in the unit cell, and $f_n$ is the atomic scattering factor, which depends on the type of atom. Hence, the peak intensities are given by the distribution of atoms *within* the unit cell. When calculating the peak intensities one should also take into account thermal vibrations by multiplying the structure factor with the Debye-Waller factor $\exp[-Q(\sin\theta/\lambda)^2]$ (which is similar to the $f$-factor in Mössbauer spectroscopy), yielding the temperature corrected structure factor $F^{\mathrm{T}}_{hkl}$

$$F^{\mathrm{T}}_{hkl} = F_{hkl} \exp[-Q(\sin\theta/\lambda)^2], \tag{2.24}$$

where $Q = 8\pi^2\langle u^2\rangle$ is the overall isotropic temperature parameter and $\langle u^2\rangle$ is the average squared displacement of the atoms due to thermal vibrations. The resulting intensity of a given peak may be calculated as

$$I_{hkl} = Cj|F^{\mathrm{T}}_{hkl}|^2 L(\theta), \tag{2.25}$$

where $j$ is the multiplicity factor (the number of planes in the same form), $L(\theta)$ is an angle dependent term known as the Lorentz-polarization factor, which depends on the experimental geometry, and $C$ is, effectively, a scale factor, but depends in principle on parameters relating to the experimental setup (e.g., the wavelength and intensity of the incident radiation) and the sample (such as the amount and density of the material).

Experimental data, specifically, the angles at which the diffraction peaks appear and the intensity of these peaks, may be obtained using a number of different geometrical setups. For example, measurements may be performed on either single crystal specimens or powder samples. As it is not feasible to do measurements on a single crystal of a nanocrystalline material, powder diffraction is commonly used for the study of such substances. Ideally, the diffraction peaks ought to be delta functions, $\delta(2\theta)$, however as real crystals do not have infinite translational symmetry, the lines will show some broadening, the extent of which may

be used to estimate the size of the crystal. The relationship between size and broadening is, as derived by Scherrer [27, 28]

$$d = \frac{K\lambda}{\Gamma \cos\theta}, \tag{2.26}$$

where $d$ is the size measured normal to the diffracting planes, $\Gamma$ is the FWHM (corrected for instrumental broadening) of the diffraction peak, and $K$ is the shape factor, which is close to 0.9. The presence of strain in the crystal may also give rise to some broadening. However, for the materials studied in this work, this broadening is insignificant compared to that originating from the finite size.

### 2.3.2 Rietveld refinement

From Eq. (2.25) one may calculate the positions and intensities of all the diffraction peaks for a given structure. Unfortunately, one cannot go the other way as information about the phases of the diffracted x-rays are lost when we take the square of the structure factor (which is what we observe experimentally). In order to work out the structure of a given material one may instead start with a reasonable model and iteratively adjust the parameters of this model until a satisfactory agreement between the calculated and observed spectra has been achieved.

We may either compare the calculated intensities to the integrated peak intensities of the observed spectrum, or if we know the shape of the diffraction peak we may directly compare a calculated spectrum to the experimentally observed one. If the observed spectrum contains several overlapping peaks, the former method runs into trouble as it may be difficult to separate the contributions from each peak. Hugo M. Rietveld used the latter approach as he noted that diffraction peaks were well-described by Gaussians. This was used to devise the method for structural refinement now bearing his name [29, 30]. The agreement which one with the Rietveld method seeks to optimize is

$$\chi^2 = \sum_i w_i [S_i^{\text{obs}} - S_i^{\text{calc}}]^2, \tag{2.27}$$

where $S_i^{\text{obs}}$ and $S_i^{\text{calc}}$ are the observed and calculated spectra, respectively, and $w_i$ is an appropriate weighting. The calculated spectrum includes a function giving the shape of the background, $B(2\theta)$. In our case this was described by a polynomial in $2\theta$, i.e.

$$B(2\theta) = \sum_{i=0}^{n} a_i (2\theta)^i, \tag{2.28}$$

where the coefficients $a_i$ were to be refined. A 4'th or 5'th order polynomial was used, depending on the complexity of the background.

# Chapter 3

# Analysis of experimental data

The determination of certain physical parameters depends on an analytical treatment of experimental data. For example, the magnetic anisotropy of a sample may be obtained through the coercive field $H_c$, which is directly observed in the hysteresis curve of the sample. A suitable model, e.g., that of Stoner and Wohlfarth [31] may then be used to obtain the magnetic anisotropy. Naturally, if we use an incorrect model, we will most likely obtain an erroneous value of the parameter in question. The choice of model may be unjustified if, e.g., the assumptions of the model are not fulfilled for the sample being studied. In the study of antiferromagnetic nanoparticles, there has been a tendency to use the same models as those used for the analysis of ferro- or ferrimagnetic samples. In this chapter the potential dangers of treating antiferromagnetic nanoparticles as ferromagnets will be considered and it is shown how the traditional ways of analyzing experimental data should be modified in order to take into account the properties of antiferromagnetic nanoparticles. The properties considered here are all related to the uncompensated spins since they give rise to a magnetic moment, which is much smaller than for ferro- or ferrimagnetic materials, and since they result in a volume-dependent magnetization.

## 3.1 Magnetization curves

Consider a single magnetic particle $i$, of volume $V_i$ and magnetization $\vec{M}_i$ in the superparamagnetic state. We will initially not make any assumptions about the type of magnetic ordering (ferro- or antiferromagnetic). In an applied field $\vec{B}$, the magnetic energy will be given as

$$E = -V_i|\vec{M}_i||\vec{B}|\cos\alpha - KV_i\cos^2\beta, \tag{3.1}$$

where the first term represents the Zeeman energy and the second term is the magnetic anisotropy energy, introduced in section 1.2.1; the various angles are defined in Fig. 3.1. For an ensemble of particles with random orientations, all having the same magnetization $M = |\vec{M}|$ and volume $V$, the average value of $\vec{M}$ along $\vec{B}$ is [32]

$$\langle M_z\rangle_T = \frac{1}{2}\int_0^\pi \langle M_z(\lambda)\rangle_T \sin\lambda\,\mathrm{d}\lambda, \tag{3.2}$$

where

$$\frac{\langle M_z(\lambda)\rangle_T}{M_0} = \frac{T(\lambda)}{N(\lambda)} \tag{3.3a}$$

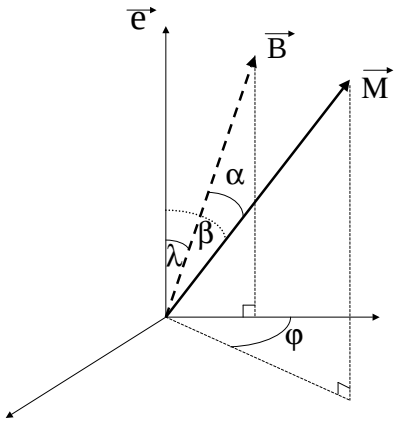


Figure 3.1: Coordinate system used in the calculations showing the angles $\alpha, \beta, \lambda$, and $\varphi$. $\vec{e}$ indicates the easy axis of magnetization (adapted from Paper II).

with

$$T(\lambda) = \int_0^\pi \left[\cos\lambda\cos\beta\bar{I}_0(\zeta\sin\beta\sin\lambda) + \sin\lambda\sin\beta\bar{I}_1(\zeta\sin\beta\sin\lambda)\right] \times e^{\zeta\cos(\lambda-\beta)+\kappa\cos^2\beta}\sin\beta\,\mathrm{d}\beta \tag{3.3b}$$

and

$$N(\lambda) = \int_0^\pi \bar{I}_0(\zeta\sin\beta\sin\lambda)e^{\zeta\cos(\lambda-\beta)+\kappa\cos^2\beta}\sin\beta\,\mathrm{d}\beta. \tag{3.3c}$$

Here, $\zeta = MVB/k_\mathrm{B}T$, $\kappa = KV/k_\mathrm{B}T$, and $\bar{I}_n(x) = \exp(-|x|)I_n(x)$, where $I_n(x)$ is the modified Bessel function of order $n$. The saturation magnetization $M_0$ is given as $NMV/V_\mathrm{sample}$, where $N$ is the number of particles and $V_\mathrm{sample}$ is the total volume of the sample. Fig. 3.2 shows the resulting magnetization as a function of $\zeta$ for different values of $\kappa$. For $\kappa = 0$ one finds

$$\langle M_z\rangle_T = M_0\mathscr{L}\left(\frac{VMB}{k_\mathrm{B}T}\right), \tag{3.4}$$

where $\mathscr{L}(x) = \coth(x) - (1/x)$ is the Langevin function; $\kappa = \infty$ corresponds to the Ising model where the magnetization is confined to $\beta = 0$ and $\pi$.

Eq. (3.4) is often used to analyze magnetization data of ferromagnetic samples in applied fields in order to obtain, e.g., estimates of the magnetic moment $VM$. Such an approach has also been used for the study of the uncompensated moment in antiferromagnetic nanoparticles. In this case, Eq. (3.4) has been extended to include the effect of the antiferromagnetic susceptibility $\chi_\mathrm{af}$ (originating from the canting of the sublattice magnetizations in an applied field), i.e.,

$$\langle M_z\rangle_T = M_0\mathscr{L}\left(\frac{VMB}{k_\mathrm{B}T}\right) + \frac{\chi_\mathrm{af}}{\mu_0}B. \tag{3.5}$$

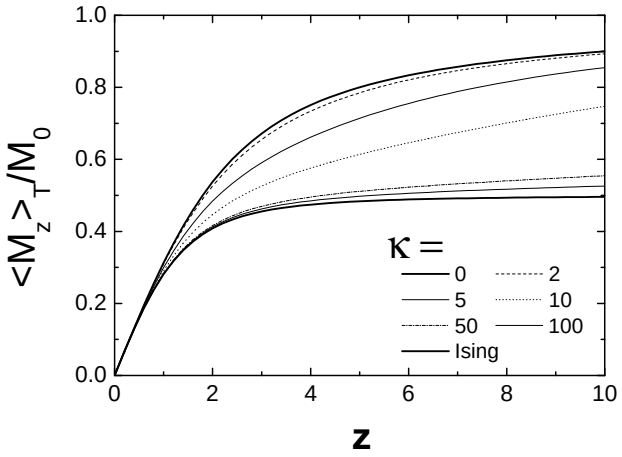


Figure 3.2: Magnetization, calculated using Eq. (3.2), as a function of $\zeta\,(= MVB/k_BT)$, for different values of the anisotropy parameter, $\kappa\,(= KV/k_BT)$ (adapted from Paper II).

A spherical particle with a diameter of 10 nm and with material properties similar to those of hematite (i.e., same density and molar mass) contains approximately $2 \cdot 10^4$ Fe atoms. Assuming a moment pr. Fe atom of 5 $\mu_{\rm B}$ this gives, for a ferromagnet, a magnetic moment of close to $10^5$ $\mu_{\rm B}$, whereas for an antiferromagnet one finds, using Eq. (1.11) with $\nu = \frac{1}{3}$, a moment of around 150 $\mu_{\rm B}$. A typical value of $K$ is around $5 \cdot 10^4$ J/m$^3$, hence for this particle size $KV/k_{\rm B} \approx 2000$ K. Consequently, in the ferromagnetic case with $B = 1 - 5$ T, $MVB \gg KV$ and the anisotropy can be safely ignored. For the antiferromagnet, however, even in large applied fields $MVB$ may still be comparable to $KV$ and the anisotropy cannot be neglected.

In a number of studies of antiferromagnetic materials the magnetic moment, obtained from magnetization curves, was surprisingly found to increase with temperature [33–38]. Silva et al. [39, 40], however, pointed out that the apparent increase of the moment may be the consequence if a distribution of moments is not considered. The consequence of ignoring the anisotropy was explored in Paper II using the same approach as Silva et al. [39, 40], i.e., by fitting magnetization curves, simulated using Eq. (3.2), with Eq. (3.5). The simulated curves were calculated without an antiferromagnetic susceptibility. However, this susceptibility was included in the subsequent fits. Fig. 3.3 shows magnetization curves at two different temperatures for different values of the uncompensated moment. The remaining parameters were chosen to be similar to those of ferritin (to be discussed in section 3.3). The lines in the figures show the fits with Eq. (3.5). In general, excellent fits were obtained. However, some discrepancies were observed, especially for the largest values of the uncompensated moment. The goodness-of-fit, however, was considerably improved as the temperature was increased. Fig. 3.4 shows the apparent values of the moment and the antiferromagnetic susceptibility obtained in the fits. It is observed that at low temperatures the apparent moment deviates considerably from its true value; this discrepancy is noted to be sensitive to the true value of the uncompensated moment. The appearance of an apparent antiferromagnetic susceptibility

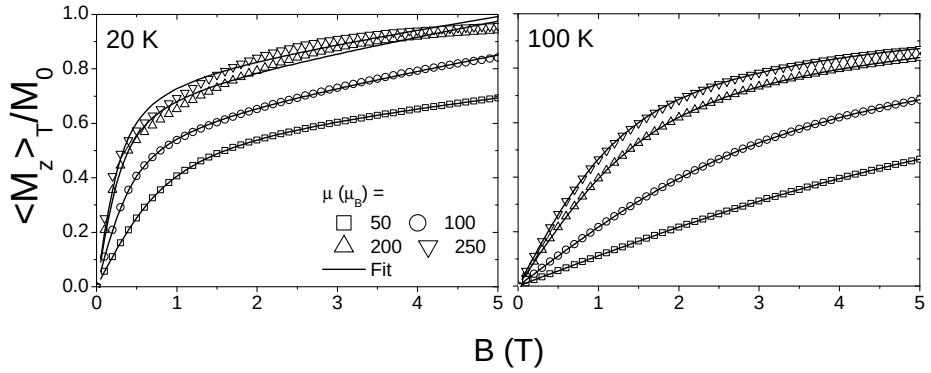


Figure 3.3: Magnetization curves simulated using Eq. (3.2) with different values of the uncompensated moment $\mu$. The lines show the fit to Eq. (3.5) (adapted from Paper II).

is also noteworthy as it was not included in the calculations; it is a consequence of using an incorrect expression to analyze the data. The antiferromagnetic susceptibility is, as it turns out, the source of the problems. In the presence of anisotropy the magnetization curve is obviously changed; however, we see from Fig. 3.2 that for intermediate values of $\zeta$ ($\sim 1-2$), the magnetization curve is close to being linear. Consequently, this change may be described by a linear background, which in the fit is interpreted as $\chi_{\rm af}$. If one had not included $\chi_{\rm af}$ in the model, the discrepancy, and hence the shortcomings of the model, would be more obvious. A distribution of volumes, as discussed by Silva et al. [39, 40], introduces the same problem. In this case the smallest particles contribute with a linear increase of the magnetization, since they are far from saturation even in a large applied field.

## 3.2 Magnetic susceptibility of an assembly of antiferromagnetic nanoparticles

As mentioned in section 1.2.3, in most cases a distribution of sizes must be taken into consideration when analyzing experimental data for magnetic nanoparticles. For ferromagnetic particles, the magnetization is, by definition, independent of volume. However, for antiferromagnetic nanoparticles, we have from section 1.3.1 that the average number of uncompensated spins equals $N^{\nu}$, with $N$ being the number of magnetic atoms. The volume and number of magnetic atoms are related as

$$N = \left( z \frac{N_{\rm A} \rho}{M_{\rm mol}} \right) V \equiv cV, \tag{3.6}$$

where $N_{\rm A}$ is Avogadro's number, $M_{\rm mol}$ and $\rho$ is the molar mass and density of the material, respectively, and $z$ is number of magnetic atoms per formula unit. These parameters are for the sake of notational convenience included in the constant $c$. Consequently, using Eq. (1.11)

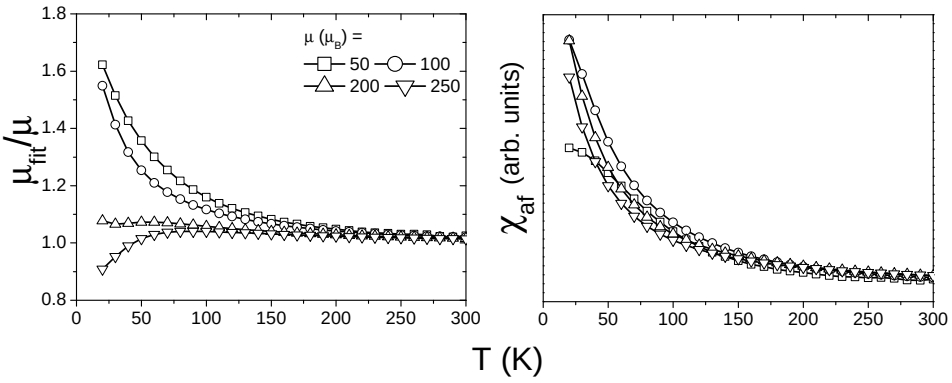


Figure 3.4: $\mu_{\rm fit}$ (apparent value of $\mu$) and $\chi_{\rm af}$ as a function of temperature for different values of $\mu$. The lines are guides to the eye.

the magnetization due to the uncompensated spins is given as

$$M = \frac{\mu}{V} = \mu_{\rm at} c^{\nu} V^{\nu-1}, \tag{3.7}$$

i.e., for an antiferromagnet where $\nu < 1$, the resulting magnetization is no longer independent of volume. This circumstance must be taken into account when studying samples in which a distribution of volumes is present. In the following, the common expressions for the ac and dc susceptibilities are therefore extended to include a volume distribution and a volume dependent magnetization.

### 3.2.1 Theoretical expressions

It is important to note that a volume distribution may be either number or volume weighted. The following example illustrates the difference. The observed magnetic moment of a single particle $i$ subjected to a magnetic field $H$, is given as

$$m_i = \chi_i V_i H, \tag{3.8}$$

where $V_i$ is the volume of the particle and $\chi_i$ its magnetic volume susceptibility. When we have a sample containing many particles

$$m_{\rm tot} = H \int_0^{\infty} \chi(V) V p_{\rm n}(V)\, {\rm d}V, \tag{3.9}$$

where $p_{\rm n}(V)\,{\rm d}V$ is the number-weighted distribution of volumes (defined as the *number* of particles with volume between $V$ and $V+$ d$V$). Normally, we normalize by the total volume (or, equivalently, the total mass) of the measured sample, in which case

$$\frac{m_{\rm tot}}{V_{\rm tot}} = \frac{H}{V_{\rm tot}} \int_0^{\infty} \chi(V) V p_{\rm n}(V)\, {\rm d}V. \tag{3.10}$$

This expression may be simplified if we introduce the volume-weighted distribution function $p_{\mathrm{v}}(V)\,\mathrm{d}V$, defined as

$$p_{\mathrm{v}}(V)\,\mathrm{d}V = \frac{1}{V_{\mathrm{tot}}} V p_{\mathrm{n}}(V)\,\mathrm{d}V, \tag{3.11}$$

in which case our expression for the observed susceptibility ($= m_{\mathrm{tot}}/V_{\mathrm{tot}}H$) becomes

$$\chi_{\mathrm{obs}} = \int_0^\infty \chi(V) p_{\mathrm{v}}(V)\,\mathrm{d}V. \tag{3.12}$$

Now, $p_{\mathrm{V}}(V)\,\mathrm{d}V$ is the *fraction* of the total volume from particles with volumes between $V$ and $V + \mathrm{d}V$. In general, it is more convenient to use the volume-weighted distribution whenever the observed signal is proportional to the volume of the sample. This is the case in magnetization measurements and Mössbauer spectroscopy. The indices n or v are in the following used to indicate whether the distribution in question is number or volume weighted.

As discussed in appendix A.1, when we use a log-normal distribution of volumes the median values of the number- and volume-weighted distributions are related as

$$V_{\mathrm{m}}^{(\mathrm{v})} = \exp(\sigma^2) V_{\mathrm{m}}^{(\mathrm{n})}, \tag{3.13}$$

while the widths of the two are the same. It should noted, though, that the normalization has to be adjusted accordingly when changing between the two.

### dc susceptibility

At a given temperature $T$, a *single* particle of volume $V$ will be unblocked (superparamagnetic) if $V < V_{\mathrm{c}}$ and blocked if $V > V_{\mathrm{c}}$, where the critical volume $V_{\mathrm{c}}$, according to Eq. (1.6), is given by

$$V_{\mathrm{c}}(T) = \frac{k_{\mathrm{B}} T \ln(\tau_{\mathrm{m}}/\tau_0)}{K}. \tag{3.14}$$

Assuming random orientations, the initial susceptibility in the blocked state is independent of temperature and is given by (for a derivation of this result, see, e.g., Chikazumi [1]).

$$\chi_0 = \frac{\mu_0 M^2}{3K}, \tag{3.15}$$

while in the superparamagnetic state, the initial susceptibility is independent of the anisotropy (as shown in Fig. 3.2), and may be found using that for small values of $x$, $\mathscr{L}(x) \approx x/3$, i.e.,

$$\chi_\infty = \frac{V \mu_0 M^2}{3 k_{\mathrm{B}} T}. \tag{3.16}$$

At a given temperature $T$, a *polydisperse* sample, described by a volume distribution $p_{\mathrm{v}}(y)\,\mathrm{d}y$ with the median volume $V_{\mathrm{m}}$, may contain a mixture of blocked and unblocked particles, where the volume fractions of the two are given as $\int_{V_c(T)/V_{\mathrm{m}}}^\infty p_{\mathrm{v}}(y)\,\mathrm{d}y$ and $\int_0^{V_c(T)/V_{\mathrm{m}}} p_{\mathrm{v}}(y)\,\mathrm{d}y$, respectively. When we consider a distribution of volumes, we may introduce the median blocking temperature $T_{\mathrm{Bm}}$ corresponding to the blocking temperature of a particle having volume $V_{\mathrm{m}}$. We have from Eq. (1.6) that the two are related as

$$k_{\mathrm{B}} T_{\mathrm{Bm}} \ln\left(\frac{\tau_{\mathrm{m}}}{\tau_0}\right) = K V_{\mathrm{m}}. \tag{3.17}$$

In a zero-field-cooled (zfc) measurement, the sample is cooled without an applied field and the susceptibility (effectively, the total magnetic moment of the sample) is recorded as a function of increasing temperature in a small applied field. The resulting susceptibility may therefore be written

$$\chi_{\rm zfc}(T) = \int_0^{V_c(T)/V_{\rm m}} \chi_\infty p_{\rm v}(y)\,{\rm d}y + \int_{V_c(T)/V_{\rm m}}^{\infty} \chi_0 p_{\rm v}(y)\,{\rm d}y. \tag{3.18}$$

In a field-cooled (fc) measurement, the sample is cooled in a small applied field, and the susceptibility is subsequently recorded also as a function of increasing temperature in a small applied field. The resulting susceptibility is derived by assuming that the susceptibility of the blocked particles equals $\chi_\infty(T_{\rm B})$, i.e.

$$\chi_{\rm fc}(T) = \int_0^{V_c(T)/V_{\rm m}} \chi_\infty p_{\rm v}(y)\,{\rm d}y + \int_{V_c(T)/V_{\rm m}}^{\infty} \chi_\infty(T_{\rm B}) p_{\rm v}(y)\,{\rm d}y. \tag{3.19}$$

If one considers the thermoremanent susceptibility $\chi_{\rm trm} = \chi_{\rm fc} - \chi_{\rm afc}$ [13], the antiferromagnetic susceptibility $\chi_{\rm af}$ and any signal from paramagnetic impurities cancel out. Using the expressions for $\chi_0$ and $\chi_\infty$ given in Eqs. (3.15) and (3.16), one obtains

$$\chi_{\rm trm}(T) = \frac{\mu_0}{3K}\left[\ln(\tau_{\rm m}/\tau_0) - 1\right] \int_{T/T_{\rm Bm}}^{\infty} M^2 p_{\rm v}(y)\,{\rm d}y. \tag{3.20}$$

This is the point where caution should be exercised. For a ferromagnetic sample one would assume that $M$ is independent of volume. However, using Eq. (3.7), we obtain

$$\chi_{\rm trm}(T) = \frac{\mu_0 M_{\rm m}^2(\nu)}{3K}\left[\ln(\tau_{\rm m}/\tau_0) - 1\right] \int_{T/T_{\rm Bm}}^{\infty} y^{2\nu-2} p_{\rm v}(y)\,{\rm d}y, \tag{3.21}$$

where $M_{\rm m}(\nu) = \mu_{\rm at} c^\nu V_{\rm m}^{\nu-1}$ is the magnetization of a particle with volume $V_{\rm m}$. If we take the derivative of this expression with respect to $T$ [13] we obtain

$$\frac{\partial \chi_{\rm trm}(T)}{\partial T} = \frac{\mu_0 M_{\rm m}^2(\nu)}{3K}\left[\ln(\tau_{\rm m}/\tau_0) - 1\right] T^{2\nu-2} p_{\rm v}(T). \tag{3.22}$$

In the ferromagnetic case ($\nu = 1$) this derivative yields directly the blocking temperature distribution but for an antiferromagnet the possible dependence on $\nu$ must be taken into consideration.

**ac susceptibility**

Subjecting a sample to an oscillating field

$$h(t) = h_0 \cos(\omega t), \tag{3.23}$$

will give rise to a time-varying magnetization

$$M(t, \omega, T) = \chi_{\rm ac}(\omega, T) h(t), \tag{3.24}$$

with a complex susceptibility that may be written

$$\chi_{\rm ac}(\omega, T) = \chi'(\omega, T) + i\chi''(\omega, T), \tag{3.25}$$

where $\chi'$ and $\chi''$ are the in-phase and out-of-phase susceptibilities, respectively. Using the model of Gittleman et al. [41] one finds for a ferromagnet

$$\chi'(\omega,T) = \frac{\mu_0 M^2}{3K}\left(\frac{KV}{k_\mathrm{B}T}\frac{1}{1+(\omega\tau)^2} + \frac{(\omega\tau)^2}{1+(\omega\tau)^2}\right) \tag{3.26a}$$

$$\chi''(\omega,T) = \frac{\mu_0 M^2}{3K}\left(\frac{\omega\tau}{1+(\omega\tau)^2} - \frac{KV}{k_\mathrm{B}T}\frac{\omega\tau}{1+(\omega\tau)^2}\right), \tag{3.26b}$$

where $\tau$, which is given by Eq. (1.6), also depends on temperature. For an antiferromagnet, the possible volume dependence of $M$ must be taken into account; with a distribution of volumes we therefore obtain

$$\chi'(\omega,T) = \frac{\mu_0 M_\mathrm{m}^2(\nu)}{3K}\int_0^\infty \left(\frac{KV_\mathrm{m}}{k_\mathrm{B}T}\frac{y}{1+(\omega\tau)^2} + \frac{(\omega\tau)^2}{1+(\omega\tau)^2}\right) y^{2\nu-2} p_\mathrm{v}(y)\,\mathrm{d}y \tag{3.27a}$$

$$\chi''(\omega,T) = \frac{\mu_0 M_\mathrm{m}^2(\nu)}{3K}\int_0^\infty \left(\frac{\omega\tau}{1+(\omega\tau)^2} - \frac{KV_\mathrm{m}}{k_\mathrm{B}T}\frac{y\omega\tau}{1+(\omega\tau)^2}\right) y^{2\nu-2} p_\mathrm{v}(y)\,\mathrm{d}y. \tag{3.27b}$$

## 3.3 Ferritin

Ferritin is a protein which in many living organisms, including mammals, is responsible for storing iron [42, 43]. Structurally it consists of a spherical iron oxide core surrounded by a protein shell. The size of the core is variable, depending on the iron uptake, but may be up to approximately 7 nm in diameter. The iron oxide in the core is antiferromagnetic [44, 45]; however, the Néel temperature has not been uniquely determined (values ranging from 240 K [46] to ∼500 K [47] have been reported). The iron oxide is generally accepted to be similar to ferrihydrite (5 $Fe_2O_3$· 9 $H_2O$) [42]. Due to the shell, in which iron is practically absent, each iron oxide core is separated from neighboring cores rendering interactions between the various cores negligible. For this reason, and since it is readily available commercially, ferritin is often used to study the basic properties of non-interacting magnetic nanoparticles. In Paper IV we use magnetization data obtained for ferritin to demonstrate the possible errors resulting from an incorrect use of models.

Fig. 3.5(a) shows a high-resolution TEM (HRTEM) image of our ferritin sample. An analysis of several such images, under the assumption that the particles are spherical, yielded the size histogram shown in Fig. 3.5(b). This size histogram could be satisfactory fitted with a log-normal distribution of diameters, yielding a median diameter $d_\mathrm{m} = 5.85 \pm 0.03$ nm and a width $\sigma_\mathrm{d} = 0.107 \pm 0.008$. Using Eq. (3.13), we find that this corresponds for a volume-weighted volume distribution to $V_\mathrm{m} = 1.16 \cdot 10^{-25}$ m$^3$ and $\sigma_\mathrm{v} = 0.321$.

### 3.3.1 Peak analysis

In a sample which undergoes a transition from a unblocked to a blocked state, a peak will appear in both $\chi'$ and $\chi''$. By varying $\omega$, the position (in temperature) of this peak as a function of $\tau_\mathrm{m} = 1/\omega$ may be obtained. Fig. 3.6 shows the in-phase and out-of-phase susceptibility of the ferritin sample studied in Paper IV. Eq. (1.6) may be written

$$\ln(\omega) = \ln(1/\tau_0) - \frac{KV_\mathrm{m}}{k_\mathrm{B}}\frac{1}{T_\mathrm{Bm}}, \tag{3.28}$$

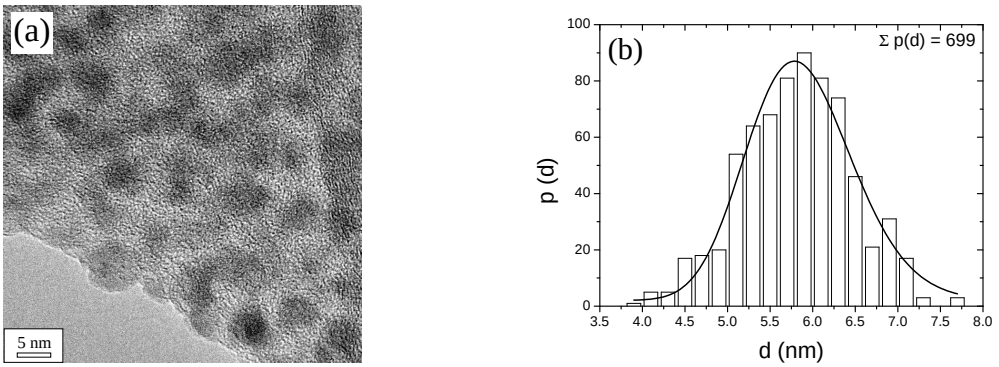


Figure 3.5: (a) HRTEM image of the ferritin sample (b) size histogram obtained from the analysis of a total of 699 particles (adapted from Paper IV).

hence if it is assumed that the peak temperature $T_{\rm p}$ equals the median blocking temperature $T_{\rm Bm}$, an analysis of $\ln(\omega)$ vs $1/T_{\rm Bm}$ will yield $\tau_0$ as well as $KV_{\rm m}/k_{\rm B}$. This is a common way to analyze ac magnetization data, which has been applied both to ferro-, ferri-, and antiferromagnetic materials. However, Fig. 3.7 shows results obtained from the data shown in Fig. 3.6. It is quite obvious that the data from $\chi'$ and $\chi''$ do not fall on the same straight line. Table 3.1 lists the values of $KV_{\rm m}$ and $\tau_0$ obtained when these data are fitted with Eq. (3.28). It is observed that different values are obtained from the $\chi'$ and $\chi''$ peak positions.

The problem is that in the presence of a distribution of volumes, the observed peak temperature does *not* correspond to the median blocking temperature. This was already demonstrated by Gittleman et al. [41] who considered a number of rather simple distributions and found in general that $T_{\rm p} = \beta T_{\rm Bm}$, where the value of $\beta$ depends on the distribution function and its parameters. Jiang and Mørup [48] later considered the peak position of the zero-field-cooled data (which resembles $\chi'$) using a log-normal distribution of volumes, and found that $\beta$ depends not only on the width of this distribution, but also on the class of magnetic material, i.e., different results were obtained for ferromagnetic and antiferromagnetic materials.

In Paper III we extend the analysis of Jiang and Mørup [48] to include ac susceptibility and several types of antiferromagnetic materials (Jiang and Mørup [48] only considered $\nu = 1/3$). Using Eqs. (3.27a) and (3.27b), a number of susceptibility curves were simulated for suitable values of the various parameters (chosen to be similar to those of ferritin). In each of these curves the peak position was determined and compared to the true blocking temperature. In general, we find that

$$T_{\rm p} = \alpha + \beta T_{\rm Bm}, \tag{3.29}$$

where $\alpha$ and $\beta$ are different for the $\chi'$ and $\chi''$ components and depend on the width of the distribution $\sigma_{\rm v}$, the class of magnetic material, and $\tau_0$. We write $\alpha'$ and $\beta'$ for $\chi'$ and $\alpha''$ and $\beta''$ for $\chi''$. When Eq. (3.29) is inserted into Eq. (3.28) one obtains

$$\ln(\omega) = \ln(1/\tau_0) - \frac{KV_{\rm m}}{k_{\rm B}} \frac{\beta}{T_{\rm p} - \alpha}, \tag{3.30}$$

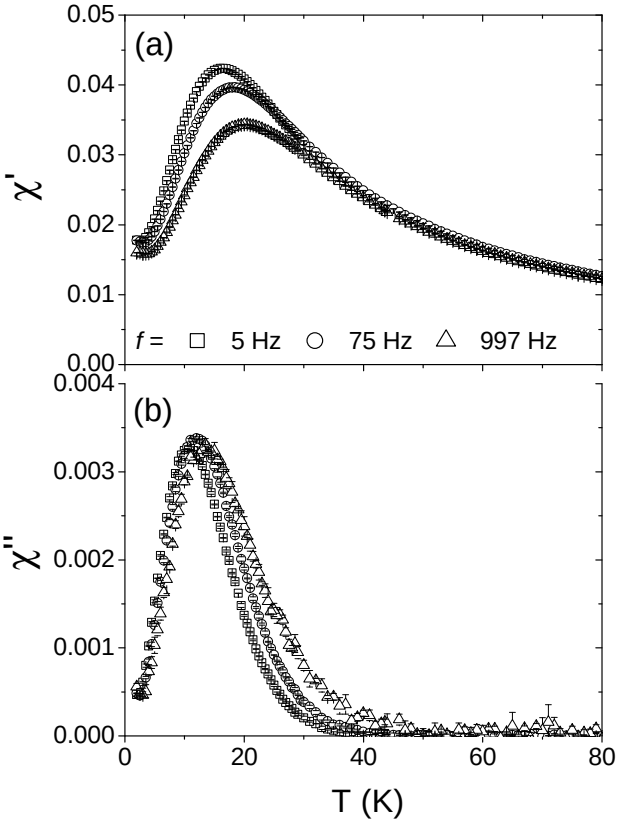


Figure 3.6: Ac data for ferritin: (a) in-phase and (b) out-of-phase components (from Paper IV).

which is, in principle, no longer linear in $T_\mathrm{p}$, although it will appear to be so. The interesting question is which parameters one obtains if the above expression is fitted with a straight line. This may be found by a first order Taylor expansion of Eq. (3.30), giving

$$\ln(\omega) \approx \ln(1/\tau_0) + \frac{KV_\mathrm{m}}{k_\mathrm{B}} \frac{\alpha\beta}{(T_0-\alpha)^2} - \frac{KV_\mathrm{m}}{k_\mathrm{B}} \frac{T_0^2\beta}{(T_0-\alpha)^2} \frac{1}{T_\mathrm{p}}, \tag{3.31}$$

where $1/T_0$ is the point of origin. From this we obtain the apparent intersect at $(1/T_\mathrm{p}) = 0$

$$\ln(\tau_0)_\mathrm{apparent} = \ln(\tau_0) - \frac{KV_\mathrm{m}}{k_\mathrm{B}} \frac{\alpha\beta}{(T_0-\alpha)^2}, \tag{3.32}$$

and the apparent slope

$$\left(\frac{KV_\mathrm{m}}{k_\mathrm{B}}\right)_\mathrm{apparent} = \frac{KV_\mathrm{m}}{k_\mathrm{B}} \frac{T_0^2\beta}{(T_0-\alpha)^2}. \tag{3.33}$$

By introducing the temperature $T^*$ fulfilling $T_0 = \alpha + \beta T^*$, the relative errors resulting from

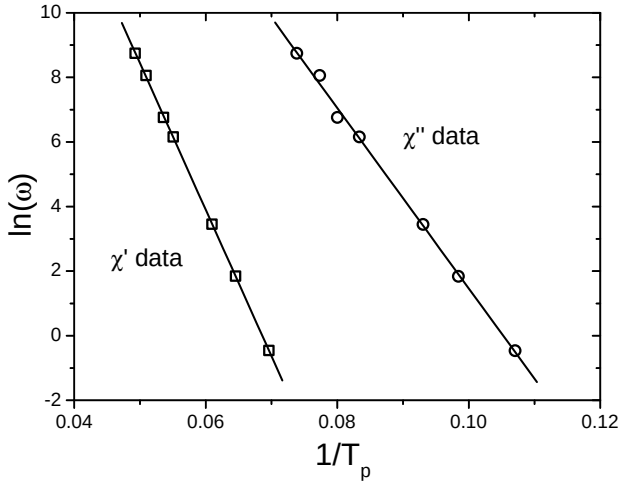


Figure 3.7: Ferritin: $\ln(\omega)$ vs. the reciprocal peak temperature of the $\chi'$ and $\chi''$ data. The lines show the fit with Eq. (3.28) (from Paper IV).

taking $T_\mathrm{p}$ as $T_\mathrm{Bm}$ becomes

$$\frac{(\tau_0)_\mathrm{apparent}}{\tau_0} = \exp\left[-\frac{KV_\mathrm{m}}{k_\mathrm{B}(T^*)^2}\frac{\alpha}{\beta}\right] \tag{3.34a}$$

$$\frac{(KV_\mathrm{m})_\mathrm{apparent}}{KV_\mathrm{m}} = \beta\left(1 + 2\frac{\alpha}{\beta}\frac{1}{T^*} + \frac{\alpha^2}{\beta^2}\frac{1}{(T^*)^2}\right). \tag{3.34b}$$

It turns out that $\alpha$ and $\beta$ for $\chi'$ and $\chi''$ are correlated. As Figs. 3.8 and 3.9 show, the ratios $\alpha/\beta$ and $\beta'/\beta''$ are functions of $\sigma_\mathrm{v}$ but independent of $\nu$ while somewhat different curves are found for different values of $\tau_0$. Consequently, the ratio between the values of $KV_\mathrm{m}/k_\mathrm{B}$ obtained from $\chi'$ and $\chi''$ data should be the same for ferromagnets and antiferromagnets, since this ratio, according to Eq. (3.34b), is approximately given by $\beta'/\beta''$. Likewise, assuming that $T^*$ is independent of $\tau_0$ and $\nu$, we may conclude that the relative error in the determination of $\tau_0$ does not depend on $\nu$. As it turns out, under ideal circumstances, this is a quite reasonable assumption. Consider the following: When we do linear regression, we optimize the parameters so that

$$\chi^2 = \sum_i (y_\mathrm{obs} - y_\mathrm{calc})^2 \tag{3.35}$$

is minimized. In the ideal case where $y_\mathrm{obs}$ are given according to Eq. (3.30) we find

$$\chi^2 \approx \sum_i \left(\frac{KV_\mathrm{m}}{k_\mathrm{B}}\right)^2 \frac{(\alpha\beta)^2}{([\alpha/T_0]-1)^6}\left(\frac{1}{T_0} - \frac{1}{T_{i,\mathrm{p}}}\right)^4, \tag{3.36}$$

where we have assumed that $y_\mathrm{obs} - y_\mathrm{calc}$ equals the second order term of the Taylor expansion.

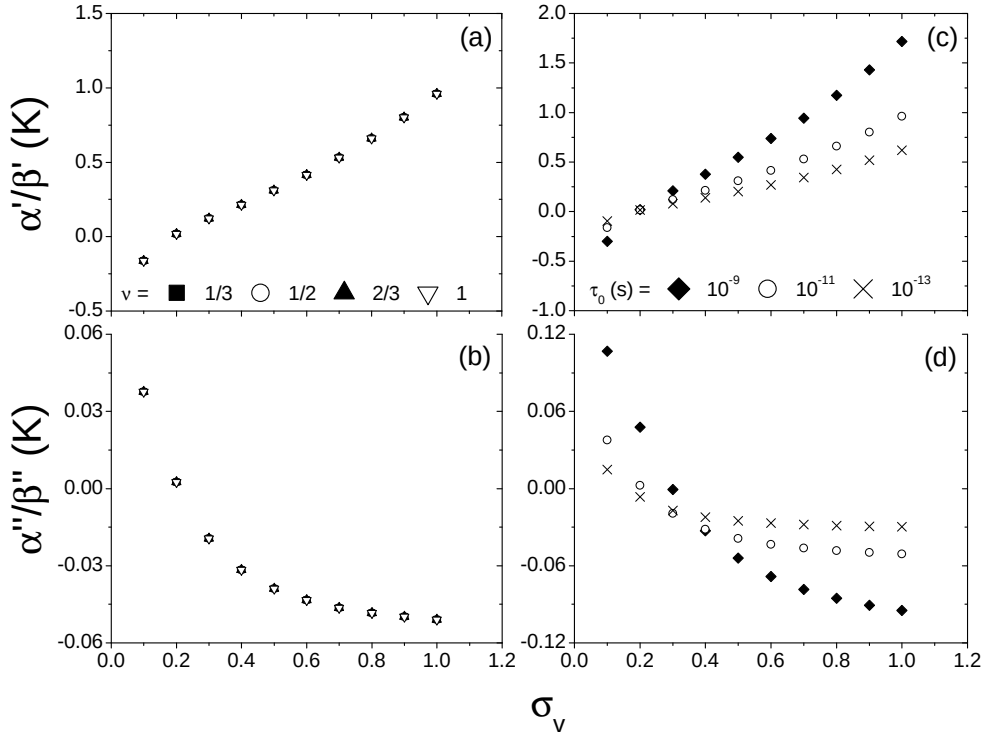


Figure 3.8: The ratio $\alpha/\beta$ as a function of $\sigma_\mathrm{v}$ for (a,b) $\tau_0 = 10^{-11}$ s and different values of $\nu$ and (c,d) $\nu = 1/2$ and different values of $\tau_0$.

A bit of algebra reveals that $\chi^2$ is minimized when

$$T_0 = \left( \frac{1}{N} \sum_{i=1}^{N} \frac{1}{T_{i,\mathrm{p}}} \right)^{-1} . \tag{3.37}$$

We now write $T_{i,\mathrm{p}} = \alpha + \beta T_{i,\mathrm{B}}$ and find for $T^*$

$$T^* = \left( \frac{1}{N} \sum_{i=1}^{N} \frac{1}{(\alpha/\beta) + T_{i,\mathrm{B}}} \right)^{-1} - \frac{\alpha}{\beta}. \tag{3.38}$$

The values of $T_{i,\mathrm{B}}$ do not depend on neither $\alpha$ nor $\beta$. Consequently, in the ideal case where $y_\mathrm{obs}$ are given by Eq. (3.30), the value of $T^*$ does not depend on $\nu$ and neither does, according to Eq. (3.34a), the relative error in $\tau_0$. Under less ideal experimental conditions, $y_\mathrm{obs}$ will probably be subject to some noise. Assuming that the data do not suffer from systematic errors, i.e., that the experimental noise is randomly distributed, the noise should average out and the value of $T_0$ should still be given by the average expressed in Eq. (3.37).

As the results from Paper III show, the values of $\alpha''$ and $\beta''$ for $\nu = 1$ are such that the error in the determination of $\tau_0$ and $KV_\mathrm{m}/k_\mathrm{B}$ is minimal. For $\nu < 1$, however, only $\tau_0$

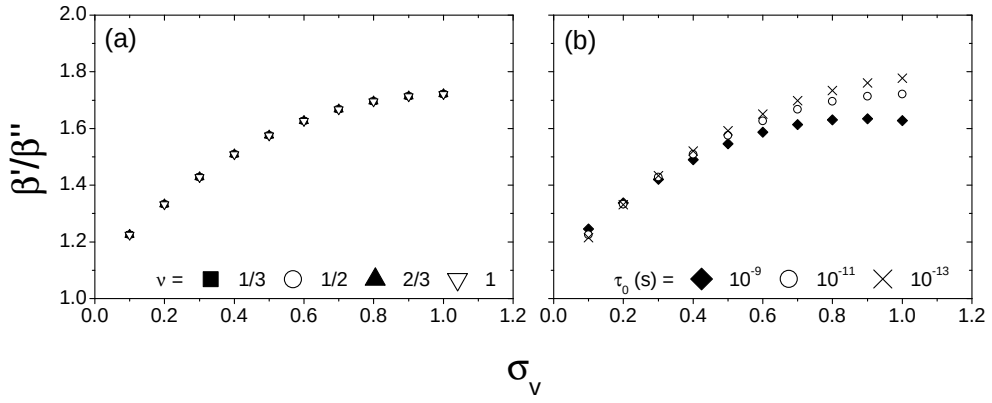


Figure 3.9: The ratio $\beta'/\beta''$ as a function of $\sigma_v$ for (a) $\tau_0 = 10^{-11}$ s and different values of $\nu$ and (b) $\nu = 1/2$ and different values of $\tau_0$.

may be correctly determined from the $\chi''$ data. In all other cases erroneous values will be obtained. It is noteworthy that one will *always* obtain inaccurate values of $\tau_0$ and $KV_m/\tau_0$ from a peak analysis of the $\chi'$ data considering how often these parameter are obtained from such an analysis in the literature.

The analysis show that the ratio between $KV_m/k_B$ obtained from the peak positions of the $\chi'$ and $\chi''$ data depends on $\beta'/\beta''$, which is a function of $\sigma_v$. For our ferritin data, we find that the ratio of $KV_m/k_B$ obtained from the $\chi'$ and $\chi''$ data equals approximately 1.6. However, from Fig. 3.9(b) we see that this ratio cannot be used to determine $\sigma_v$ unless we know $\tau_0$. Fortunately, as the analysis show, the value of $\tau_0$ can be determined with good accuracy from the $\chi''$ data. Hence, the parameters of the size distribution can in principle be obtained from the peak positions, although only through a somewhat cumbersome analysis of the data.

| Method | $KV_m/k_B$ (K) | $\tau_0$ (s) | $\sigma_v$ | $\nu$ |
|---|---|---|---|---|
| $\chi'$, peak positions | $454 \pm 2$ | $(3.1 \pm 0.3) \cdot 10^{-14}$ | - | - |
| $\chi''$, peak positions | $279 \pm 6$ | $(2 \pm 1) \cdot 10^{-13}$ | - | - |
| $\chi''$, full curve analysis | $341 \pm 2$ | $(2 \pm 1) \cdot 10^{-13}$ | $0.50 \pm 0.01$ | $0.46 \pm 0.01$ |
| $\chi_{trm}$ | $332 \pm 3$ | $[2 \cdot 10^{-13}]$ | $0.51 \pm 0.01$ | [1/2] |
| Mössbauer data | $339 \pm 4$ | $[2 \cdot 10^{-13}]$ | $0.52 \pm 0.02$ | - |

Table 3.1: Parameters obtained for ferritin. [ ] indicates that the parameter was not part of the fit. For $\chi_{trm}$ and the Mössbauer data, $\tau_0$ was only used to calculate $KV_m/k_B$.

### 3.3.2 Full-curve analysis

The simplest and most straightforward way to take into account the parameters of the volume distribution is to fit the experimental data directly with the appropriate expressions, such as

Eq. (3.27). This is done in Paper IV, where the volume distribution was also obtained directly from TEM images, and indirectly from Mössbauer spectroscopy measurements.

From the dc data (zfc and fc susceptibilities) we obtained the thermoremanent data, which when differentiated gave the blocking temperature distributions shown in Fig. 3.10. This serves to demonstrate that different distributions are obtained for different values of $\nu$, as expected from Eq. (3.22). In the present case, only the distribution obtained with $\nu = 1/2$ could be satisfactory fitted with a log-normal distribution, yielding the parameters $T_{\mathrm{B}} = 9.8 \pm 0.1$ K and $\sigma_{\mathrm{v}} = 0.51 \pm 0.01$. The value $\nu = 1/2$ was chosen since the ferrihydrite in the core is known to have a partly disordered structure [49].

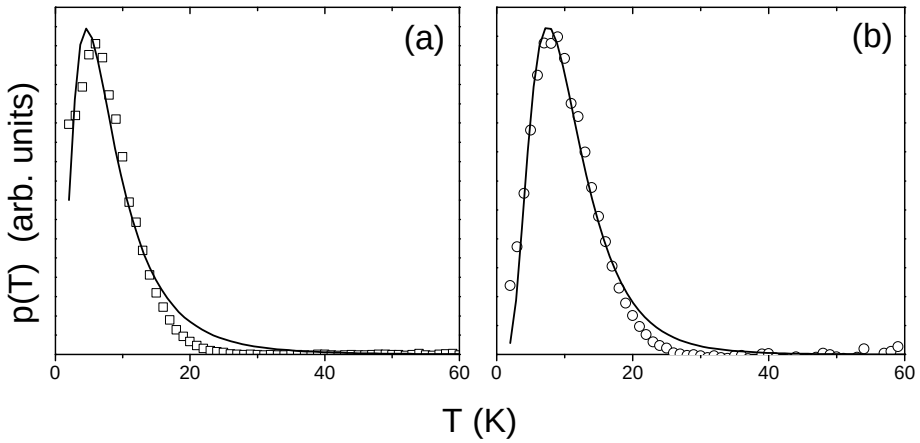


Figure 3.10: The blocking temperature distribution $p(T)$ obtained from the thermoremanent data using Eq. (3.22) with (a) $\nu = 1$ and (b) $\nu = \frac{1}{2}$. The full lines show the fit with a log-normal distribution of blocking temperatures.

The ac data were fitted with Eq. (3.27). It was observed that quite different parameters were obtained for the $\chi'$ and $\chi''$ data. We suspect that this may be due to the presence of a paramagnetic impurity. Since the out-of-phase data are not affected by such an impurity we consider the parameters obtained in the fit of the $\chi''$ data, $KV_{\mathrm{m}} = 341 \pm 2$ K, $\nu = 0.46 \pm 0.01$, $\sigma_{\mathrm{v}} = 0.50 \pm 0.01$ and $\tau_0 = (2 \pm 1) \cdot 10^{-13}$ s, to be the most reliable. It is important here, again, to note the importance of including the volume dependence of the magnetization. Fits of a similar quality could be achieved if $\nu$ was locked to 1 *and* $M_{\mathrm{m}}$ was left as a free parameter. However, the estimated value of $KV_{\mathrm{m}}$ differed considerably from that obtained when $\nu$ was a free parameter. The explanation for this is that, as discussed in appendix A.1, if $p(x)\,\mathrm{d}x$ is a log-normal distribution, so $x^n p(x)\,\mathrm{d}x$ will *appear* to be, although with a different normalization and median value. Consequently, if the magnetization is just introduced as a scale parameter instead of being calculated from $\nu$, the shortcomings of using $\nu = 1$ will not be apparent.

In the Mössbauer spectra the relative area of the sextet component as a function of temperature $A(T)$ was determined. As discussed in section 2.1.3, this area represents the fraction

of particles still being blocked and may be calculated using

$$A(T) = A_0 \int_T^\infty p_{\mathrm{T}}(T')\,\mathrm{d}T', \tag{3.39}$$

where $p_{\mathrm{T}}(T')\,\mathrm{d}T'$ is the blocking temperature distribution and $A_0$ is the area of the sextet at zero temperature. When the observed area fractions were fitted with Eq. (3.39), if $A_0$ was locked to 100%, rather unsatisfactory fits were obtained. However, if $A_0$ was a free parameter, the quality of the fit was significantly improved, yielding the parameters $\sigma_{\mathrm{v}} = 0.52 \pm 0.02$, $T_{\mathrm{Bm}} = 40.8 \pm 0.5$ K, and $A_0 = 87\%$. It is puzzling that $A_0$ differs from 100%, however, it could be due to a paramagnetic impurity, the presence of which the ac susceptibility data also seem to suggest. St. Pierre et al. [50] observed a doublet in the Mössbauer spectra at very low temperature, and in this case attributed it to very small particles.

While the full curve analysis of the $\chi''$ data yielded directly the median energy barrier, in the cases of Mössbauer spectroscopy and dc magnetization measurements, only the median blocking temperature was obtained. A meaningful comparison requires that we calculate the median energy barrier in these cases as well. The ratio between the two should be given by $\ln(\tau_{\mathrm{m}}/\tau_0)$, and for the dc data we use $\tau_0 = 2 \cdot 10^{-13}$ s as found from the ac data analysis and $\tau_{\mathrm{m}} = 100$ s (a value typically assumed). In Mössbauer spectroscopy the value of $\tau_{\mathrm{m}}$ is usually assumed to be $2 - 5 \cdot 10^{-9}$ s. However, we have simulated Mössbauer spectra of relaxing particles in order to obtain a better estimate of this parameter. We used for the simulations the model of Blume and Tjon [22] in the presence of a distribution of volumes. The results of these simulations were briefly discussed in section 1.2.2. The resulting spectra were then fitted with a distribution of sextets and a singlet. Fig. 3.11 shows the resulting area of the singlet as a function of $\sigma_{\mathrm{v}}$ and $B_{\mathrm{hf}}$ for $\tau_0 = 2 \cdot 10^{-13}$ s. It is important to note that this approach is deliberately wrong as the lines in the Mössbauer spectra of relaxing particles are not Lorentzian in shape. Using sextets, doublets and singlets in the fit is therefore, at least in principle, not possible. However, the results are noteworthy considering that this is the most common way to analyze such spectra. As Fig. 3.11 shows, the value of $\ln(\tau/\tau_0) = KV_{\mathrm{m}}/k_{\mathrm{B}}T$ where the singlet constitute 50% of the spectrum, decreases with increasing $\sigma_{\mathrm{v}}$. Consequently, the value of $\ln(\tau_{\mathrm{m}}/\tau_0)$ that we should use to obtain the median energy barrier from our Mössbauer spectra is smaller than that obtained with $2 - 5 \cdot 10^{-9}$ s. A close inspection of the results shown in Fig. 3.11 reveals that for $\sigma_{\mathrm{v}} = 0.5$, $\ln(\tau_{\mathrm{m}}/\tau_0) \approx 8.3$, hence $KV_{\mathrm{m}}/k_{\mathrm{B}} = 339 \pm 4$ K.

Table 3.1 lists all the parameter obtained for ferritin with the different methods. A comparison of the parameters obtained for the different data sets and methods clearly shows that consistent results are obtained when the volume dependence of the magnetization due to uncompensated spins is taken into account. However, the width obtained directly from the TEM images is somewhat smaller. This could possibly be due to a volume dependence of the anisotropy constant $K$.

## 3.4 Summary

While antiferromagnetic nanoparticles may exhibit properties not common for other classes of magnetic materials, it is important to keep in mind that certain observations may be the result of an incorrect analysis of the data. In this chapter it has been shown that when studying antiferromagnetic nanoparticles, one should not blindly use models originally developed

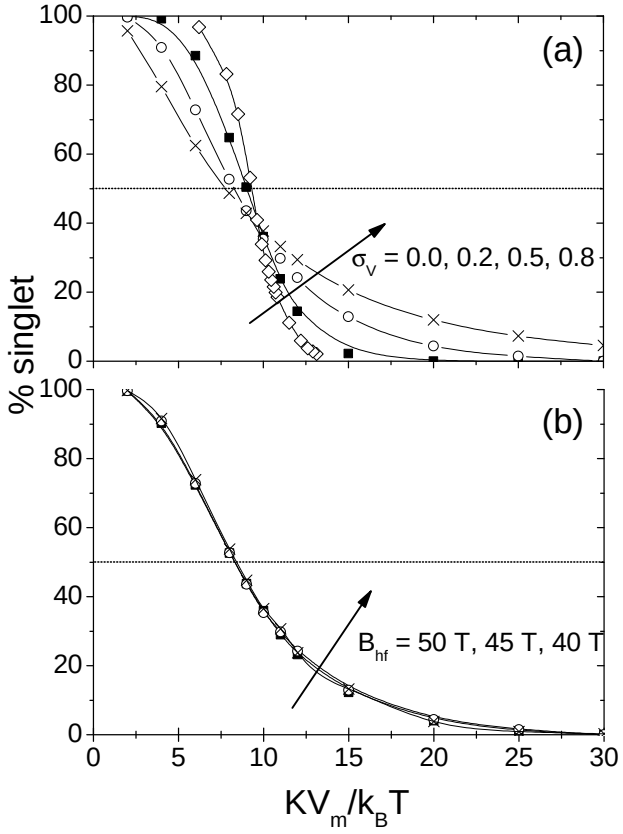


Figure 3.11: Singlet area (%) as a function of $KV_{\mathrm{m}}/k_{\mathrm{B}}T$ for (a) $B_{\mathrm{hf}} = 45$ T and different values of $\sigma_{\mathrm{v}}$ and (b) $\sigma_{\mathrm{v}} = 0.5$ and different values of $B_{\mathrm{hf}}$. In both cases, $\tau_0 = 2 \cdot 10^{-13}$ s. The lines are guides to the eye.

for ferromagnetic materials. The problem with such models is that they are often based on assumptions that are not fulfilled for antiferromagnetic nanoparticles. As shown here, when considering magnetization curves of antiferromagnetic nanoparticles, it should be kept in mind that even in an applied field of considerable strength, the associated Zeeman energy may be small compared to the anisotropy energy due to the minuscule magnetic moment of antiferromagnetic nanoparticles. Consequently, magnetization curves cannot be analyzed with a simple Langevin function modified to take into account an antiferromagnetic susceptibility. The second example concerns a volume distribution, which must often be taken into consideration when experimental data are analyzed. However, for antiferromagnetic nanoparticles, the volume dependence of the magnetization is often ignored. In both cases, neglecting to take into consideration these specific properties of antiferromagnetic nanoparticles results in erroneous estimates of the parameters, which further may exhibit, for instance, an incorrect temperature behavior.

# Chapter 4

# Uniform spin precession

The magnetic configurations shown in Fig. 1.1, typical of the various classes of magnetic materials, are only realized at absolute zero temperature. At non-zero temperatures, excitations of the spin structure take place leading to a reduction of the magnetic moment. In nanoparticles at low temperatures, these excitations are predominately in the form of collective magnetic excitations, which may be described as a uniform precession of the spins in combination with transitions between states with different precession angles. The energy of the uniform mode of precession in antiferromagnets has been extensively studied [51–54] as it is of relevance to magnetic resonance experiments. It has also been shown that the two sublattices in an antiferromagnet are not exactly antiparallel during the precession [51, 52] and it has been suggested [55] that this difference in angles may lead, in nanoparticles, to a small thermoinduced moment that increases with temperature.

As discussed in chapter 3 it has been common to disregard certain properties of the uncompensated moment, such as its volume dependence. However, it has also been common to completely neglect its existence. In this chapter we consider two such cases where the effects of an uncompensated moment have not previously been considered, namely (a) the energy levels of the uniform mode of precession and (b) the thermoinduced moment.

## 4.1 Spin waves

In general, the excitations of the spin structure are in the form of spin waves and a simple calculation yields the result that for a one dimensional ferromagnetic chain of particles $\omega \propto q^2$, where $q$ is the wave vector of the spin wave. The spin waves are quantized in the same way as lattice vibrations and are denoted magnons. For a certain mode $q$, the total energy is given by

$$E_{\mathrm{q}} = \left( n_{\mathrm{q}} + \frac{1}{2} \right) \hbar \omega_{\mathrm{q}}, \tag{4.1}$$

where $n_{\mathrm{q}}$ is the number of magnons. The average $\langle n_{\mathrm{q}} \rangle$ is given by the Planck distribution function, i.e., $\langle n_{\mathrm{q}} \rangle = 1/[\exp(\hbar\omega_{\mathrm{q}}/k_{\mathrm{B}}T) - 1]$. This leads at low temperatures to the well-known Bloch $\mathrm{T}^{3/2}$ law for the magnetization $M$

$$\frac{\langle M(T) \rangle}{M(0)} = 1 - cT^{3/2}, \tag{4.2}$$

where $c$ is some constant. In an antiferromagnet, $\omega \propto q$ [56] which leads to a $T^2$ dependence of the magnetization. An in-depth discussion of spin waves can be found in the book by Martin [57].

In analogy with phonons, the separation, in $q$-space, between adjacent $q$ states scales inversely with the size $d$ of the sample. For example, it has been shown that in a particle of diameter $d$, the first $q \neq 0$ state has $q \approx 4.5/d$ [58]. Consequently, the $q = 0$ mode is expected to be predominant in nanoscale systems, as this state has the lowest energy and is separated from the $q \neq 0$ states by a considerable energy gap. For the 16 nm hematite particles studied by Klausen et al. [59] an energy gap of 5.6 meV (65 K in units of temperature) was estimated, whereas for the 8 nm nanoparticles studied in Paper V, a gap of more than 10 meV was expected.

The collective magnetic excitations of nanoparticles correspond to the $q = 0$ mode. They give rise to a linear decrease of the magnetization at low temperatures [60]

$$\frac{\langle M(T)\rangle}{M(0)} = 1 - \frac{k_{\mathrm{B}}T}{2KV}, \tag{4.3}$$

i.e., the magnetization of nanoparticles is expected to display a different temperature dependence than in bulk.

## 4.2 The uniform ($q = 0$) mode of precession

We take into account an uncompensated moment by considering an antiferromagnetic particle as a ferrimagnet. The energy of the uniform mode of precession for such a system was first found by Kittel [51]. The derivation is for completeness repeated in the following. The problem may be treated quantum mechanically by solving the equations of motion for the spin operators; however, this approach is rather tedious, and as recently shown [61] one arrives at the same result. So, in the following we will consider the total spin of each sublattice as a classical vector and solve the equations of motion

$$\frac{\partial \vec{M}_i}{\partial t} = \gamma_i(\vec{M}_i \times \vec{H}_{\mathrm{m},i}), \tag{4.4}$$

where $\gamma_i$ is the gyromagnetic ratio for the $i$'th sublattice. In the following we consider only low temperatures where the precession angles are small. The magnetic exchange coupling is in the mean field approximation represented by the exchange fields $\vec{H}_{\mathrm{E},i}$, and the magnetic anisotropy, which is assumed to be uniaxial, is represented by the anisotropy fields $\vec{H}_{\mathrm{K},i}$. These fields constitute the internal magnetic field in which the spins precess; to this we add an external field $\vec{H}_0$ such that

$$\vec{H}_{\mathrm{m},i} = \vec{H}_0 + \vec{H}_{\mathrm{E},i} + \vec{H}_{\mathrm{K},i}. \tag{4.5}$$

In this derivation we limit ourselves to the case of two sublattices. This situation is depicted in Fig. 4.1. The exchange fields are given as $\vec{H}_{\mathrm{E},1} = \lambda_{12}\vec{M}_2$ and $\vec{H}_{\mathrm{E},2} = \lambda_{12}\vec{M}_1$, where $\lambda_{12}$ is the exchange coupling constant. To simplify the calculations it is assumed that the external field is applied along $z$ (unit vector $\hat{z}$), i.e., $\vec{H}_0 = H_0\hat{z}$ which is also the easy axis of magnetization (i.e. the anisotropy axis) such that $\vec{H}_{\mathrm{K},1} = (K/|\vec{M}_1|)\hat{z}$ and $\vec{H}_{\mathrm{K},2} = -(K/|\vec{M}_2|)\hat{z}$. As we are considering an antiferromagnetic system, we assume that all the sites are identical, hence we

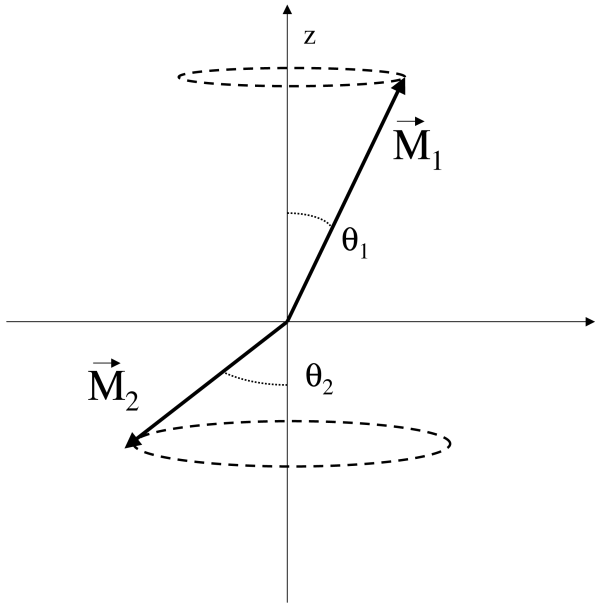


Figure 4.1: An antiferromagnetic system (adapted from Paper VI). Please note that the differences in angles and lengths are exaggerated.

may further simplify the expressions by choosing $\gamma_1 = \gamma_2 = \gamma$ and $|H_{\mathrm{K},1}| \approx |H_{\mathrm{K},2}| \equiv |H_{\mathrm{K}}|$. For each sublattice we write

$$\vec{M}_i(t) = \begin{pmatrix} M_i^x(t) \\ M_i^y(t) \\ M_i^s + M_i^z(t) \end{pmatrix}, \tag{4.6}$$

where $M_i^s$ is, approximately, the saturation magnetization. If we write the time dependent part of these components as $e^{i\omega t}$, Eq. (4.4) may be written as the eigenequation

$$\mathbb{R} \begin{pmatrix} M_1^x \\ M_1^y \\ M_2^x \\ M_2^y \end{pmatrix} = \omega \begin{pmatrix} M_1^x \\ M_1^y \\ M_2^x \\ M_2^y \end{pmatrix}, \tag{4.7}$$

where $\mathbb{R}$ is given by

$$\mathbb{R} = \begin{pmatrix} 0 & -ia & 0 & -ib \\ ia & 0 & ib & 0 \\ 0 & id & 0 & -ic \\ -id & 0 & ic & 0 \end{pmatrix}, \tag{4.8}$$

with $a = \gamma(H_0 + \lambda_{12} M_2^s + H_{\mathrm{K}})$, $b = \gamma \lambda_{12} M_1^s$, $c = \gamma(H_0 - \lambda_{12} M_1^s - H_{\mathrm{K}})$, and $d = \gamma \lambda_{12} M_2^s$. $M_1^z(t) \approx 0$ and $M_2^z(t) \approx 0$ as they are proportional to factors of the type $M_1^x M_2^y$ and as we are only considering small precession angles, such factors are negligible.

When solving Eq. (4.7) one finds the following eigenstates

$$(M_1^x, M_1^y, M_2^x, M_2^y) = \begin{cases} (-i\eta_+, -\eta_+, i, 1) \\ (i\eta_-, -\eta_-, -i, 1) \\ (-i\eta_-, -\eta_-, i, 1) \\ (i\eta_+, -\eta_+, -i, 1) \end{cases} \tag{4.9}$$

where the factor $\eta_\pm$ is given by

$$\eta_\pm = 1 + \frac{\delta^2}{2} + \frac{\xi}{2} \pm \frac{1}{2}\sqrt{\delta^4 + 2\delta^2(2+\xi) + \xi^2}. \tag{4.10}$$

Here, $\xi = (M_1^s - M_2^s)/M_2^s$ and $\delta = \sqrt{2H_\mathrm{K}/H_\mathrm{E}}$. If we introduce the vector $M_i^{xy} \equiv (M_i^x, M_i^y)$ describing the precession of the magnetization of sublattice $i$ in the $xy$ plane, all of the above modes may be written $\vec{M_1^{xy}} = -\eta_\pm \vec{M_2^{xy}}$. Hence, we are only dealing with two distinct states. The corresponding frequencies are found to be

$$\frac{\omega_\pm}{\gamma} = H_0 - \frac{\xi H_\mathrm{E}}{2} \pm H_\mathrm{E}\sqrt{\frac{\delta^4}{4} + \delta^2(1+\frac{\xi}{2}) + \frac{\xi^2}{4}}, \tag{4.11}$$

which for $\xi = 0$ and $\delta \ll 1$ gives

$$\omega_\pm \approx \gamma\left[H_0 \pm \sqrt{2H_\mathrm{K}H_\mathrm{E}}\right] \tag{4.12}$$

as expected for an antiferromagnet [51]. Using inelastic neutron scattering, it is possible to determine at which energies an incoming neutron is able to induce a transition between two different states. Such two states could constitute two different precession states of the uniform mode, and as it turns out, the typical neutron energy is in the same range as the typical precession energies, which hence may be experimentally determined. In Paper V, 8 nm particles of hematite were studied with inelastic neutron scattering. In the paper, the results obtained for coated and non-coated particles were compared. It should be noted, though, that I did not take part in acquiring these data. In the following, we will only consider the results for the coated particle, as these were assumed to be non-interacting. For these particles, it was found that the energy $\hbar\omega$ of the uniform mode was considerably different from that expected for a perfect antiferromagnet (Eq. (4.12)). This discrepancy may be explained by the influence of the uncompensated moment. Fig. 4.2 shows $\varepsilon_0^{(\pm)} = \hbar\omega_\pm$ as function of $\xi$ calculated using Eq. (4.11) with $\mu_0 H_0 = 0$ T, $\mu_0 H_\mathrm{E} = 900$ T, and $\mu_0 H_\mathrm{K} = 0.014$ T (which are the values found for the non-interacting sample in Paper V). The influence of the uncompensated moment is clearly demonstrated, as it is observed that even for small values of $\xi$, $\varepsilon_0^{(-)}$ is considerably reduced compared to the value at $\xi = 0$. With the parameters for the non-interacting hematite sample in Paper V, an energy $\varepsilon_0 = 0.58$ meV would be expected according to Eq. (4.12) whereas the observed value was 0.214(5) meV. It was found that a relative uncompensated moment of approximately 1.1 % could account for this difference. Using Néel's expression for the average size of the uncompensated moment, Eq. (1.11), we find that this value corresponds to $\nu \simeq 0.4$, which is not unreasonable.

It is important here also to note the dependence on the volume (through the anisotropy). In the 15 nm particles studied previously [62] a much smaller anisotropy field of 0.0033 T was found. With this value an energy $\varepsilon_0 = 0.28$ meV would be expected according to Eq. (4.12), whereas a value of 0.26 meV was experimentally determined. It is interesting to note that this

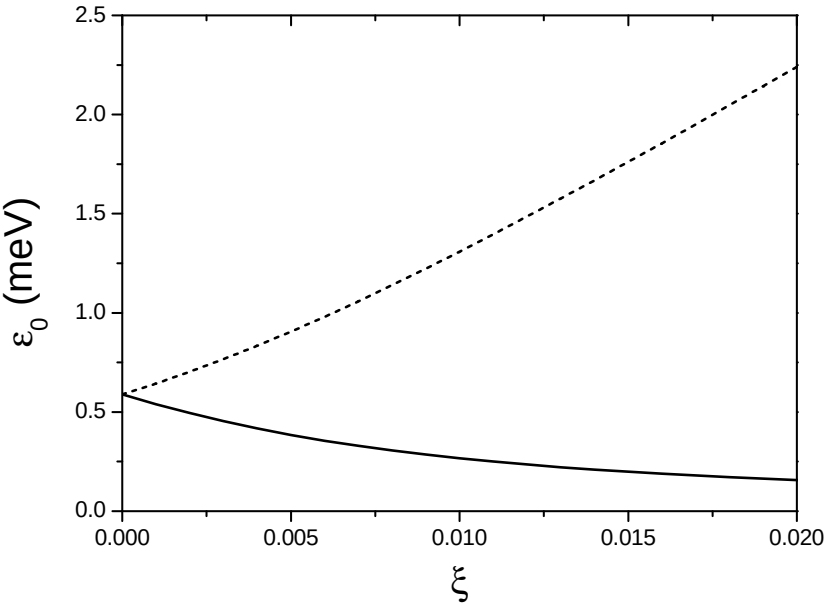


Figure 4.2: Plot of $\varepsilon_0^{(\pm)} = \hbar\omega_\pm$ vs $\xi$. The full line shows $\varepsilon_0^{(-)}$ and the dotted line shows $\varepsilon_0^{(+)}$ (adapted from Paper VI).

difference, according to Eq. (4.11), may be accounted for by a relative uncompensated moment of 0.04%. Using, again, Néel's expression from the uncompensated moment, this corresponds to $\nu \simeq 0.3$, in close agreement with the value found for the 8 nm particles.

These results demonstrate that small antiferromagnetic nanoparticles due to their uncompensated moment exhibit a behavior similar to that of ferrimagnetic particles, albeit with a small difference between the sublattice magnetizations.

## 4.3 Thermoinduced magnetization

For a bulk ferrimagnet, the two modes of precession found in the previous section are occasionally referred to as the ferromagnetic resonance mode and the exchange resonance mode [63]. In the ferromagnetic mode, the two sublattices are collinear during the precession, whereas the precession angles differ in the exchange resonance mode. For a pure antiferromagnet, on the other hand, only a single mode is expected in which the precession angles also differ, with [51, 52]

$$\frac{\sin\theta_1}{\sin\theta_2} \approx 1 \pm \delta. \tag{4.13}$$

The suggestion that this difference leads to a thermoinduced moment has lead to some debate in the literature [39, 40, 64–68]. In particular, it has been argued that the uncompensated moment in most cases may be predominant and that the thermoinduced moment is therefore

not distinguishable. To address this concern, we have in Paper VI considered how the presence of an uncompensated moment effects the possibility of detecting the thermoinduced moment.

The starting point for such a consideration is depicted in Fig. 4.1. We consider the same system as before, i.e., a two-lattice system, with sublattice magnetizations $\vec{M}_1$ and $\vec{M}_2$, which precess around the $z$-axis with angles $\theta_1$ and $\theta_2$. The difference between these two angles is denoted $\theta_\delta = \theta_2 - \theta_1$. We consider, again, only low temperatures where the precession angles are small and the $q = 0$ mode is predominant. We introduce an uncompensated moment by the assuming that $|\vec{M}_1| \neq |\vec{M}_2|$ and we write the magnetization due to this uncompensated moment as $|\vec{M}_{\rm u}| = |\vec{M}_1| - |\vec{M}_2|$. Based on this, the net moment in the $z$-direction may be written as

$$\begin{aligned} M_{\rm r}^z &= |\vec{M}_1|\cos\theta_1 - |\vec{M}_2|\cos\theta_2 \\ &= (|\vec{M}_1|\cos\theta_\delta - |\vec{M}_2|)\cos\theta - |\vec{M}_1|\sin\theta\sin\theta_\delta \\ &\approx |\vec{M}_{\rm u}|\cos\theta - |\vec{M}_1|\sin\theta\sin\theta_\delta \end{aligned} \tag{4.14}$$

where $\theta$ represents the average value of $\theta_1$ and $\theta_2$ and we have assumed that $\cos\theta_\delta \approx 1$.

In the previous section it was shown that $\vec{M}_1^{xy} = -\eta_\pm \vec{M}_2^{xy}$ and since $|\vec{M}_i|$, $|\vec{M}_i^{xy}|$, and $\theta_i$ are related as

$$|M_i^{xy}| = |\vec{M}_i|\sin\theta_i, \tag{4.15}$$

it is obtained that

$$\frac{|\vec{M}_1|}{|\vec{M}_2|}\frac{\sin\theta_1}{\sin\theta_2} = 1 + \frac{\delta^2}{2} + \frac{\xi}{2} \pm \frac{1}{2}\sqrt{\delta^4 + 2\delta^2(2+\xi) + \xi^2}. \tag{4.16}$$

For the left hand side of Eq. (4.16) one finds

$$\frac{\sin\theta_1}{\sin\theta_2} \approx 1 + \cot\theta\sin\theta_\delta, \tag{4.17}$$

and the right hand side yields

$$1 + \frac{\delta^2}{2} + \frac{\xi}{2} \pm \frac{1}{2}\sqrt{\delta^4 + 2\delta^2(2+\xi) + \xi^2} \approx 1 + \frac{\xi}{2} \pm \delta \tag{4.18}$$

in the limit where $\xi \ll \delta$. By combining Eqs. (4.17)-(4.18) and solving for $\sin\theta_\delta$ one finds

$$\sin\theta_{(\delta_\pm)} = \left(\frac{1}{2}\frac{M_{\rm r}^z}{|\vec{M}_1|\cos\theta} - \frac{|\vec{M}_{\rm u}|}{|\vec{M}_1|} \pm \delta\frac{|\vec{M}_2|}{|\vec{M}_1|}\right)\tan\theta. \tag{4.19}$$

When inserted in Eq. (4.14) this yields after we have averaged over the fast precessional motion

$$M_{{\rm r}(\pm)}^z \approx |\vec{M}_{\rm u}|\left(\frac{2\cos\theta}{2-\sin^2\theta}\right) \pm 2\delta\left(\frac{\cos\theta}{2\cot^2\theta + 1}\right). \tag{4.20}$$

The average value of $M_{{\rm r}(\pm)}^z$ is found using Boltzmann statistics, i.e.,

$$\langle M_{\rm r}^z\rangle_T = \frac{1}{Z}\sum_s M_{\rm r,s}^z \exp\left[-\frac{\varepsilon_s}{k_{\rm B}T}\right], \tag{4.21}$$

where the sum is over all available states $s$ having energies $\varepsilon_s$. $M^z_{\mathrm{r,s}}$ is the value of $M^z_{\mathrm{r}}$ in state $s$, and

$$Z = \sum_s \exp\left[-\frac{\varepsilon_s}{k_{\mathrm{B}}T}\right] \tag{4.22}$$

is the partition function. In Paper VI we limit ourselves to the case where the external field is applied along the easy axis (here, the $z$ axis). With two different precession states and with two possible orientations with respect to an applied field $B$, one finds four states, the energies of which are given as

$$\begin{aligned} \varepsilon_1 &= -|\vec{M}^z_{\mathrm{r}+}|VB \quad \varepsilon_2 = -(-|\vec{M}^z_{\mathrm{r}+}|)VB \\ \varepsilon_3 &= -|\vec{M}^z_{\mathrm{r}-}|VB \quad \varepsilon_4 = -(-|\vec{M}^z_{\mathrm{r}-}|)VB. \end{aligned} \tag{4.23}$$

This gives for $\langle M^z_{\mathrm{r}(\pm)}\rangle_T$

$$\begin{aligned} \langle M^z_{\mathrm{r}(\pm)}\rangle_T = \frac{1}{Z}\sum_\theta p(\theta)|\vec{M}^z_{\mathrm{r}+}|\left(\exp\left[\frac{V|\vec{M}^z_{\mathrm{r}+}|B}{k_{\mathrm{B}}T}\right] - \exp\left[-\frac{V|\vec{M}^z_{\mathrm{r}+}|B}{k_{\mathrm{B}}T}\right]\right) \\ + \frac{1}{Z}\sum_\theta p(\theta)|\vec{M}^z_{\mathrm{r}-}|\left(\exp\left[\frac{V|\vec{M}^z_{\mathrm{r}-}|B}{k_{\mathrm{B}}T}\right] - \exp\left[-\frac{V|\vec{M}^z_{\mathrm{r}-}|B}{k_{\mathrm{B}}T}\right]\right), \end{aligned} \tag{4.24}$$

where $p(\theta)$ is the probability of finding a precession state with angle $\theta$. If we consider only the initial susceptibility $\chi_{\mathrm{i}} = \mu_0 MV/B$, i.e., the limit where $V|\vec{M}^z_{\mathrm{r}\pm}|B \ll k_{\mathrm{B}}T$, we may use the approximation $\exp x \approx 1 + x$ and find

$$\chi_{\mathrm{i}} = \frac{1}{2}\frac{\mu_0 V}{k_{\mathrm{B}}T}\sum_\theta p(\theta)\left(|\vec{M}^z_{\mathrm{r}+}|^2 + |\vec{M}^z_{\mathrm{r}+}|^2\right) \tag{4.25}$$

since

$$|\vec{M}^z_{\mathrm{r}\pm}|\left(\exp\left[\frac{V|\vec{M}^z_{\mathrm{r}\pm}|B}{k_{\mathrm{B}}T}\right] - \exp\left[-\frac{V|\vec{M}^z_{\mathrm{r}\pm}|B}{k_{\mathrm{B}}T}\right]\right) \approx \frac{2V|\vec{M}^z_{\mathrm{r}\pm}|^2 B}{k_{\mathrm{B}}T}. \tag{4.26}$$

and $Z \approx 4$. Using the expression for the anisotropy energy, Eq. (1.5), we find

$$p(\theta) = \frac{\exp[-\kappa\sin^2\theta]}{\sum_\theta \exp[-\kappa\sin^2\theta]} \tag{4.27}$$

where $\kappa = KV/k_{\mathrm{B}}T$. The sum in Eq. (4.25) may be turned into an integral if we assume that the precession states are close-lying. By combining Eqs. (4.20), (4.25), and (4.27) we then obtain

$$\begin{aligned} \chi_{\mathrm{i}} = \mu_0 V\left[\frac{|\vec{M}_{\mathrm{u}}|^2}{k_{\mathrm{B}}T}\frac{\int_0^{\pi/2}\exp[-\kappa\sin^2\theta]\frac{4\cos^2\theta\sin\theta}{(2-\sin^2\theta)^2}d\theta}{\int_0^{\pi/2}\sin(\theta)\exp[-\kappa\sin^2\theta]d\theta}\right] \\ + \mu_0 V\left[\frac{4\delta^2|\vec{M}_2|^2}{k_{\mathrm{B}}T}\frac{\int_0^{\pi/2}\exp[-\kappa\sin^2\theta]\frac{\cos\theta\sin\theta}{(2\cot^2\theta+1)^2}d\theta}{\int_0^{\pi/2}\sin(\theta)\exp[-\kappa\sin^2\theta]d\theta}\right]. \end{aligned} \tag{4.28}$$

As we limit ourselves to temperatures where only the lowest precession states are occupied, we may use the approximation $\sin^2\theta \approx \theta^2$ and we find

$$\chi_{\rm i} \approx \mu_0 V \left( \frac{|\vec{M}_{\rm u}|^2}{k_{\rm B}T} + \frac{4k_{\rm B}T}{\mu_0^2 H_{\rm K} H_{\rm E}} \right) \tag{4.29}$$

where we have taken $|\vec{M}_2| = |\vec{M}_{\rm S}|$, where $|\vec{M}_{\rm S}|$ is the saturation magnetization, which is assumed to be independent of temperature (a reasonable assumption for temperatures well below the Néel temperature). The first term of this expression is the familiar result for a single particle with magnetization $|\vec{M}_u|$ which decreases with temperature while the second part equals the thermoinduced contribution found by Mørup and Frandsen [55], which is seen to increase linearly with temperature.

Before we consider examples of how the thermoinduced contribution manifests itself, we should consider for which temperatures the assumptions concerning small angles are fulfilled. The relative population of states with $\theta > \theta_c$, where $\theta_c$ is some critical angle, may be found as

$$p_{\theta>\theta_c} = \frac{\int_{\theta_c}^{\pi/2} p(\theta) \sin\theta \, {\rm d}\theta}{\int_0^{\pi/2} p(\theta) \sin\theta \, {\rm d}\theta}, \tag{4.30}$$

where $p(\theta)$ is given by Eq. (4.27). Fig. 4.3 shows $\kappa = KV/k_{\rm B}T$ as a function of $\theta_c$, for $p = 1\%$ and $10\%$, respectively. The temperatures at which our assumption concerning the angle is fulfilled of course depend on what we consider "an acceptably small angle". Choosing $P = 10\%$ and $\theta_{\rm c} = 20^\circ$ (for which the error in using $\sin\theta \approx \theta$ and $\cos\theta \approx 1$ are less than 10%) we find that the angles are adequately small for $\kappa > 20$.

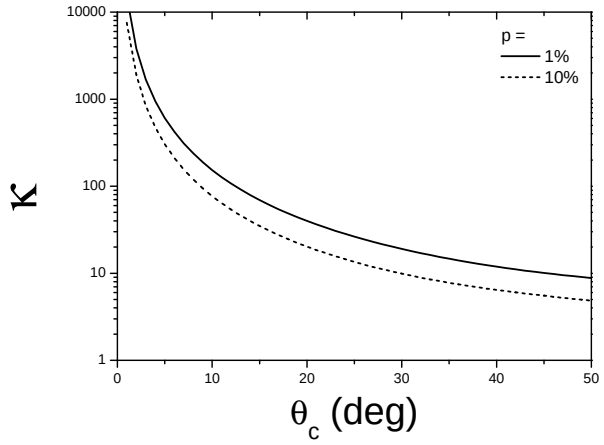


Figure 4.3: $\kappa$ as a function of $\theta_c$ for $p = 1\%$ and $10\%$.

An example of a susceptibility curve resulting from the combined presence of a thermoinduced and a uncompensated moment was in Paper VI obtained with the parameters $V = 1 \cdot 10^{-24}$ m$^3$, $\mu_0 H_{\rm K} = 0.01$ T, and $\mu_0 H_{\rm E} = 300$ T. This corresponds to $KV/k_{\rm B} = 724$ K and, using $\ln(\tau_{\rm m}/\tau_0) \approx 30$, a blocking temperature of approximately 25 K. For this set of

parameters we find that the assumptions concerning the angles are fulfilled for $T < 100$ K. Fig. 4.4 shows the results for different values of the uncompensated moment. It is observed that for favorable combinations of $|\vec{M}_{\rm u}|$, $H_{\rm K}$, and $H_{\rm E}$, the thermoinduced contribution may in fact be predominant.

## 4.4 Simulated ac susceptibility data

The results presented in Paper VI concern only the dc susceptibility in the special case where the external field is applied along the $z$ axis. In the following, some additional results on the ac susceptibility in the presence of a thermoinduced contribution will be discussed. We have first considered the effect of a random orientation of the applied field, however, as shown in appendix A.2, it only gives rise to an additional factor of $\frac{1}{3}$ appearing in the expression for $\chi_{\rm i}$, and hence does not influence the relative strengths of the two contributions. The effects of a distribution of volumes and a volume dependent magnetization, as discussed in chapter 3, are also considered. Expressions for the ac-susceptibility of antiferromagnetic particles were derived in section 3.2.1; we introduce the thermoinduced contribution by adjusting $\chi_0$ and $\chi_\infty$ (Eqs. (3.15) and (3.16)) so that they read

$$\chi_0 = \chi_0^{\rm u} + \chi_0^{\delta} \tag{4.31a}$$

$$\chi_\infty = \chi_\infty^{\rm u} + \chi_\infty^{\delta} \tag{4.31b}$$

where u and $\delta$ refer to the contributions from the uncompensated and thermoinduced moments, respectively. Since fluctuations between different $q = 0$ states take place without a energy barrier being surmounted [55] we assume that $\chi_0^{\delta} = \chi_\infty^{\delta} \equiv \chi^{\delta}$. By repeating the derivations outlined in section 3.2.1 with the expression for $\chi^{\delta}$ from Eq. (4.29) it is obtained that

$$\chi'(\omega,T) = \chi'_{\rm u} + \frac{4k_{\rm B}T}{3\mu_0 V H_{\rm K} H_{\rm E}} \tag{4.32a}$$

$$\chi''(\omega,T) = \chi''_{\rm u} \tag{4.32b}$$

i.e., the out-of-phase susceptibility is unaffected by the presence of a thermoinduced moment, whereas the in-phase component is modified in a way similar to the dc case [69]. Hence, in the following we will only consider the in-phase component, which in the presence of a distribution of volumes and a volume-dependent uncompensated moment becomes

$$\begin{aligned}\chi'_{\rm u}(\omega,T) = {} & \frac{\mu_0 M_{\rm m}^2}{3K}\left[\frac{KV_{\rm m}}{k_{\rm B}T}\int_0^\infty \frac{y^{2\nu-1}p_{\rm v}(y)}{1+(\omega\tau)^2}\,{\rm d}y + \int_0^\infty \frac{(\omega\tau)^2 y^{2\nu-2}p_{\rm v}(y)}{1+(\omega\tau)^2}\,{\rm d}y\right] \\ & + \frac{4k_{\rm B}T}{3\mu_0 V_{\rm m} H_{\rm K} H_{\rm E}}\int_0^\infty \frac{p_{\rm v}(y)}{y}\,{\rm d}y.\end{aligned} \tag{4.33}$$

We have simulated a number of in-phase ac susceptibility curves with a log-normal distribution of volumes. In addition to $K = 10^4\,{\rm J\cdot m^{-3}}$ and $\tau_0 = 10^{-11}$ s, the parameters used were similar to those of Paper VI. Fig. 4.5 shows the resulting susceptibility as a function of temperature for frequencies $f = 10, 100$ and $10000\,{\rm Hz}$ with (using $\sigma_{\rm v} = 1/2$ and $\nu = 1/2$) and without a distribution of volumes. It is observed that the presence of a volume distribution smears out the signal for the uncompensated moment. The thermoinduced contribution alone, however, increases with increasing $\sigma_{\rm v}$ since

$$\int_0^\infty \frac{p(y)}{y}\,{\rm d}y = \exp[\sigma_{\rm v}^2/2] \tag{4.34}$$

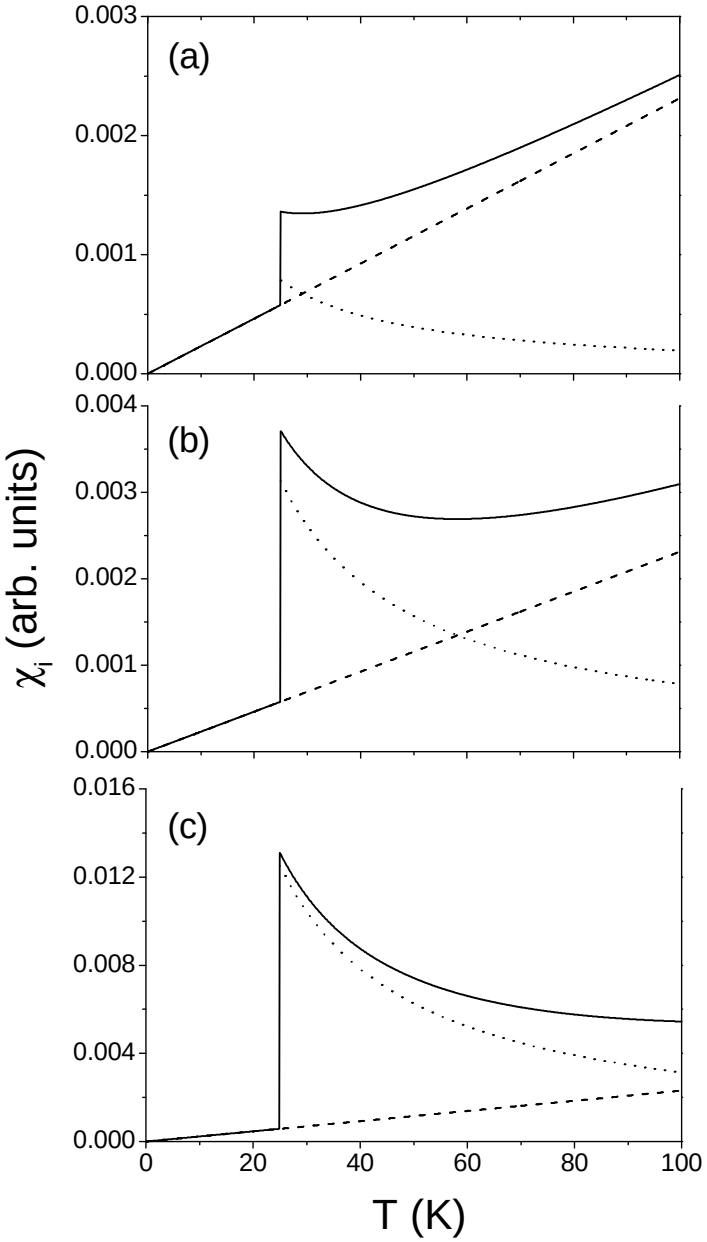


Figure 4.4: Simulated volume susceptibility curves ($\chi_i$) as a function of temperature with an uncompensated moment of (a) 50 $\mu_B$ (b) 100 $\mu_B$ and (c) 200 $\mu_B$. The dotted line shows the contribution from the uncompensated moment, the dashed line shows the thermoinduced contribution, and the full line shows the sum (adapted from Paper VI).

if $p(y)\,\mathrm{d}y$ is a log-normal distribution.

### 4.4.1 Where to look for thermoinduced magnetization

Knowing for which combinations of $H_\mathrm{K}$, $H_\mathrm{E}$, and $\mu_\mathrm{u} = M_\mathrm{u}/V$ the thermoinduced contribution to the susceptibility is predominant, it is worth considering in which materials to look for the phenomenon. As the magnitude of the uncompensated moment plays a crucial role, it is particularly important to consider which values of $\mu_\mathrm{u}$ to expect from various materials. Table 4.1 shows, for a number of antiferromagnetic materials, the uncompensated moment calculated using Eq. (1.11) for a particle with a volume of $10^{-24}\,\mathrm{m}^3$ with different values of $\nu$.

| | | $\mu_\mathrm{u}$ [$\mu_\mathrm{B}$] | | |
|---|---|---|---|---|
| Sample | $M_\mathrm{s}$ [$10^5$ A/m] | $\nu = 1/3$ | $\nu = 1/2$ | $\nu = 2/3$ |
| $Cr_2O_3$ | 5.75 | 104 | 610 | 3588 |
| ($\alpha$)-FeOOH | 6.60 | 153 | 844 | 4662 |
| NiO | 5.02 | 76 | 466 | 2864 |
| CuO | 2.22 | 36 | 219 | 1317 |
| $Co_3O_4$ | 2.13 | 74 | 371 | 1847 |

Table 4.1: Calculated uncompensated moments for particles of volume $1 \cdot 10^{-24}$ m$^3$. Notes: For $Co_3O_4$ it is assumed that only $Co^{2+}$ contributes to the magnetic properties

The values of $H_\mathrm{K}$ and $H_\mathrm{E}$ expected from some of these materials can be found in the literature. Based on these, we have simulated the in-phase susceptibility curves for particles of NiO, and $Cr_2O_3$ (where data on the relevant parameters were available). The volume of the particles considered is the same as before (i.e. $10^{-24}$ m$^3$). The parameters used were (for NiO) $\mu_0 H_\mathrm{K}$=0.014 T and $\mu_0 H_\mathrm{E}$=980 T (the same as those used by Bahl et al. [70]), and for $Cr_2O_3$, $\mu_0 H_\mathrm{E}$ = 245 T and K=$2 \cdot 10^4$ J·m$^{-3}$ [71]. In both cases an uncompensated moment of 100 $\mu_\mathrm{B}$ was assumed, based on the average values shown in Table 4.1. Fig. 4.6 shows the resulting curves. The thermoinduced contribution is in both cases readily distinguishable. Similar simulations with the parameters of ferritin, however, reveal that for this material the thermoinduced contribution is insignificant due to a large uncompensated moment (as discussed in section 3.3, $\nu \simeq 1/2$ in ferritin).

Although it is possible to say in which materials it is theoretically possible to detect the thermoinduced moment, a number of practical circumstances have to be considered as well. It may be challenging, at best, to obtain particles that are, at the same time, small, monodisperse, and have a small uncompensated moment. Additionally, a concern may be that as the particle size is decreased, the crystallinity may be affected to such an extent that $\nu = 1/3$ cannot be obtained. In addition to this, it must be kept in mind that for very small particles, the range of temperatures for which the assumptions of this model are fulfilled, is narrowed. The most promising approach may therefore be single particle magnetization measurements at very low temperatures on carefully selected specimens.

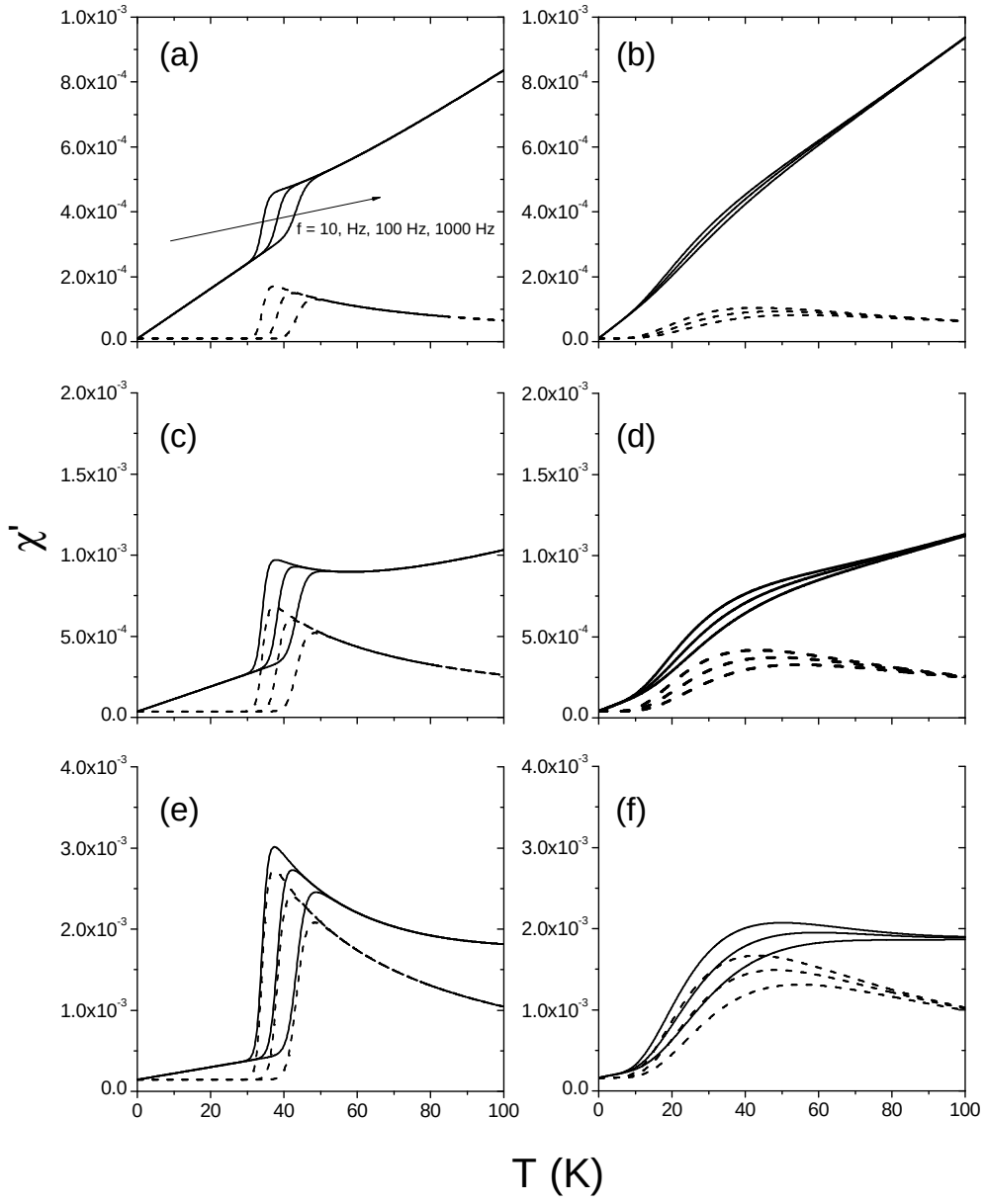


Figure 4.5: Simulated ac susceptibility curves, with (b,d,f) and without (a,c,e) a distribution of volumes (with $\sigma_v = 1/2$ and $\nu = 1/2$) for different values of the uncompensated moment: (a,b) 50 $\mu_B$, (c,d) 100 $\mu_B$, and (e,f) 200 $\mu_B$. The dashed lines are the contributions from the uncompensated moments.

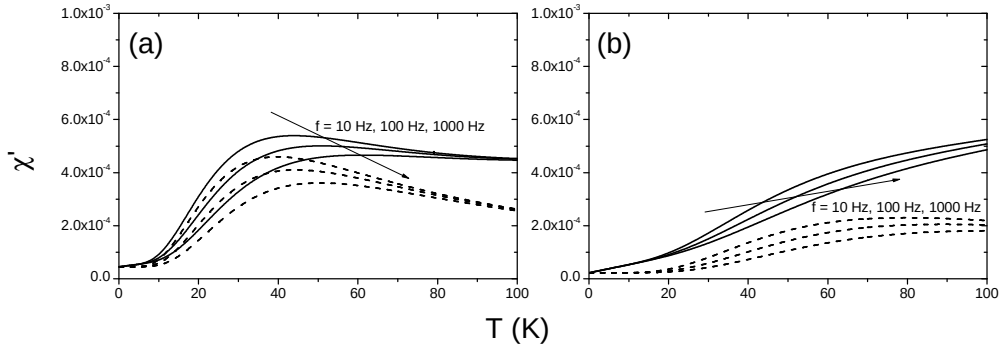


Figure 4.6: Simulated ac susceptibility curves based on parameters typical of (a) NiO and (b) $Cr_2O_3$, with a distribution of volumes (with $\sigma_v = 1/2$ and $\nu = 1/3$). The dashed lines are the contributions from the uncompensated moments.

## 4.5 Summary

The uniform mode of precession is of particular importance in nanoparticles due to the discreetness of the spin wave spectrum. As shown in this chapter, antiferromagnetic nanoparticles should be considered as small ferrimagnets for which the energy levels of the $q = 0$ mode, in accordance with experimental data, are modified.

Another intriguing aspect of the uniform mode is the difference in precession angles, which previously has been predicted to give rise to a thermoinduced magnetic moment that increases with temperature. As demonstrated in this chapter, even when an uncompensated moment is taken into account, under favorable conditions, the thermoinduced moment may still be predominant. However, from an experimental point of view, detecting the uncompensated moment may prove extremely challenging due in particular to the distribution of uncompensated moments that is almost inevitably present in most samples.

# Chapter 5

# Interactions between particles of goethite

As discussed in section 1.2.4, in ferro- or ferrimagnetic samples, the interaction between neighboring particles is often mediated by dipole-dipole interactions. However, in antiferromagnetic nanoparticles the ordering temperature resulting from such an interaction is typically on the order of a few Kelvin or less due to the small size of the uncompensated moment. Hence, dipole interactions should not be important at elevated temperatures. Interactions effects, however, do play an important role even in antiferromagnetic particles, but they are due to direct exchange coupling between the surface atoms of neighboring particles [72, 73]. In this chapter it will be shown how the Mössbauer spectra of goethite ($\alpha$-FeOOH), which for decades have been the topic of intense debate, may be explained by such inter-particle interactions.

## 5.1 Properties of goethite

Goethite was first identified as a mineral in 1806 and is named after the German polymath Johann Wolfgang von Goethe (1749-1832). It is the most stable of the iron oxyhydroxides and is therefore the end product of many transformations [49]. Its presence in rocks on Mars as detected by the Mars Exploration Rovers [74, 75] has been taken as an indication that Mars once had a much wetter climate than is presently the case. On Earth, the characteristic reddish color of the soils found many places is (often) due to the presence of various iron oxides, and among these goethite is one of the most abundant together with hematite ($\alpha$-$Fe_2O_3$), which is the most stable of the iron oxides. Consequently, goethite is also one of the most studied members of the iron oxide family.

### 5.1.1 Structural properties

Most of the iron oxides (akaganeite, $\beta$-FeOOH, being the exception) share a common structure, namely that of an *hcp* or *ccp* framework of $O^{2-}/OH^{-}$ anions. Within such a dense packing of anions, interstitial voids exist which can be occupied by various cations. It is the distribution of these cations (in this case, $Fe^{2+}$ or $Fe^{3+}$), which distinguishes the various Fe-oxides from each other. The structure of goethite is based on a *hcp* anion configuration. In the *hcp* structure, the interstices may be of either octahedral or tetrahedral configuration. What characterizes the goethite structure is that half the octahedral voids are occupied by $Fe^{3+}$

cations, such that each $Fe^{3+}$ cation has three $O^{2-}$ and three $OH^-$ neighbors, together forming a $FeO_3(OH)_3$ octahedron. The $Fe^{3+}$ cations are arranged such that two ions are followed by two voids, followed two ions...etc. This is shown in terms of linked octahedra in Fig. 5.1. The

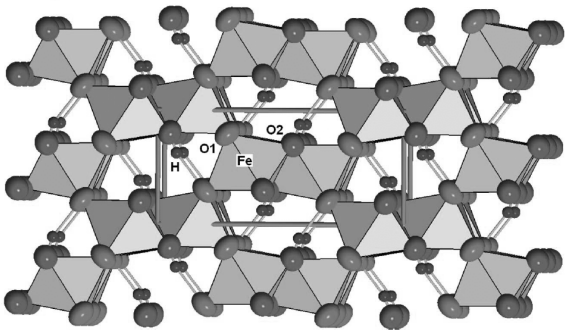


Figure 5.1: The structure of goethite showing the network of linked octahedra. From [76]

unit cell of goethite is orthorhombic with space group $Pnma$. It is a source of some confusion that it was previously assigned to space group $Pnmb$. As a result, one should be aware that the indexing of directions and lattice planes may vary in the literature. The unit cell parameters as found by Szytula et al. [77] are $a = 0.9956$ nm, $b = 0.30215$ nm, and $c = 0.4608$ nm. These parameters are sensitive to a number of factors, including structural disorder and the presence of impurities [49]. The overall structure may be described as double chains of linked octrahedra, running along the $b$ direction, along which the particles are often found to be elongated.

### 5.1.2 Magnetic properties

Goethite is antiferromagnetic with a reported Néel temperature of around 400 K. The magnetic structure has been determined by Forsyth et al. [78], who from neutron diffraction studies found that the magnetic unit cell is the same as the crystallographic unit cell. It was further determined that the spins are oriented along the $b$ axis, with all the spins within a given octahedra chain having the same direction, opposite to that in neighboring chains. More detailed studies have since suggested that the spins might be inclined $\sim 13^\circ$ with respect to the $b$ axis [79].

## 5.2 Experimental studies of goethite

In Papers VII and VIII we study the properties of goethite nanoparticles. This includes studies of untreated particles (in the followed referred to as the as-prepared sample) and samples subjected to heating (Paper VII) and ball-milling (Paper VIII). The as-prepared sample, provided by Dr. C. B. Koch from the Faculty of Life Sciences, University of Copenhagen, was synthesized by acid hydrolysis of an iron nitrate solution. In an attempt to separate

the particles, we subjected a sample to low-energy ball-milling for 48 hours with nano-sized NaCl as a dispersion medium. The sample was subsequently washed several times in order to remove the NaCl. The heated sample was obtained with a temperature of 150°C for 48 hours in atmospheric air.

All of these samples have been characterized with XRD and TEM. Fig. 5.2 shows examples

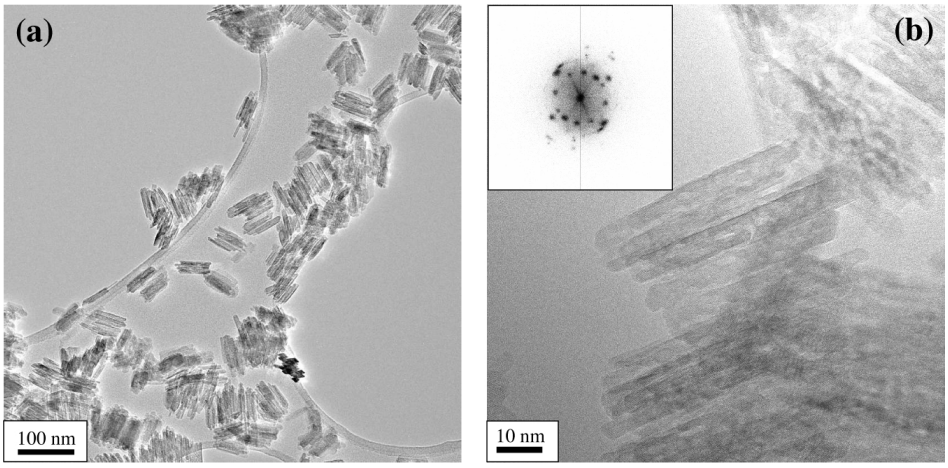


Figure 5.2: (a) TEM and (b) HRTEM image of the as-prepared sample. The insert shows the Fourier transform of the image.

of the TEM images of the as-prepared sample. We observe several rod-like entities forming small bundles of 5-10 rods. Such a morphology is quite common for small particles of goethite [49]. A close inspection of Fig. 5.2(b) reveals that the lattice planes extend throughout each rod and even continue from one rod to the next. It therefore seams reasonable, at first, to assume that each rod constitute a single goethite crystal. From the images we see that the rods are on average 5 nm in width and 50 nm in length. As we are unable to obtain information about the depth of the rods from the TEM images, estimating the volume of the rods is not straightforward. However, assuming that the depth is comparable to the width, as some studies seem to indicate [80, 81], we obtain an approximate volume $V_{\text{rod}} \approx (5 \times 5 \times 50)$ nm$^3$ = 1250 nm$^3$. The insert of Fig. 5.2(b) shows the Fourier transform of the image; in such images, each dot represents a periodicity in the parent image and its distance from the center indicates the magnitude of the wave number of the periodicity. It is the visualization of the lattice planes of the sample, which gives rise to these patterns in the Fourier transform. Consequently, we may from the Fourier transform obtain knowledge of which lattice spacings $d$ are present and the distribution of their orientations. In principle, we may use this information (the presence of certain lattice spacings) to identify the material; however, the determination of $d$ is often subject to some uncertainty, rendering this approach challenging, at best. The observation of a few discrete dots (instead of continuous rings) indicates that only a discrete number of crystal orientations are present in the image. A detailed analysis show that only a single crystal orientation is present within each rod. TEM images of the heated sample shows no indications that any morphological changes have been induced as a result of the heating. The ball-milling, on the other hands, has lead to considerable changes in the morphology as shown in Fig. 5.3; it is readily observed that the rods have been divided into smaller fragments. In the Fourier transform shown in the insert of Fig. 5.3(b), we see that a large number of dots are

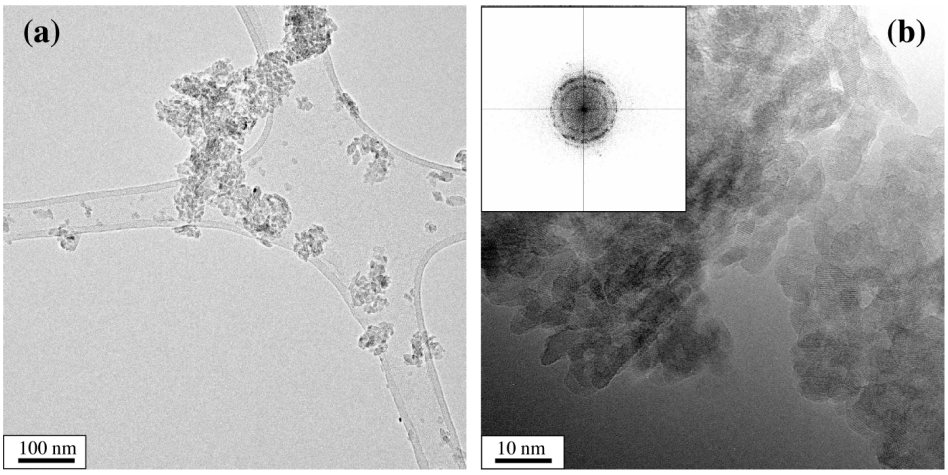


Figure 5.3: (a) TEM and (b) HRTEM image of the ball-milled sample. The insert shows the Fourier transform of the image.

present and that these dots are almost forming continuous rings. Based on this we conclude that the fragments are more or less randomly oriented.

Fig. 5.4 shows the XRD spectrum of the as-prepared sample. The sizes estimated from a Rietveld refinement of these data were $d_{[100]} = (12 \pm 2)$ nm, $d_{[010]} = (20 \pm 2)$ nm, and $d_{[001]} = (7 \pm 1)$ nm, which are considerably different from those obtained from the TEM images. Table 5.1 lists the dimensions obtained from XRD for the other two samples, for which similar discrepancies between XRD and TEM are observed. The source of these discrepancies will be discussed after we have considered the results obtained from Mössbauer spectroscopy.

| Sample | $d_{[100]}$ | $d_{[010]}$ | $d_{[001]}$ |
|---|---|---|---|
| as-prepared | 12(2) | 20(2) | 7(1) |
| heated | 9(2) | 16(2) | 3(1) |
| ball-milled | 7(1) | 9(1) | 5(1) |

Table 5.1: Dimensions obtained from a Rietveld refinement of XRD data.

### 5.2.1 The Mössbauer spectrum of goethite

Being a Fe-bearing material, goethite is ideally studied with $^{57}$Fe Mössbauer spectroscopy. Fig. 5.5 shows a comparison between the Mössbauer spectra of a bulk sample (obtained from Cornwall, UK [82]) and the as-prepared sample. It is observed that while the lines of the bulk sample remain narrow even at the highest temperatures, the lines of the as-prepared sample are asymmetrically broadened even at low temperatures. It is also observed that the sextet has almost collapsed to a doublet at 320 K, which is considerably lower than the Néel temperature. This behavior, which has been observed in numerous samples over the years, is different from that observed for particles exhibiting superparamagnetic relaxation. As discussed in section 1.2.2, in such a case, we would expect a sextet and a doublet (or singlet), each with narrow lines, to co-exist in a limited temperature interval. The behavior, in particular the asymmetric

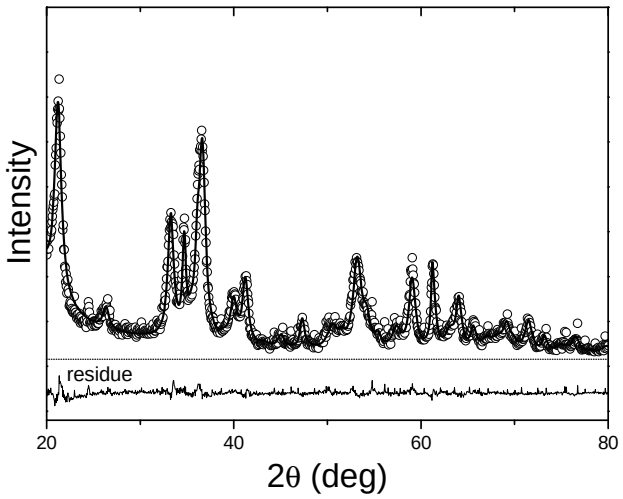


Figure 5.4: XRD spectrum of the as-prepared sample. The line shows the result of the Rietveld refinement. The residue is shown below the plot.

broadening over a wide temperature range, however, do bear a certain resemblance to that observed for small interacting hematite particles as shown in Fig. 5.6(b).

The interpretation of the Mössbauer spectra of goethite, however, has been the source of considerable debate [see, e.g., 79, 82–102]. One of the controversies involves the anisotropy of the particles. When the volume of the as-prepared sample as determined from TEM is combined with the anisotropy constant reported for goethite ($\sim 5 \cdot 10^4$ J/m$^3$) [79, 93] one obtains $KV/k_\mathrm{B} \approx 4500$ K. Hence, the blocking temperature observed with Mössbauer spectroscopy should be well above room temperature, which seems to contradict the interpretation that the spectral broadening and collapse are due to superparamagnetic relaxation. Bocquet and Kennedy [97] also dismissed the possibility of superparamagnetic behavior as they had observed the same transition temperature using techniques with timescales $\tau_\mathrm{m}$ differing by several orders of magnitude. They suggested instead that each particle contains a number of exchange coupled clusters, originating from broken Fe chains. The presence of such chains was originally suggested by van Oosterhout [83]. A quantitative model was later set up for this mechanism [98], and excellent fits to experimental data were, according to the authors, obtained. Mørup et al. [82], on the other hand, used for their analysis a model termed the "superferromagnetism" model, in which the broadening results from interactions between superparamagnetic particles. Excellent fits were also achieved with this model; however, the anisotropy was, surprisingly, found to be negligible.

### 5.2.2 Superferromagnetism

The superferromagnetism model attempts to describe the effects of interactions between particles. This, however, is not a simple task and the description of interaction effects has, in general, been the topic of considerable debate in the literature (see, e.g., [14–17, 103–112]).

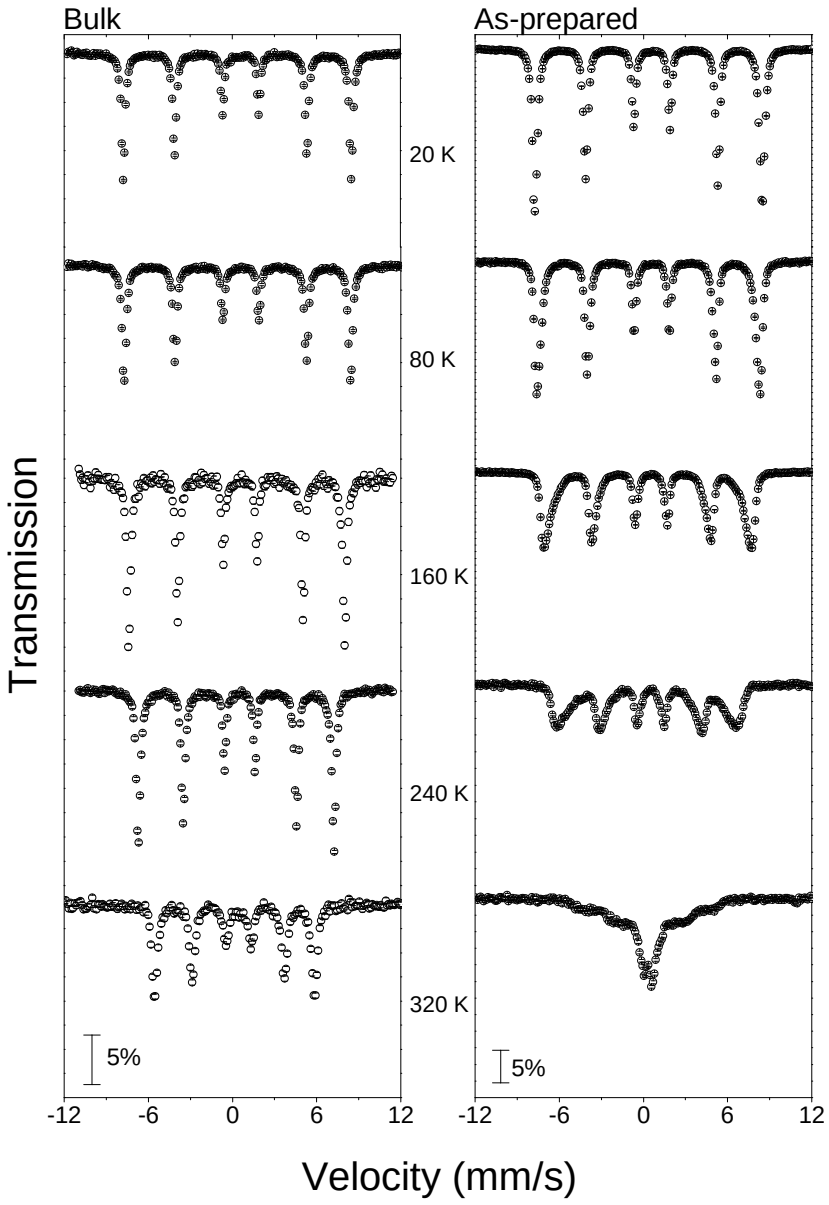


Figure 5.5: Mössbauer spectra at selected temperatures for the bulk (left) and as-prepared (right) sample. The vertical bars correspond to 5% transmission.

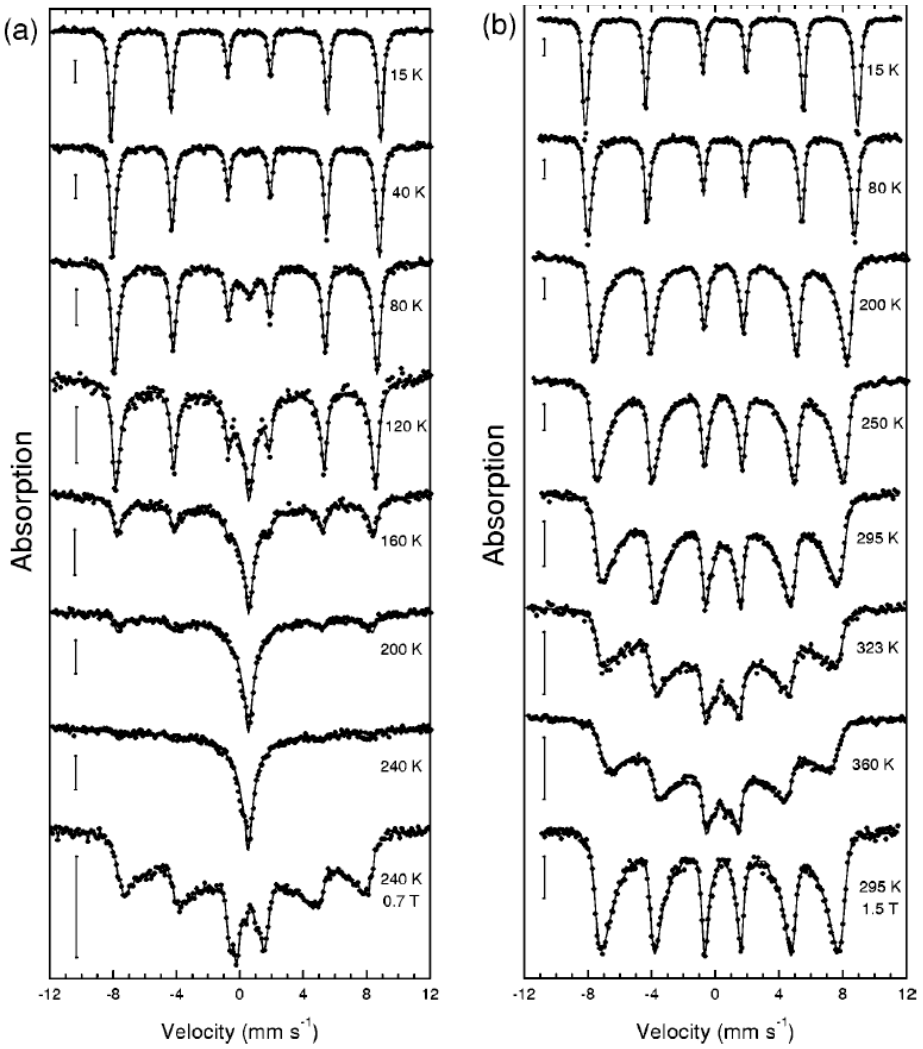


Figure 5.6: A comparison between the Mössbauer spectra of (a) non-interacting and (b) interacting particles of hematite (from Hansen et al. [72]).

Consequently, this model should be considered a first approximation. In the model the interaction energy between two crystallites $i$ and $j$ with sublattice magnetizations $M_i$ and $M_j$ is written [82]

$$E_{ij} = -\vec{M}_i(T) \cdot K_{\mathrm{ex}}^{ij} \vec{M}_j(T), \tag{5.1}$$

where $K_{\mathrm{ex}}$ is the exchange coefficient, which depends on the coupling strength between the two particles. Summing over all neighbors one arrives at

$$E_i = -\vec{M}_i(T) \cdot \sum_j K_{\mathrm{ex}}^{ij} \vec{M}_j(T), \tag{5.2}$$

which in a mean-field approximation reduces to

$$E_i = -K_{\mathrm{m}} \vec{M}_i(T) \cdot \langle \vec{M}(T) \rangle, \tag{5.3}$$

where $K_{\mathrm{m}} \langle \vec{M}(T) \rangle$ is the mean field from the all neighboring crystallites, and $K_{\mathrm{m}} = \langle \sum_j K_{\mathrm{ex}}^{ij} \rangle$ is the effective exchange coefficient. If one introduces the order parameter $b(T)$ as

$$b(T) = \frac{|\langle \vec{M}(T) \rangle|}{M_0(T)}, \tag{5.4}$$

where $M_0 = |\vec{M}_i|$ is the saturation value of the (sublattice) magnetization, Eq. (5.3) may be rewritten

$$E_i = -K_{\mathrm{m}} M_0^2(T) b(T) \cos\theta, \tag{5.5}$$

where $\theta$ is the angle between $\vec{M}_i$ and $\langle \vec{M}(T) \rangle$. Including also the term for the magnetic anisotropy energy, Eq. (1.5), the total magnetic energy of the crystallite $i$ becomes

$$E_{\mathrm{tot}} = -KV \cos^2\varphi - K_{\mathrm{m}} M_0^2(T) b(T) \cos\theta, \tag{5.6}$$

where $\varphi$ is the angle between $\vec{M}_i$ and an easy axis of magnetization.

It has been observed that nanoparticles in close contact may display what is known as oriented attachment whereby the particles share a common crystallographic orientation. This may be observed directly with TEM where certain sets of lattice planes are found to extend across the boundary between two particles. This was observed by Penn and Banfield [113] in nanoparticles of $TiO_2$ using TEM, and later in many other systems, such as hematite [114] and goethite [115–117]. We see from Fig. 5.2 that the samples discussed here seem to exhibit oriented attachment as well. In such a case, the easy axes of the particles must be pointing in almost the same direction. As a first approximation one may therefore assume that $\langle \vec{M}(T) \rangle$ is parallel to the easy axis of particle $i$ and the above expression reduces to

$$E_{\mathrm{tot}} = -KV \cos^2\theta - K_{\mathrm{m}} M_0^2(T) b(T) \cos\theta. \tag{5.7}$$

Using Boltzmann statistics, we find using the above expression for the energy

$$b(T) = \frac{\int_0^\pi \exp\left(-\beta E_{\mathrm{tot}}\right) \sin\theta \cos\theta \, \mathrm{d}\theta}{\int_0^\pi \exp\left(-\beta E_{\mathrm{tot}}\right) \sin\theta \, \mathrm{d}\theta}, \tag{5.8}$$

where $\beta = (k_{\mathrm{B}}T)^{-1}$. Simulations using the expression show that an ordered state is formed below a temperature $T_{\mathrm{p}}$. If $KV = 0$

$$b^0(T) = \mathscr{L}\left(\beta K_{\mathrm{m}} M_0^2(T) b^0(T)\right), \tag{5.9}$$

where $\mathscr{L}(x)$ is the Langevin function discussed in chapter 3. For $b^0 \ll 1$ we use that for small $x$, $\mathscr{L}(x) \approx x/3$, and we obtain

$$b^0(T_{\mathrm{p}}^0) \approx \frac{1}{3k_{\mathrm{B}}T_{\mathrm{p}}^0} K_{\mathrm{m}} M_0^2(T_{\mathrm{p}}^0) b^0(T_{\mathrm{p}}^0). \tag{5.10}$$

From this we find

$$T_{\mathrm{p}}^0 = \frac{K_{\mathrm{m}} M_0 (T_{\mathrm{p}}^0)^2}{3k_B}, \tag{5.11}$$

which is the ordering temperature in the case of zero anisotropy. In the case where $KV \neq 0$, $b(t)$ is found by numerically solving Eq. (5.8). The interaction energy $E_{\mathrm{int}}$ is obtained from Eq. (5.11) as $3k_{\mathrm{B}}T_{\mathrm{p}}^0$.

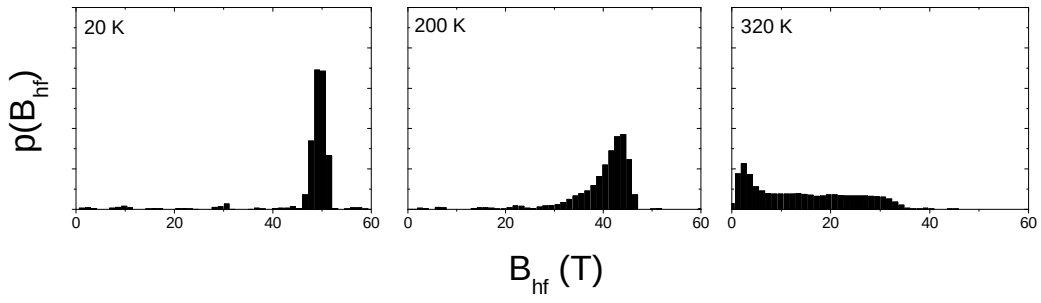


Figure 5.7: Hyperfine field distributions for the as-prepared sample at selected temperatures.

In the superferromagnetism model, the Mössbauer spectra are, at each temperature, fitted with a distribution of sextets with the same isomer shift and quadrupole shift but with different hyperfine fields [118]. As an example, Fig. 5.7 shows the resulting hyperfine field distributions at selected temperatures for the as-prepared sample. In previous studies (e.g., [82, 91, 92]), the analysis has been based on the *average* hyperfine field obtained from these distributions, in which case the anisotropy, when using the superferromagnetism model, was found to be negligible. However, in a similar study of hematite nanoparticles, Hansen et al. [72] found that this was only the case when the average hyperfine field was considered. The anisotropy had to be considered if the temperature dependence of the individual quantiles of the hyperfine field distributions was analyzed. The reason for this, they argued, was that the effect of anisotropy is averaged out when the average hyperfine field is considered. In our analysis we have used the same approach and have fitted $b(T)$ (Eq. (5.8)) to the experimentally determined

$$b_f(T) = \frac{B_{\mathrm{hf}}^f(T)}{B_0(T)}, \tag{5.12}$$

where $B_{\mathrm{hf}}^{f}(T)$ is the $f$-quantile of the hyperfine field distribution $p(B_{\mathrm{hf}})\,\mathrm{d}B_{\mathrm{hf}}$ defined by

$$f = \int_{0}^{B_{\mathrm{hf}}^{f}(T)} p(B_{\mathrm{hf}})\,\mathrm{d}B_{\mathrm{hf}}, \tag{5.13}$$

and $B_0(T)$ is the hyperfine field of a bulk sample. Fig. 5.8 shows the temperature dependence of selected quantiles for the as-prepared sample. The fits yielded in all cases the anisotropy

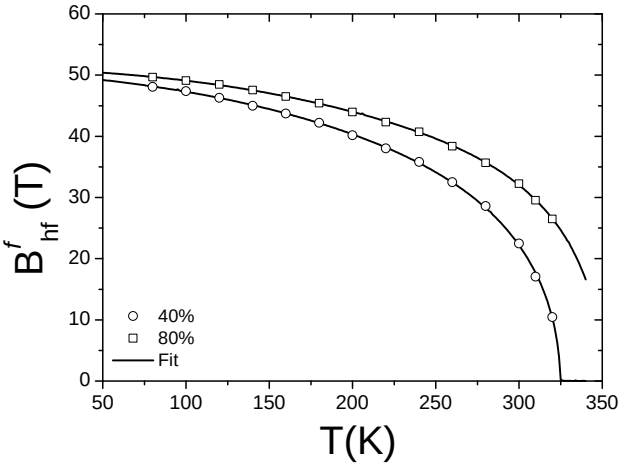


Figure 5.8: Temperature dependence of selected quantiles of the hyperfine field distribution for the as-prepared sample. The line shows the fit with the superferromagnetism model.

and interaction energies as a function of $f$. In the following we consider the results obtained with this model.

### 5.2.3 Results

#### The as-prepared and ball-milled samples

Fig. 5.9 shows the anisotropy and interaction energies obtained for the as-prepared and the ball-milled samples. As the figure shows, for the as-prepared sample, the anisotropy energy (in units of temperature) increases from approximately 400 K to around 1600 K with increasing $f$ while the interaction energy (also in units of temperature) remains practically constant around 800 K. For the ball-milled sample, very similar values are observed although the anisotropy energy seems to be slightly reduced. The absence of any major differences is surprising as the TEM images suggest that the ball-milling has lead to considerable changes in the morphology of the particles.

#### The heated sample

Fig. 5.10 shows the Mössbauer spectra of the heated sample compared with the spectra of the as-prepared sample. We find that the differences are only obvious for the highest temperatures. Fig. 5.11 shows the values of the anisotropy and interaction energies obtained from an

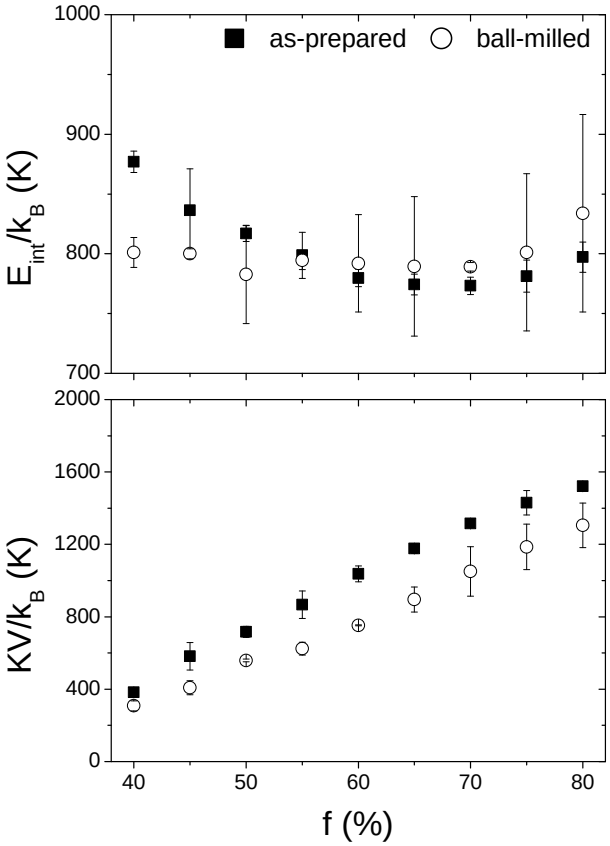


Figure 5.9: Anisotropy ($KV/k_{\mathrm{B}}$) and interaction ($E_{\mathrm{int}}/k_{\mathrm{B}}$) energies as a function of $f$ for the as-prepared and ball-milled sample (from Paper VIII).

analysis of these spectra with the superferromagnetism model. While the anisotropy energy is practically unchanged, the interaction energy is observed to be increased in the heated sample. It is interesting to correlate these observations with the low temperature spectra of both samples. Fig. 5.12 shows the isomer shift $\delta$, the quadrupole shift $\varepsilon$, and the hyperfine field $B_{\mathrm{hf}}$ at low temperatures of the as-prepared and heated samples and the bulk reference sample. It is observed that the absolute value of $\varepsilon$ is decreased in the heated sample whereas the other parameters are practically unchanged (although they differ from those of the bulk sample).

### 5.2.4 Interpretations

Assuming that the different quantiles of the as-prepared sample represented different size fractions, we attempted to separate them through centrifugation (after the as-prepared sample had been subjected to ultrasound treatment). However, none of the attempts were successful. As it turns out, there may be a good explanation for that.

The results presented in Papers VII and VIII contain a number of discrepancies if we maintain the assumption that each rod observed in TEM is a single crystal. At first, it is

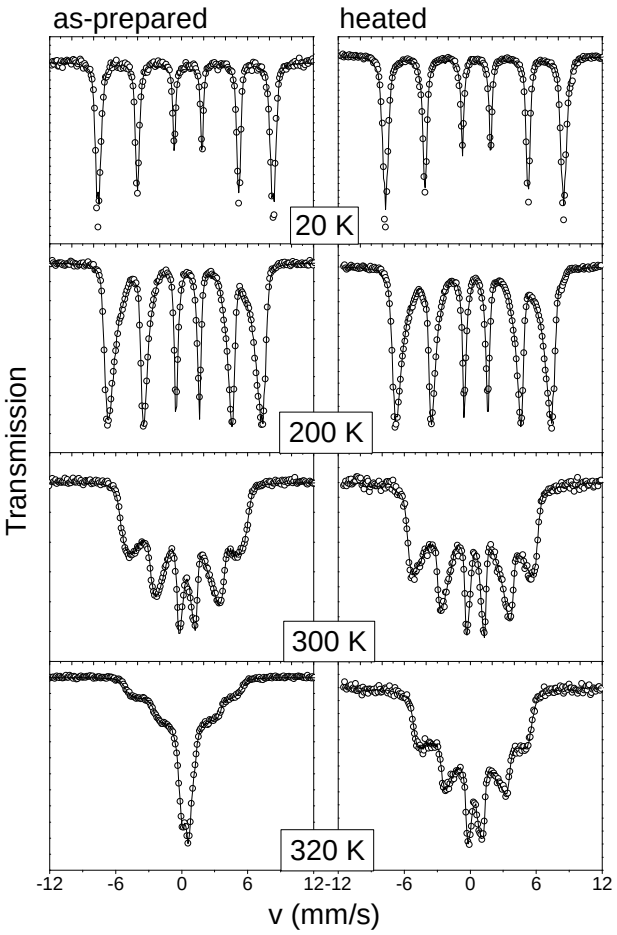


Figure 5.10: Mössbauer spectra at selected temperatures of the as-prepared sample (left) and the heated sample (right) (from Paper VII).

important to note that in XRD, the width of a given *hkl* peak is a measure of the correlation length along the direction perpendicular to the corresponding set of lattice planes. For an isolated particle this gives its dimension along [*hkl*]; however, for two particles in close contact along the direction [*hkl*], the observed correlation length corresponds, in the ideal case of perfect attachment, to the total length along [*hkl*]. For example, Frandsen et al. [114] observed in nanoparticles of hematite that the widths of certain XRD peaks suggested a correlation length much larger than the average dimensions of the particles, whereas other peaks were in agreement with the observed dimensions. TEM images confirmed that the particles exhibited oriented attachment along the directions that in XRD showed an increased correlation length. In our case, it is particularly noteworthy that the length along the long axis [010] is considerably smaller (20 nm) than obtained from TEM (50 nm) while some of the smaller dimensions seem to be larger than those observed with TEM. It seems to be common for the sizes obtained from XRD and TEM to differ, as a comparison, by Bocquet et al. [98], of the size estimates

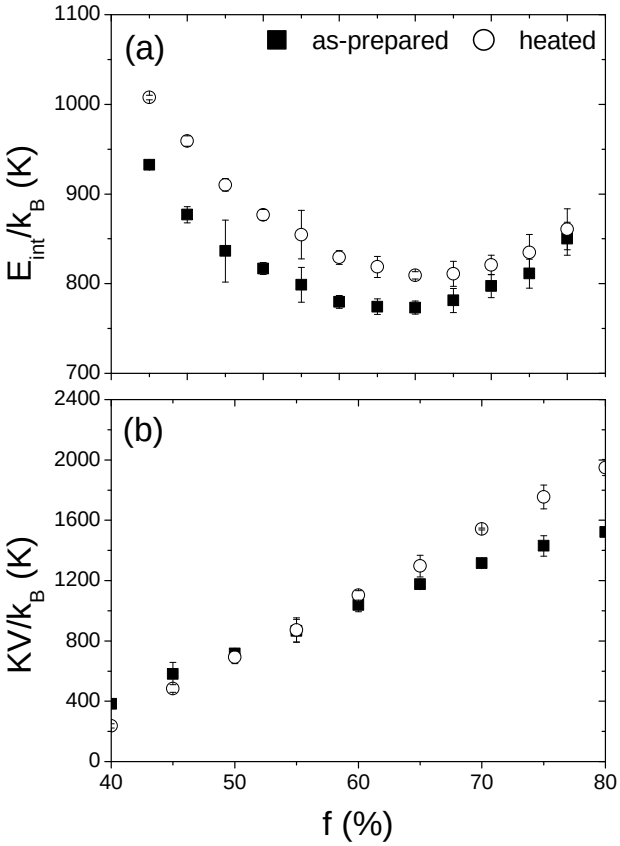


Figure 5.11: Anisotropy ($KV/k_B$) and interaction ($E_{int}/k_B$) energies as a function of $f$ for the as-prepared sample and the heated sample (adapted from Paper VII).

of a number of samples has shown. It is therefore a plausible explanation that the observed rods are not single crystals of goethite but contain several smaller crystals in close contact exhibiting oriented attachment. Such an interpretation is supported by the growth mechanisms of goethite. Guyodo et al. [119] have shown that nanorods of goethite grow by oriented aggregation of ferrihydrite nanoparticles. It is possible that, as the ferrihydrite is transformed into goethite, these precursor particles maintain their separation due to imperfections in the attachment (originating, e.g., from surface roughness). In Paper VIII, HRTEM images obtained at the Center for Electron Nanoscopy (CEN) at DTU, show that such imperfections are indeed present in the crystal in the form of dislocations, low-angle grain boundaries and other defects. Using $K = 5 \cdot 10^4$ J/m$^3$ we also find that the anisotropy energies obtained from the Mössbauer analysis correspond to volumes of 100-500 nm$^3$, considerably smaller than those obtained from TEM. This would also explain why it is not possible to separate the different quantiles through centrifugation, since we in that case fractionate the sample according to the size of the rods and not according to the size of the constituent crystallites.

In a sense, the notion of goethite presented here is somewhat similar to that of Bocquet and Kennedy [97], where the interacting entities were assumed to be clusters formed as a result

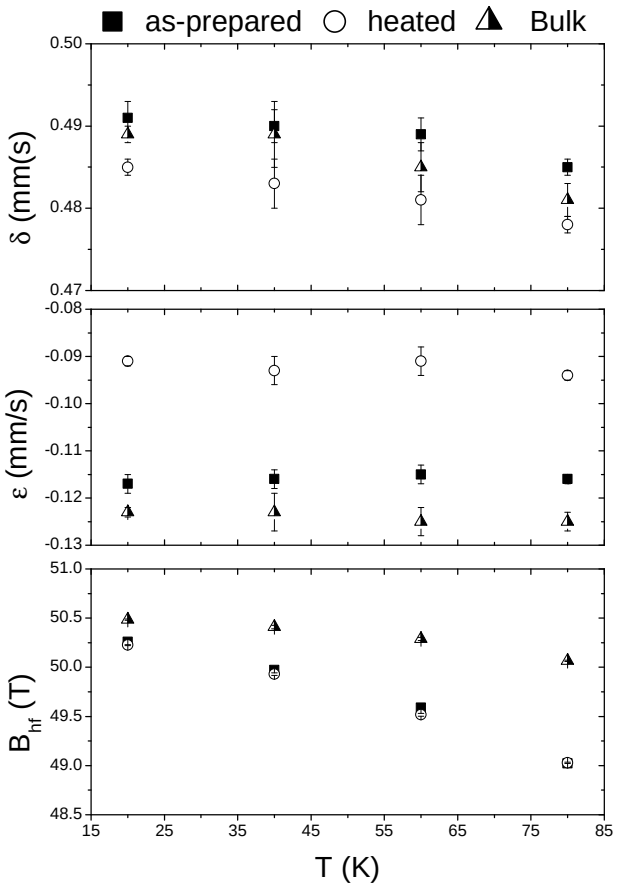


Figure 5.12: Isomer shit ($\delta$), quadrupole shift ($\varepsilon$), and magnetic hyperfine field ($B_{\mathrm{hf}}$) as a function of temperature of the as-prepared sample and the heated sample. The results for the bulk reference sample are also shown for comparison (from Paper VII).

of vacancies within each crystal of goethite. It is a matter of perception whether a crystal containing many vacancies should be considered as a single entity or as an assembly of smaller interacting entities. It should be noted, however, that the analytical treatment of Bocquet and Kennedy [97] differs from that presented here. It is puzzling, though, that the coupling between particles in such close contact are not much stronger. As we show in Paper VIII, however, the antiferromagnetic ordering may be the reason as various defects can lead to a disruption of the magnetic order.

As shown in Fig. 5.12, for the heated sample, we observed a reduced quadrupole shift. Frandsen and Mørup [120] observed a similar effect in nanoparticles of hematite, where the interaction strength was modified through coating of the particles. As discussed in section 2.1.2, the quadrupole shift depends, among other things, on the angle between the magnetic hyperfine field and the principal axis of the EFG, hence Frandsen and Mørup [120] suggested that the increased interactions had lead to a rotation of the sublattice spins. In Paper VII we suggest that a similar effect may be in play in goethite. Another possibility is of course that the

EFG has been changed as a result of the heating. However, measurements at high temperatures where only a doublet is present in the spectra gave identical values of the quadrupole splitting (which depends only on the EFG). Consequently, we do not attribute the observed differences to changes in the EFG. Concerning the mechanism behind this spin rotation, we suggest that as the sample is heated, interfacial water is evaporated whereby the particles are brought into closer contact thereby strengthening the inter-particle interactions.

## 5.3 Discussion

As mentioned earlier, the superferromagnetism model was dismissed by Bocquet and Kennedy [97] as they had observed a transition temperature that was independent of $\tau_{\mathrm{m}}$ (by considering characteristic features in the Mössbauer spectroscopy, neutron scattering and magnetization measurement data). However, as shown in Paper VIII, for our samples we obtained Mössbauer spectra at high temperatures in an applied field of 6 T and observed a splitting of the doublet. This indicates that the collapse of the sextet should be attributed to superparamagnetic relaxation and not to a reduction of the Néel temperature as it has been suggested by Bocquet and Kennedy [97]. It is not impossible, though, that the collapse observed in their sample should indeed be attributed to a reduced Néel temperature, as the magnetic properties of goethite have been found to be sensitive to a number of structural parameters such as, e.g., the degree of crystallinity [101, 102] and the presence of foreign ions [99]. Different synthesis conditions may result in samples where such parameters differ, hence it may be difficult to directly compare results obtained for different samples by different authors, unless these samples have been carefully characterized.

## 5.4 Summary

The magnetic properties of goethite, in the particular the Mössbauer spectra, have for the past many decades been the topic of intense research and the interpretations have been subject of a just as intense debate. By considering the individual quantiles of the hyperfine field distributions we have been able to obtain results that are in better agreement with the large anisotropy energy expected for goethite. Our analysis has shown that the shape of the Mössbauer spectra may be explained with interactions between smaller entities within each goethite rod.

# Chapter 6

# Conclusions and Outlook

## 6.1 Conclusions

The purpose of this work has been to consider different aspects of antiferromagnetic nanoparticles. The main conclusions are as follows:

- Due to the uncompensated moment, nanoparticles of antiferromagnetic materials are, strictly speaking, not antiferromagnets, but ferrimagnets, albeit with a resulting magnetic moment that is much smaller than that expected for a traditional ferrimagnet. We have in this thesis considered cases where the uncompensated moment plays a significant role as well as cases where the perfect antiferromagnetic behavior is prevailing.

- When taking into account the uncompensated moment, we have found that even a small difference in sublattice magnetizations may lead to a considerable change in the energy of the uniform mode of precession. This is confirmed by the experimental study of hematite. Hence, in this particular case the uncompensated moment plays a crucial role. When we consider the thermoinduced moment, we also found that any sample in which we attempt to observe this effect must have as small an uncompensated moment as possible. Thermoinduced magnetization is a phenomenon, which is only clearly observable in a pure antiferromagnet. The more ferrimagnetic our sample is, the less likely it is that we will be able to observe the effect.

- The uncompensated moment must also be taken into account when we analyze magnetization data for antiferromagnetic nanoparticles. Whenever a new experimental situation is encountered, one should, in principle, make sure that the assumptions of any model used for the analysis are (still) fulfilled. As discussed in chapter 3, this has not always been the case when antiferromagnetic nanoparticles have been the topic. As discussed in the present work, the magnetic properties of nanoparticles of antiferromagnetic materials are more sensitive to distributions of volumes and moments, and any analysis cannot yield reliable results unless such effects are taken into account.

- The uncompensated moment, on the other hand, is not expected to play a role for inter-particle interactions as the moment is so small that dipole-interactions are negligible. In nanoparticles of goethite, we find that the Mössbauer spectra, which for decades have been the topic of intense debate, may be explained by exchange mediated inter-particle

interactions. This behavior is not contradicted by the apparent large size of the particles if we assume that each "particle" of goethite contains several smaller crystallites.

## 6.2 Outlook

Hopefully, the work presented here will contribute to a better understanding of nanoparticles of antiferromagnetic materials. Many aspects, however, still need to be addressed. In the following some suggestions for further work related to the results of this thesis are considered.

- Silva et al. [39] considered a distribution of uncompensated moments while we in this thesis have been using a distribution of volumes and have assumed that the uncompensated moment and the volume are related according to Eq. (1.11). However, it is important to note that even a monodisperse sample may contain a distribution of uncompensated moments $p(\mu)$ due to the random nature of this moment. Such a distribution may be taken into account by writing, e.g., Eq. (3.26) as

$$\chi'(\omega,T) = \frac{\mu_0}{3KV^2}\left(\frac{KV}{k_\mathrm{B}T}\frac{1}{1+(\omega\tau)^2} + \frac{(\omega\tau)^2}{1+(\omega\tau)^2}\right)\int_0^\infty \mu^2 p(\mu)\,\mathrm{d}\mu \tag{6.1a}$$

$$\chi''(\omega,T) = \frac{\mu_0}{3KV^2}\left(\frac{\omega\tau}{1+(\omega\tau)^2} - \frac{KV}{k_\mathrm{B}T}\frac{\omega\tau}{1+(\omega\tau)^2}\right)\int_0^\infty \mu^2 p(\mu)\,\mathrm{d}\mu, \tag{6.1b}$$

  where we have assumed that the magnitude of $\mu = M/V$ has no effect on $\tau$. We note that the distribution of $\mu$ is effectively taken into account by replacing $M^2$ with $\langle\mu^2\rangle/V^2$. If we assume that this distribution is log-normal with width $\sigma_\mu$, $\langle\mu^2\rangle/V^2 = M^2\exp[2\sigma_\mu^2]$, i.e., the effective magnetization is increased due to the distribution. We may express this difference by introducing an effective $\nu$ value $\nu_e$ fulfilling $\mu_\mathrm{at}^2 c^{2\nu_e} V_\mathrm{m}^{2\nu_e-2} = \mu_\mathrm{at}^2 c^{2\nu} V_\mathrm{m}^{2\nu-2}\exp[2\sigma^2]$. Solving for $\nu_e$ yields

$$\nu_e = \nu + \frac{\sigma^2}{\ln(V_\mathrm{m}) + \ln(c)}, \tag{6.2}$$

  where we assume that $\sigma_\mu$ is independent of volume. As long as $\sigma$ is not too large, the change of $\nu$ is, in the case of ferritin, negligible. However, it is difficult to estimate $\sigma_\mu$ or to even ascertain if the log-normal distribution is a reasonable approximation. Consequently, it is an effect, which we have not considered in Papers III and IV. However, this effect should be investigated further in order to determine if a log-normal distribution accurately describes both a distribution of volumes and of uncompensated moments.

- The superferromagnetism model used for the analysis of the goethite Mössbauer spectra represents an attempt at describing the interaction effects. It is, however, difficult to ascertain if this model yields results that are in quantitative agreement with results obtained from other methods. In addition to the results presented in Papers VII and VIII the Mössbauer spectra of numerous other goethite samples, have, as part of this work, been analyzed with the superferromagnetism model. The anisotropy and interactions energies obtained for samples synthesized under similar conditions are in general very similar. It is noteworthy, though, that for a sample, which from XRD was indicated to have much larger crystallites than those discussed here, a much larger anisotropy energy was found. On the other hand, a much small interaction energy was obtained for a

sample precipitated from a solution containing $SiO_2$, which in a previous study [121], was found to exhibit reduced interactions. In relation to the study of the heated sample, it should be noted that the quadrupole shift of the sample showing reduced interactions was much larger than for the samples discussed in Papers VII and VIII. However, these additional samples need to be much more carefully characterized before anything can be safely concluded from these results. In general, it could be interesting to consider the results obtained with the superferromagnetism model for different well-characterized samples.

- Harris et al. [36] studied the relationship between the volume and the uncompensated moment in ferritin, and found the dependence was well described using Eq. (1.11) with $\nu = 1/2$. However, these moments were obtained by the use of Eq. (3.5), where neither the anisotropy nor a distribution of volumes have been considered. It could be interesting to re-investigate this relationship using the analysis presented in chapter 3.

- So far, there is no experimental evidence for the thermoinduced moment. With the results from this thesis in mind it should be possible to focus attention on those materials in which we predict the thermoinduced moment to be most easily observed (for example, NiO or $Cr_2O_3$).

- When deriving the thermoinduced moment, it is assumed that only the $q = 0$ states are occupied. However, as the temperature is increased, the $q \neq 0$ states become populated as well. It could be interesting to consider what effect a population of the $q \neq 0$ states has on the resulting thermoinduced moment. For example, it could be even more challenging to observe the thermoinduced moment, if states with $q \neq 0$ do not contribute to the thermoinduced moment.

# Appendix A

# Appendix

## A.1 Distribution functions

### A.1.1 General definitions

The median value of any distribution $p(x)\,\mathrm{d}x$ is defined such that

$$\int_{x_{\min}}^{x_{\mathrm{m}}} p(x)\,\mathrm{d}x = \int_{x_{\mathrm{m}}}^{x_{\max}} p(x)\,\mathrm{d}x, \tag{A.1}$$

where $x_{\min}$ and $x_{\max}$ correspond to the lower and upper value of the distribution, respectively. It is readily seen that the median value corresponds to the 50% quantile. The average value $\langle x \rangle$, on the other hand, is given as

$$\langle x \rangle = \int_{x_{\min}}^{x_{\max}} x p(x)\,\mathrm{d}x. \tag{A.2}$$

A third parameter of interest is the peak value $x_{\mathrm{p}}$, i.e., the value of maximum probability, which fulfills

$$\left.\frac{\partial p(x)}{\partial x}\right|_{x=x_{\mathrm{p}}} = 0. \tag{A.3}$$

Note, that that $x_{\mathrm{m}}$, $\langle x \rangle$, and $x_{\mathrm{p}}$ for a given distribution function may be different.

### A.1.2 Normal distribution

For a normal distribution we have

$$p(x, x_{\mathrm{m}}, \sigma)\,\mathrm{d}x = \frac{1}{\sqrt{2\pi}\sigma} \exp\left(-\frac{[x - x_{\mathrm{m}}]^2}{2\sigma^2}\right)\,\mathrm{d}x, \tag{A.4}$$

where $x_{\mathrm{m}}$ is median value and $\sigma$ is the width. For the normal distribution, $x_{\mathrm{m}} = \langle x \rangle = x_{\mathrm{p}}$.

### A.1.3 The log-normal distribution

The log-normal distribution is obtained by considering a normal distribution of $\ln(x)$. In this case $x_\mathrm{m}$, $\langle x \rangle$, and $x_\mathrm{p}$ differ, with

$$\langle x \rangle = \exp\left(\frac{1}{2}\sigma^2\right) x_\mathrm{m} \tag{A.5a}$$

$$x_\mathrm{p} = \exp\left(-\sigma^2\right) x_\mathrm{m}. \tag{A.5b}$$

Fig. A.1 shows plots of the log-normal distribution function for different values of the width.

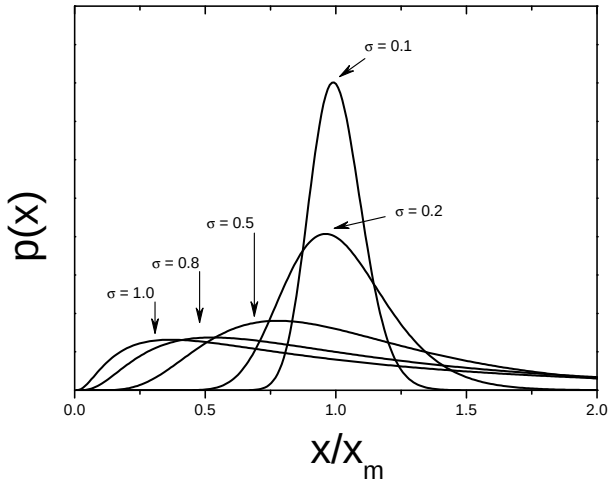


Figure A.1: The log-normal distribution for different values of the width $\sigma$.

For any two variables $x$ and $x'$, related through a power law such as $x' = ax^n$, if $x$ is log-normal distributed, so $x'$ will be, with $\sigma' = n\sigma$ and $x'_\mathrm{m} = ax^n_\mathrm{m}$. This can be shown through insertion of $x' = ax^n$ in Eq. (1.7) and a bit of algebra. It is also interesting to note that the function $y^n p(y)\,\mathrm{d}y$ will have the appearance of a log-normal distribution with the same width but a different median $x'_\mathrm{m} = x_\mathrm{m}\exp(n\sigma^2)$. However, the normalization will be different, i.e.,

$$\int_0^\infty x^n p(x, x_\mathrm{m}, \sigma) \neq 1. \tag{A.6}$$

This relationship is important when we compare the volume-weighted and the number-weighted distributions. We have from Eq. (3.11) that if the number-weighted distribution $p_\mathrm{n}(x)$ is log-normal, the volume-weighted distribution may be written $p_\mathrm{v} = xp_\mathrm{n}(x)$, corresponding to the case discussed above with $n = 1$, in which case the median values are related as $V^{(\mathrm{v})}_\mathrm{m} = \exp(\sigma^2)V^{(\mathrm{n})}_\mathrm{m}$.

## A.2 Adding random orientations

The derivations of the thermoinduced magnetization have so far only considered a situation where the external magnetic field is applied along the easy axis of the particles. We now want

to consider the effect of a random orientation. We denote the angle between the easy axis and the applied field $\beta$, and assume that the two precession angles and their difference are not affected by the random orientation. Two precession states have been found, and with two possible orientations with respect to $B_{\rm app}$ one is left with four possible combinations. Hence, using Boltzmann statistics one obtains (compare with Eq. (4.24))

$$\begin{aligned}\langle M^z_{\rm r(\pm)}\rangle_T &= \frac{1}{Z}\sum_\theta p(\theta)\times \\ &\quad (|\vec{M}^z_{\rm r+}|\cos\beta[e^{-V|\vec{M}^z_{\rm r+}|B\cos\beta/k_{\rm B}T} - e^{V|\vec{M}^z_{\rm r+}|B\cos\beta/k_{\rm B}T}] \\ &\quad +|\vec{M}^z_{\rm r-}|\cos\beta[e^{-V|\vec{M}^z_{\rm r-}|B\cos\beta/k_{\rm B}T} - e^{V|\vec{M}^z_{\rm r-}|B\cos\beta/k_{\rm B}T}]),\end{aligned} \tag{A.7}$$

where $Z$ is the partition function

$$\begin{aligned}Z &= e^{-V|\vec{M}^z_{\rm r+}|B\cos\beta/k_{\rm B}T} + e^{V|\vec{M}^z_{\rm r+}|B\cos\beta/k_{\rm B}T} \\ &\quad +e^{-V|\vec{M}^z_{\rm r-}|B\cos\beta/k_{\rm B}T} + e^{V|\vec{M}^z_{\rm r-}|B\cos\beta/k_{\rm B}T},\end{aligned} \tag{A.8}$$

and $p(\theta)$ is the probability of finding a precession state with angle $\theta$. In the following we consider the initial susceptibility $\chi_{\rm i}$ for a single particle, i.e. the limit where $V|\vec{M}^z_{\rm r\pm}|B_{\rm app} \ll k_{\rm B}T$. In this case $Z \approx 4$, and we find from Eq. (A.7)

$$\chi_{\rm i} = \frac{1}{2}\frac{V\mu_0}{k_{\rm B}T}\sum_\theta p(\theta)\left(|\vec{M}^z_{\rm r+}|^2 + |\vec{M}^z_{\rm r-}|^2\right)\cos^2\beta. \tag{A.9}$$

The rest of the calculations proceed without any change, and we end up with

$$\chi_{\rm i}(\beta) \approx \frac{\mu_0}{V}\left[\frac{\mu_{\rm u}^2}{k_{\rm B}T} + \frac{4k_{\rm B}T}{B_{\rm a}B_{\rm E}}\right]\cos^2\beta, \tag{A.10}$$

which gives us

$$\langle\chi_{\rm i}\rangle_\beta \approx \frac{\mu_0}{V}\left[\frac{\mu_{\rm u}^2}{k_{\rm B}T} + \frac{4k_{\rm B}T}{B_{\rm a}B_{\rm E}}\right]\langle\cos^2\beta\rangle, \tag{A.11}$$

and for a random distribution of orientations we find

$$\langle\chi_{\rm i}\rangle_\beta = \frac{\mu_0 V M_{\rm u}^2}{3k_{\rm B}T} + \frac{4\mu_0 k_{\rm B}T}{3VB_{\rm a}B_{\rm E}}, \tag{A.12}$$

as $\langle\cos^2\beta\rangle = 1/3$. We note that there is no change in the relative strengths of the two contributions.

# Bibliography


[1] S. Chikazumi, *Physics of Ferromagnetism* (Oxford: Clarendon Press, 1997), 2nd ed.

[2] C. Zener, Phys. Rev. **96**, 1335 (1954).

[3] F. Bødker, S. Mørup, and S. Linderoth, Phys. Rev. Lett. **72**, 282 (1994).

[4] L. Néel, Ann. Geophys. **5**, 99 (1949).

[5] W. F. Brown, Phys. Rev. **130**, 1677 (1963).

[6] A. Aharoni, Phys. Rev. **135**, A447 (1964).

[7] D. H. Jones and K. K. P. Srivastava, J. Magn. Magn. Mater. **78**, 320 (1989).

[8] D. Weller and A. Moser, IEEE T. Magn. **35**, 4423 (1999).

[9] Q. A. Pankhurst, J. Connolly, S. K. Jones, and J. Dobson, J. Phys. D: Appl. Phys. **36**, R167 (2003).

[10] W. Wernsdorfer, D. Mailly, and A. Benoit, J. Appl. Phys. **87**, 5094 (2000).

[11] R. A. Granqvist, C. G.and Buhrman, J. Appl. Phys. **47**, 2200 (1976).

[12] T. Jonsson, J. Mattsson, P. Nordblad, and P. Svedlindh, J. Magn. Magn. Mater. **168**, 269 (1997).

[13] J. L. Dormann, D. Fiorani, and E. Tronc, Adv. Chem. Phys. **98**, 283 (1997).

[14] J. L. Dormann, L. Bessais, and D. Fiorani, J. Phys. C: Solid State **21**, 2015 (1988).

[15] S. Mørup and E. Tronc, Phys. Rev. Lett. **72**, 3278 (1994).

[16] M. F. Hansen and S. Mørup, J. Magn. Magn. Mater. **184**, 262 (1998).

[17] J. L. Dormann, D. Fiorani, and E. Tronc, J. Magn. Magn. Mater. **202**, 251 (1999).

[18] L. Néel, C. R. Hebd. Seances Acad. Sci. **252**, 4075 (1961).

[19] URL `www.nobelprize.org`.

[20] N. N. Greenwood and T. C. Gibb, *Mössbauer spectroscopy* (London: Chapman and Hall Ltd., 1971).

[21] P. Gütlich, R. Link, and A. Trautwein, *Mössbauer spectroscopy and transition metal chemistry* (Berlin: Springer, 1978).

[22] M. Blume and J. A. Tjon, Phys. Rev. **165**, 446 (1968).

[23] R. C. Jaklevic, J. J. Lambe, A. H. Silver, and J. E. Mercereau, Phys. Rev. Lett. **12**, 274 (1964).

[24] R. C. Jaklevic, A. H. Silver, J. Lambe, and J. E. Mercereau, Phys. Rev. Lett. **12**, 159 (1964).

[25] R. C. Jaklevic, J. Lambe, J. E. Mercereau, and A. H. Silver, Phys. Rev. **140**, 1628 (1965).

[26] J. Als-Nielsen and D. McMorrow, *Elements of Modern X-Ray Physics* (Chichester: John Wiley & Sons, 2001).

[27] P. Scherrer, Nachr. Ges. Wiss. Göttingen p. 98 (1918).

[28] J. I. Langford and A. J. C. Wilson, J. Appl. Cryst. **11**, 102 (1978).

[29] H. M. Rietveld, Acta Cryst. **22**, 151 (1967).

[30] H. M. Rietveld, J. Appl. Cryst. **2**, 65 (1969).

[31] E. C. Stoner and E. P. Wohlfarth, Philos. T. R. Soc. S.-A **240**, 599 (1948).

[32] M. Hanson, C. Johansson, and S. Mørup, J. Phys.: Cond. Matter **5**, 725 (1993).

[33] S. H. Kilcoyne and R. Cywinski, J. Magn. Magn. Mater. **140-144**, 1466 (1995).

[34] D. Vollath, D. V. Szabo, and J. O. Willis, Mater. Lett. **29**, 271 (1996).

[35] S. Makhlouf, F. T. Parker, and A. E. Berkowitz, Phys. Rev. B **55**, R14717 (1997).

[36] J. G. E. Harris, J. E. Grimaldi, D. D. Awschalom, A. Chiolero, and D. Loss, Phys. Rev. B **60**, 3453 (1999).

[37] M. S. Seehra, V. S. Babu, A. Manivannan, and J. W. Lynn, Phys. Rev. B **61**, 3513 (2000).

[38] M. Banobre-Lopez, C. Vazquez-Vazquez, J. Rivas, and M. A. Lopez-Quintela, Nanotechnology **14**, 318 (2003).

[39] N. J. O. Silva, V. S. Amaral, and L. D. Carlos, Phys. Rev. B **71**, 184408 (2005).

[40] N. J. O. Silva, L. D. Carlos, and V. S. Amaral, Phys. Rev. Lett. **94**, 039707 (2005).

[41] J. I. Gittleman, B. Abeles, and S. Bozowski, Phys. Rev. B **9**, 3891 (1974).

[42] G. C. Ford, P. M. Harrison, D. W. Rice, J. M. A. Smith, A. Treffry, J. L. White, and J. Yariv, Phil. Trans. R. Soc. Lond. **304**, 551 (1984).

[43] E. C. Theil, Ann. Rev. Biochem. **56**, 289 (1987).

[44] A. Blaise, J. Chappert, and J. L. Girardet, C. R. Hebd. Acad. Sci. **261**, 2310 (1965).

[45] G. Schoffa, Z. Naturf. **B 20**, 167 (1965).

[46] E. R. Bauminger and I. Nowik, Hyperfine Interact. **50**, 489 (1989).

[47] C. Gilles, P. Bonville, H. Rakoto, J. M. Broto, K. K. W. Wong, and S. Mann, J. Magn. Magn. Mater. **241**, 430 (2002).

[48] J. Z. Jiang and S. Mørup, Nanostruct. Mater. **9**, 375 (1997).

[49] R. M. Cornell and U. Schwertmann, *The Iron Oxides* (Weinheim: Wiley-VCH, 2003).

[50] T. G. St. Pierre, N. T. Gorham, P. D. Allen, J. L. Costa-Krämer, and K. V. Rao, Phys. Rev. B **65**, 024436 (2001).

[51] C. Kittel, Phys. Rev. **82**, 565 (1951).

[52] F. Keffer and C. Kittel, Phys. Rev. **85**, 329 (1952).

[53] R. K. Wangsness, Phys. Rev. **86**, 146 (1952).

[54] R. K. Wangsness, Phys. Rev. **91**, 1085 (1953).

[55] S. Mørup and C. Frandsen, Phys. Rev. Lett. **92**, 217201 (2004).

[56] R. Orbach, Phys. Rev. **115**, 1181 (1959).

[57] D. H. Martin, *Magnetism in solids* (Cambridge: Iliffe Books Ltd., 1967).

[58] P. V. Hendriksen, S. Linderoth, and P. A. Lindgård, Phys. Rev. B **48**, 7259 (1993).

[59] S. N. Klausen, K. Lefmann, P. A. Lindgard, L. T. Kuhn, C. R. H. Bahl, C. Frandsen, S. Morup, B. Roessli, N. Cavadini, and C. Niedermayer, Phys. Rev. B **70**, 214411 (2004).

[60] S. Mørup and H. Topsøe, Appl. Phys. **11**, 63 (1976).

[61] C. R. H. Bahl, J. Garde, K. Lefmann, T. B. S. Jensen, P. A. Lindgård, D. E. Madsen, and S. Mørup, Eur. Phys. J. B **62**, 53 (2008).

[62] M. F. Hansen, F. Bødker, S. Mørup, K. Lefmann, K. N. Clausen, and P. A. Lindgård, Phys. Rev. Lett. **79**, 4910 (1997).

[63] A. H. Morrish, *The Physical Principles of Magnetism* (New York: John Wiley & Sons, Inc., 1965).

[64] S. Mørup and B. R. Hansen, Phys. Rev. B **72**, 024418 (2005).

[65] S. Mørup and C. Frandsen, Phys. Rev. Lett. **94**, 039708 (2005).

[66] S. Mørup and C. Frandsen, Phys. Rev. Lett. **94**, 089702 (2005).

[67] G. Brown, A. Janotti, M. Eisenbach, and G. M. Stocks, Phys. Rev. B **72**, 140405R (2005).

[68] A. H. MacDonald and C. M. Canali, Phys. Rev. Lett. **94**, 089701 (2005).

[69] D. E. Madsen and S. Mørup, Phys. Rev. B **74**, 014405 (2006).

[70] C. R. H. Bahl, M. F. Hansen, T. Pedersen, S. Saadi, K. H. Nielsen, B. Lebech, and S. Mørup, J. Phys.: Condens. Matter **18**, 4161 (2006).

[71] S. Foner, Phys. Rev. **130**, 183 (1963).

[72] M. F. Hansen, C. B. Koch, and S. Mørup, Phys. Rev. B **62**, 1124 (2000).

[73] C. Frandsen and S. Mørup, J. Magn. Magn. Mater. **266**, 36 (2003).

[74] R. V. Morris, G. Klingelhöfer, C. Schröder, D. S. Rodionov, A. Yen, D. W. Ming, P. A. de Souza, I. Fleischer, T. Wdowiak, R. Gellert, et al., J. Geophys. Res.-Planet. **111**, E02S13 (2006).

[75] G. Klingelhöfer, E. DeGrave, R. V. Morris, A. Alboom, V. G. de Resende, P. A. De Souza, D. Rodionov, C. Schröder, D. W. Ming, and A. Yen, Hyperfine Interact. **166**, 549 (2006).

[76] H. X. Yang, R. Lu, R. T. Downs, and G. Costin, Acta. Crystallogr. E **62**, i250 (2006).

[77] A. Szytula, A. Burewicz, Z. Dimitrij, S. Krasnick, H. Rzany, J. Todorovi, A. Wanic, and W. Wolski, Phys. Status Solidi **26**, 429 (1968).

[78] J. B. Forsyth, I. G. Hedley, and C. E. Johnson, J. Phys. C **1**, 179 (1968).

[79] J. M. D. Coey, A. Barry, J. M. Brotto, H. Rakoto, S. Brennan, W. N. Mussel, A. Collomb, and D. Fruchart, J. Phys.: Condens. Matter **7**, 759 (1995).

[80] H. Kurokawa, Mat. Sci. Eng. A **202**, 201 (1995).

[81] M. Kosmulski, S. Durand-Vidal, E. Maczka, and J. B. Rosenholm, J. Colloid. Interf. Sci. **271**, 261 (2004).

[82] S. Mørup, M. B. Madsen, J. Franck, J. Villadsen, and C. J. W. Koch, J. Magn. Magn. Mater. **40**, 163 (1983).

[83] G. W. van Oosterhout, in *Proceedings of the international conference on magnetism, Notthingham, September 1964* (1964).

[84] A. Z. Hrynkiewicz, D. S. Kulgawczuk, and K. Tomala, Phys. Lett. **17**, 93 (1965).

[85] F. van der Woude and A. J. Dekker, Phys. Stat. Sol. **13**, 181 (1966).

[86] A. Govaert, C. Dauwe, E. De Grave, and J. Desitter, Solid State Commun. **18**, 389 (1976).

[87] A. Govaert, C. Dauwe, J. Desitter, E. De Grave, and G. Robbrecht, Physica B & C **86**, 1427 (1977).

[88] E. Murad, Mineral. Mag. **43**, 355 (1979).

[89] E. Murad, Am. Mineral. **67**, 1007 (1982).

[90] U. Schwertmann, P. Cambier, and E. Murad, Clay. Clay. Miner. **33**, 369 (1985).

[91] C. J. W. Koch, M. B. Madsen, and S. Mørup, Surf. Sci. **156**, 249 (1985).

[92] C. J. W. Koch, M. B. Madsen, S. Mørup, G. Christiansen, L. Gerward, and J. Villadsen, Clay. Clay Miner. **34**, 17 (1986).

[93] A. Meagher, Q. A. Pankhurst, and D. P. E. Dickson, Hyperfine Interact. **28**, 533 (1986).

[94] Q. A. Pankhurst and R. J. Pollard, J. Phys.: Condens. Matter **2**, 7329 (1990).

[95] D. Broz, J. Strakova, J. Subrt, J. Vins, B. Sedlak, and S. I. Reiman, Hyperfine Interact. **54**, 479 (1990).

[96] D. Broz, S. I. Reiman, and B. Sedlak, Hyperfine Interact. **60**, 1011 (1990).

[97] S. Bocquet and S. J. Kennedy, J. Magn. Magn. Mater. **109**, 260 (1992).

[98] S. Bocquet, R. J. Pollard, and J. D. Cashion, Phys. Rev. B **46**, 11657 (1992).

[99] C. A. Barrero, R. E. Vandenberghe, and E. De Grave, Hyperfine Interact. **122**, 39 (1999).

[100] J. Y. Lee, S. J. Oh, J. G. Sohn, and S. J. Kwon, Corros. Sci. **43**, 803 (2001).

[101] J. D. Betancur, C. A. Barrero, J. M. Greneche, and G. F. Goya, J. Alloy. Compd. **369**, 247 (2004).

[102] C. A. Barrero, J. D. Betancur, J. M. Greneche, G. F. Goya, and T. S. Berquo, Geophys. J. Int. **164**, 331 (2006).

[103] S. Shtrikman and E. P. Wohlfarth, Phys. Lett. **85A**, 467 (1981).

[104] R. W. Chantrell and E. P. Wohlfarth, J. Magn. Magn. Mater. **40**, 1 (1983).

[105] L. Bessais, L. Benjaffel, and J. L. Dormann, Phys. Rev. B **45**, 7805 (1992).

[106] C. Johansson, M. Hanson, P. V. Hendriksen, and S. Mørup, J. Magn. Magn. Mater. **122**, 125 (1993).

[107] S. Linderoth, L. Balcells, A. Labarta, J. Tejada, P. V. Hendriksen, and S. A. Sethi, J. Magn. Magn. Mater. **124**, 269 (1993).

[108] R. W. Chantrell, G. N. Coverdale, M. El Hilo, and K. O'Grady, J. Magn. Magn. Mater. **157–158**, 250 (1996).

[109] R. W. Chantrell, N. S. Walmsley, J. Gore, and M. Maylin, J. Magn. Magn. Mater. **196–197**, 118 (1999).

[110] R. W. Chantrell, N. Walmsley, J. Gore, and M. Maylin, Phys. Rev. B **63**, 024410 (2001).

[111] A. O. Ivanov and O. B. Kuznetsova, J. Magn. Magn. Mater. **252**, 135 (2002).

[112] D. E. Madsen, M. F. Hansen, C. B. Koch, and S. Mørup, J. Phys.: Condens. Matter **20**, 135215 (2008).

[113] R. L. Penn and J. F. Banfield, Geochim. Cosmochim. Ac. **63**, 1549 (1999).

[114] C. Frandsen, C. R. H. Bahl, B. Lebech, K. Lefmann, L. Theil Kuhn, L. Keller, N. H. Andersen, M. v. Zimmermann, E. Johnson, S. N. Klausen, et al., Phys. Rev. B **73**, 214406 (2005).

[115] M. Nesterova, J. Moreau, and J. F. Banfield, Geochim. Cosmochim. Ac. **67**, 1177 (2003).

[116] D. J. Burleson and R. L. Penn, Langmuir **22**, 402 (2006).

[117] R. L. Penn, J. J. Erbs, and D. M. Gulliver, J. Cryst. Growth **293**, 1 (2006).

[118] C. Wivel and S. Mørup, J. Phys. E **14**, 605 (1981).

[119] Y. Guyodo, A. Mostrom, R. L. Penn, and S. K. Banerjee, Geophys. Res. Lett. **30**, 1512 (2003).

[120] C. Frandsen and S. Mørup, Phys. Rev. Lett. **94**, 027202 (2005).

[121] C. J. W. Koch, M. B. Madsen, and S. Mørup, Hyperfine Interact. **28**, 549 (1986).

# English summary

In this thesis, several aspects of antiferromagnetic nanoparticles are studied. In a perfect antiferromagnet, the spins are oppositely oriented, such that it carries no external magnetic moment. However, in nanoparticles of antiferromagnetic materials, the cancelation is, due to various finite-size effects, not perfect, and as a result, such particles have a small uncompensated magnetic moment. The magnetization due to this moment is, unlike in ferro- or ferrimagnetic materials, dependent on the volume of the particle.

Traditionally, when analyzing, e.g., magnetization data for antiferromagnetic nanoparticles, people have used models originally derived for ferro- or ferrimagnetic particles. However, such models may contain assumptions that are not necessarily fulfilled for antiferromagnetic nanoparticles. In this thesis it is shown that the uncritical use of such models may lead to inaccurate estimates of the various parameters. For example, when analyzing the magnetization curves of antiferromagnetic nanoparticles, it has rarely been considered that due to the small size of the uncompensated moment $\mu$, even in a large applied field $B$ at high temperatures, the Zeeman energy ($\mu B$) may still be comparable to the anisotropy energy. We show that an incorrect temperature dependence of the uncompensated moment is obtained when the anisotropy is not taken into account. Another example involves polydisperse samples, where the volume dependence of the uncompensated magnetization must also be taken into consideration. We consider the values of the anisotropy energy and the superparamagnetic attempt time obtained from a peak analysis of ac susceptibility data, and find that these are incorrectly determined if the volume dependence is not correctly taken into account. The best estimates of such parameters are obtained from a direct analysis of the susceptibility curves; however, also in this case should the volume dependence of the uncompensated magnetization be kept in mind.

Excitations in magnetic particles are typically in the form of spin waves. The lowest energy mode may be described as a uniform precession of the spins in combination with transitions between states with different precession angles. According to classical calculations, the energy of the uniform state differs for ferri- and antiferromagnetic particles. As shown in this thesis, the energy obtained in 8 nm particles of hematite ($\alpha$-$Fe_2O_3$) is different from that expected for a perfect antiferromagnet. However, the discrepancy may be explained if we as a consequence of the uncompensated moment consider the particles as small ferrimagnets. The magnitude of the uncompensated moment required to explain this difference in energies is found to agree with predictions.

It can be shown that in the state of uniform precession, the sublattice magnetizations are not entirely antiparallel. It has previously been theorized that this difference in precession angles may lead, in a perfect antiferromagnet, to the appearance of a so-called thermoinduced magnetic moment, which, unlike the ordinary magnetic moment, increases with temperature. In this thesis, we consider the antiferromagnetic nanoparticles as small ferrimagnets, and study

the effect of the resulting uncompensated moment in regards to the thermoinduced moment. It is shown that, although the uncompensated moment in some cases may be predominant, under favorable conditions, the thermoinduced moment may still be detectable.

A final concept considered is that of inter-particle interactions. Goethite ($\alpha$-FeOOH), an antiferromagnetic iron oxyhydroxide, has been intensely studied for the past decades. Nanoparticles of goethite have long been known to have a peculiar Mössbauer spectrum in that the lines of the constituent sextet, indicating magnetic order, show asymmetrical broadening as the temperature is increased. Further, the sextet collapses to a doublet at a temperature that is much lower than the expected Néel temperature. Several explanations have over the years been proposed, including interactions between otherwise superparamagnetic particles. One problem with such an interpretation is that the particles have hitherto been estimated, e.g., from TEM, to be too large (specifically to have a large magnetic anisotropy) to exhibit superparamagnetic relaxation. In this work we show that such an interpretation may still be valid since the particles previously assumed to be single crystals may contain several smaller interacting crystallites.

# Dansk resumé

I denne Ph.D. afhandling studeres forskellige egenskaber ved antiferromagnetiske nanopartikler. I en ideel antiferromagnet er spinnene orienteret således at der ikke er et resulterende magnetisk moment. I nanopartikler af antiferromagnetiske materialer er denne kompensation på grund af forskellige størrelseseffekter dog ikke perfekt, hvorfor sådanne partikler har et lille ukompenseret magnetisk moment.

Traditionelt set er, blandt andet, magnetiseringsdata for antiferromagnetiske nanopartikler blevet analyseret med modeller der oprindelig er blevet udledt for ferro- eller ferrimagnetiske partikler. Disse modeller kan dog være baseret på antagelser som ikke nødvendigvis er opfyldt for antiferromagnetiske nanopartikler. I denne afhandling demonstreres, at den ukritiske anvendelse af sådanne modeller kan føre til en ukorrekt bestemmelse af forskellige parametre. For eksempel, når magnetiseringskurver for antiferromagnetiske nanopartikler er blevet analyseret, er det sjældent blevet taget i betragtning, at på grund af det ukompenserede moments lille størrelse vil Zeeman-energien selv ved høje temperaturer og i et stort påtrykt felt være sammenlignelig med anisotropi-energien. Det bliver vist hvorledes en ukorrekt temperaturafhængighed af det ukompenserede moment følger når anisotropi-energien ikke inkluderes i analysen. I et andet eksempel betragtes polydisperse prøver, hvor volumen-afhængigheden af det ukompenserede moment også skal medtages i analysen. I dette tilfælde betragter vi værdierne af anisotropien-energien og præfaktoren i den superparamagnetiske relaksationslov bestemt fra en analyse af peak-værdierne i ac susceptibilitetsdata. Vi demonstrerer at disse værdier bliver unøjagtigt bestemt hvis ikke volumen-afhængigheden tages i betragtning. Det bedste estimat af disse parametre opnås ved en direkte analyse af susceptibilitetskurverne. I dette tilfældet skal volumen-afhængigheden dog også inddrages.

Eksitationer i magnetiske partikler har typisk form af spinbølger. Den laveste energitilstand kan beskrives som en uniform præsession af spinnene kombineret med overgange mellem tilstande med forskellige præsessionsvinkler. Ifølge klassiske beregninger er energien i den uniforme tilstand forskellig for ferri- og antiferromagnetiske partikler. I denne afhandling diskuteres, hvorledes energien i 8 nm store hæmatit partikler afviger fra hvad der forventes for en antiferromagnetisk nanopartikel. Denne uoverensstemmelse kan dog forklares hvis vi som følge af det ukompenserede moment betragter partiklerne som små ferrimagneter. Størrelsen på det ukompenserede moment der skal til for at forklare forskellen i energier viser sig at være i overensstemmelse med de teoretiske forudsigelser.

Det kan vises, at undergittermagnetiseringerne i den uniforme præsessionstilstand ikke er fuldstændigt antiparallelle. Det er tidligere blevet foreslået at denne forskel i præsessionsvinkler i en ideel antiferromagnet kan føre til eksistensen af et såkaldt termoinduceret magnetisk moment, der, modsat det normale magnetiske moment, stiger med temperaturen. I denne afhandling betragter vi antiferromagnetiske nanopartikler som små ferrimagneter og undersøger hvilken effekt tilstedeværelsen af et ukompenseret moment har på muligheden for at

observere det termoinducerede moment. Det vises, at omend det ukompenserede moment i mange tilfælde vil være fremtrædende, vil der også være situationer hvor det termoinducerede moment er tydeligt observerbart.

Endelig betragtes også vekselvirkninger mellem partikler. Goethit er en antiferromagnetisk jern oxyhydroxid som gennem de seneste årtier er blevet grundigt studeret. Det har længe været kendt at små goethite partikler har et besynderligt Mössbauer spektrum eftersom linierne af den sekstet, der indikerer magnetisk orden, forbredes asymmetrisk med stigende temperatur. Desuden kollapser sekstetten til en dublet ved en temperatur der ligger væsentlig under den forventede Néel temperatur. Adskillige forklaringer er gennem årene blevet fremsat, herunder at det skulle skyldes vekselvirkninger mellem ellers superparamagnetiske partikler. Et problem med en sådan fortolkning har været, at partiklerne hidtil er blevet estimeret til at være for store til at udvise superparamagnetisk relaksation. I denne afhandling vises det, at en sådan fortolkning alligevel kan være korrekt, eftersom partikler der tidligere har været antaget at være en-krystaller formentlig indeholder adskillige mindre, vekselvirkende krystaller.

# Part II

# Papers

# Paper I

IOP PUBLISHING JOURNAL OF PHYSICS: CONDENSED MATTER

J. Phys.: Condens. Matter **19** (2007) 213202 (31pp) doi:10.1088/0953-8984/19/21/213202

**TOPICAL REVIEW**

# Experimental and theoretical studies of nanoparticles of antiferromagnetic materials

**Steen Mørup[1], Daniel E Madsen[1], Cathrine Frandsen[1], Christian R H Bahl[2] and Mikkel F Hansen[3]**

[1] Department of Physics, Building 307, Technical University of Denmark, DK-2800 Kgs. Lyngby, Denmark
[2] Fuel Cells and Solid State Chemistry Department, Building 227, Risø National Laboratory, DK-4000 Roskilde, Denmark
[3] MIC—Department of Micro and Nanotechnology, Building 345 East, Technical University of Denmark, DK-2800 Kgs. Lyngby, Denmark

Received 23 January 2007, in final form 13 March 2007
Published 2 May 2007
Online at stacks.iop.org/JPhysCM/19/213202

**Abstract**

The magnetic properties of nanoparticles of antiferromagnetic materials are reviewed. The magnetic structure is often similar to the bulk structure, but there are several examples of size-dependent magnetic structures. Owing to the small magnetic moments of antiferromagnetic nanoparticles, the commonly used analysis of magnetization curves above the superparamagnetic blocking temperature may give erroneous results, because the distribution in magnetic moments and the magnetic anisotropy are not taken into account. We discuss how the magnetic dynamics can be studied by use of magnetization measurements, Mössbauer spectroscopy and neutron scattering. Below the blocking temperature, the magnetic dynamics in nanoparticles is dominated by thermal excitations of the uniform mode. In antiferromagnetic nanoparticles, the frequency of this mode is much higher than in ferromagnetic and ferrimagnetic nanoparticles, but it depends crucially on the size of the uncompensated moment. Excitation of the uniform mode results in a so-called thermoinduced moment, because the two sublattices are not strictly antiparallel when this mode is excited. The magnetic dipole interaction between antiferromagnetic nanoparticles is usually negligible, and therefore such particles present a unique possibility to study exchange interactions between magnetic particles. The interactions can have a significant influence on both the magnetic dynamics and the magnetic structure. Nanoparticles can be attached with a common crystallographic orientation such that both the crystallographic and the magnetic order continue across the interfaces.

  

## Contents



## 1. Introduction

Nanoparticles of magnetic materials have attracted much attention because their properties in several ways differ from those of the corresponding bulk materials [1–4]. Therefore, they provide opportunities to make materials and devices with new magnetic properties. Magnetic nanoparticles have numerous technological applications, one of the most important being for data storage in, for example, hard disks in computers [5]. Applications related to medicine and biotechnology are becoming increasingly important [6, 7]. Stable colloidal suspensions of magnetic nanoparticles—so-called ferrofluids—have numerous applications [8], e.g. in loudspeakers. In most applications, ferromagnetic or ferrimagnetic particles are used, because they possess large magnetic moments, and many experimental and theoretical investigations have focused on these types of particles. Nanostructured antiferromagnetic materials have important applications in, for example, spin valves [9, 10] and in the new technology of magnetic random access memory (MRAM) [11]. It has been proposed that nanostructured antiferromagnetic materials may be used to stabilize the magnetization direction of ferromagnetic particles in magnetic recording media [12]. Nanoparticles of antiferromagnetic materials may have interesting applications in, for example, new types of hard magnetic materials consisting of composites of antiferromagnetic and ferromagnetic or ferrimagnetic nanoparticles [13–16].

It is a general feature of magnetic nanoparticles that the (sublattice) magnetization directions may fluctuate because the anisotropy energy may be comparable to the thermal energy. The magnetic anisotropy of nanoparticles is usually assumed to be uniaxial, with the anisotropy energy given by

$$E(\theta) = KV \sin^2 \theta, \tag{1}$$

where $K$ is the magnetic anisotropy energy constant, $V$ is the particle volume and $\theta$ is the angle between the (sublattice) magnetization direction and an easy direction of magnetization. Thus, for a nanoparticle with magnetic anisotropy energy given by equation (1), there are minima at $\theta = 0$ and $\pi$, separated by an energy barrier, $KV$. The superparamagnetic relaxation time, i.e., the average time between thermally induced reversals of the (sublattice) magnetization, is approximately given by the Néel–Brown expression [17, 18],

$$\tau = \tau_0 \exp\left(\frac{KV}{k_B T}\right), \tag{2}$$

where $k_B$ is Boltzmann's constant and $T$ is the temperature. The value of $\tau_0$ is typically in the range $10^{-13}$–$10^{-9}$ s. The dependence of $\tau_0$ on temperature, particle size, magnetic anisotropy, etc in ferromagnetic nanoparticles has been the subject of several investigations [1]. The superparamagnetic blocking temperature, $T_B$, is defined as the temperature at which the relaxation time is equal to the timescale of the experimental technique used for studies of the magnetic properties. Thus, the blocking temperature is different for different experimental techniques. In DC magnetization measurements, the timescale is typically of the order of 10 s. Above the blocking temperature, the measured magnetization is the thermal equilibrium value and therefore the coercivity vanishes. Below $T_B$, the coercivity increases with decreasing temperature. Often, the so-called zero-field-cooled (ZFC) and the field-cooled (FC) magnetization curves are measured after cooling the sample in zero field or in a (small) applied field, respectively, followed by measuring the magnetization as a function of temperature during warming up in the (small) applied field. In the ZFC magnetization curves of magnetic nanoparticles, one can observe a peak at a temperature of the same order of magnitude as the blocking temperature. AC magnetization measurements have the advantage compared to many other techniques that the timescale can be varied by varying the frequency. In Mössbauer spectroscopy, the timescale $\tau_M$ is of the order of the nuclear Larmor precession time, i.e., typically a few nanoseconds. Below $T_B$, the Mössbauer spectra are magnetically split and in the case of $^{57}$Fe Mössbauer spectroscopy they consist of a six-line component (a sextet) for each iron site in the material. Above $T_B$, the spectra consist of singlets or doublets. Because of the distribution of anisotropy energy barriers, $KV$, the spectra of samples of magnetic nanoparticles normally consist of a superposition of sextets and doublets or singlets in a broad temperature range.

Below the blocking temperature, the thermal energy is insufficient to give rise to frequent magnetization reversals within a time corresponding to the timescale of the experimental technique. However, the (sublattice) magnetization direction may still fluctuate in directions close to an easy direction of magnetization. These fluctuations, termed collective magnetic excitations, can be described as a uniform precession of the (sublattice) magnetization direction around an easy direction in combination with transitions between precession states with different precession angles [19].

It is noteworthy that the uniform precession mode, which can be considered as a spin wave with wavevector $q = 0$, is predominant compared to the spin waves with $q \neq 0$ because of the energy gaps in the spin wave spectrum of nanoparticles [19]. In Mössbauer spectroscopy, the precession and the transitions between the precession states can be considered fast compared to the experimental timescale, and one therefore observes an average value of the magnetic hyperfine field, which for a particle with magnetic energy given by equation (1) can be written at low temperatures [20]:

$$B_{obs} \approx B_0\left[1 - \frac{k_B T}{2KV}\right]. \tag{3}$$

Here $B_0$ is the saturation hyperfine field. Expressions for the magnetic hyperfine splitting in Mössbauer spectra of nanoparticles with arbitrary form of the anisotropy have also been derived [21], and it has been found as a general rule that collective magnetic excitations give rise to a linear temperature dependence of the (sublattice) magnetization in nanoparticles. This is in contrast to the temperature dependence at low temperatures in bulk materials for which the decrease in (sublattice) magnetization with increasing temperature is predominantly due to spin waves with $q > 0$ and is proportional to $T^\alpha$, with $\alpha = 3/2$ in ferromagnetic and ferrimagnetic materials and $\alpha = 2$ in antiferromagnetic materials [22]. According to equation (3), measurements of the temperature dependence of the magnetic hyperfine splitting

can be used to estimate the anisotropy constant. There are several contributions to the anisotropy, such as magnetocrystalline anisotropy, shape anisotropy and stress anisotropy. In nanoparticles, the low symmetry around surface ions can also result in a large surface anisotropy [23], and the effective magnetic anisotropy constant is expected to increase with decreasing particle size because of the increase of the relative number of surface atoms.

The timescale in inelastic neutron scattering experiments is much shorter than that of Mössbauer spectroscopy, and this technique can be used to measure the transition energy for transitions between neighbouring uniform precession states [24, 25].

As discussed in sections 3 and 4.4, nanoparticles of antiferromagnetic materials have non-zero magnetic moments and are therefore, strictly speaking, not antiferromagnetic. Anyway, we will for simplicity here use the term 'antiferromagnetic nanoparticles' instead of the more correct term 'nanoparticles of antiferromagnetic materials'. Furthermore, to ease the language we will refer to $B$ $(= \mu_0 H)$ as the magnetic field (in vacuum) as is common in the literature, instead of using the more correct term 'magnetic induction'.

The size dependence of the magnetic properties of antiferromagnetic nanoparticles differs in several ways from that of ferromagnetic and ferrimagnetic nanoparticles [1, 3, 19, 26, 27], and this is one of the reasons for the current interest in antiferromagnetic nanoparticles. In this paper we give a review of the special properties of antiferromagnetic nanoparticles and we will compare with those of ferromagnetic and ferrimagnetic nanoparticles. We emphasize studies of magnetic dynamics and the influence of interparticle interactions on the magnetic properties. In section 2, we give some examples, that illustrate how magnetic structures in antiferromagnetic nanoparticles can deviate from those of the corresponding bulk materials. Although an ideal antiferromagnetic crystal has no net magnetic moment, nanoparticles of antiferromagnetic particles usually have non-zero magnetic moments, and this is discussed in section 3. Section 4 deals with fluctuations of the sublattice magnetization direction in antiferromagnetic nanoparticles, and it is discussed how such fluctuations can be studied by different experimental techniques, such as magnetization measurements, Mössbauer spectroscopy and neutron scattering. We discuss the special features of the uniform mode in antiferromagnetic nanoparticles, and furthermore, the existence of thermoinduced magnetization and macroscopic quantum tunnelling phenomena are discussed. In section 5 we give a short review of studies of the influence of magnetic interactions between antiferromagnetic nanoparticles.

## 2. Magnetic structure of antiferromagnetic nanoparticles

The magnetic structure of nanoparticles may for several reasons differ from that of the corresponding bulk materials. By use of $^{57}$Fe Mössbauer spectroscopy, one can often get information about magnetic structures by measuring the relative areas of the six absorption lines. In the case of nanoparticles of ferrimagnetic materials, several $^{57}$Fe Mössbauer studies have shown that the intensity of lines 2 and 5 does not vanish when large magnetic fields are applied parallel to the gamma-ray direction, as expected for a perfect ferrimagnet for which the sublattice magnetization directions should be parallel or antiparallel to the applied field [28–30]. This suggests that the reduced number of magnetic neighbour ions at the surface may give rise to magnetic frustration and a related localized spin-canting. It has been suggested [29] that ferrimagnetic nanoparticles can be described as consisting of a magnetically ordered core and a disordered (canted) shell with a thickness of the order of 1–2 nm. However, this model may be too simple in most cases, because defects in the interior of the particles also can result in spin-canting [31]. It is likely that spin-canting is also present in nanoparticles of antiferromagnetic materials [26]. In a recent Mössbauer study of nanoparticles of antiferromagnetic $^{57}$Fe-doped NiO [32], a strong indication of spin-canting was observed.

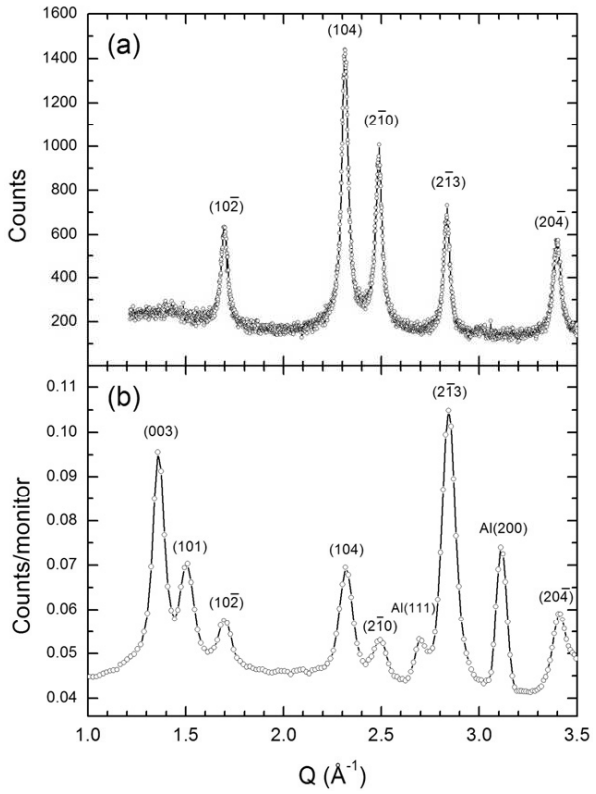


**Figure 1.** (a) X-ray diffraction data and (b) neutron diffraction data for 15 nm hematite nanoparticles. Reprinted with permission from [35]. Copyright 2000 by the American Physical Society.

Theoretical studies of NiO nanoparticles [33, 34] have shown that the interior magnetic structure can differ from the bulk magnetic structure, because of the influence of surface effects. NiO nanoparticles may have a complex magnetic structure with as many as eight sublattices [33], in contrast to bulk NiO, which has a simple two-sublattice structure.

Neutron diffraction allows for resolving magnetic structures of crystals. Figure 1(b) shows room-temperature neutron powder diffraction data of 15 nm $\alpha$-$Fe_2O_3$ particles [35]. For comparison, x-ray powder diffraction data for the same particles are displayed in figure 1(a). The neutron data show the hexagonal (003) and (101) diffraction peaks at the scattering vectors $Q = 1.37$ and 1.50 Å$^{-1}$, respectively. These peaks are not present in the x-ray data as they are purely magnetic. The magnetic diffraction data are in accordance with the magnetic structure of bulk $\alpha$-$Fe_2O_3$ at the same temperature. The magnetic correlation length can be estimated from the width of these diffraction lines using the Scherrer formula in the same way as the crystallographic correlation length can be estimated from the width of the x-ray diffraction lines. The analysis of the data in figure 1 showed that the magnetic and the crystallographic correlation length are identical, i.e., each particle seems to consist of a single magnetic domain [35]. Similar results were found in neutron diffraction studies of NiO [36]. MnO nanoparticles also have the same magnetic structure as the bulk material, but the magnetic correlation length was reported to be smaller than the crystallographic correlation length [37].

Cr nanoparticles have been found to have a simple antiferromagnetic structure, which differs from the spin-density wave structure of bulk Cr [38].

The reduced number of magnetic neighbour ions at the surface results in a smaller exchange field at the surface than in the interior of particles. As a consequence, the (sublattice) magnetization near the surface decreases more quickly with temperature than the (sublattice) magnetization in bulk materials. This has been illustrated by Mössbauer spectroscopy studies of particles of $\alpha$-$Fe_2O_3$, which were prepared with a core with only $^{56}$Fe and a thin surface layer with $^{57}$Fe, such that only the surface atoms contribute to the spectra [39]. Similar results have been found for $\beta$-FeOOH [40] and $\alpha$-FeOOH [41]. The experimental results show an almost linear temperature dependence of the surface magnetization, which is qualitatively in accordance with theoretical models [26, 36, 39, 42]. The temperature dependence of the surface magnetization of these antiferromagnetic nanoparticles is similar to that of ferrimagnetic $\gamma$-$Fe_2O_3$ (maghemite) nanoparticles [39].

When determining the Néel temperature of antiferromagnetic nanoparticles, it is important to be able to distinguish between a transition from a blocked to a superparamagnetic state and a transition to a paramagnetic state. This is not always straightforward, and therefore a careful data analysis may be needed in studies of the size dependence of the Néel temperature. Neutron diffraction studies of plate-shaped, NiO nanoparticles with a thickness of only 2 nm indicated a reduction of the Néel temperature by around 60 K [36]. This is in accordance with theoretical estimates, which showed a lowering of the Néel temperature that depends crucially on the thickness of the NiO plates. Similar neutron studies of much bigger $\alpha$-FeOOH nanoparticles (particle length $\sim$50 nm and width $\sim$12 nm) [43] also suggested a significant lowering of the Néel temperature (by about 40 K). Both magnetization [44] and $\mu$SR [45] measurements of CuO nanoparticles seem to indicate a decreasing Néel temperature with decreasing particle size. In a neutron diffraction study of MnO particles with dimensions of about 14 nm in a porous silica matrix, a slight increase of the Néel temperature has been reported [37]. It was suggested that this could be explained by interaction with the support.

Another type of size dependence of the magnetic structure has been reported in antiferromagnetic $\alpha$-$Fe_2O_3$ (hematite) nanoparticles. In bulk $\alpha$-$Fe_2O_3$, the sublattice magnetization directions are parallel to the hexagonal [001] direction below the so-called Morin temperature, $T_M \approx 263$ K. The Morin transition takes place because of a change of the sign of the magnetic anisotropy constant. Above this temperature, the sublattice magnetization directions lie in the (001) plane, and the two sublattices are not strictly antiparallel, but form an angle of about 0.15°, which results in a small net magnetization. In nanoparticles it has been found that the Morin transition temperature decreases with decreasing particle size [46–48], and it has been reported to be absent for particles with diameters below around 20 nm. This size dependence of the Morin transition temperature can be explained by a size dependence of the magnetic anisotropy constants [49].

Antiferromagnetic materials may perform a so-called spin–flop transition in large applied magnetic fields, such that the sublattice magnetization vectors become nearly perpendicular to the applied magnetic field. If the magnetic field is applied along the easy axis of a simple two-sublattice uniaxial antiferromagnet, the spin–flop transition field at low temperatures is given by [22]

$$B_{sf} \approx \sqrt{2B_E B_A}, \tag{4}$$

where $B_E$ is the exchange field and $B_A = K/M_S$ is the anisotropy field of an antiferromagnet with sublattice magnetization $M_S$. It is here assumed that $B_E \gg B_A$. If an uncompensated moment (see section 3) is present, the spin–flop transition field will be enhanced [50]. In a study of the spin–flop transition in samples of $\alpha$-$Fe_2O_3$ nanoparticles with average size in

the range from 36 to 159 nm, it was found that the critical field for the spin–flop transition decreases with decreasing particle size [51]. These particles are so large that the influence of an uncompensated magnetic moment may be insignificant. It was suggested that the size dependence of the spin–flop transition field may be explained by a decrease of the exchange field with decreasing particle size due to surface effects.

Ferritin is an iron storage protein with an antiferromagnetic iron-containing core. In a recent study of ferritin particles with a magnetic core size of about 7 nm, no spin–flop transition was found even in applied fields up to 55 T [52], although $B_{sf}$ of ferritin according to equation (4) should be less than 10 T [53]. This result may be explained by the large uncompensated magnetic moment in these particles (see section 3) [50].

## 3. The magnetic moment of antiferromagnetic nanoparticles

Numerous magnetization studies of antiferromagnetic nanoparticles have shown that both the initial susceptibility and the magnetization in large applied fields are considerably larger than in the corresponding bulk materials. It was suggested by Néel [54] that this may be due to the finite number of magnetic atoms in nanoparticles, which may lead to a difference in the numbers of spins in the two sublattices because of random occupancy of lattice sites. This results in an uncompensated magnetic moment, $\mu_u$. In one specific model, Néel considered nanoparticles with a random occupancy of all the lattice sites and found that the number of uncompensated spins should be of the order of $N^{1/2}$, where $N$ is the total number of spins in a particle. If the interior of the particles is assumed defect-free, but there is a random occupancy of surface sites, the number of uncompensated spins should instead be proportional to the square root of the number of surface sites, i.e., proportional to $N^{1/3}$. In a third model, Néel considered particles consisting of either an even or an odd number of planes with parallel spins, but with alternating magnetization directions. In this case, the number of uncompensated spins should rather be proportional to $N^{2/3}$.

In experimental studies of the magnetization of antiferromagnetic nanoparticles, the presence of impurities can be crucial [55]. Even tiny amounts of strongly magnetic phases, which may not be visible in x-ray diffraction measurements, may dominate the magnetization of the samples. During the preparation of many antiferromagnetic nanoparticles, impurity phases can be difficult to avoid. For example, when preparing CoO nanoparticles, the samples may be contaminated with ferromagnetic metallic Co or antiferromagnetic $Co_3O_4$ with a lower Néel temperature. Similarly, CuO nanoparticles may be contaminated with $Cu_2O$, which seems to become increasingly stable with decreasing particle size [56]. In samples of $\alpha$-$Fe_2O_3$ nanoparticles, a few per cent of ferrihydrite, which also is antiferromagnetic, can give a large contribution to the magnetization [35].

Experimental studies of the magnetization of samples of NiO nanoparticles with different average size [55] and without impurities of either ferromagnetic metallic Ni or $Ni^{3+}$ ions have suggested that the size dependence of the magnetic moment was proportional to $N^{1/3}$, i.e., the magnetic moments can be explained by a random occupation of surface sites, and the magnetic moment of a nanoparticle is then approximately proportional to its diameter. Recently, high-field Mössbauer studies of plate-shaped NiO nanoparticles have been used to estimate the magnitude of the uncompensated magnetic moment [32]. The spectra were analysed by use of a model [57], in which the influence of the magnetic anisotropy and the uncompensated magnetic moment on the positions and relative areas of the Mössbauer lines was taken into account. The estimated value of $\mu_u$ was also in this case in accordance with a random occupation of surface sites [32].

The magnetic core in ferritin is usually poorly crystalline. For such particles, the uncompensated magnetic moment has been found to be of the order of $N^{1/2}$ [53, 58–60],

suggesting a more or less random occupation of all lattice sites. Ferrihydrite particles, which have a disordered structure similar to that of ferritin cores, also have magnetic moments of the order of $N^{1/2}$ [61].

It has recently been suggested that the magnetic moment of nanoparticles of antiferromagnetic materials has a contribution, $\mu_t$, from so-called thermoinduced magnetization [62]. This contribution is related to the fact that the two sublattices of a simple antiferromagnet are not strictly antiparallel when the uniform mode is excited, and the difference in precession angles increases with increasing temperature, such that the net magnetic moment increases with increasing temperature. This is discussed in more detail in section 4.4. In general, the total magnetic moment of an antiferromagnetic nanoparticle is expected to have contributions from both uncompensated spins and a thermoinduced moment [62, 63].

In many experimental studies of the magnetization of magnetic nanoparticles, the magnetization has been measured as a function of the applied magnetic field, $B_{ext}$, at different temperatures. Typically, the magnetization curves above the blocking temperature have been fitted with a Langevin function

$$L\left(\frac{\mu B_{ext}}{k_B T}\right) = \coth\left(\frac{\mu B_{ext}}{k_B T}\right) - \frac{k_B T}{\mu B_{ext}}, \tag{5}$$

where $\mu$ is the magnetic moment of a particle. This model has been successfully used to fit data for ferromagnetic and ferrimagnetic nanoparticles. In most fits of magnetization data for antiferromagnetic nanoparticles, a linear term was also included to account for the antiferromagnetic susceptibility such that the magnetization curves were fitted to the expression

$$\langle M\rangle_T = M_0(T)L\left(\frac{\mu B_{ext}}{k_B T}\right) + \mu_0^{-1}\chi_{AF}B_{ext}, \tag{6}$$

where $M$ is the magnetization, $M_0(T)$ is the saturation magnetization at temperature $T$, $\mu_0$ is the vacuum permeability and $\chi_{AF}$ is the antiferromagnetic susceptibility. It has been found in many experimental studies of antiferromagnetic nanoparticles that this model gives good fits to the experimental data. In several studies, the estimated magnetic moments were surprisingly found to increase with increasing temperature [58, 59, 61, 64, 65]. This is consistent with a contribution from thermoinduced magnetization [62]. It has, however, been pointed out by Silva *et al* [66] that the distribution of the magnitude of the magnetic moments in a sample also can explain such data. This is because the smallest magnetic moments are far from being saturated at high temperatures and therefore give an almost linear contribution to the magnetization, which may be attributed to the antiferromagnetic susceptibility. Thus, when the temperature is increased, the fitted Langevin functions will be increasingly dominated by the larger magnetic moments, and this may at least partly explain the apparent increase of the magnetic moment.

The magnetic anisotropy is usually neglected in the fits of magnetization curves of nanoparticles, but especially in the case of antiferromagnetic nanoparticles this can result in erroneous results [67]. The Langevin function may be a good approximation to the magnetization above the blocking temperature if the Zeeman energy ($\sim\mu B_{ext}$) is large compared to the anisotropy energy ($\sim KV$). However, even for ferromagnetic and ferrimagnetic nanoparticles with relatively large magnetic moments, a finite magnetic anisotropy can give rise to deviations from the Langevin behaviour [68, 69]. In antiferromagnetic nanoparticles with relatively small magnetic moments, the Zeeman energy will often be small compared to the anisotropy energy, and the deviation of the magnetization curves from the Langevin function may therefore be significant. Figure 2 shows simulated magnetization curves for particles with

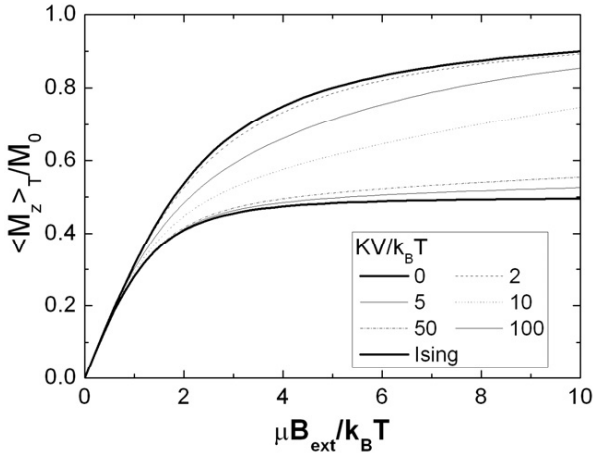


**Figure 2.** Simulated magnetization curves of antiferromagnetic nanoparticles above the blocking temperature showing the normalized magnetization as a function of $\mu B_{\text{ext}}/k_{\text{B}}T$ for various values of the anisotropy parameter $KV/k_{\text{B}}T$. Reprinted with permission from [67]. Copyright 2006 by Elsevier.

uniaxial anisotropy and a random orientation of the easy axes as a function of $\mu B_{\text{ext}}/k_{\text{B}}T$ for various values of the anisotropy energy parameter $KV/k_{\text{B}}T$. In the simulations, it was assumed that the temperature is above the blocking temperature. No linear terms due to the antiferromagnetic susceptibility were included in these simulations. It is clearly seen that a finite anisotropy changes the shape of the magnetization curves, and especially for values of $KV/k_{\text{B}}T$ of the order of 5–10, the magnetization curves show a slope at high fields, which erroneously might be attributed to an antiferromagnetic susceptibility. For this reason, the parameters obtained from fits of magnetization curves for antiferromagnetic nanoparticles with equation (6) may be incorrect.

Above the blocking temperature, the initial susceptibility of a sample of non-interacting nanoparticles with a finite anisotropy and with a random orientation of easy axes is given by [32, 67, 70]

$$\chi_i = \frac{n\mu_0}{3k_{\text{B}}T}\langle\mu^2\rangle + \chi_{\text{AF}}, \tag{7}$$

where $n$ is the number of particles per volume and $\chi_{\text{AF}}$ is the antiferromagnetic susceptibility, which may be comparable to the bulk value [55]. It is remarkable that the first term in equation (7) is independent of the anisotropy energy constant. Moreover, it is also independent of the detailed shape of the distribution of the magnetic moments of the particles in the sample. It has therefore been suggested [32, 67] that one should focus on the initial susceptibility in magnetization studies of antiferromagnetic particles.

As will be discussed in section 5, antiferromagnetic nanoparticles may interact strongly via exchange interactions between surface atoms of neighbouring particles. Interparticle interactions can also have a large influence on the magnetic moments that are derived by use of equation (7) [32, 71, 72]. Therefore, equation (7) should only be used to estimate magnetic moments of non-interacting nanoparticles.

Below the blocking temperature, the hysteresis loops of samples of antiferromagnetic nanoparticles show some unusual properties. Studies of, for example, ferritin [60], NiO [33, 73], CuO [44], $Co_3O_4$ [74], MnO [75] and $Cr_2O_3$ [65] have shown very large coercivities, and after field cooling antiferromagnetic nanoparticles often show exchange bias.

These features can be explained by the exchange coupling between the uncompensated spins and the antiferromagnetic regions. In the case of NiO nanoparticles it has also been suggested that the phenomena can be explained by a multi-sublattice structure [33, 76].

## 4. Magnetic fluctuations in non-interacting antiferromagnetic nanoparticles

As discussed in section 1, the magnetization direction in nanoparticles fluctuates at finite temperatures, such that the magnetization directions frequently are reversed in the superparamagnetic region and are affected by collective magnetic excitations at lower temperatures. Here, we give an overview of the application of various experimental techniques for studies of magnetic fluctuations in antiferromagnetic nanoparticles.

### *4.1. Magnetization measurements*

In DC magnetization studies of nanoparticles, the magnetic dynamics are commonly studied by ZFC and FC magnetization measurements. If a sample of non-interacting particles is truly monodisperse, the ZFC magnetization curve will have a maximum at the blocking temperature. However, a sample of ferromagnetic or ferrimagnetic particles with a particle size distribution will have its maximum at a higher temperature, $T_{\text{peak}}$ [77, 78], i.e., $T_{\text{peak}} = \beta T_{\text{bm}}$, where $\beta > 1$ and $T_{\text{bm}}$ is the median blocking temperature corresponding to the median volume $V_{\text{m}}$, defined such that the sum of the volumes of the particles with $V > V_{\text{m}}$ contributes 50% of the total volume. The value of the parameter $\beta$ depends on the size distribution. For samples with a log-normal distribution, $\beta$ increases from 1.0 to around 2.0 when $\sigma_V$ (the standard deviation of $\ln V$) is increased from 0.0 to 1.5 [79]. In antiferromagnetic nanoparticles with an uncompensated magnetic moment, the magnetic moment is not proportional to the volume as is the case for ferromagnetic particles. Therefore, there may not be a simple relation between the values of $\beta$ and $\sigma_V$. Some experimental studies have suggested that the uncompensated moment may be proportional to the diameter [32, 55]. In this case, the value of the parameter $\beta$ has been found to decrease with increasing values of $\sigma_V$ in a log-normal distribution [79].

It is important to realize that the magnetic susceptibility of antiferromagnets has a maximum at the Néel temperature [22]. Therefore, a peak in a ZFC magnetization curve may not always be related to a superparamagnetic blocking temperature, but it may be due to a transition from an antiferromagnetic state to a paramagnetic state.

If the moment distribution is known, the superparamagnetic blocking temperature can be estimated from $T_{\text{peak}}$ in a ZFC magnetization curve, but since there usually are two unknown parameters, $\tau_0$ and $K$, in equation (2), both of these parameters cannot be estimated from a ZFC magnetization curve. However, this is possible by using AC susceptibility measurements with different frequencies. In AC susceptibility measurements one measures the complex susceptibility, which can be written [78]

$$\chi_{\text{AC}}(\omega, T) = \chi'(\omega, T) + \mathrm{i}\chi''(\omega, T), \tag{8}$$

where $\chi'$ and $\chi''$ are the in-phase and the out-of-phase components of the measured susceptibility, respectively, and $\omega$ is the angular frequency. The in-phase susceptibility has a maximum at a temperature $T_{\text{max}}$, which is related to the blocking temperature and the particle size distribution as for the ZFC magnetization curve. The temperature corresponding to the maximum of the out-of-phase susceptibility is less sensitive to the size distribution and thus an analysis based on just the maxima is better carried out using $\chi''$ data. Such data can, however, be difficult to measure accurately for low-moment samples, and therefore in many studies of antiferromagnetic nanoparticles only $\chi'$ data have been reported. Several AC susceptibility

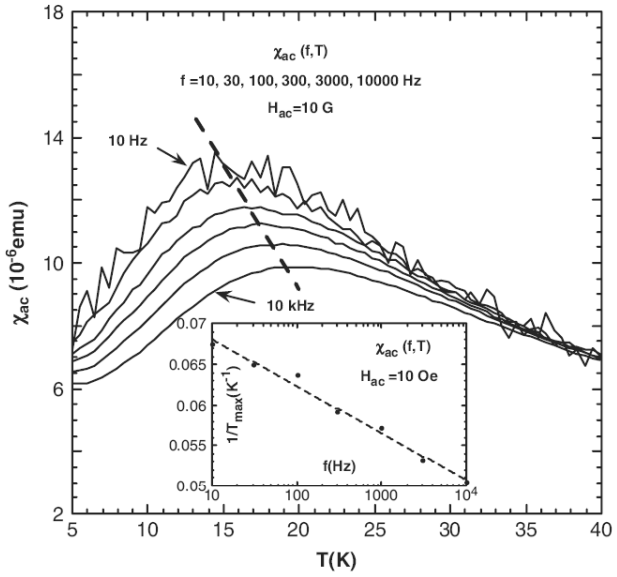


**Figure 3.** In-phase AC magnetic susceptibility of horse spleen ferritin as a function of temperature at several frequencies, $f$. The dashed line indicates the peak positions. In the inset is shown $1/T_{\max}$ versus $\log f$. Reprinted with permission from [52]. Copyright 2007 Elsevier.

measurements have been made on ferritin [52, 59, 80, 81] and $\alpha$-$Fe_2O_3$ [35]. In studies of superparamagnetic relaxation, ferritin has the advantage that the magnetic cores are well separated by organic non-magnetic material such that the influence of interparticle interaction is negligible. Figure 3 shows in-phase susceptibility data for horse spleen ferritin obtained at frequencies in the range $f = \omega/2\pi = 10$–$10\,000$ Hz [52]. As indicated by the dashed line, the peak position is, as expected, shifted towards higher temperatures, when the frequency is increased. The inset shows that $1/T_{\max}$ varies linearly with $\log f$ in accordance with equation (2). From these data an anisotropy energy constant of $K = 2.5 \times 10^4$ J m$^{-3}$ and a value of $\tau_0$ s $\approx 10^{-12}$–$10^{-13}$ were estimated [52].

### *4.2. Mössbauer spectroscopy studies*

Mössbauer spectroscopy has been extensively used for studies of superparamagnetic relaxation and collective magnetic excitations in nanoparticles. As the timescale of Mössbauer spectroscopy, $\tau_{\mathrm{M}}$, is of the order of a few nanoseconds, it is a good supplement to DC and AC magnetization measurements. By combining ZFC magnetization measurements and Mössbauer data for ferritin, Dickson *et al* [82] estimated a value of $\tau_0$ similar to that obtained by the AC susceptibility measurements discussed above.

The values of $\tau_0$ and $K$ can also be estimated from series of Mössbauer spectra obtained at different temperatures. As an example of such a Mössbauer study of non-interacting antiferromagnetic nanoparticles, figure 4 shows spectra of 15 nm $\alpha$-$Fe_2O_3$ particles at different temperatures [35]. The spectra show the typical features of superparamagnetic nanoparticles. At low temperatures, the spectra are magnetically split because the superparamagnetic relaxation is slow compared to $\tau_{\mathrm{M}}$. With increasing temperature, an increasing number of particles have relaxation times shorter than $\tau_{\mathrm{M}}$, resulting in an increasing area of a

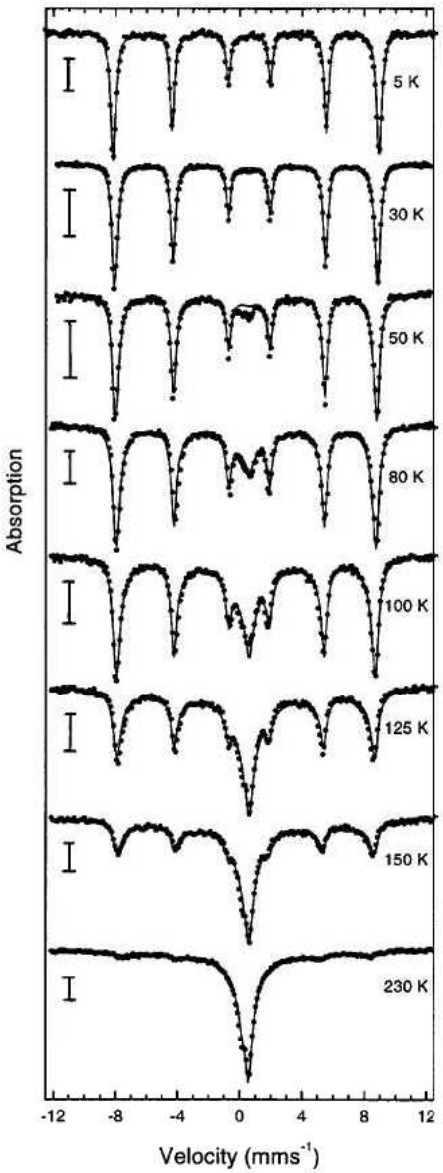


**Figure 4.** Mössbauer spectra of 15 nm hematite nanoparticles measured at the indicated temperatures. The solid lines are fits obtained as described in the text. Reprinted with permission from [35]. Copyright 2000 by the American Physical Society.

central doublet in the spectra. The fits shown in the figure were obtained using the Blume–Tjon model [83] for Mössbauer relaxation spectra, taking into account the particle size distribution [35]. All the spectra were fitted simultaneously, assuming that the superparamagnetic relaxation time is given by equation (2). From the fits, the values $\tau_0 \approx 5.0 \times 10^{-11}$ s and $KV/k_B \approx 600$ K (corresponding to $K \approx 4500$ J m$^{-3}$) were estimated [35]. Similar fits of temperature series of Mössbauer spectra of a number of samples of $\alpha$-$Fe_2O_3$

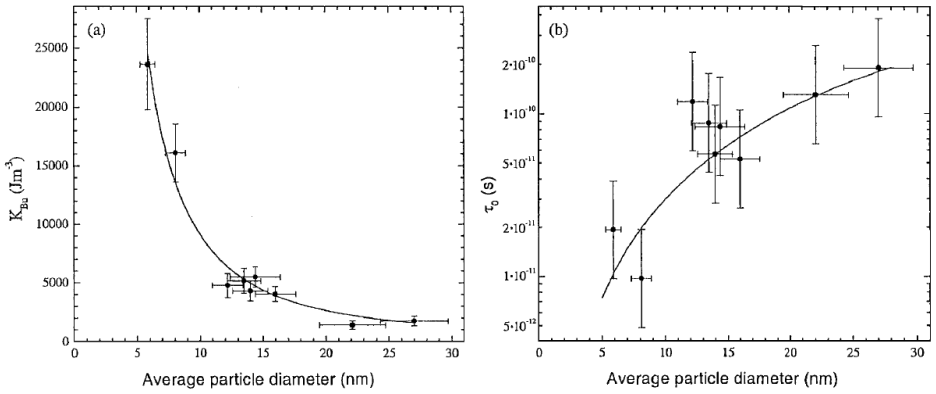


**Figure 5.** (a) Magnetic anisotropy constant and (b) the prefactor $\tau_0$ for $\alpha$-$Fe_2O_3$ nanoparticles as a function of particle diameter. Reprinted with permission from [46].

nanoparticles with average particle diameter in the range $d \approx 6$–30 nm have been used to estimate the size dependence of $K$ and $\tau_0$ [46]. The data are shown in figure 5. It can be seen in figure 5(a) that the magnetic anisotropy constant increases significantly with decreasing particle size, especially for the smallest particles. This is presumably because of the influence of surface anisotropy. Qualitatively similar results for the size dependence of the magnetic anisotropy constants have been found for ferrimagnetic $\gamma$-$Fe_2O_3$ [84] and ferromagnetic $\alpha$-Fe particles [85]. The data for $\alpha$-$Fe_2O_3$ nanoparticles can be fitted well with an empirical $d^{-2}$ dependence of the magnetic anisotropy constant [46, 86]. This implies, according to equation (3), that the reduction of the magnetic hyperfine field at a given temperature should be proportional to $d^{-1}$. Such a size dependence has also been found for maghemite nanoparticles [84] and in several studies of magnetic nanoparticles in soil samples [86]. The data in figure 5(b) show that the value of $\tau_0$ decreases with decreasing particle size.

Ferromagnetic and ferrimagnetic nanoparticles usually have relatively large magnetic moments, typically in the range $10^3$–$10^5$ Bohr magnetons, and even in relatively small applied fields ($B_{\text{ext}} \lesssim 1$ T) at ambient temperature, the Zeeman energy may be larger than the thermal energy. Consequently, the superparamagnetic relaxation above $T_B$ can be suppressed by relatively small external fields. As discussed in section 3, the Zeeman energy of ferromagnetic and ferrimagnetic nanoparticles in moderate applied fields is typically also larger than the anisotropy energy. The magnetic splitting of the Mössbauer spectra is then to a good approximation proportional to the sum of the external field and a contribution proportional to the Langevin function. At large applied fields ($\mu B_{\text{ext}} \gg k_B T$) the hyperfine splitting can be approximated by the simple expression [87]

$$B_{\text{obs}} = B_0\left(1 - \frac{k_B T}{\mu B_{\text{ext}}}\right) - B_{\text{ext}}. \tag{9}$$

(The minus in front of $B_{\text{ext}}$ is due to the fact that the direction of the hyperfine field is usually opposite to that of the applied field.) Thus a plot of $B_{\text{obs}} + B_{\text{ext}}$ as a function of $B_{\text{ext}}^{-1}$ gives a straight line with a slope from which the magnetic moment can be estimated.

In antiferromagnetic nanoparticles which have smaller magnetic moments (typically of the order of a few hundred Bohr magnetons), much larger fields are required to suppress the superparamagnetic relaxation to the same extent. Figure 6 shows Mössbauer spectra of human spleen ferritin at 100 K in applied magnetic fields up to 10 T [88]. The zero-field spectrum

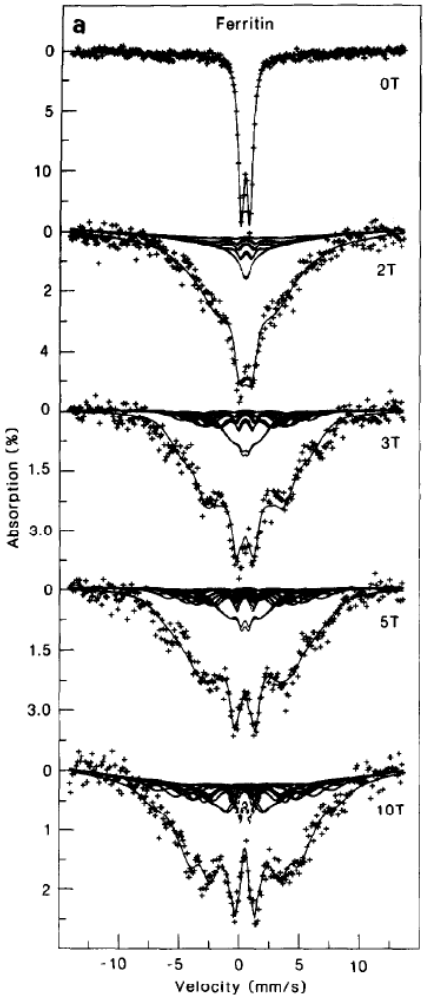


**Figure 6.** Mössbauer spectra of human spleen ferritin at 100 K obtained in the indicated applied magnetic fields. Reprinted with permission from [88]. Copyright 1987 by Elsevier.

consists of a doublet, indicating that the particles are superparamagnetic at this temperature, but a magnetic splitting is induced when external magnetic fields are applied. The saturation hyperfine field in ferritin is of the order of 45 T, corresponding to a splitting of lines 1 and 6 in the spectrum around 15 mm $s^{-1}$. The figure shows that even at the largest applied fields, the average magnetic hyperfine splitting is much smaller, indicating that the particles are far from being magnetically saturated. The analysis of the spectra of antiferromagnetic nanoparticles in applied fields is much more complex than that of the corresponding spectra of ferromagnetic and ferrimagnetic nanoparticles. For small applied fields, the anisotropy energy may be large compared to the Zeeman energy, and therefore the relaxation takes place between two minima with different energies, which depend on the size and direction of the applied field. At large applied fields, this model may not be appropriate, because the Zeeman and the anisotropy

energies may be comparable. Because of these complications it is not straightforward to obtain reliable values for the magnetic moments from such Mössbauer measurements on antiferromagnetic nanoparticles [53, 88].

### *4.3. Neutron scattering studies*

Neutron scattering is another technique that is useful for studies of time-dependent phenomena. Magnetic dynamics in solids can be studied by inelastic neutron scattering. In such studies, one can measure, for example, the energy distribution of neutrons that are diffracted at a wavevector corresponding to a magnetic diffraction peak. This gives information about magnetic excitations, such as spin waves, and in studies of magnetic nanoparticles this technique can give information on both superparamagnetic relaxation and uniform magnetic excitations [24, 25]. The timescale of neutron scattering is much shorter than that of Mössbauer spectroscopy. Therefore, neutron scattering makes it possible to study details of magnetic fluctuations that are not revealed in Mössbauer spectroscopy and magnetization measurements. For example, neutron scattering can be used to estimate the energy related to transitions between uniform precession states, whereas Mössbauer spectroscopy only allows measurement of a magnetic hyperfine field that is averaged over all magnetic fluctuations. Before discussing neutron data, it is useful to look in more detail at magnetic excitations in nanoparticles.

For a cubic ferromagnetic or ferrimagnetic material with lattice constant $a$, the dispersion relation for spin waves for which $aq \ll 1$ can be written [3, 19, 89, 90] as

$$\hbar\omega_q = Dq^2 + g\mu_B B_A, \tag{10}$$

where $\omega_q$ is the angular frequency of a spin wave with wavevector $q$, $D$ is the exchange stiffness constant, $g$ is the Landé factor, $\mu_B$ is the Bohr magneton and $B_A = 2K/M$ is the anisotropy field with $M$ being the magnetization. In nanoparticles with cubic shape, in which surface effects are neglected, the allowed values of the wavevector are given by [19, 91]

$$q = n\pi/d, \qquad n = 0, 1, 2, 3 \ldots \tag{11}$$

where $d$ is the side length. Similar quantization of the spin wave spectrum can be found also in real nanoparticles [92]. Because of this quantization, there are in very small particles large energy gaps between the uniform ($n = 0$) mode and the modes with $n > 0$. Therefore, spin waves with $q = 0$ are predominant in nanoparticles, and the first term in equation (10) can often be neglected [19]. In many theoretical investigations of magnetic excitations in nanoparticles, the $q = 0$ mode has been neglected, and the calculations therefore only give information on the modes with $q > 0$. However, if a sufficiently large magnetic field is applied, the excitations of the uniform mode are suppressed, and the magnetic dynamics can then be dominated by modes with $q > 0$ [91]. The $z$-components of the magnetic moments of neighbouring precession states of the uniform mode, with slightly different precession angles, differ by $g\mu_B$ [22]. In inelastic neutron spectra, the uniform mode gives rise to separate peaks at energies corresponding to the energy difference, $\varepsilon_0$, between neighbouring precession states. In ferromagnetic and ferrimagnetic nanoparticles this energy difference is given by [19, 25]

$$\varepsilon_0 = \hbar\omega_0 = g\mu_B B_A. \tag{12}$$

Typically, $B_A$ is of the order of 0.1 T, corresponding to $\varepsilon_0 \approx 0.01$ meV. Thus, the peaks are hard to observe in a typical neutron spectrometer with an energy resolution of the order of 0.1 meV [25]. However, if a large magnetic field, $B_{ext} \gg B_A$, is applied, the energy difference is given by

$$\varepsilon_0 \approx g\mu_B B_{ext} \tag{13}$$

and the inelastic peaks may then be visible for applied fields larger than ∼1 T [25].

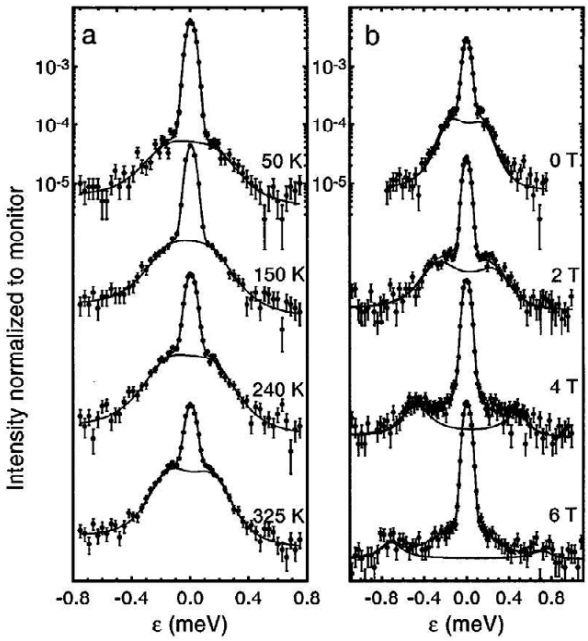


**Figure 7.** Inelastic neutron scattering data for 15 nm hematite nanoparticles. (a) Data obtained at zero applied magnetic field at the indicated temperatures. (b) Data obtained at 268 K at the indicated applied magnetic fields. Reprinted with permission from [24]. Copyright 1997 by the American Physical Society.

In antiferromagnetic nanoparticles the situation is different because the dispersion relation for spin waves is given by the more complex expression [22]

$$\hbar\omega_q = g\mu_B[(B_E + B_A)^2 - B_E^2(1 - Cq^2)]^{1/2}. \tag{14}$$

Here $B_A = K/M_S$ is the anisotropy field for an antiferromagnet with sublattice magnetization $M_S$, $B_E$ is the exchange field and $C$ is a constant. Thus, in nanoparticles, in which the uniform mode is predominant, the energy difference between neighbouring precession states, for $B_E \gg B_A$, is given by [93, 94]

$$\varepsilon_0 = \hbar\omega_0 \approx g\mu_B\sqrt{2B_E B_A}. \tag{15}$$

The exchange field may be up to around 1000 T and the energy, $\varepsilon_0$, of the uniform mode in antiferromagnetic nanoparticles can therefore be much larger than that of ferromagnetic and ferrimagnetic nanoparticles and can more easily be observed in inelastic neutron scattering experiments in zero applied field.

As an example, we consider inelastic neutron scattering studies of 15 nm $\alpha$-$Fe_2O_3$ nanoparticles from the same batch as the sample used for the neutron and x-ray diffraction data in figure 1 and the Mössbauer spectra in figure 4. The energy distribution of neutrons scattered at $Q = 1.37$ Å$^{-1}$, corresponding to the (003) peak, is shown in figure 7 [24]. Data are displayed for different temperatures and applied magnetic fields. The neutron data in figure 7(a) show a relatively narrow, quasielastic line, centred at energy $\varepsilon = 0$ meV. On both sides of this quasielastic line, inelastic lines can be seen with an intensity that increases with increasing temperature. The energy distribution (apart from background terms) can be

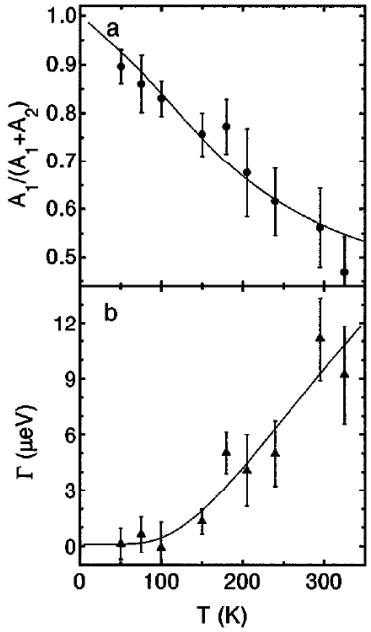


**Figure 8.** Parameters obtained from fits of the inelastic neutron data shown in figure 7(a). (a) Relative area of the quasielastic peaks. (b) Superparamagnetic relaxation parameter Γ obtained from the line width of the quasielastic peak. Reprinted with permission from [24]. Copyright 1997 by the American Physical Society.

described by [24, 95, 96]

$$I(\varepsilon) = \frac{A_1}{\pi} D(\varepsilon) \frac{\Gamma}{\varepsilon^2 + \Gamma^2} + \frac{A_2}{\pi} D(\varepsilon) \frac{2\gamma\varepsilon_0^2}{(\varepsilon^2 - \varepsilon_0^2)^2 + 4\gamma^2\varepsilon^2}, \tag{16}$$

where $A_1$ is the area of the quasielastic peak and $A_2$ is the area of the inelastic components. $\pm\varepsilon_0$ are the positions of the inelastic peaks, $\gamma$ is the width of these peaks and $\Gamma$ is the width of the quasielastic peak. $D(\varepsilon)$ is the detailed balance factor due to the difference in the population of the creation and annihilation states of the uniform excitations. Due to the presence of adsorbed water on the surface of the particles there is a strong incoherent elastic signal increasing the signal at $\varepsilon = 0$ meV. Before comparing with experimental data, the sum of $I(\varepsilon)$ and the incoherent signal must be convoluted with the experimental resolution function. Some of the parameters, derived from fits to the zero-field experimental data of figure 7(a), are shown in figure 8. The relative area of the inelastic peaks is proportional to $\langle \sin^2\theta \rangle$ and therefore it increases with temperature. At low temperatures the area ratio is given by

$$\frac{A_1}{A_1 + A_2} \approx 1 - \frac{k_B T}{KV}. \tag{17}$$

The fit to the temperature dependence of $A_1/(A_1 + A_2)$, shown in figure 8(a), was obtained using a more exact analytical expression [24], and the value $KV/k_B \approx 700$ K was obtained. The width of the quasielastic line increases with increasing temperature due to superparamagnetic relaxation as seen in figure 8(b), and the line broadening is inversely proportional to the superparamagnetic relaxation time, $\Gamma = h/\tau$ [95]. From the temperature dependence of $\Gamma$, the values $KV/k_B \approx 500$ K and $\tau_0 \approx 1.4 \times 10^{-11}$ s were estimated [95].

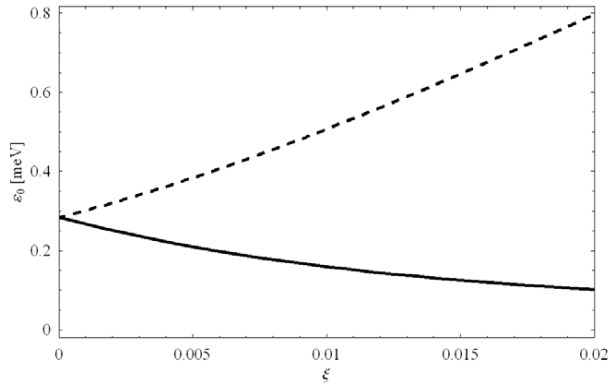


**Figure 9.** Energy of the uniform mode as a function of the uncompensated magnetic moment of antiferromagnetic nanoparticles. The lines were calculated using equation (18) with $B_A = 0.01$ T and $B_E = 300$ T. Reprinted with permission from [63]. Copyright 2006 by the American Physical Society.

The values of magnetic anisotropy energy and $\tau_0$, obtained from neutron scattering, are in good agreement with those obtained from the Mössbauer studies (section 4.1).

The inelastic neutron data in figure 7(b), measured at 260 K in various applied magnetic fields, show that the inelastic peaks are shifted to larger energies when the field is increased with a related decrease of the relative area. The field dependence of $\varepsilon_0$ at high fields was found to be in accordance with equation (13), with $g \cong 2$ as expected for $Fe^{3+}$ [24].

The expression for the energy of the uniform mode in an antiferromagnet (equation (15)) was derived for a perfect two-sublattice antiferromagnet with anisotropy energy given by equation (1), i.e., the existence of an uncompensated magnetic moment, $\mu_u$, was not taken into account. It is, however, noteworthy that even a small difference in the sublattice magnetic moments can have an influence on the value of $\varepsilon_0$. An antiferromagnetic nanoparticle with an uncompensated magnetic moment should in principle be considered as a ferrimagnet with a small difference between the values of the sublattice magnetizations, and equation (15) should then be replaced by [93, 97–100]

$$\varepsilon_0^{\pm} = \tfrac{1}{2} g \mu_B B_E (\sqrt{4\lambda^2 + 4\lambda(2+\xi) + \xi^2} \pm \xi). \tag{18}$$

Here, $\lambda = B_A/B_E$ and $\xi = \mu_u/(M_S V)$ is the ratio of the uncompensated moment and the sublattice magnetic moment. Thus, instead of the single mode in the ideal antiferromagnet with energy given by equation (15), there are now two modes with energies that depend on the magnitude of the uncompensated magnetic moment. The dependence of $\varepsilon_0^{\pm}$ on the value of $\xi$, calculated by use of equation (18), is shown in figure 9. Because of the different thermal populations of the two modes, the low-energy mode will give the predominant contribution to the magnetic dynamics. Even small values of the uncompensated moment can result in significant changes of the energies. For example, a value of $\xi$ around 0.01 reduces the energy of the low-energy mode by a factor of about two. Since the value of $\xi$ in general is expected to increase with decreasing particle size, the effect should be largest in very small particles. In accordance with this, it has been found that the effect is insignificant in 15 nm $\alpha$-$Fe_2O_3$ nanoparticles, but clearly visible in 8 nm $\alpha$-$Fe_2O_3$ nanoparticles [99].

The use of the anisotropy energy given by equation (1) is only a rough approximation for $\alpha$-$Fe_2O_3$ nanoparticles, because the particles have both a small in-plane anisotropy and a larger out-of-plane anisotropy. If this is taken into account, one finds that there are two different uniform modes even in the absence of an uncompensated moment. The inelastic

neutron scattering data, shown in figure 7, give information about a low-energy uniform mode, which is characterized by an elliptic precession very close to the (001) plane, and the parameters obtained from this mode give information on the in-plane anisotropy. It has been shown [49] that inelastic neutron data for neutrons scattered at $Q = 1.50$ Å$^{-1}$ give information about a high-energy uniform mode, which is characterized by fluctuations out of the plane. Neutron data therefore make it possible to estimate the values of both the in-plane and the out-of-plane anisotropy constants [49].

NiO particles also have a small in-plane anisotropy, but a much larger out-of-plane anisotropy. In this case the energies of the uniform modes are less dependent on the magnitude of the uncompensated moment [100]. The energy of the low-energy uniform mode of NiO nanoparticles, estimated from inelastic neutron scattering experiments, was considerably smaller than predicted by equation (15), when inserting the bulk exchange field and an anisotropy field derived from the temperature dependence of the relative area of the inelastic peaks [100]. This suggests that the effective exchange field in the nanoparticles is smaller than the bulk value, as studies of the spin–flop transition in $\alpha$-$Fe_2O_3$ nanoparticles also have suggested [51].

### *4.4. The uniform mode in antiferromagnetic nanoparticles and thermoinduced magnetization*

In early studies of superparamagnetism [17, 18] and collective magnetic excitations [20, 21], ferromagnetic, ferrimagnetic and antiferromagnetic particles were all treated as classical spins, i.e., it was assumed that the total spin of a particle was so large that quantization could be neglected. This is a good approximation for ferromagnetic and ferrimagnetic particles for which the total spin $S$ typically is of the order of $10^3$–$10^5$. When the uniform mode is excited, the possible values of the $z$-component of the spin are $S_z = S, S-1, S-2, \ldots, -(S-2), -(S-1), -S$, i.e., there are $2S+1$ precession states with $z$-components of the magnetic moments given by $g\mu_B S_z$. This results in the energy differences between neighbouring states given by equations (12) and (13).

In ferromagnetic nanoparticles all ionic spins precess in parallel in the uniform mode. However, in antiferromagnetic nanoparticles the two sublattices are not strictly antiparallel when the uniform mode is excited, but form different angles $\theta_A$ and $\theta_B$ with the easy axis [93, 94], as illustrated in figure 10. These different precession angles result in a contribution to the magnetic moment of the particle. For simplicity, we first consider an antiferromagnetic nanoparticle with magnetic anisotropy energy given by equation (1) and without an uncompensated magnetic moment. For a particle with $B_A \ll B_E$ the two angles are related by [19, 101]

$$\frac{\sin\theta_A}{\sin\theta_B} = 1 \pm \delta, \tag{19}$$

where

$$\delta \approx \sqrt{\frac{2B_A}{B_E}}. \tag{20}$$

The number of precession states in an antiferromagnetic nanoparticle is determined by the fact that the difference in magnetic moments of neighbouring precession states is given by $g\mu_B$ [19]. Because the differences between the precession angles and $\theta_B$ are small, the number of precession states in an antiferromagnetic nanoparticle is much smaller than the corresponding number of states in a ferromagnetic nanoparticle (by a factor of the order of $\delta$ [19]). For this reason the temperature dependence of the average hyperfine field deviates from equation (3) at low temperatures due to quantum effects [19].

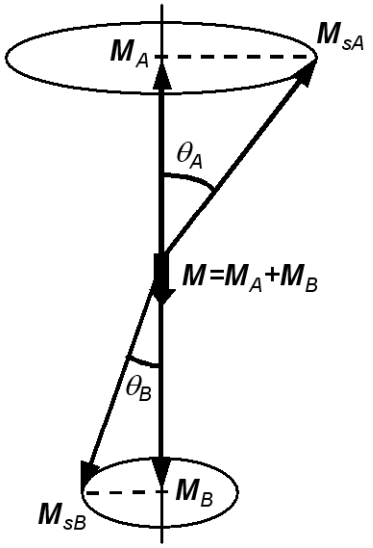


**Figure 10.** Schematic illustration of the uniform mode in nanoparticles of antiferromagnetic nanoparticles. Reprinted with permission from [62]. Copyright 2004 by the American Physical Society.

The magnetic moment due to the different precession angles (the thermoinduced moment) has at low temperatures an absolute value given by [19]

$$|\mu_{\mathrm{t}}| = M_{\mathrm{S}} V |\cos\theta_{\mathrm{A}} - \cos\theta_{\mathrm{B}}| \approx M_{\mathrm{S}} V \delta \sin^2\theta_{\mathrm{B}}. \tag{21}$$

In zero applied field, precession states with magnetic moments up and down are degenerate, and the average magnetic moment is therefore zero, but the average of the absolute value of $\mu_{\mathrm{t}}$ is given by [19, 62]

$$\langle|\mu_{\mathrm{t}}|\rangle \approx \frac{2k_{\mathrm{B}}T}{\sqrt{2B_{\mathrm{A}}B_{\mathrm{E}}}}. \tag{22}$$

Thus, the absolute value of the moment increases linearly with temperature and the thermoinduced moment is independent of the particle volume. This can be deduced from equation (21), since $\langle\sin^2\theta_{\mathrm{B}}\rangle$ is inversely proportional to the volume, $V$ [19].

In an applied magnetic field the degeneracy is lifted, and therefore a finite magnetization can be observed. The initial susceptibility due to the thermoinduced magnetization is given by [19, 62]

$$\chi_i = \frac{4\mu_0}{V}\frac{k_{\mathrm{B}}T}{B_{\mathrm{A}}B_{\mathrm{E}}}, \tag{23}$$

i.e., the initial susceptibility also increases linearly with temperature.

Because nanoparticles of antiferromagnetic materials usually also have an uncompensated magnetic moment, $\mu_{\mathrm{u}}$, the initial susceptibility will have a contribution related to $\mu_{\mathrm{u}}$ and is then given by [63]

$$\chi_i \approx \frac{\mu_0}{V}\left(\frac{\mu_{\mathrm{u}}^2}{k_{\mathrm{B}}T} + \frac{4k_{\mathrm{B}}T}{B_{\mathrm{A}}B_{\mathrm{E}}}\right). \tag{24}$$

According to equation (24), the contribution to the initial susceptibility due to thermoinduced magnetization will be predominant for $T > \mu_{\mathrm{u}}\sqrt{B_{\mathrm{A}}B_{\mathrm{E}}}/2k_{\mathrm{B}}$.

### *4.5. Macroscopic quantum tunnelling*

Thermally activated magnetization reversal is a well established phenomenon, which has been studied by a number of experimental techniques [1]. It has, however, been suggested that macroscopic quantum tunnelling between the minima of the anisotropy energy also may take place [102–104]. Below a crossover temperature, the relaxation due to quantum tunnelling should be predominant and the relaxation should therefore be independent of temperature. Theoretical investigations have shown that such macroscopic quantum tunnelling should be easier to detect in antiferromagnetic nanoparticles than in ferromagnetic and ferrimagnetic particles [103, 104].

Several experimental studies of ferromagnetic, ferrimagnetic and antiferromagnetic nanoparticles have indicated a temperature-independent relaxation below a crossover temperature of the order of 1 K [105–108]. This may be ascribed to macroscopic quantum tunnelling. However, it has been suggested that thermoinduced magnetization also can contribute to a temperature-independent relaxation [62]. It has also been pointed out that an apparent temperature independence of the relaxation time at low temperatures could be due to a distribution of energy barriers, $\Delta E$, which diverges for $\Delta E \rightarrow 0$ [109]. Both experimental [110] and theoretical [31, 76, 111] investigations have shown that such distributions of energy barriers can be found in magnetic nanoparticles.

## 5. Magnetic interactions between antiferromagnetic nanoparticles

The superparamagnetic relaxation of nanoparticles is very sensitive to interparticle interactions. Experimental studies of frozen suspensions of ferromagnetic and ferrimagnetic nanoparticles have shown that magnetic dipole interactions can lead to a divergence of the relaxation time at a finite temperature, such that equation (2) may be replaced by a Vogel–Fulcher law [112] or by an expression based on spin-glass models [113]. The critical temperature at which the relaxation time diverges is of the order of [114]

$$T_{\mathrm{p}} \approx \frac{\mu_0}{4\pi k_{\mathrm{B}}} \frac{\mu^2}{d_{\mathrm{p}}^3}, \tag{25}$$

where $d_{\mathrm{p}}$ is the average distance between the particles. Thus, $T_{\mathrm{p}}$ increases with increasing concentration of particles in the suspensions. Below the critical temperature, the samples may have magnetic properties, which have similarities to those of spin-glasses [113–116].

The magnetic moments of antiferromagnetic nanoparticles are typically much smaller than those of ferromagnetic and ferrimagnetic nanoparticles, and therefore the dipole interactions are insufficient to significantly affect the superparamagnetic relaxation [117]. In fact, the dipole interactions between antiferromagnetic nanoparticles in close proximity are typically so small that the related critical temperature is well below 1 K. For example, for particles with magnetic moments of the order of 300 $\mu_{\mathrm{B}}$ (typical for ferritin [58, 59]) and with an average centre to centre distance of 8 nm (corresponding to the diameter of typical ferritin cores) the critical temperature, estimated from equation (25), is of the order of 0.2 K. For 20 nm hematite particles, which have a magnetic moment due to its canted spin structure, one finds that even if the particles are in close proximity, the value of $T_{\mathrm{p}}$ is also of the order of 0.2 K [117]. Nevertheless, in several experimental studies of samples of uncoated antiferromagnetic nanoparticles, it has been found that aggregation can change the magnetic dynamics drastically. For instance, the temperature where the particles become superparamagnetic can increase by more than 100 K [117–119]. It has been concluded that exchange interaction between surface ions of neighbouring particles is responsible for the effect. This implies that the particles are

in such close proximity that the electronic wavefunctions of atoms at the interfaces overlap. Because the dipole interactions can be considered negligible in samples of antiferromagnetic nanoparticles, such samples present a unique possibility to study exchange coupling between magnetic nanoparticles.

The magnetic energy of a particle, $p$, which interacts with its neighbour particles, $q$, may be written as [21, 99, 117, 120, 121]

$$E_i = KV_p \sin^2\theta - \vec{M}_p \cdot \sum_q J_{pq}\vec{M}_q, \tag{26}$$

where $\vec{M}_p$ and $\vec{M}_q$ represent the (sublattice) magnetization of the particles $p$ and $q$, respectively, and $J_{pq}$ is an effective exchange coupling constant due to exchange coupling between surface atoms belonging to the neighbouring particles. The summation in the last term may be considered as an effective interaction field. If the first term in equation (26) is predominant, superparamagnetic relaxation may take place between the easy directions close to $\theta = 0$ and $\pi$. However, if the interaction is significant, the energy at the two minima will differ and the thermal populations will therefore also differ. For strong interactions, there may be only one energy minimum. At finite temperatures, the sublattice magnetization vectors will mainly fluctuate around the direction corresponding to the lower energy minimum. If the fluctuations of the sublattice magnetization directions are fast compared to the timescale of Mössbauer spectroscopy, the magnetic splitting in the spectra will be proportional to the average hyperfine field. Variations of the magnitude and direction of the interaction field in the sample result in a distribution of magnetic hyperfine splittings, which leads to spectra with broadened sextets.

The interactions between nanoparticles can often be modified by varying the preparation technique. Samples of non-interacting or weakly interacting particles can be obtained by coating the particles with, for example, oleic acid. Samples of strongly interacting particles may be obtained by drying, for example, suspensions of uncoated $\alpha$-$Fe_2O_3$ nanoparticles. Figures 11(a) and (b) show Mössbauer spectra of coated (weakly interacting) and uncoated (strongly interacting) 20 nm $\alpha$-$Fe_2O_3$ particles, respectively [117]. The spectra of the coated nanoparticles (figure 11(a)) show the typical behaviour of non-interacting magnetic nanoparticles, i.e., the simultaneous presence of a doublet and a sextet with a temperature-dependent area ratio over a broad range of temperatures. Around 240 K, the sextet vanishes and only a doublet is present, indicating that all particles exhibit fast superparamagnetic relaxation above this temperature. The spectra of the interacting particles (figure 11(b)) show a completely different evolution with increasing temperature. Instead of the appearance of a doublet, the spectra show a substantial asymmetric broadening of the lines of the sextet, and even at 360 K there is no visible doublet. As discussed above, this is typical for Mössbauer spectra of interacting particles with a distribution of interaction fields. Thus, the large differences between the spectra in figures 11(a) and (b) illustrate the importance of interparticle interactions in samples of antiferromagnetic nanoparticles. The spectra of the interacting particles in figure 11(b) have similarities to the spectrum of superparamagnetic particles at 240 K in an applied field (figure 11(a), bottom). This is in accordance with the description of the influence of interactions in terms of an effective interaction field. From an analysis of the temperature dependence of the hyperfine field distribution, the effective interaction energy and the magnetic anisotropy constant could be determined [117].

The collective magnetic excitations can also be suppressed by interparticle interactions, and the expression for the average magnetic hyperfine field (equation (3)) may then be replaced by [21, 117, 121]

$$B_{\text{obs}} \approx B_0\left[1 - \frac{k_{\text{B}}T}{2KV + E_{\text{int}}}\right], \tag{27}$$

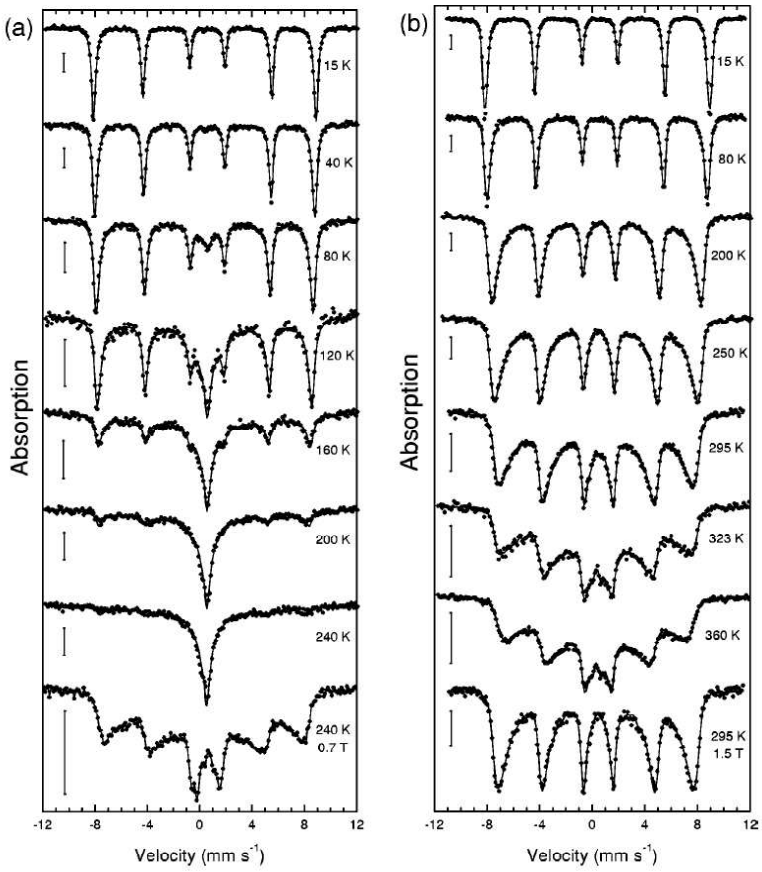


**Figure 11.** Mössbauer spectra of coated (weakly interacting) (a) and uncoated (strongly interacting) (b) 20 nm hematite nanoparticles obtained at the indicated temperatures [117]. Reprinted with permission from [117]. Copyright 2000 by the American Physical Society.

where $E_{\text{int}}$ is related to the strength of the interparticle interactions. Figure 12 shows the temperature dependence of the magnetic hyperfine fields at low temperatures of 8 nm non-interacting and interacting $\alpha$-$Fe_2O_3$ nanoparticles [122]. The linear temperature dependence of the data is in accordance with equations (3) and (27). Assuming that the anisotropy energy constants are identical for the particles of the two samples, an effective interaction energy, $E_{\text{int}}/k_{\text{B}} \approx 1300$ K could be estimated from the slopes of the curves in figure 12.

Figure 13 shows inelastic neutron scattering data at $Q = 1.37$ Å$^{-1}$ for weakly and strongly interacting 8 nm $\alpha$-$Fe_2O_3$ nanoparticles [99]. The data, obtained in zero applied magnetic field for weakly (a) and strongly (c) interacting particles, show that strong interactions shift the positions of the inelastic peaks to higher energies, but their relative areas decrease. The interactions affect both the excitation energy and the area ratio in a way that is similar to the effect of an applied field (figure 13(b)). Similar results have been found in an inelastic neutron scattering study of NiO nanoparticles [100].

Recent neutron diffraction experiments [123] have shown that $\alpha$-$Fe_2O_3$ nanoparticles prepared by a gel–sol method may be attached in such a way that neighbouring particles have a common crystallographic orientation and a magnetic correlation in the [001]

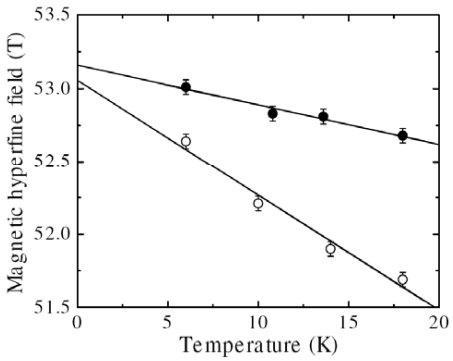


**Figure 12.** Magnetic hyperfine field of coated (open circles) and uncoated 8 nm hematite nanoparticles obtained from low-temperature Mössbauer spectra. The lines are linear fits to the data extrapolated to $T = 0$ K. Reprinted with permission from [122]. Copyright 2005 by the American Physical Society.

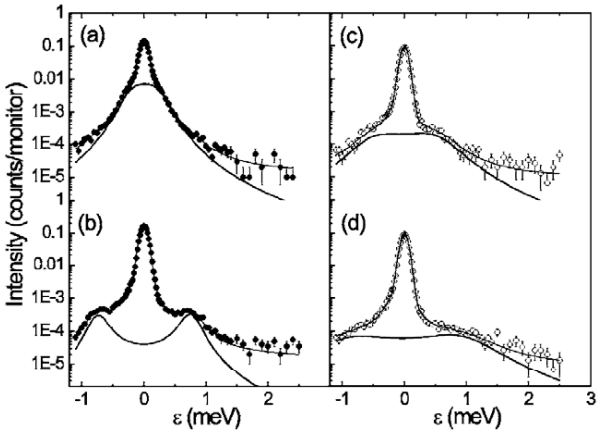


**Figure 13.** Inelastic neutron data for 8 nm $\alpha$-$Fe_2O_3$ nanoparticles. Data for coated nanoparticles in (a) zero field and (b) in an applied field of 6 T, respectively. Data for uncoated nanoparticles in (c) zero field and (d) in an applied field of 6 T, respectively. Reprinted with permission from [99]. Copyright 2006 by the American Physical Society.

direction. Figure 14(a) shows neutron diffraction data for such a sample of 8 nm $\alpha$-$Fe_2O_3$ nanoparticles [123]. Most of the diffraction lines have line widths that are considerably larger than the instrumental broadening, but in accordance with the particle size estimated from x-ray diffraction data and electron micrographs. However, the width of the magnetic (003) reflection is considerably narrower than that of the other peaks. This peak could be well fitted with two components, one with a line width corresponding to a particle size of about 8 nm and another with a relative area of about 36% and a width corresponding to a correlation length of $\sim$22 nm. This suggests that about a third of the particles are present in chains with around three particles that show oriented attachment such that both the crystallographic and the magnetic order continue across the interfaces. High-resolution electron microscopy studies confirmed the existence of such chains of particles with a common crystallographic orientation [123].

Mössbauer studies of interacting $\alpha$-$Fe_2O_3$ nanoparticles have also shown that the interactions between particles with different relative crystallographic orientations can lead to

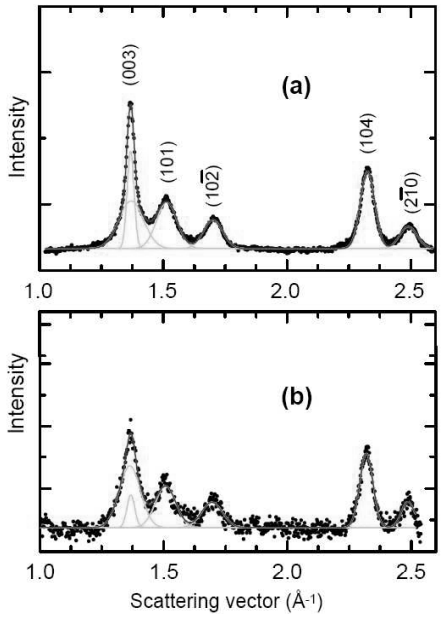


**Figure 14.** Neutron diffraction data for 8 nm hematite particles obtained at room temperature. (a) Data for the as-prepared (strongly interacting) sample. (b) Data for the ground sample. Reprinted with permission from [123]. Copyright 2005 by the American Physical Society.

(This figure is in colour only in the electronic version)

a rotation of the sublattice magnetization directions [122]. In the spectra of $\alpha$-$Fe_2O_3$, there is a small quadrupole shift, $\varepsilon_{qs}$, because of the non-cubic environments of the iron ions, which give rise to an electric field gradient along the [001] direction. In general, the quadrupole shift in a Mössbauer spectrum depends on the angle $\alpha$ between the electric field gradient and the magnetic hyperfine field according to the expression

$$\varepsilon_{qs} = \varepsilon^0_{qs}(3\cos^2\alpha - 1)/2, \tag{28}$$

where $\varepsilon^0_{qs} = 0.20$ mm s$^{-1}$ in $\alpha$-$Fe_2O_3$. Below the Morin transition temperature, the magnetic hyperfine field is parallel to the electric field gradient, and the quadrupole shift is therefore 0.20 mm s$^{-1}$. Above the Morin transition in bulk $\alpha$-$Fe_2O_3$ and in non-interacting nanoparticles at all temperatures, the magnetic hyperfine field is perpendicular to the electric field gradient and the quadrupole shift is then $-0.1$ mm s$^{-1}$. However, in samples of interacting $\alpha$-$Fe_2O_3$ nanoparticles the quadrupole shift can deviate from this value. Figure 15 shows the quadrupole shift of non-interacting and interacting 8 nm $\alpha$-$Fe_2O_3$ nanoparticles as a function of temperature. For the non-interacting nanoparticles, the quadrupole shifts are close to $-0.10$ mm s$^{-1}$, but the interacting nanoparticles show quadrupole shifts of the order of $-0.07$ to $-0.08$ mm s$^{-1}$, indicating that the value of $\alpha$ differs from 90° and rather is of the order of 75°. This can be explained by rotation of the sublattice magnetization directions induced by the exchange interactions between neighbouring particles with different crystallographic orientation [122].

It is also noteworthy that the extrapolations of the temperature dependence of the hyperfine fields to $T = 0$ K differ for the non-interacting and the interacting nanoparticles (figure 12). This is in accordance with a rotation of the sublattice magnetization directions, because the contribution to the magnetic hyperfine field from the dipole fields of neighbouring magnetic

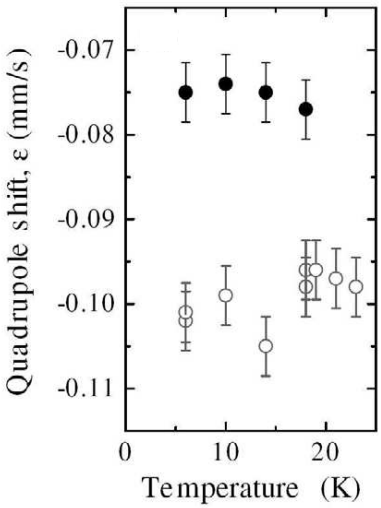


**Figure 15.** Quadrupole shift of coated (weakly interacting) (open circles) and uncoated (strongly interacting) (solid circles) 8 nm hematite nanoparticles as a function of temperature. Reprinted with permission from [122]. Copyright 2005 by the American Physical Society.

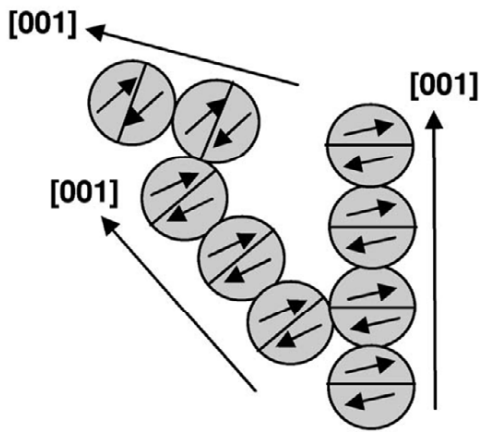


**Figure 16.** Schematic illustration of a network of interacting $\alpha$-$Fe_2O_3$ nanoparticles. Reprinted with permission from [123]. Copyright 2005 by the American Physical Society.

ions depends on the angle between the sublattice magnetization and the [001] direction in $\alpha$-$Fe_2O_3$ [124]. The measured difference between the extrapolated hyperfine fields was in accordance with the rotation angle obtained from the analysis of the quadrupole shift [122].

It is likely that the strong suppression of superparamagnetic relaxation in samples of agglomerated $\alpha$-$Fe_2O_3$ nanoparticles is governed by larger networks of interacting particles with both parallel and non-parallel [001] axes [122, 123]. Figure 16 shows a schematic illustration of such a network [123]. Here particles are attached in small chains with parallel [001] axes, but the neighbouring chains or particles may have different orientations of their [001] axes. This model describes most of the measured features well.

The establishment of strong interactions between $\alpha$-$Fe_2O_3$ nanoparticles is a reversible process [125]. Exposure of an agglomerated sample of 8 nm $\alpha$-$Fe_2O_3$ particles in water to ultrasound can result in a change of the Mössbauer spectrum from a sextet with broadened lines to a doublet, but after subsequent drying, the sextet can be re-established. Several Mössbauer studies have shown that gentle grinding of samples of interacting $\alpha$-$Fe_2O_3$ particles also can lead to a significant reduction of the interactions [123, 125, 126]. The neutron diffraction studies of 8 nm $\alpha$-$Fe_2O_3$ nanoparticles (figure 14) showed that the narrow (003) reflection of interacting particles (figure 14(a)) became broader and had a width comparable to that of the other reflections after gentle grinding (figure 14(b)). Thus, the oriented attachment seems to have been destroyed by the grinding.

Goethite ($\alpha$-FeOOH) is a common mineral and it is usually poorly crystalline, both when formed in nature and when synthesized in the laboratory. Well crystallized goethite has a Néel temperature around 393 K [120]. Mössbauer spectra of goethite commonly show sextets with asymmetrically broadened lines with average hyperfine fields much smaller than the bulk value. Only in a small temperature range does a doublet coexist with the sextet. The temperature dependence of the average hyperfine field of goethite nanoparticles has been found to be in accordance with a simple mean-field model for interacting particles [120]. It has been suggested [127] that goethite particles consist of smaller, interacting clusters, and that the spectra may explained by a distribution of precession states in the clusters with different precession angles, which give rise to different hyperfine fields. In this model, transitions between the precession states were neglected, and this may not be realistic [117]. Recent studies have shown that goethite particles may grow via oriented attachment [128–130], and this suggests that goethite particles in fact may consist of smaller interacting clusters. The different interpretations have given rise to some debate in the literature [117, 127, 131].

Interactions between NiO nanoparticles have been studied by electron magnetic resonance [132] and by DC and AC magnetization measurements [133]. As in the case of $\alpha$-$Fe_2O_3$ nanoparticles, it was found that the superparamagnetic relaxation to a large extent was suppressed in samples of uncoated particles in comparison with particles coated with oleic acid. Mössbauer studies of nanoparticles of $^{57}$Fe-doped NiO, prepared by heat treatment of $Ni(OH)_2$, showed similar effects [118]. It has also been found that interparticle interactions between NiO nanoparticles can be reduced by grinding the samples or by exposing them to ultrasound [134]. Even suspension in water or long-term exposure to air leads to reduction of the interparticle interactions. However, unlike $\alpha$-$Fe_2O_3$ nanoparticles, the strong interactions could not be re-established by drying suspensions of weakly interacting NiO nanoparticles. It is likely that the different behaviour of $\alpha$-$Fe_2O_3$ and NiO nanoparticles can be explained by differences in the affinity of the particles to water [134]. Adsorption of water on the surface of the NiO particles may prevent the formation of strong exchange bonds between the particles, reducing the interactions between particles.

Mössbauer studies have shown that interactions between nanoparticles of different antiferromagnetic materials can have unexpected effects on the magnetic properties [119]. For example, the superparamagnetic relaxation of 9 nm $\alpha$-$Fe_2O_3$ particles was to a large extent suppressed when they were mixed with nanoparticles of CoO, whereas the opposite effect was found when the iron oxide particles were mixed with nanoparticles of NiO. The different influence of CoO and NiO particles may be explained by the smaller magnetic anisotropy of the NiO nanoparticles [119], but a large affinity of NiO to water may also contribute to a reduction of the interactions. In samples of mixtures of $\alpha$-$Fe_2O_3$ and NiO nanoparticles, it was surprisingly found that a Morin transition took place although there was no Morin transition in the sample consisting solely of the $\alpha$-$Fe_2O_3$ nanoparticles [119]. Mixtures of antiferromagnetic nanoparticles with ferromagnetic or ferrimagnetic nanoparticles with strong

interparticle interactions have shown exchange bias and enhanced coercivity [13–16, 135]. Such nanocomposites may therefore have applications as permanent magnets. In a recent study of core–shell Co–CoO nanoparticles it was shown that exchange interactions between the antiferromagnetic CoO shells of neighbouring particles can have a significant effect on the blocking temperature, the coercivity and the exchange bias [136].

## 6. Summary

The size dependence of the magnetic properties of nanoparticles of antiferromagnetic materials is in many respects substantially different from that of nanoparticles of ferromagnetic and ferrimagnetic materials. The magnetic moment of a nanoparticle of a ferromagnetic or ferrimagnetic material is basically determined by the particle volume and the magnetization, which may be similar to the bulk value, although surface effects and defects often result in a (slightly) smaller magnetization. In contrast, the magnetic moment of an antiferromagnetic nanoparticle is mainly a result of imperfections or finite-size effects, e.g., different numbers of spins in the sublattices, which lead to an uncompensated moment and a related increase of the saturation magnetization with decreasing particle size, but thermoinduced magnetization is also expected to give a contribution to the moment of very small particles.

The small magnetic moments of antiferromagnetic nanoparticles makes the analysis of magnetization and in-field Mössbauer data much less straightforward than the analysis of data for ferromagnetic and ferrimagnetic nanoparticles. This is because the isothermal magnetization curves of particles with very small moments are often far from saturation in the superparamagnetic regime. Furthermore, the anisotropy may be large compared to the Zeeman energy, such that the Langevin function is not a good approximation to the magnetization curves.

As in ferromagnetic and ferrimagnetic nanoparticles, the magnetic excitations of antiferromagnetic nanoparticles at low temperatures are dominated by the uniform excitations ($q = 0$ spin waves). This leads to a linear decrease of the sublattice magnetization with increasing temperature and a small net magnetic moment that increases with increasing temperature. The excitation energy of the uniform mode in antiferromagnetic nanoparticles is much larger than that of ferromagnetic and ferrimagnetic nanoparticles, but even a small uncompensated moment can have a significant influence on the excitation energy.

Interactions between nanoparticles can have a large influence on the magnetic dynamics, e.g., the superparamagnetic relaxation. The dipole interaction between antiferromagnetic nanoparticles in close proximity is insignificant; therefore, the effects must be explained by exchange interaction between surface atoms of neighbouring nanoparticles. This exchange interaction can to a large extent be varied by exposing the samples to appropriate macroscopic treatments such as gentle grinding or exposure to ultrasound. It has been found that nanoparticles of $\alpha$-$Fe_2O_3$ can be attached in such a way that the crystallographic and magnetic order continue across the interfaces. Interactions between antiferromagnetic nanoparticles with different crystallographic orientations can result in rotation of the sublattice magnetization directions.

## References

[1] Dormann J L, Fiorani D and Tronc E 1997 *Adv. Chem. Phys.* **98** 283
[2] Dormann J L and Fiorani (ed) 1992 *Magnetic Properties of Fine Particles* (Amsterdam: North-Holland)
[3] Kodama R H 1999 *J. Magn. Magn. Mater.* **200** 359
[4] Fiorani D (ed) 2005 *Surface Effects in Magnetic Nanoparticles* (New York: Springer)
[5] Zhu J-G 2003 *Mater. Today* **6** 22
[6] Pankhurst Q A, Conolly J, Jones S K and Dobson J 2003 *J. Phys. D: Appl. Phys.* **36** R167

[7] Tartaj P, del Puerto Morales M, Veintemillas-Verdaguer S, Gonzalez-Carreno T and Serna C J 2003 *J. Phys. D: Appl. Phys.* **36** R182
[8] Holm C and Weis J-J 2005 *Curr. Opin. Colloid Interface Sci.* **10** 133
[9] Nogués J and Schuller I K 1999 *J. Magn. Magn. Mater.* **192** 203
[10] Berkowitz A E and Takano K 1999 *J. Magn. Magn. Mater.* **200** 552
[11] Comstock R L 2002 *J. Mater. Sci. Mater. Electron.* **13** 509
[12] Skumryev V, Stoyanov S, Zhang Y, Hadjipanayis G, Givord D and Nogués J 2003 *Nature* **423** 850
[13] Sort J, Nogués J, Amils X, Suriñach S, Muñoz J S and Baro M D 1999 *Appl. Phys. Lett.* **75** 3177
[14] Sort J, Suriñach S, Muñoz J S, Baró M D, Nogués J, Chouteau G, Skumryev V and Hadjipanayis G C 2002 *Phys. Rev.* B **65** 174420
[15] Nogués J, Sort J, Langlais V, Skumryev V, Surinach S, Munoz J S and Baro M D 2005 *Phys. Rep.* **422** 65
[16] Anhøj T A, Jacobsen C S and Mørup S 2004 *J. Appl. Phys.* **95** 3649
[17] Néel L 1949 *Ann. Geophys.* **5** 99
[18] Brown W F Jr 1963 *Phys. Rev.* **130** 167
[19] Mørup S and Hansen B R 2005 *Phys. Rev.* B **72** 024418
[20] Mørup S and Topsøe H 1976 *Appl. Phys.* **11** 63
[21] Mørup S 1983 *J. Magn. Magn. Mater.* **37** 39
[22] Martin D H 1967 *Magnetism in Solids* (Cambridge, MA: MIT Press)
[23] Néel L 1954 *J. Phys. Rad.* **15** 225
[24] Hansen M F, Bødker F, Mørup S, Lefmann K, Clausen K N and Lindgård P-A 1997 *Phys. Rev. Lett.* **79** 4910
[25] Lefmann K, Bødker F, Klausen S N, Hansen M F, Clausen K N, Lindgård P-A and Mørup S 2001 *Europhys. Lett.* **54** 526
[26] Trohidou K N 2005 *Surface Effects in Magnetic Nanoparticles* ed D Fiorani (New York: Springer) p 45
[27] Kodama R H and Berkowitz A E 2005 *Surface Effects in Magnetic Nanoparticles* ed D Fiorani (New York: Springer) p 189
[28] Coey J M D 1971 *Phys. Rev. Lett.* **27** 1140
[29] Morrish A H and Haneda K 1983 *J. Magn. Magn. Mater.* **35** 105
[30] Coey J M D 1987 *Can. J. Phys.* **65** 1210
[31] Mørup S 2003 *J. Magn. Magn. Mater.* **266** 110
[32] Bahl C R H, Hansen M F, Pedersen T, Saadi S, Nielsen K H, Lebech B and Mørup S 2006 *J. Phys.: Condens. Matter* **18** 4161
[33] Kodama R H, Makhlouf S A and Berkowitz A E 1997 *Phys. Rev. Lett.* **79** 1393
[34] Lindgård P-A 2003 *J. Magn. Magn. Mater.* **266** 88
[35] Bødker F, Hansen M F, Koch C B, Lefmann K and Mørup S 2000 *Phys. Rev.* B **61** 6826
[36] Klausen S N, Lindgård P-A, Lefmann K, Bødker F and Mørup S 2002 *Phys. Status Solidi* a **189** 1039
[37] Golosovsky I V, Mirebeau I, André G, Kurdyukov D A, Kumzerov Yu A and Vakhrushev S B 2001 *Phys. Rev. Lett.* **86** 5783
[38] Tsunoda Y, Nakano H and Matsuo S 1993 *J. Phys.: Condens. Matter* **5** L29
[39] Shinjo T, Kiyama M, Sugita N, Watanabe K and Takada T 1983 *J. Magn. Magn. Mater.* **35** 133
[40] Yamamoto A, Kiyama M and Shinjo T 1994 *Hyperfine Interact.* **92** 1311
[41] Yamamoto A, Honmyo T, Hosoito N, Kiyama M and Shinjo T 1993 *Nucl. Instrum. Methods* B **76** 202
[42] Trohidou K N, Zianni X and Blackman J A 1998 *J. Appl. Phys.* **84** 2795
[43] Bocquet S and Kennedy S J 1992 *J. Magn. Magn. Mater.* **109** 260
[44] Punnoose A, Magnone H, Seehra M S and Bonevich J 2001 *Phys. Rev.* B **64** 174420
[45] Zheng X G, Xu C N, Nishikubo N, Nishiyama K, Higemoto W, Moon W J, Tanaka E and Otabe E S 2005 *Phys. Rev.* B **72** 014464
[46] Bødker F and Mørup S 2000 *Europhys. Lett.* **52** 217
[47] Kündig W, Ando K J, Constabaris G and Lindquist R H 1966 *Phys. Rev.* **142** 327
[48] Schroeer D and Nininger R C 1967 *Phys. Rev. Lett.* **19** 632
[49] Klausen S N, Lefmann K, Lindgård P-A, Kuhn L T, Bahl C R H, Frandsen C, Mørup S, Roessli B, Cavadini N and Niedermayer C 2004 *Phys. Rev.* B **70** 214411
[50] Mørup S 1985 *Surf. Sci.* **156** 888
[51] Zysler R D, Fiorani D, Testa A M, Suber L, Agostinelli E and Godinho M 2003 *Phys. Rev.* B **68** 212408
[52] Guertin R P, Harrison N, Zhou Z X, McCall S and Drymiotis F 2007 *J. Magn. Magn. Mater.* **308** 97
[53] Gilles C, Bonville P, Wong K K W and Mann S 2000 *Eur. Phys. J.* B **17** 417
[54] Néel L 1961 *C.R. Acad. Sci. Paris* **252** 4075
[55] Richardson J T, Yiagas D I, Turk B, Forster K and Twigg M V 1991 *J. Appl. Phys.* **70** 6977
[56] Palkar V R, Ayyub P, Chattopadhyay S and Multani M 1996 *Phys. Rev.* B **53** 2167

[57] Pankhurst Q A 1991 *J. Magn. Magn. Mater.* **101** 291
[58] Harris J G E, Grimaldi J E, Awschalom D D, Chiolero A and Loss D 1999 *Phys. Rev.* B **60** 3453
[59] Kilcoyne S H and Cywinski R 1995 *J. Magn. Magn. Mater.* **140–144** 1466
[60] Makhlouf S A, Parker F T and Berkowitz A E 1997 *Phys. Rev.* B **55** R14717
[61] Seehra M S, Babu V S, Manivannan A and Lynn J W 2000 *Phys. Rev.* B **61** 3513
[62] Mørup S and Frandsen C 2004 *Phys. Rev. Lett.* **92** 217201
[63] Madsen D E and Mørup S 2006 *Phys. Rev.* B **74** 014405
[64] Vollath D, Szabó D V and Willis J O 1996 *Mater. Lett.* **29** 271
[65] Bañobre-López M, Vázquez-Vázquez C, Rivas J and López-Quintela M A 2003 *Nanotechnology* **14** 318
[66] Silva N J O, Amaral V S and Carlos L D 2005 *Phys. Rev.* B **71** 184408
[67] Madsen D E, Mørup S and Hansen M F 2006 *J. Magn. Magn. Mater.* **305** 95
[68] Hanson M, Johansson C and Mørup S 1993 *J. Phys.: Condens. Matter* **5** 725
[69] Respaud M 1999 *J. Appl. Phys.* **86** 556
[70] García-Palacios J L 2000 *Adv. Chem. Phys.* **112** 1
[71] Chantrell R W, Walmsley N, Gore J and Maylin M 2001 *Phys. Rev.* B **63** 024410
[72] Taketomi S and Shull R D 2003 *J. Magn. Magn. Mater.* **266** 207
[73] Makhlouf S A, Parker F T, Spada F E and Berkowitz A E 1997 *J. Appl. Phys.* **81** 5561
[74] Makhlouf S A 2002 *J. Magn. Magn. Mater.* **246** 184
[75] Lee G H, Huh S H, Jeong J W, Choi B J, Kim S H and Ri H-C 2002 *J. Am. Chem. Soc.* **124** 12094
[76] Kodama R H and Berkowitz A E 1999 *Phys. Rev.* B **59** 6321
[77] Hansen M F and Mørup S 1999 *J. Magn. Magn. Mater.* **203** 214
[78] Gittleman J I, Abeles B and Bozowski S 1974 *Phys. Rev.* B **9** 3891
[79] Jiang J Z and Mørup S 1997 *Nanostruct. Mater.* **9** 375
[80] Luis F, del Barco E, Hernández J M, Remiro E, Bartolome J and Tejada J 1999 *Phys. Rev.* B **59** 11837
[81] Allen P D, St Pierre T G, Chua-anusorn W, Ström V and Rao K V 2000 *Biochim. Biophys. Acta* **1500** 186
[82] Dickson D P E, Reid N M K, Hunt C, Williams H D, El-Hilo M and O'Grady K 1993 *J. Magn. Magn. Mater.* **125** 345
[83] Blume M and Tjon J A 1968 *Phys. Rev.* **165** 446
[84] Tronc E 1996 *Nuovo Cimento* D **18** 163
[85] Bødker F, Mørup S and Linderoth S 1994 *Phys. Rev. Lett.* **72** 282
[86] Mørup S and Ostenfeld C W 2001 *Hyperfine Interact.* **136** 125
[87] Mørup S, Clausen B S and Christensen P H 1987 *J. Magn. Magn. Mater.* **68** 160
[88] St Pierre T G, Jones D H and Dickson D P E 1987 *J. Magn. Magn. Mater.* **69** 276
[89] Morrish A H 1965 *The Physical Principles of Magnetism* (New York: Wiley)
[90] Yosida K 1996 *Theory of Magnetism* (Berlin: Springer)
[91] Mørup S 2007 *Europhys. Lett.* **77** 27003
[92] Hendriksen P V, Linderoth S and Lindgård P-A 1993 *Phys. Rev.* B **48** 7259
[93] Kittel C 1951 *Phys. Rev.* **82** 565
[94] Keffer F and Kittel C 1952 *Phys. Rev.* **85** 329
[95] Hansen M F, Bødker F, Mørup S, Lefmann K, Clausen K N and Lindgård P-A 2000 *J. Magn. Magn. Mater.* **221** 10
[96] Klausen S N, Lefmann K, Lindgård P-A, Clausen K N, Hansen M F, Bødker F, Mørup S and Telling M 2003 *J. Magn. Magn. Mater.* **266** 68
[97] Wangsness R K 1952 *Phys. Rev.* **86** 146
[98] Wangsness R K 1953 *Phys. Rev.* **91** 1085
[99] Kuhn L T, Lefmann K, Bahl C R H, Ancona S N, Lindgård P-A, Frandsen C, Madsen D E and Mørup S 2006 *Phys. Rev.* B **74** 184406
[100] Bahl C R H, Lefmann K, Kuhn L T, Lindgård P-A, Christensen N B, Melis H V and Mørup S 2006 *J. Phys.: Condens. Matter* **18** 11203
[101] Chikazumi S 1997 *Physics of Ferromagnetism* 2nd edn (Oxford: Clarendon)
[102] Chudnovsky E M and Günther L 1988 *Phys. Rev. Lett.* **60** 661
[103] Barbara B and Chudnovsky E M 1990 *Phys. Lett.* A **145** 205
[104] Chudnovsky E M 1995 *J. Magn. Magn. Mater.* **140–144** 1821
[105] Gider S, Awschalom D D, Douglas T, Mann S and Chaparala M 1995 *Science* **268** 77
[106] Barbara B, Wernsdorfer W, Sampaio L C, Park J G, Paulsen C, Novak M A, Ferré R, Mailly D, Sessoli R, Caneschi A, Hasselbach K, Benoit A and Thomas L 1995 *J. Magn. Magn. Mater.* **140–144** 1825
[107] Tejada J, Hernandez J M and del Barco E 1999 *J. Magn. Magn. Mater.* **196/197** 552
[108] Awschalom D D, Smyth J F, Grinstein G, DiVincento D P and Loss D 1992 *Phys. Rev. Lett.* **68** 3092

[109] Barbara B, Paulsen C, Sampaio L C, Uehara M, Fruchard F, Tholence J L, Marghand A, Tejada J and Linderoth S 1992 *Studies of Magnetic Properties of Small Particles* (New York: Elsevier Science) p 235
[110] St Pierre T G, Gorham N T, Allen P D, Costa-Krämer J L and Rao K V 2002 *Phys. Rev.* B **65** 024436
[111] Kodama R H, Berkowitz A E, McNiff E J and Foner S 1996 *Phys. Rev. Lett.* **77** 394
[112] Zhang J, Boyd C and Luo W 1996 *Phys. Rev. Lett.* **77** 390
[113] Djurberg C, Svedlindh P, Nordblad P, Hansen M F, Bødker F and Mørup S 1997 *Phys. Rev. Lett.* **79** 5154
[114] Hansen M F and Mørup S 1998 *J. Magn. Magn. Mater.* **184** 262
[115] Mamiya H, Nakatani I and Furubayashi T 1998 *Phys. Rev. Lett.* **80** 177
[116] Fiorani D, Dormann J L, Cherkaoui R, Tronc E, Lucari F, D'Orazio F, Spinu L, Nogues M, Garcia A and Testa A M 1999 *J. Magn. Magn. Mater.* **196/197** 143
[117] Hansen M F, Koch C B and Mørup S 2000 *Phys. Rev.* B **62** 1124
[118] Bødker F, Hansen M F, Koch C B and Mørup S 2000 *J. Magn. Magn. Mater.* **221** 32
[119] Frandsen C and Mørup S 2003 *J. Magn. Magn. Mater.* **266** 36
[120] Mørup S, Madsen M B, Franck J, Villadsen J and Koch C J W 1983 *J. Magn. Magn. Mater.* **40** 163
[121] Mørup S, Frandsen C, Bødker F, Klausen S N, Lefmann K, Lindgård P-A and Hansen M F 2002 *Hyperfine Interact.* **144/145** 347
[122] Frandsen C and Mørup S 2005 *Phys. Rev. Lett.* **94** 027202
[123] Frandsen C, Bahl C R H, Lebech B, Lefmann K, Kuhn L T, Keller L, Andersen N H, v Zimmermann M, Johnson E, Klausen S N and Mørup S 2005 *Phys. Rev.* B **72** 214406
[124] Tobler L, Kündig W and Savic I 1981 *Hyperfine Interact.* **10** 1017
[125] Frandsen C and Mørup S 2006 *J. Phys.: Condens. Matter* **18** 7079
[126] Xu M, Bahl C R H, Frandsen C and Mørup S 2004 *J. Colloid Interface Sci.* **279** 132
[127] Bocquet S, Pollard R J and Cashion J D 1992 *Phys. Rev.* B **46** 11657
[128] Banfield J F, Welch S A, Zhang H, Ebert T T and Penn R L 2000 *Science* **289** 751
[129] Burleson D J and Penn R L 2006 *Langmuir* **22** 402
[130] Penn R L, Erbs J J and Gulliver D M 2006 *J. Cryst. Growth* **293** 1
[131] Madsen D E, Hansen M F, Koch C B and Mørup S 2007 unpublished
[132] Seehra M S, Shim H, Dutta P and Manivannan A 2005 *J. Appl. Phys.* **97** 10J509
[133] Shim H, Manivannan A, Seehra M S, Reddy K M and Punoose A 2006 *J. Appl. Phys.* **99** 08Q503
[134] Bahl C R H and Mørup S 2006 *Nanotechnology* **17** 2835
[135] Frandsen C, Ostenfeld C W, Xu M, Jacobsen C S, Keller L, Lefmann K and Mørup S 2004 *Phys. Rev.* B **70** 134416
[136] Nogués J, Skumryev V, Sort J, Stoyanov S and Givord D 2006 *Phys. Rev. Lett.* **97** 157203

# Paper II

Available online at www.sciencedirect.com
SCIENCE DIRECT®
Journal of Magnetism and Magnetic Materials 305 (2006) 95–99
Journal of magnetism and magnetic materials
www.elsevier.com/locate/jmmm

# On the interpretation of magnetization data for antiferromagnetic nanoparticles

Daniel Esmarch Madsen[a,*], Steen Mørup[a], Mikkel Fougt Hansen[b]

[a]Department of Physics, Bldg. 307, Technical University of Denmark, DK-2800 Kgs Lyngby, Denmark
[b]MIC - Department of Micro and Nanotechnology, Bldg. 345 East, Technical University of Denmark, DK-2800 Kgs Lyngby, Denmark

Received 11 October 2005
Available online 21 December 2005

**Abstract**

We have investigated the influence of anisotropy on the magnetization curves of antiferromagnetic nanoparticles. We show that if such curves are analyzed in a conventional way, i.e. using a Langevin function in combination with a linear term, this usually results in good quality fits, but with an apparent temperature dependence of parameters such as the magnetic moment per particle and the antiferromagnetic susceptibility. In order to avoid the problems associated with anisotropy as well as volume/moment distributions we propose that the initial susceptibility is used when analyzing the temperature dependence of the magnetic moment.


*PACS:* 75.30.Gw; 75.40.Mg; 75.50.Ee; 75.50.Tt

*Keywords:* Antiferromagnetic nanoparticles; Magnetization measurements; Magnetic anisotropy

## 1. Introduction

The magnetic properties of nanoparticles of antiferromagnetic materials have attracted much attention and a number of puzzling observations have been made.

In large particles of antiferromagnetic materials, the magnetic moment is negligible, and the only contribution to the magnetization is the canting of the sublattices in response to an externally applied field as described by the antiferromagnetic susceptibility $\chi_{AF}$. However, particles with sizes in the nanometer range carry a small magnetic moment, $\mu$, attributed by Néel [1] to the presence of uncompensated spins, and suggested to have a value of $\mu_s(N_s)^x$, where $\mu_s$ is the magnetic moment per atom, $N_s$ is the number of magnetic atoms in each particle, and $x$ is a parameter ranging from $\frac{1}{3}$ to $\frac{2}{3}$ depending on how the uncompensated spins are distributed in the crystal lattice. In addition to this, the existence of a thermoinduced contribution to the moment has recently been suggested [2,3]. This thermoinduced moment has the unusual property that it increases with increasing temperature.

Several experimental investigations have been carried out on antiferromagnetic nanoparticles, and in studies using magnetization measurements a number of intriguing properties have been reported, specifically in the form of unusual temperature dependencies of $\mu$ (which has been found to increase with temperature) and $\chi_{AF}$ (which decreases with temperature) above the superparamagnetic blocking temperature. This has so far been reported for particles of e.g., ferrihydrite [4], and the iron storage protein ferritin [5,6]. In these studies, the analysis of isothermal magnetization data was based on an antiferromagnetically modified Langevin model in which the magnetization is assumed to be the sum of a single Langevin function and a term varying linearly with the applied field, $B$. However, according to Silva et al. [7] this model is too simple to obtain the correct temperature variation of the parameters. To demonstrate this, they calculated theoretical magnetization curves for a number of temperatures, based on the modified Langevin formula, but assuming a log-normal distribution of magnetic moments. When they fitted these curves to the modified

*Corresponding author. Tel.: +45 4525 3133; fax: +45 4593 2399.
*E-mail address:* daniel.madsen@fysik.dtu.dk (D.E. Madsen).

0304-8853/$ - see front matter © 2005 Elsevier B.V. All rights reserved.
doi:10.1016/j.jmmm.2005.11.033

Langevin model (where only a single value of $\mu$ is considered), the estimated parameter $\mu$ was found to increase with temperature. In a subsequent study by Silva et al. [8], the model including a distribution of moments, was applied to the analysis of magnetization data for ferritin, and they found that the magnetic moment decreases with temperature, contrary to the previous investigations cited above.

Silva et al. [7,8] did not consider the role of the magnetic anisotropy which can also be important [9]. As demonstrated by a number of authors [10–13] deviations from the classical Langevin form of the magnetization curves for ferro- and ferrimagnetic nanoparticles due to anisotropy become particularly pronounced at low temperatures. In the following we analyze the influence of anisotropy on the magnetization curves of *antiferromagnetic* nanoparticles, and we show that neglecting the anisotropy can also lead to erroneous conclusions if the data are fitted with the modified Langevin model. Due to their small magnetic moments, the magnetic properties of antiferromagnetic particles are difficult to characterize using the full magnetization curve, and we therefore propose that the interpretation of such data can be based on the initial susceptibility.

## 2. Models

As noted above, the key issue is how to reliably analyze magnetization data for nanoparticles above the superparamagnetic blocking temperature. Several models have been used, and in the following we present a brief overview of the most commonly applied ones. We assume that interparticle interactions are negligible.

### 2.1. Langevin model

In the simplest case where the magnetic anisotropy is considered negligible, the magnetization is given by the classical Langevin function, which is obtained when assuming that the energy, $\varepsilon$, of a single particle with a magnetic moment $\vec{\mu}$ in an applied magnetic field, $\vec{B}$, is given by *only* the Zeeman contribution

$$\varepsilon = -\vec{\mu}\cdot\vec{B} = -\mu B\cos\alpha, \tag{1}$$

where $\alpha$ is the angle between $\vec{B}$ and $\vec{\mu}$. Using Boltzmann statistics one obtains

$$\frac{\langle M_z\rangle_{\mathrm{T}}}{M_0} = \coth\xi - \frac{1}{\xi} \equiv \mathscr{L}(\xi), \tag{2}$$

where $\langle M_z\rangle_{\mathrm{T}}$ is the thermal average of the magnetization of the sample along the applied field, $M_0 = \mu n$ is the saturation magnetization, $\mathscr{L}$ is the Langevin function with $\xi = \mu B/k_B T$, and $n$ is the number of particles per unit volume of the sample. For antiferromagnetic nanoparticles an additional linear term is added to account for the antiferromagnetic susceptibility such that the full expression is assumed to be given by

$$\langle M_z\rangle_{\mathrm{T}} = n\mu\mathscr{L}\left(\frac{\mu B}{k_B T}\right) + \chi_{\mathrm{AF}}\mu_0^{-1}B, \tag{3}$$

which is the model most commonly applied (see, e.g., [4–6]) in the interpretation of magnetization data for antiferromagnetic nanoparticles. We will be referring to this as the antiferromagnetically modified Langevin model.

### 2.2. Model including anisotropy

The effect of anisotropy has earlier been included in the analysis of magnetization data for ferri- and ferromagnetic nanoparticles [10,11]. However, it has generally been ignored when analyzing data for *antiferromagnetic* particles, although a model based on an Ising-like behavior of the uncompensated moments has been applied by, e.g., Gilles et al. [14].

Expressions for the magnetization curve where anisotropy is included have been derived by a number of authors [10–13]. We have based our calculations on a derivation by Hanson et al. [10] and Respaud [13].

In order to examine the effect of magnetic anisotropy one must in Eq. (1) include the term

$$E_{\mathrm{an}} = -KV\cos^2\beta, \tag{4}$$

where $\beta$ is the angle between $\vec{\mu}$ and the easy axis unit vector $\vec{e}$, $K$ is the second-order anisotropy constant, and $V$ the volume of the particles (we have only considered the second-order term of a uniaxial anisotropy). Using Boltzmann statistics the expectation value for the magnetization of a particle with a given orientation of the easy axis is found as

$$\frac{\langle M_z(\vec{e})\rangle_{\mathrm{T}}}{M_0} = \frac{\int_0^{2\pi}\mathrm{d}\varphi\int_0^{\pi}\cos\alpha\mathrm{e}^{-E(\alpha,\beta,\varphi)/k_BT}\sin\beta\,\mathrm{d}\beta}{\int_0^{2\pi}\mathrm{d}\varphi\int_0^{\pi}\mathrm{e}^{-E(\alpha,\beta,\varphi)/k_BT}\sin\beta\,\mathrm{d}\beta}, \tag{5}$$

where the various angles are defined in Fig. 1. Using that $\cos\alpha = \sin\lambda\sin\beta\sin\varphi + \cos\lambda\cos\beta$, one obtains after performing the integration over $\varphi$

$$\frac{\langle M_z(\lambda)\rangle_{\mathrm{T}}}{M_0} = T(\lambda)/N(\lambda), \tag{6}$$

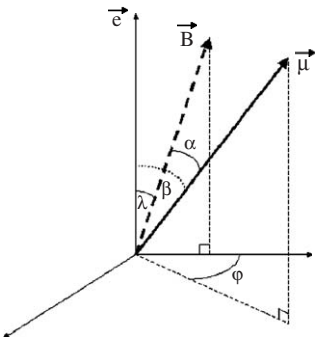


Fig. 1. Coordinate system used in the calculations showing the angles $\alpha$, $\beta$, $\lambda$, and $\varphi$.

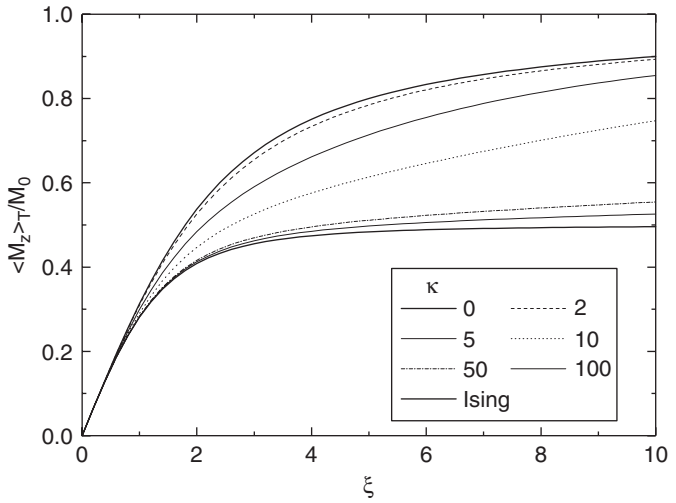


Fig. 2. Relative magnetization as a function of $\xi$ ($= \mu B/k_B T$), for various values of the anisotropy parameter, $\kappa$ ($= KV/k_B T$).

where

$$T(\lambda) = \int_0^{\pi} [\cos\lambda\cos\beta\,\bar{I}_0(\xi\sin\beta\sin\lambda) + \sin\lambda\sin\beta\,\bar{I}_1(\xi\sin\beta\sin\lambda)] \times e^{\xi\cos(\lambda-\beta)+\kappa\cos^2\beta}\sin\beta\,d\beta \quad (7)$$

and

$$N(\lambda) = \int_0^{\pi} \bar{I}_0(\xi\sin\beta\sin\lambda)e^{\xi\cos(\lambda-\beta)+\kappa\cos^2\beta}\sin\beta\,d\beta, \quad (8)$$

with $\kappa = KV/k_B T$, and $\bar{I}_n(x) = e^{-|x|}I_n(x)$, where $I_n(x)$ is the modified Bessel function of order $n$. (Because of a printing error in Ref. [10], Eqs. (7) and (8) are not identical to Eqs. (8) and (9) in Ref. [10]. The correct expressions are also given in Ref. [13]. The numerical calculations in Ref. [10] were made using the correct expressions.)

When considering a random distribution of anisotropy axes one finally obtains

$$\langle M_z\rangle_T = \frac{1}{2}\int_0^{\pi}\langle M_z(\lambda)\rangle_T\sin\lambda\,d\lambda, \quad (9)$$

which is the expression used in our calculations. Magnetization curves as a function of $\xi$ are shown for various values of $\kappa$ in Fig. 2, together with the classical Langevin curve ($\kappa = 0$) and the extreme Ising case.

## 3. Simulations

### 3.1. Procedure

Based on the model discussed above, we have used Eq. (9) to calculate a number of theoretical $\langle M_z\rangle_T/M_0$ vs. $B$ magnetization curves at different temperatures. For simplicity, we have here neglected the moment distribution. We subsequently fitted the theoretical curves with the antiferromagnetically modified Langevin model, Eq. (3). As a result we have obtained values of the parameters $\mu, n$ and $\chi_{AF}$. These fitted parameters have in the following been denoted $\mu_{fit}, n_{fit}$ and $\chi_{fit}$ in order to distinguish them from those used for generating the theoretical curves. The parameters for the theoretical curves were chosen to be comparable to those of ferritin [5,15,16], hence $\mu =$ 50, 100, 200 and 250 $\mu_B$ (assumed independent of temperature), and for the anisotropy ($KV/k_B$) we used an estimated value of 220 K (based on Mössbauer investigations on ferritin [17]). $\chi_{AF}$ was not included in the theoretical magnetization curves in order to focus on the uncompensated moment. The temperature range was chosen to be 20–300 K, and each curve was calculated to a maximum field of 5.0 T in order to simulate typical experimental conditions.

### 3.2. Results

Some of the calculated magnetization curves along with the fits are shown in Fig. 3. At the lowest temperature

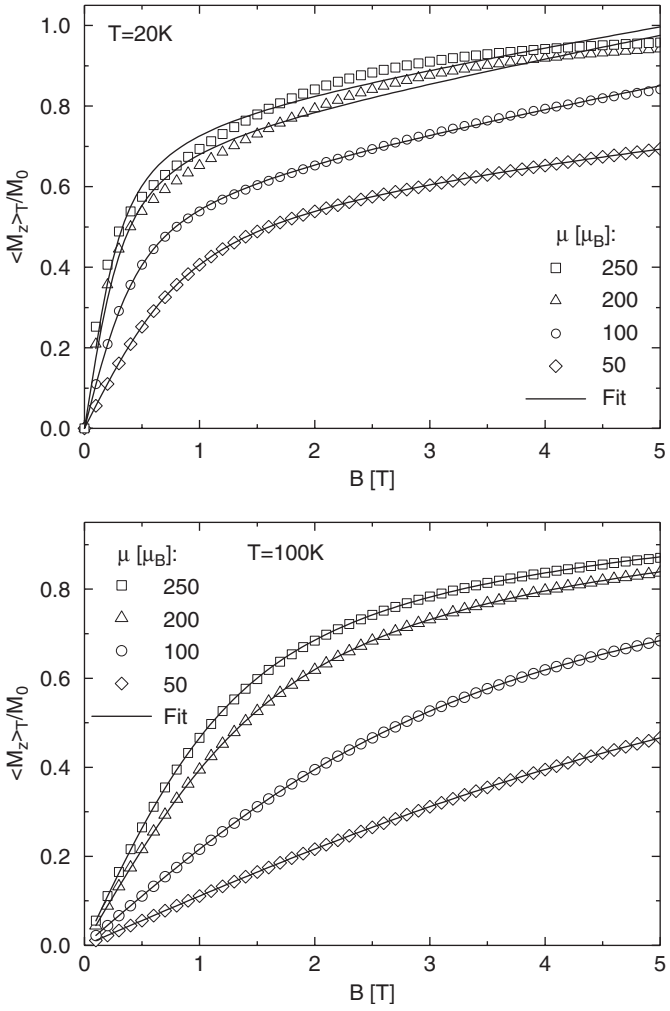


Fig. 3. Calculated magnetization curves (open symbols, using Eq. (9)), and the fits to Eq. (3) (lines) for $T = 20$ K (top) and $T = 100$ K (bottom), for different values of $\mu$ (in units of $\mu_B$).

(20 K), a discrepancy between the simulated data and the fits to the antiferromagnetically modified Langevin function is clearly visible for the curves with $\mu = 200$ and $250\,\mu_B$. However, the discrepancy is not obvious for smaller moments and at higher temperatures.

Fig. 4 shows the apparent moment $\mu_{fit}$ as a function of temperature. For the smallest moments, the apparent moment is found to decrease with increasing temperature. However, this behavior depends on the size of the moment. For $\mu = 250\,\mu_B$, $\mu_{fit}$ is found to increase with increasing temperature, but it should be noted that in this case, the low-temperature data were derived from fits, which clearly deviate from the calculated magnetization curves (Fig. 3).

The apparent number of particles per unit volume, $n_{fit}$, is found to increase with temperature as shown in Fig. 5.

For $\chi_{fit}$, for which the temperature dependence is shown in Fig. 6, we observe that despite the fact that the antiferromagnetic susceptibility term is not included in the model, an apparent susceptibility appears, that decreases with temperature. In order to compare the value obtained here to that of ferritin, one must multiply our result with the estimated saturation magnetization for ferritin. We find in this case that the apparent susceptibility is of the same order of magnitude as that reported by Silva et al. [8].

### 3.3. Discussion

Our simulations show, in accordance with previous work [10–13], that the anisotropy changes the shape of the magnetization curve. However, as demonstrated by the above examples, especially for small magnetic moments, the magnetization curve still resembles a Langevin curve *plus* a term linear in the applied field, i.e. the antiferromagnetically modified Langevin function. As a result, the goodness-of-fit obtained when using this model is often quite reasonable considering the statistical errors that real experimental data are most often subject to. However, as we have also demonstrated, the parameters estimated when fitting to this model (especially $\mu_{fit}$ and $\chi_{fit}$) are both inaccurate and show an apparent temperature dependence. As pointed out by Silva et al. [8], a similar effect is observed if one neglects the distribution of moments. In the analysis of the influence of anisotropy we find, however, that the estimated values do approach their real values as the temperature is increased. Hence, the error introduced by ignoring the anisotropy is largest in the low-temperature region. It should also be noted that the temperature, at which the apparent values approach the real ones, is strongly dependent on the size of the magnetic moment.

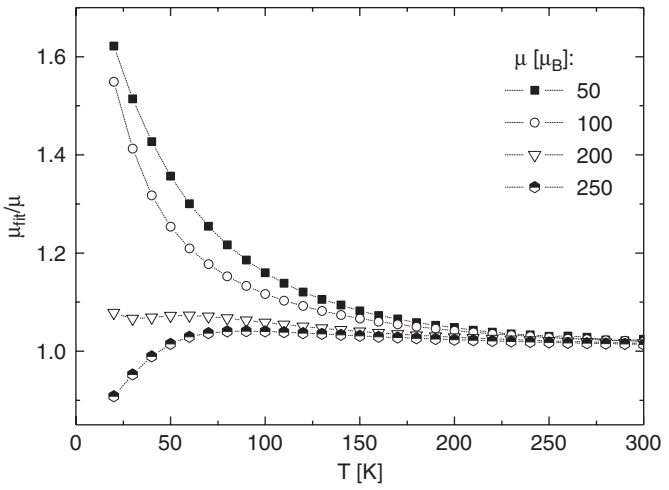


Fig. 4. Values of the apparent moment, $\mu_{fit}$, relative to $\mu$ obtained by fitting calculated magnetization curves (using Eq. (9)) with the sum of a Langevin function and a linear term, for different values of $\mu$ (in units of $\mu_B$).

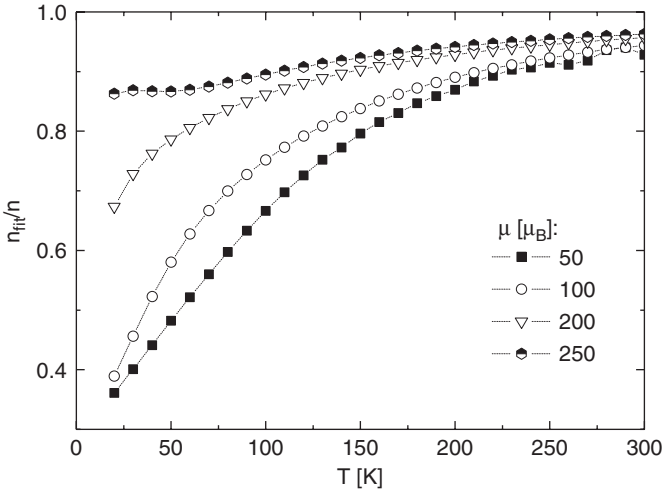


Fig. 5. Values of the apparent density of particles, $n_{fit}$, relative to $n$ obtained by fitting calculated magnetization curves (using Eq. (9)) with the sum of a Langevin function and a linear term, for different values of $\mu$ (in units of $\mu_B$).

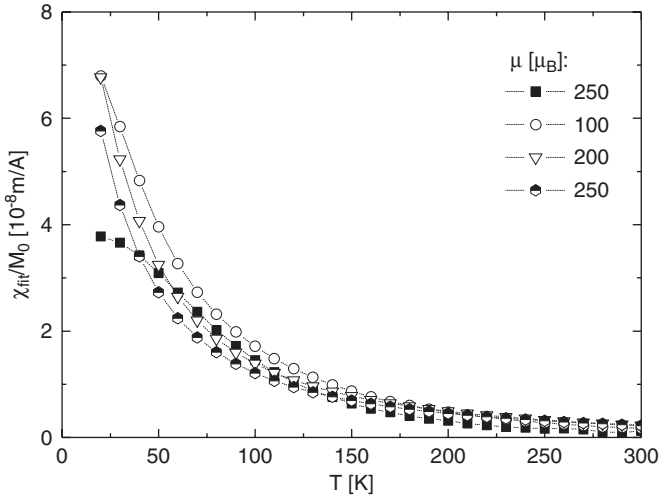


Fig. 6. Values of the apparent antiferromagnetic susceptibility $\chi_{fit}$ relative to $M_0$, obtained by fitting calculated magnetization curves (using Eq. (9)) with the sum of a Langevin function and a linear term, for different values of $\mu$ (in units of $\mu_B$).

Silva et al. [8] suggested to use a scaling-law method to analyze the temperature dependence of $\mu$ and $\chi_{AF}$. This approach is based on the assumption that if $\langle\mu\rangle$ is independent of temperature, the superparamagnetic part of the magnetization curve scales with $B/T$. However, when anisotropy is considered this is no longer the case, and this approach should therefore be used with care.

In order to obtain more realistic estimates of the various parameters, one should, in principle, apply a model that includes the effect of a distribution of moments as well as anisotropy energies. However, such a model is, from a practical point of view, difficult to use due to the considerable number of computations involved, and, furthermore, it may not be possible to distinguish between features due to anisotropy and features due to a moment distribution.

## 4. Initial susceptibility

A way to avoid problems associated with anisotropy and a distribution of moments is to base the analysis on the initial susceptibility. It can be shown [12,18] that in a sample where the easy axes are distributed at random, the initial susceptibility is independent of the anisotropy. Using the low-field expansion of the Langevin function, $\mathscr{L}(\xi) \approx \xi/3$, one finds in the case of a distribution of moments, that

$$\begin{aligned} M &= \int_0^\infty n\mu p(\mu)\,\frac{\mu B}{3k_BT}\,\mathrm{d}\mu \\ &= \frac{nB}{3k_BT}\int_0^\infty \mu^2 p(\mu)\,\mathrm{d}\mu \\ &= \frac{nB}{3k_BT}\,\langle\mu^2\rangle, \end{aligned} \tag{10}$$

where $p(\mu)\,\mathrm{d}\mu$ is the fraction of particles with a moment between $\mu$ and $\mu+\mathrm{d}\mu$. Thus for the initial susceptibility, defined as $\chi_0 = M/H = \mu_0(M/B)$, (for $H$ or $B \to 0$) one obtains that

$$\chi_0 = \frac{n\langle\mu^2\rangle\mu_0}{3k_BT} \tag{11}$$

*independent of anisotropy and the specific distribution function considered*. By using the initial susceptibility it is therefore possible to avoid the problems associated with the analysis of the full magnetization curve. Assuming that $n$ is constant, this can be used to analyze the possible temperature dependence of $\mu$. However, one problem remains: the antiferromagnetic susceptibility will also contribute to the full initial susceptibility, thus for an antiferromagnet the above expression should read

$$\chi_0 = \frac{n\langle\mu^2\rangle\mu_0}{3k_BT} + \chi_{AF}. \tag{12}$$

In order to use the initial susceptibility for analyzing the temperature behavior of the magnetic moment, one must therefore be assured that the contribution from $\chi_{AF}$ is negligible. Under the assumption that the antiferromagnetic susceptibility in nanoparticles is of the same order of magnitude as in bulk samples, this will most often be the case. It should, however, also be noted that inter-particle interactions can have a significant influence on magnetization data [19,20], and that the above derivations are only valid for non-interacting particles.

## 5. Summary

We have shown that the shape of the magnetization curve for superparamagnetic nanoparticles of antiferromagnetic materials can be significantly influenced by magnetic anisotropy. Often such data can be successfully fitted to a model in which the magnetization is described by the sum of a Langevin function and a linear term. We point out that such a fit will give erroneous values for the magnetic moment and the antiferromagnetic susceptibility. We suggest that the information on the magnetic moment per particle should be derived from the initial susceptibility, which in a sample of randomly oriented particles is independent of the anisotropy and the form of a distribution of magnetic moments.

## Acknowledgements

The work was supported by the Danish Technical Research Council.

## References

[1] L. Néel, C.R. Hebd. Seances Acad. Sci. 252 (1961) 4075.
[2] S. Mørup, C. Frandsen, Phys. Rev. Lett. 92 (2004) 217201.
[3] S. Mørup, B.R. Hansen, Phys. Rev. B 72 (2005) 24418.
[4] M.S. Seehra, V.S. Babu, A. Manivannan, J.W. Lynn, Phys. Rev. B 61 (2000) 3513.
[5] J.G.E. Harris, J.E. Grimaldi, D.D. Awschalom, A. Chiolero, D. Loss, Phys. Rev. B 60 (1999) 3453.
[6] S.H. Kilcoyne, R. Cywinski, J. Magn. Magn. Mater. 140–144 (1995) 1466.
[7] N.J.O. Silva, L.D. Carlos, V.S. Amaral, Phys. Rev. Lett. 94 (2005) 039707.
[8] N.J.O. Silva, V.S. Amaral, L. Carlos, Phys. Rev. B 71 (2005) 184408.
[9] S. Mørup, C. Frandsen, Phys. Rev. Lett. 94 (2005) 039708.
[10] M. Hanson, C. Johansson, S. Mørup, J. Phys.: Condens. Matter 5 (1993) 725.
[11] H.D. Williams, K. O'Grady, M. El Hilo, R.W. Chantrell, J. Magn. Magn. Mater. 122 (1993) 129.
[12] J.L. García-Palacios, Adv. Chem. Phys. 112 (2000).
[13] M. Respaud, J. Appl. Phys. 86 (1999) 556.
[14] C. Gilles, P. Bonville, K.K.W. Wong, S. Mann, Eur. Phys. J. B 17 (2000) 417.
[15] S. Makhlouf, F.T. Parker, A.E. Berkowitz, Phys. Rev. B 55 (1997) R14717.
[16] C. Gilles, P. Bonville, H. Rakoto, J.M. Broto, K.K.W. Wong, S. Mann, J. Magn. Magn. Mater. 241 (2002) 430.
[17] D.P.E. Dickson, N.M.K. Reid, C. Hunt, H.D. Williams, M. El-Hilo, K. O'Grady, J. Magn. Magn. Mater. 125 (1993) 345.
[18] H. Kachkachi, M. Azeggagh, Eur. Phys. J. B 44 (2005) 299.
[19] M. Holmes, K. O'Grady, R.W. Chantrell, A. Bradbury, IEEE Trans. Magn. 24 (1988) 1659.
[20] C.R.H. Bahl, T. Pedersen, K.H. Nielsen, S. Saadi, S. Mørup, M.F. Hansen, B. Lebech, (2005) (to be published).

# Paper III

IOP PUBLISHING JOURNAL OF PHYSICS: CONDENSED MATTER

J. Phys.: Condens. Matter **20** (2008) 345209 (6pp) doi:10.1088/0953-8984/20/34/345209

# The correlation between superparamagnetic blocking temperatures and peak temperatures obtained from ac magnetization measurements

**Daniel Esmarch Madsen**[1], **Mikkel Fougt Hansen**[2] **and Steen Mørup**[1]

[1] Department of Physics, Technical University of Denmark, DTU Physics, Building 307, DK-2800 Kongens Lyngby, Denmark
[2] Department of Micro- and Nanotechnology, Technical University of Denmark, DTU Nanotech, Building 345 East, DK-2800 Kongens Lyngby, Denmark

E-mail: demadsen@fysik.dtu.dk

Received 25 March 2008, in final form 16 July 2008
Published 1 August 2008
Online at stacks.iop.org/JPhysCM/20/345209

**Abstract**

We study the correlation between the superparamagnetic blocking temperature $T_B$ and the peak positions $T_p$ observed in ac magnetization measurements for nanoparticles of different classes of magnetic materials. In general, $T_p = \alpha + \beta T_B$. The parameters $\alpha$ and $\beta$ are different for the in-phase ($\chi'$) and out-of-phase ($\chi''$) components and depend on the width $\sigma_V$ of the log-normal volume distribution and the class of magnetic material (ferromagnetic/antiferromagnetic). Consequently, knowledge of both $\alpha$ and $\beta$ is required if the anisotropy energy barrier $KV$ and the attempt time $\tau_0$ are to be reliably obtained from an analysis based solely on the peak positions.

## 1. Introduction

Magnetic nanoparticles have been a topic of intense research due to their many novel properties [1–6]. However, when studying these new phenomena, attention should be paid to the fact that the traditional ways of analysing and interpreting experimental data may no longer be adequate when dealing with effects induced as a consequence of the finite size. This is particularly important in studies of antiferromagnetic nanoparticles [6]. For example, due to the small magnetic moment in antiferromagnetic nanoparticles, the Zeeman energy is often comparable to the anisotropy energy, which consequently must be considered when analysing, e.g., magnetization data [7]. Moreover, since most samples are not monodisperse, it is important to consider the consequences of the size distribution. Silva *et al* [8] recently discussed the effect of a magnetic moment distribution on the interpretation of magnetization data for antiferromagnetic nanoparticles. Another important aspect is the different size dependence of the magnetic moment for ferromagnetic and antiferromagnetic nanoparticles. In antiferromagnetic nanoparticles at low magnetic fields, the magnetization is due to the presence of an uncompensated moment, which is assumed to have a median size given by

$$\mu_u = \mu_{at} n_u \approx \mu_{at} N^p, \tag{1}$$

where $n_u$ is the number of uncompensated magnetic atoms, $N$ is the total number of magnetic atoms, $\mu_{at}$ the magnetic moment per atom, and $p$ is a parameter ranging from $1/3$ to $2/3$ [9–11], which depends on how the uncompensated spins are distributed in the particle. If the nanoparticles have random occupancy of all lattice sites, $p \simeq 1/2$. If the interior of the particles is assumed defect-free, but there is a random occupancy of surface sites, the number of uncompensated spins should be proportional to the square root of the number of surface sites, i.e. $p \simeq 1/3$. In the case of cubic particles consisting of either an even or an odd number of planes with parallel spins, but with alternating magnetization directions, $p \simeq 2/3$. In poorly crystalline antiferromagnetic particles such as ferritin and ferrihydrite it has been found that $p \simeq 1/2$

 

whereas $p \simeq 1/3$ has been obtained in some samples of NiO nanoparticles [6]. In a ferromagnet, $p = 1$.

In this work we study the relationship between the peak temperature $T_p$ obtained from ac magnetization measurements and the superparamagnetic blocking temperature $T_B$ for several values of $p$ (1/3, 1/2, 2/3, and 1). Although the peak position of the in-phase component ($\chi'$) of the ac susceptibility has previously been discussed for some of the above cases [12], to our knowledge this is the first time that the relationship between $T_B$ and the peak positions of both the in-phase ($\chi'$) and out-of-phase ($\chi''$) component is systematically studied.

## 2. Theory

Superparamagnetic relaxation takes place when the thermal energy $k_B T$ becomes sufficiently large in relation to the anisotropy energy barrier separating the easy directions of magnetization. In that case it becomes possible for the magnetization to surmount this barrier. It is often assumed that the magnetic anisotropy is uniaxial with an anisotropy energy given by

$$E_a = KV \sin^2 \theta, \tag{2}$$

where $K$ is the anisotropy constant, $V$ is the volume of the particle, and $\theta$ is the angle between the magnetization direction and the easy axis of magnetization. Equation (2) represents two energy minima separated by an energy barrier of height $KV$. For non-interacting particles the average time between magnetization reversals is usually assumed to be given by the Arrhenius-like Néel–Brown expression [13, 14]

$$\tau = \tau_0 \exp\left(\frac{KV}{k_B T}\right), \tag{3}$$

where $\tau_0 \sim 10^{-9}$–$10^{-13}$ s and depends only weakly on temperature. Experimental data are usually obtained as the result of measuring a signal on a timescale $\tau_m$, characteristic of the experimental method. If $\tau \ll \tau_m$, the observed magnetization will be the thermal equilibrium value. On the other hand, if $\tau \gg \tau_m$, the observed magnetization will appear static. The temperature at which $\tau_m = \tau$ is denoted the blocking temperature $T_B$. Since for a single particle

$$KV = -\ln\left(\frac{\tau_0}{\tau_m}\right) k_B T_B, \tag{4}$$

$T_B$ is directly related to the size of the energy barrier. In the presence of a distribution of volumes, the blocking temperature refers to a suitable parameter of this distribution, either the median volume $V_m$ or the average volume $\langle V \rangle$. In this work, we relate the blocking temperature to the median volume $V_m$ of a volume-weighted volume distribution (i.e., particles with $V < V_m$ constitute half the total volume). Note, that in the case of ac susceptibility, $\tau_m$ is related to the angular frequency $\omega = 2\pi f$ of the applied field rather than its frequency $f$, that is, $\tau_m = 1/\omega$ [15, 16].

From an experimental point of view, one is often interested in determining the blocking temperature in order to obtain knowledge about the anisotropy energy barrier and $\tau_0$ of a given sample. In magnetization measurements (dc in zero-field-cooled (ZFC) data, or ac in $\chi'$ and $\chi''$ data) a peak in the signal is observed at a temperature $T_p$, which is often interpreted as the blocking temperature. However, as a number of authors (e.g., [12, 17, 18]) have discussed, the observed peak temperature does not necessarily correspond to the blocking temperature if a distribution of volumes is present. In general, the relationship between the two may be expressed through a parameter $\beta$, such that $T_p = \beta T_B$. Gittleman *et al* [12] examined the peak positions of the in-phase component of the ac susceptibility ($\chi'$) and found $\beta$ for a number of simple volume distributions. Jiang and Mørup [17] considered ZFC data using a log-normal distribution of volumes and examined the dependence of $\beta$ on the width $\sigma_V$ of the distribution for $p = 1$ and 1/3. They also found that the value of $\beta$ is different for ferromagnetic and antiferromagnetic systems.

## 3. Simulation procedure

In the following, we derive the expressions used to calculate $\chi'$ and $\chi''$. Consider a sample subjected to a time-varying magnetic field

$$h(t) = h_0 \cos(\omega t). \tag{5}$$

The resulting magnetization of the sample is

$$M(t) = \chi_{ac}(\omega, T) h(t), \tag{6}$$

where the susceptibility can be written as

$$\chi_{ac}(\omega, T) = \chi'(\omega, T) + i\chi''(\omega, T). \tag{7}$$

$\chi'$ and $\chi''$ are the in-phase and out-of-phase components, respectively. These may be found using the model by Gittleman *et al* [12] where the susceptibility in the time domain is expressed as

$$\chi_{ac}(t, T) = \chi_0 + (\chi_\infty - \chi_0)(1 - e^{-t/\tau}). \tag{8}$$

Here, $\chi_0$ and $\chi_\infty$ are the susceptibility of the blocked and unblocked (superparamagnetic) particles, respectively. A Fourier transformation of equation (8) yields

$$\chi_{ac}(\omega, T) = \frac{\chi_\infty + i\omega\tau\chi_0}{1 + i\omega\tau}, \tag{9}$$

and insertion of the following expressions for $\chi_0$ and $\chi_\infty$ [12]

$$\chi_0 = \frac{\mu_0 M^2(V)}{3K} \tag{10}$$

$$\chi_\infty = \frac{\mu_0 M^2(V) V}{3k_B T} \tag{11}$$

gives

$$\chi_{ac}(\omega, T) = \frac{\mu_0 M^2(V)}{1 + i\omega\tau}\left[\frac{V}{3k_B T} + \frac{i\omega\tau}{3K}\right], \tag{12}$$

which leads to

$$\chi'(\omega, T) = \frac{\mu_0 M^2(V)}{3K}\left(\frac{KV}{k_B T}\frac{1}{1 + (\omega\tau)^2} + \frac{(\omega\tau)^2}{1 + (\omega\tau)^2}\right) \tag{13}$$

$$\chi''(\omega, T) = \frac{\mu_0 M^2(V)}{3K}\left(\frac{\omega\tau}{1+(\omega\tau)^2} - \frac{KV}{k_B T}\frac{\omega\tau}{1+(\omega\tau)^2}\right). \tag{14}$$

Note, that $\tau$ also depends on the temperature as given by (3). In the above expressions we have written the magnetization as $M(V)$ to emphasize the volume dependence. It should be noticed that because of the randomness of the occupation of the lattice sites, particles with identical volumes can have different magnetic moments. As shown in the appendix, this can be taken into account by replacing $M^2(V)$ by the second order moment of the distribution of magnetization, $\mu_u/V$, for particles with volume $V$. Using equation (1), one finds

$$M(V) = \frac{\mu_u}{V} = \mu_{at} c^p V^{p-1}. \tag{15}$$

This is different from ferromagnetic particles where the magnetization is independent of volume. The constant $c$ appearing in this expression is found using that the volume and the number of atoms are related as $N = [zN_A\rho/M_{mol}]V \equiv cV$. Here, $\rho$ is the density of the material, $M_{mol}$ is the molar mass, $z$ is the number of magnetic atoms per formula unit, and $N_A$ is Avogadro's number.

We now proceed by considering a sample with a distribution of volumes. Defining $y = V/V_m$, we get

$$\frac{M(V)}{M_m} = \frac{cV^{p-1}}{cV_m^{p-1}} = y^{p-1}, \tag{16}$$

where $M_m$ is the magnetization of a particle with median volume $V_m$. We now write the expressions for $\chi'$ and $\chi''$ as

$$\chi'(\omega, T) = \frac{\mu_0 M_m^2}{3K}\int_0^\infty \left(\frac{KV_m}{k_B T}\frac{y}{1+(\omega\tau)^2} + \frac{(\omega\tau)^2}{1+(\omega\tau)^2}\right) y^{2p-2} p_V(y)\,dy \tag{17}$$

$$\chi''(\omega, T) = \frac{\mu_0 M_m^2}{3K}\int_0^\infty \left(\frac{\omega\tau}{1+(\omega\tau)^2} - \frac{KV_m}{k_B T}\frac{y\omega\tau}{1+(\omega\tau)^2}\right) y^{2p-2} p_V(y)\,dy, \tag{18}$$

where $p_V(y)\,dy$ is the volume-weighted volume distribution (i.e., the volume fraction of the sample with volume between $V$ and $V + dV$ is $p_V(V/V_m)\,d(V/V_m)$). For the simulations we use the log-normal distribution

$$p_V(y, \sigma_V)\,dy = \frac{1}{\sqrt{2\pi}\sigma_V y}\exp\left(-\frac{\ln^2 y}{2\sigma_V^2}\right)dy, \tag{19}$$

which is commonly encountered in the literature. In the following simulations, $V_m$ enters as a parameter. However, we report for convenience the particle sizes in terms of the diameter $d_m$ of a spherical particle having volume $V_m$.

## 4. Results and analysis

The ac susceptibility at different frequencies $f$ as a function of temperature was calculated for $K = 5 \times 10^4$ J m$^{-3}$ and

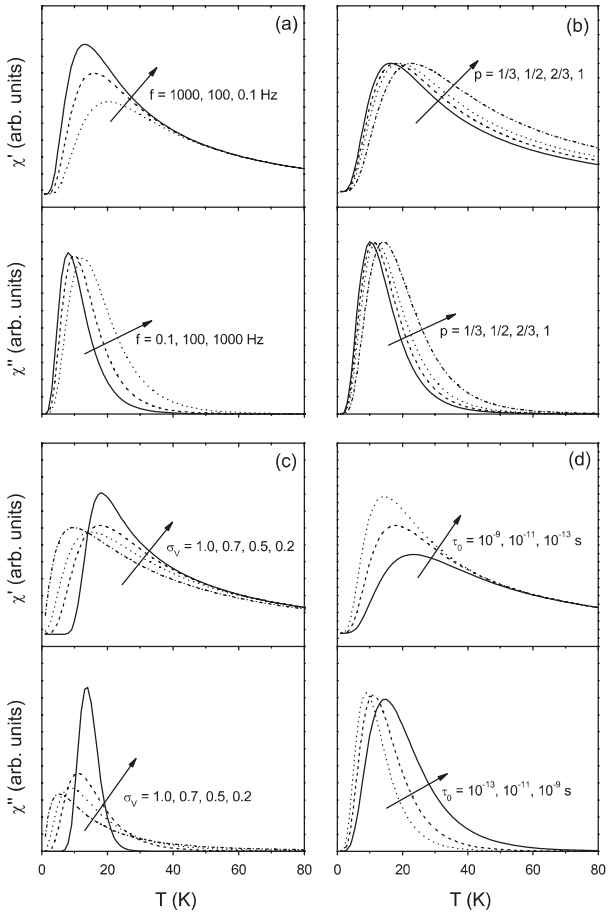


**Figure 1.** $\chi'$ and $\chi''$ as a function of temperature for various values of (a) $f$, (b) $p$, (c) $\sigma_V$ and (d) $\tau_0$. Parameters that were not varied were fixed to $f = 100$ Hz, $\sigma_V = 0.5$, $p = 1/2$, $\tau_0 = 10^{-11}$ s, and $d_m = 5.2$ nm. The curves in (b) were normalized by the peak temperature value.

different values of $p$, $\sigma_V$, $\tau_0$ and $d_m$. For the calculations (with $\chi'$ and $\chi''$ in arbitrary units) the parameters $c$ and $\mu_{at}$, can be randomly chosen as they only affect the total scaling through $M_m$, but not the positions of the peaks. Figure 1 shows examples of the resulting data for selected combinations of $p$, $\sigma_V$, $f$, and $\tau_0$.

For each of these datasets the peak positions, designated $T_p'$ and $T_p''$, for the in-phase and out-of-phase components, respectively, were determined and compared to the value of $T_B$ calculated from equation (4). For each set of the parameters $p$, $\sigma_V$, and $\tau_0$ we obtained a range of ($T_p$, $T_B$) values by varying $f$. Figure 2 shows selected results.

From figure 2 one may notice that $T_p'$ and $T_p''$, respectively, are approximately linearly related to $T_B$. This was the case for all combinations of the parameters. Consequently, we have fitted the observed peak temperatures to the expressions

$$T_p' = \alpha' + \beta' T_B \tag{20}$$

$$T_p'' = \alpha'' + \beta'' T_B \tag{21}$$

in order to obtain the parameters $\alpha$ and $\beta$. Figures 3 and 4 show the results. In all cases excellent fits were obtained. However,

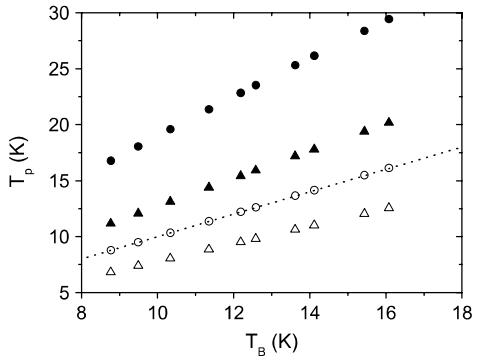


**Figure 2.** The peak positions $T_p'$ (full symbols) and $T_p''$ (open symbols) as a function of $T_B$ for selected datasets (triangles: $p = 1/2, \sigma_V = 0.5$, circles: $p = 1, \sigma_V = 1.0$). $\tau_0 = 10^{-11}$ s and $d_m = 5.2$ nm were used in the simulations. The dotted line corresponds to $T_p = T_B$.

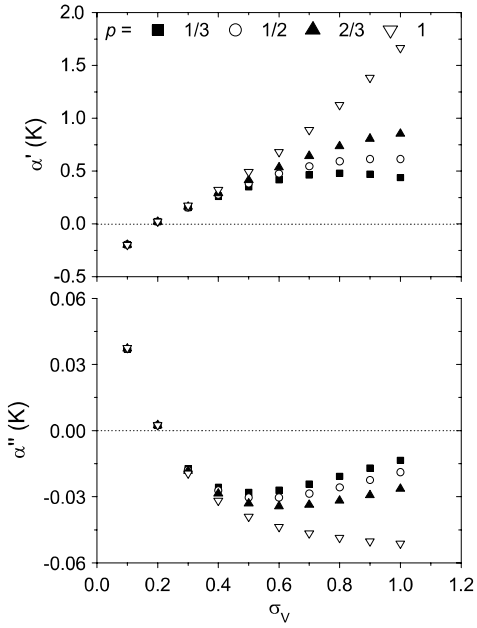


**Figure 3.** $\alpha'$ and $\alpha''$ as a function of $\sigma_V$. The values $\tau_0 = 10^{-11}$ s and $d_m = 5.2$ nm were used in the calculations.

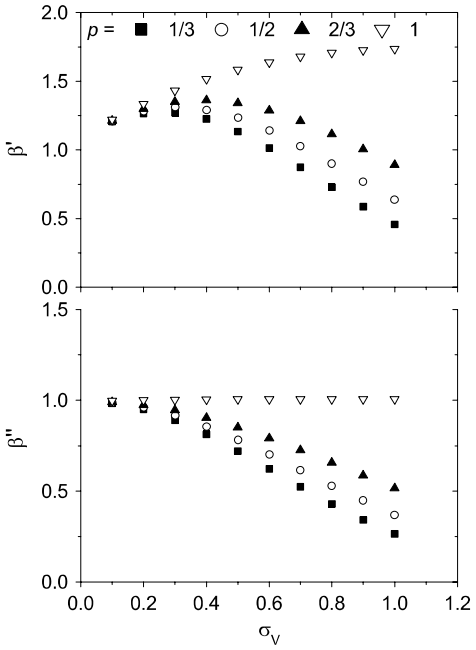


**Figure 4.** $\beta'$ and $\beta''$ as a function of $\sigma_V$. The values $\tau_0 = 10^{-11}$ s and $d_m = 5.2$ nm were used in the calculations.

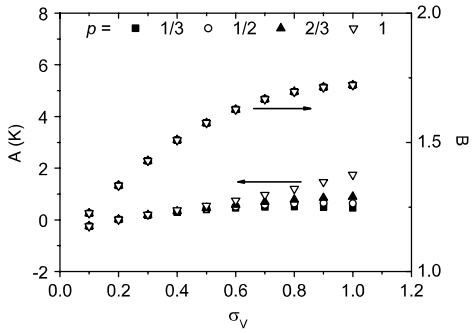


**Figure 5.** The parameters $A$ and $B$ as a function of $\sigma_V$. The values $\tau_0 = 10^{-11}$ s and $d_m = 5.2$ nm were used in the calculations.

it was necessary to have $\alpha \neq 0$. We obtained similar results for other values of $\tau_0$ and $d_m$.

It can be seen from figure 3 that $\alpha'$ increases with increasing $\sigma_V$ and that $\alpha'$ varies considerably with $p$. For $\sigma_V > 0.8$ and $p = 1/3$, $\alpha'$ is found to decrease slightly. Although $\alpha''$ exhibits some dependence on $p$, its magnitude remains almost negligible compared to the peak temperatures.

From figure 4 it is seen that $\beta'$ increases with increasing $\sigma_V$ in the entire range only for $p = 1$, whereas for $p < 1$, $\beta'$ first increases slightly and then decreases for $\sigma_V > 0.3$. This is in agreement with the calculations by Jiang and Mørup [17]. $\beta''$ remains close to 1 for $p = 1$, whereas for $p < 1$, it decreases with increasing $\sigma_V$.

It is interesting to consider the dependence of $T_p'$ on $T_p''$, which we write as $T_p' = A + BT_p''$. According to (20) and (21), $A = \alpha' - (\beta'/\beta'')\alpha''$ and $B = \beta'/\beta''$. Figure 5 shows the values of A and B calculated from the parameters shown in figures 3 and 4. It is remarkable that the values of $B$ all fall on the same line for all $p$ values. The values of $A$, however, show some variation. Figure 6 shows $B$ for other values of $\tau_0$ and $d_m$. As one may notice, slightly different curves are found for other values of $\tau_0$. However, no differences were observed if $d_m$ was changed. $A$ (not shown) showed some dependence on all parameters.

## 5. Discussion

The values of $\tau_0$ and $KV_m$ can be determined from an analysis of $\ln(\omega)$ versus $1/T_B$. As equation (3) can be rewritten

$$\ln(\omega) = \ln(1/\tau_0) - \frac{KV_m}{k_B}\frac{1}{T_B}, \tag{22}$$

this should give a straight line with slope $-KV_m/k_B$ and intersect $\ln(1/\tau_0)$ at $1/T_B = 0$. If, as it is common, $T_p$ is

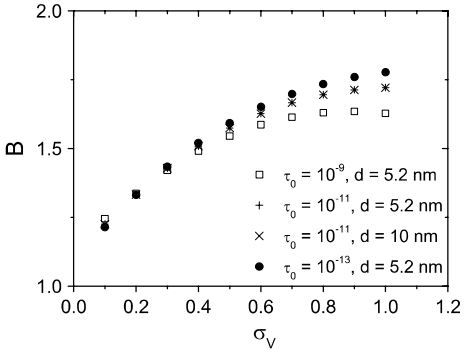


**Figure 6.** The parameter $B$ for $p = 1/2$ and various values of $\tau_0$ and $d_m$.

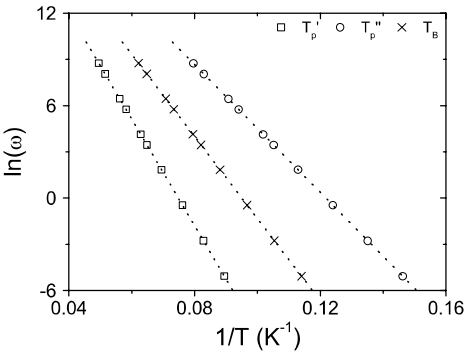


**Figure 7.** $\ln(\omega)$ as a function of $1/T_p$, with $T_p$ obtained from simulated $\chi'$ (□) and $\chi''$ (○) data (with $p = 1/2$, $\sigma_V = 0.5$, and $\tau_0 = 10^{-11}$ s), respectively. We also show the fits to equation (22) (lines), and, for comparison, $\ln(\omega)$ as a function of $1/T_B$ (×).

taken as $T_B$, erroneous values of $\tau_0$ and $KV_m$ will be obtained. Figure 7 illustrates this problem. We plot $\ln(\omega)$ as a function of $1/T_p$ for a selected dataset, in this case with $p = 1/2$, $\sigma_V = 0.5$, and $\tau_0 = 10^{-11}$ s. The corresponding plot with the real values of $1/T_B$ is shown for comparison. The difference is quite distinct. Table 1 lists the values of $KV_m$ and $\tau_0$ obtained from linear regression. The values obtained for $p = 1$ and $\tau_0 = 10^{-9}$ s are also shown. A considerable discrepancy is observed for both $KV_m$ and $\tau_0$. The value of $\tau_0$ determined from the $\chi''$ peaks, however, is quite close to the correct value.

To estimate in a more general sense the deviation resulting from this incorrect use of $T_p$, we use the replacement $T_B = (1/\beta)(T_p - \alpha)$ and obtain

$$\ln(\omega) = \ln(1/\tau_0) - \frac{KV_m}{k_B}\frac{\beta}{T_p - \alpha}. \tag{23}$$

While this is not a linear function in $1/T_p$, it closely resembles one when $T_p$ falls within the range of values typically encountered. The slope and intersect, however, are different from $KV_m/k_B$ and $\ln(1/\tau_0)$ as may be shown by a first order Taylor expansion of equation (23) around a point $1/T_0$, suitably chosen in the middle of the range of $1/T_p$ for the dataset. This gives

$$\ln(\omega) \approx \ln(1/\tau_0) + \frac{KV_m}{k_B}\frac{\alpha\beta}{(T_0-\alpha)^2} - \frac{KV_m}{k_B}\frac{T_0^2\beta}{(T_0-\alpha)^2}\frac{1}{T_p} \tag{24}$$

from which we obtain

$$\ln(\tau_0)_{\text{apparent}} = \ln(\tau_0) - \frac{KV_m}{k_B}\frac{\alpha\beta}{(T_0-\alpha)^2}, \tag{25}$$

and the slope

$$\left(\frac{KV_m}{k_B}\right)_{\text{apparent}} = \frac{KV_m}{k_B}\frac{T_0^2\beta}{(T_0-\alpha)^2}. \tag{26}$$

This demonstrates why different values of $KV_m/k_B$ and $\tau_0$ are found when $T_B$ is replaced by $T_p$ in equation (22). Note the consequences of having $\alpha \neq 0$. If $\alpha = 0$, the intersect would be unaffected and the slope would simply be modified by the factor $\beta$, making the analysis much simpler. As shown here, simply using $T_p$ as $T_B$ will lead to erroneous values of $KV_m$ and $\tau_0$. This is also the case if it is assumed that $T_p = \beta T_B$. Thus, the finite value of $\alpha$ generally cannot be ignored.

From (25) we see that the sign of $\alpha$ determines whether the value of $\tau_0$ is over- or underestimated. From figure 3 we see that for $\sigma_V > 0.2$, $\alpha' > 0$, hence $\tau_0$ will in most cases be underestimated. A detailed analysis (not shown here) has revealed that the relative error in the determination of $\tau_0$ depends mainly on $\sigma_V$, whereas it is independent of $p$ and depends only weakly on $\tau_0$. This is also demonstrated by the values listed in table 1. As the present analysis has shown, however, the magnitude of $\alpha''$ is typically small compared to the peak values. Consequently, the error in the determination of $\tau_0$ will be minimal when peaks of the out-of-phase susceptibility data are used, whereas using the in-phase data will give considerable errors. It is important, however, to keep in mind that this only holds when $T_B$ is defined in terms of the median volume. Had we used instead the average volume, different results would have been obtained, since for a log-normal distribution it is well known that $\langle V\rangle/V_m = \exp(\sigma_V^2/2)$. Consequently, the blocking temperature defined in terms of $\langle V\rangle$ would be larger, giving different values of $\alpha'$, $\beta'$, $\alpha''$, $\beta''$.

The advantage of using equation (22) to determine $\tau_0$ and $KV_m$ is that one avoids having to do a full-curve fit

**Table 1.** Apparent values of $KV_m/k_B$ and $\tau_0$ (for $\sigma_V = 0.5$) obtained when $T_p$ is taken as $T_B$ in (22). The correct value of $KV_m/k_B$ is 267 K.

| $\tau_0$ (s) | $10^{-11}$ | $10^{-11}$ | $10^{-9}$ | $10^{-9}$ |
|---|---|---|---|---|
| $p$ | 1/2 | 1 | 1/2 | 1 |
| | | $(KV_m)_{\text{apparent}}/k_B$ (K) | | |
| From $\chi'$ | 346 | 444 | 346 | 445 |
| From $\chi''$ | 207 | 266 | 207 | 266 |
| | | $(\tau_0)_{\text{apparent}}$ (s) | | |
| From $\chi'$ | $5.8 \times 10^{-12}$ | $5.8 \times 10^{-12}$ | $5.6 \times 10^{-10}$ | $5.6 \times 10^{-10}$ |
| From $\chi''$ | $1.1 \times 10^{-11}$ | $1.1 \times 10^{-11}$ | $1.1 \times 10^{-9}$ | $1.1 \times 10^{-9}$ |

to expressions like (17) and (18). The analysis presented here, however, shows that, without knowledge of $\alpha$ and $\beta$, this approach may yield systematic errors in the estimates of $KV_m$ and $\tau_0$. It should be noted, though, that for $p = 1$, $\alpha'' \approx 0$ and $\beta'' \approx 1$ and is almost independent of $\sigma_V$. Thus, for ferromagnetic particles the error in $\tau_0$ and $KV_m$ will be negligible if the $\chi''$ data are used for the analysis. In the case of antiferromagnetic particles, the $\chi''$ data will give almost correct values for $\tau_0$, but not for $KV_m$. If the $\chi'$ data are used in the analysis, the values of $\tau_0$ and $KV_m$ will be incorrect both for ferromagnetic and antiferromagnetic particles. Better estimates of $KV_m$ may, in principle, be obtained by using (25) and (26) and the appropriate values of $\alpha$ and $\beta$, which may be obtained if the values of $\tau_0$, $p$ and $\sigma_V$ are approximately known. However, if the data are not compromised by, e.g., impurity signals, a full-curve analysis may prove rather simple and will yield more accurate values of not only $KV_m$ and $\tau_0$, but also $\sigma_V$ and $p$ [19]. If the quality of the data does not permit such an analysis, it should be kept in mind, though, that the most accurate results are obtained from the $\chi''$ peak positions.

## 6. Summary

We have studied the correlation between superparamagnetic blocking temperatures and peak temperatures obtained from ac magnetization measurements. We obtain different results for ferromagnetic materials and antiferromagnetic materials due to the different relation between volume and magnetic moment. If the anisotropy energy barrier $KV_m$ and the attempt time $\tau_0$ are determined directly from the peak positions, these relationships must be taken into consideration. Otherwise, only rough estimates of $KV_m$ and $\tau_0$ may be obtained. Through the analysis presented here we have quantified the error resulting from the uncritical use of the peak positions, and have found that the magnitude of this error depends on the parameters $p$, $\tau_0$, $\sigma_V$. For ferromagnetic particles, though, using the peak positions of $\chi''$ will give rather accurate results. For $p < 1$ the value of $\tau_0$, but not $KV_m$, may be determined with good accuracy from $\chi''$ peak positions. Furthermore, if one compares peaks temperatures obtained from $\chi'$ data with those obtained from $\chi''$, a relationship is found which is independent of the type of (magnetic) material. This may be utilized to determine the width of the particle size distribution.

## Acknowledgments

This work was supported by the Danish Research Council for Technology and Production Sciences.

## Appendix

In the expressions for $\chi'$ and $\chi''$ (12)–(14) it is usually assumed that there is a relationship between the particle volume and the magnetic moment. However, if the magnetic moments are due to randomness of the occupation of lattice sites as in antiferromagnetic nanoparticles, this is not the case. Particles with a given volume, $V$, can have different moments, described by a distribution function, $\rho_V(\mu_u)$. The contribution to the ac susceptibility from the particles with volume $V$ is then given by

$$\chi_{ac}(\omega, T) = \int_0^\infty \frac{\chi_\infty + i\omega\tau\chi_0}{1 + i\omega\tau}\rho_V(\mu_u)\,d\mu_u. \tag{A.1}$$

Because $M(V) = \mu_u/V$ we find by inserting (10) and (11) in equation (A.1)

$$\chi_{ac}(\omega, T) = \frac{\mu_0}{1 + i\omega\tau}\left[\frac{V}{3k_BT} + \frac{i\omega\tau}{3K}\right] \times \frac{1}{V^2}\int_0^\infty \mu_u^2\rho_V(\mu_u)\,d\mu_u. \tag{A.2}$$

Thus one obtains the correct expressions for $\chi_{ac}(\omega, T)$ by substituting $M^2(V)$ by the second order moment of the magnetization distribution

$$M^2(V) = V^{-2}\int_0^\infty \mu_u^2\rho_V(\mu_u)\,d\mu_u \tag{A.3}$$

in (12)–(14).

## References

[1] Leslie-Pelecky D L and Rieke R D 1996 *Chem. Mater.* **8** 1770
[2] Dormann J L, Fiorani D and Tronc E 1997 *Adv. Chem. Phys.* **98** 283
[3] Kodama R H 1999 *J. Magn. Magn. Mater.* **200** 359
[4] Batlle X and Labarta A 2002 *J. Phys. D: Appl. Phys.* **35** R15
[5] Fiorani D (ed) 2005 *Surface Effects in Magnetic Nanoparticles* (New York: Springer)
[6] Mørup S, Madsen D E, Frandsen C, Bahl C R H and Hansen M F 2007 *J. Phys.: Condens. Matter* **19** 213202
[7] Madsen D E, Mørup S and Hansen M F 2006 *J. Magn. Magn. Mater.* **305** 95
[8] Silva N J O, Amaral V S and Carlos L D 2005 *Phys. Rev.* B **71** 184408
[9] Néel L 1961 *C.R. Hebd. Seances Acad. Sci.* **252** 4075
[10] Néel L 1962 *Low-Temperature Physics* ed C DeWitt *et al* (New York: Gordon and Breach)
[11] Richardson J T, Yiagas D I, Turk B, Forster K and Twigg M V 1991 *J. Appl. Phys.* **70** 6977
[12] Gittleman J I, Abeles B and Bozowski S 1974 *Phys. Rev.* B **9** 3891
[13] Néel L 1949 *Ann. Geophys.* **5** 99
[14] Brown W F 1963 *Phys. Rev.* **1** 1677
[15] Lundgren L, Svedlindh P and Beckman O 1981 *J. Magn. Magn. Mater.* **25** 33
[16] Lundgren L, Svedlindh P and Beckman O 1982 *Phys. Rev.* B **26** 3990
[17] Jiang J Z and Mørup S 1997 *Nanostruct. Mater.* **9** 375
[18] Hansen M F and Mørup S 1999 *J. Magn. Magn. Mater.* **203** 214
[19] Madsen D E, Hansen M F, Bendix J and Mørup S 2008 *Nanotechnology* **19** 315712

# Paper IV

Nanotechnology **19** (2008) 315712 (7pp) doi:10.1088/0957-4484/19/31/315712

# On the analysis of magnetization and Mössbauer data for ferritin

**D E Madsen[1], M F Hansen[2], J Bendix[3] and S Mørup[1]**

[1] Department of Physics, Technical University of Denmark, DTU Physics, Building 307, DK-2800 Kongens Lyngby, Denmark
[2] Department of Micro- and Nanotechnology, Technical University of Denmark, DTU Nanotech, Building 345 East, DK-2800 Kongens Lyngby, Denmark
[3] Department of Chemistry, University of Copenhagen, Universitetsparken 5, DK-2100 København Ø, Denmark

E-mail: demadsen@fysik.dtu.dk

Received 21 April 2008, in final form 29 May 2008
Published 24 June 2008
Online at stacks.iop.org/Nano/19/315712

**Abstract**
Experimental data for antiferromagnetic nanoparticles are often analyzed as if the particles were ferromagnetic. However, due to the volume dependence of the magnetization resulting from uncompensated spins, such analysis will yield erroneous results. This is demonstrated as we analyze ac and dc magnetization data as well as Mössbauer spectra obtained for ferritin. The values of the median energy barrier obtained from the different data are in very close agreement when a distribution of volumes and a volume dependence of the magnetization are taken into account. However, when the volume dependence of the magnetization is neglected, erroneous values of the anisotropy energy barrier and the attempt time $\tau_0$ are obtained.

## 1. Introduction

Antiferromagnetic nanoparticles have recently received considerable attention due to a number of properties specific to this class of material [1]. For example, it has been suggested that antiferromagnetic nanoparticles may exhibit macroscopic quantum tunneling under experimental conditions that are more easily realized than for ferromagnets or ferrimagnets [2].

Due to the perfect cancelation of the sublattice magnetic moments, *bulk* antiferromagnets are not expected to carry an externally detectable moment of any significance. Nanoparticles of antiferromagnetic materials, however, do. As a consequence of the finite size, the cancelation of the sublattice moments may no longer be perfect; the result is an uncompensated moment, which has an average size

$$\mu_{\mathrm{u}} = \mu_{\mathrm{at}} n_{\mathrm{u}} \approx \mu_{\mathrm{at}} N^{p}, \tag{1}$$

where $n_{\mathrm{u}}$ is the average number of uncompensated atoms, $N$ is the total number of magnetic atoms, $\mu_{\mathrm{at}}$ the magnetic moment per atom, and the value of $p$ depends on the spatial distribution of uncompensated spins within the particle [3–5]. Since the volume and the number of atoms are related as $N = [zN_{\mathrm{A}}\rho/M_{\mathrm{mol}}]V \equiv cV$, where $\rho$ is the density of the material, $M_{\mathrm{mol}}$ is the molar mass, $z$ is the number of magnetic atoms per formula unit, and $N_{\mathrm{A}}$ is Avogadro's number, one finds that the magnetization $M$ is given by

$$M = \mu_{\mathrm{at}} c^{p} V^{p-1}. \tag{2}$$

Unlike the ferromagnetic case ($p = 1$) the magnetization due to the uncompensated moment depends on the volume of the particle for $p < 1$. Uncompensated moments are typically on the order of a few hundred Bohr magnetons ($\mu_{\mathrm{B}}$), which should be compared to the thousands of $\mu_{\mathrm{B}}$ expected for ferromagnetic or ferrimagnetic nanoparticles.

The magnetic anisotropy of a small particle of volume $V$ is often assumed to be uniaxial and the anisotropy energy is usually written

$$E_{\mathrm{K}} = KV \sin^{2}\theta, \tag{3}$$

where $K$ is the anisotropy constant, typically on the order of $10^{3}$–$10^{5}$ J m$^{-3}$, and $\theta$ is the angle between the sublattice magnetization and the easy axis. Usually, the possible size and temperature dependence of $K$ is neglected. When the thermal energy $k_{\mathrm{B}}T$ of the particle increases relative to the barrier $KV$ separating the easy directions at $\theta = 0$ and $\pi$, the probability of a magnetization reversal increases. The average time $\tau$ between such successive reversals is approximately

 

given by [6, 7]

$$\tau = \tau_0 \exp\left(\frac{KV}{k_B T}\right), \tag{4}$$

where $\tau_0 \sim 10^{-13}$–$10^{-9}$ s. In an experiment where one measures the magnetization on a timescale $\tau_m$, the magnetization will appear static when $\tau \gg \tau_m$. On the other hand, if $\tau \ll \tau_m$ the thermal equilibrium value will be observed and the particle is said to exhibit superparamagnetic behavior. The temperature at which $\tau = \tau_m$ is termed the blocking temperature $T_B$.

The above considerations apply to a homogeneous sample containing identical particles. However, most samples contain a distribution of volumes, and in this case one refers to suitable parameters of the distribution, typically the median volume $V_m$ and the median blocking temperature $T_{Bm}$, i.e.,

$$k_B T_{Bm} = \ln\left(\frac{\tau_0}{\tau_m}\right) K V_m, \tag{5}$$

where we assume that $K$ is independent of volume and temperature.

The parameters $KV_m$ and $\tau_0$ for a specific sample may be obtained from a number of different techniques. However, when analyzing and interpreting the experimental data, the somewhat special nature of antiferromagnetic nanoparticles must be taken into account. For example, when studying samples that contain a distribution of different volumes by magnetization measurements [8] or neutron scattering [9], the volume dependence of the magnetization due to the uncompensated moment must also be considered. However, this is often ignored and data are interpreted using models for ferromagnets.

In this work, we examine and analyze data for ferritin from ac and dc magnetization measurements and Mössbauer spectroscopy. We demonstrate a consistent way of analyzing the data that correctly takes a distribution of volumes of antiferromagnetic particles into account.

Ferritin is an iron storage protein in many living organisms, including mammals [10, 11]. It has an iron-containing core surrounded by a protein shell. The size of the core is variable, but it may be up to 7 nm in diameter and contain up to approximately 4000 Fe atoms. The core is antiferromagnetic [12, 13], with a Néel temperature that has not been uniquely determined (values ranging from 240 K [14] to ∼500 K [15] have been reported). The iron in the core is in a form similar to that of ferrihydrite [10]. As the protein shell limits interactions between the cores, ferritin represents an ideal system of non-interacting magnetic nanoparticles. Since the core is not well crystallized, it is often assumed that the lattice sites are randomly occupied such that one should expect $p \simeq 1/2$ in the expression for the uncompensated moment. Experimental results [16–18] are in agreement with this prediction. The relatively large uncompensated moment in ferritin is considerably larger than the estimated value of the thermoinduced moment [19, 20], which is therefore not considered in this study.

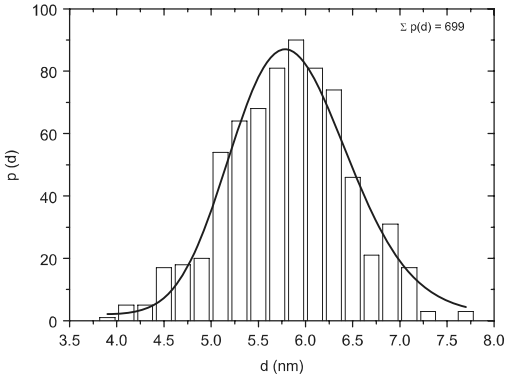


**Figure 1.** Size histogram based on sizes estimated from TEM. The line is a fit to a log-normal distribution.

## 2. Experimental details

Samples of horse-spleen ferritin were obtained from Sigma-Aldrich (Prod. No. 96701-1G-F, Steinheim, Germany) and were freeze-dried prior to the measurements. Ac and dc magnetization measurements were performed with a Quantum Design MPMS XL 5 using a SQUID detector. The zero field cooled (ZFC) magnetization measurement was performed with increasing temperature from 2 to 100 K in an applied field of 1.59 kA m$^{-1}$ after the sample had been cooled from approximately 100 K in zero field. This field was small enough to ensure a linear response of the measured magnetic moment. The sample was subsequently cooled with the field still applied, and the field cooled (FC) magnetization measurement was also performed with increasing temperature. Ac measurements were performed at frequencies $f$ ranging from 0.1 to 1000 Hz with an ac field amplitude of $h_0 = 302$ A m$^{-1}$. The mass of the entire sample was 48.5 mg, and an Fe content of 15.9 (±0.5) wt% was found by atomic absorption spectroscopy. A mass density of Fe in ferritin of $\rho_{Fe} = 2302$ kg m$^{-3}$ was used in order to obtain the volume susceptibility from the observed moments. This density was obtained using the molar mass of $M_{mol} = 0.9606$ kg mol$^{-1}$ and density $\rho = 3960$ kg m$^{-3}$ for ferrihydrite [21]. Transmission electron microscopy (TEM) images were obtained on an FEI Tecnai T20 (tungsten filament) operated at 200 kV equipped with a CCD camera. The ferritin sample was sonicated in ethanol and dispersed onto a standard carbon-film-covered TEM grid. Mössbauer spectra were obtained in the transmission geometry operating in constant acceleration mode using as a source $^{57}$Co in Rh. Room-temperature calibration was performed with a 12.5 $\mu$m thick $\alpha$-Fe foil. Temperatures above 80 K were obtained with a liquid nitrogen cryostat. A closed-cycle helium refrigerator was used for temperatures between 20 and 80 K.

## 3. Results and analysis

### *3.1. TEM*

Particle sizes were determined directly from the TEM images. Figure 1 shows the resulting size histogram. The size

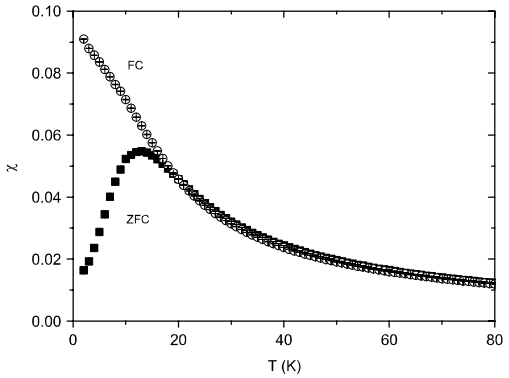


**Figure 2.** Zero field cooled (ZFC) and field cooled (FC) volume susceptibility data (dimensionless in SI units) for ferritin.

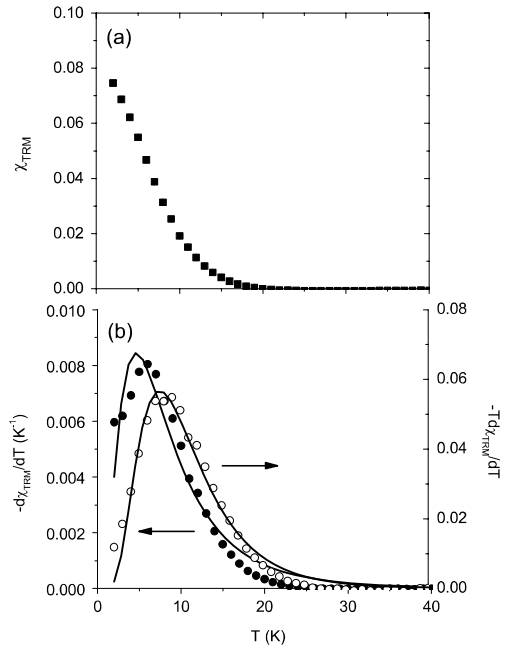


**Figure 3.** (a) $\chi_{\mathrm{TRM}}(=\chi_{\mathrm{FC}}-\chi_{\mathrm{ZFC}})$ as a function of temperature. (b) $-\mathrm{d}\chi_{\mathrm{TRM}}/\mathrm{d}T$ and $-T\,\mathrm{d}\chi_{\mathrm{TRM}}/\mathrm{d}T$ as a function of temperature. The lines show the fits described in the text.

histogram containing 699 particles was fitted to a log-normal distribution of diameters

$$p(d, d_{\mathrm{m}}, \sigma_{\mathrm{d}})\,\mathrm{d}d = \frac{1}{\sqrt{2\pi}\sigma_{\mathrm{d}}d}\exp\left(-\frac{(\ln d - \ln d_{\mathrm{m}})^2}{2\sigma_{\mathrm{d}}^2}\right)\mathrm{d}d, \tag{6}$$

yielding the following parameters: $d_{\mathrm{m}} = 5.85 \pm 0.03$ nm and $\sigma_{\mathrm{d}} = 0.107 \pm 0.008$. From these parameters we obtain for a number-weighted distribution of volumes $V_{\mathrm{m}}^{N} = 1.05 \times 10^{-25}$ m$^3$ and $\sigma_{\mathrm{V}} = 0.321$, and for a volume-weighted distribution of volumes $V_{\mathrm{m}}^{V} = 1.16 \times 10^{-25}$ m$^3$ and $\sigma_{\mathrm{V}} = 0.321$.

### *3.2. Dc magnetization data*

Figure 2 shows the results of the ZFC/FC measurements. Figure 3 shows the thermoremanent (TRM) susceptibility

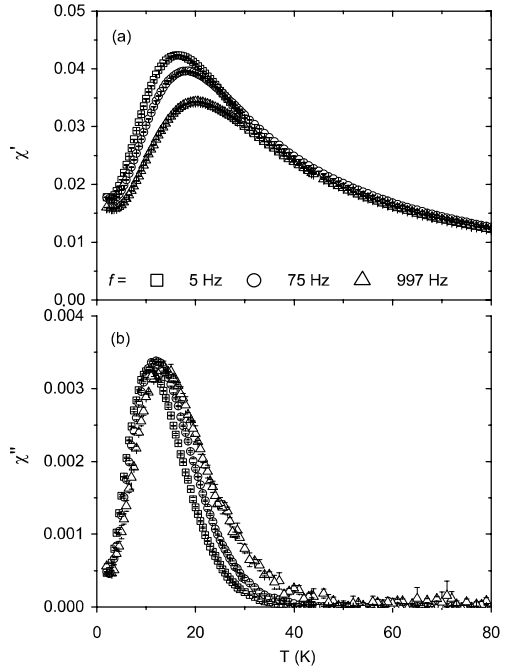


**Figure 4.** (a) In-phase ($\chi'$) susceptibility data and (b) out-of-phase ($\chi''$) susceptibility data for ferritin.

$\chi_{\mathrm{TRM}}$, defined as the difference between the FC and ZFC data [22]. Using the expressions for $\chi_{\mathrm{ZFC}}$ and $\chi_{\mathrm{FC}}$ as given by Hansen and Mørup [23] with the magnetization given by (1), one finds

$$\chi_{\mathrm{TRM}}(T) = \frac{\mu_{\mathrm{at}}^2\mu_0 c^{2p}V_{\mathrm{m}}^{2p-2}}{3K}[\ln(\tau_{\mathrm{m}}/\tau_0) - 1] \times \int_{T_{\mathrm{B}}/T_{\mathrm{Bm}}}^{\infty} y^{2p-2}p_{\mathrm{T}}(y)\,\mathrm{d}y, \tag{7}$$

where the volume dependence of the magnetization has been taken into consideration and $p_{\mathrm{T}}(y)\,\mathrm{d}y$ is a volume-weighted distribution of blocking temperatures with $y = T_{\mathrm{B}}/T_{\mathrm{Bm}}$.

An often used way to analyze dc data is by considering the temperature derivative of the TRM data [24], which from (7) we find as

$$\frac{\mathrm{d}\chi_{\mathrm{TRM}}(T)}{\mathrm{d}T} \propto -T^{2p-2}p_{\mathrm{T}}(T). \tag{8}$$

In the ferromagnetic case ($p = 1$) we see that the derivative yields, directly, the blocking temperature distribution. Figure 3(b) shows the resulting distributions (not normalized) derived using $p = 1/2$ and 1 together with fits to log-normal distributions. The case of $p = 1/2$ could be well fitted with a log-normal distribution, giving the parameters $T_{\mathrm{Bm}} = 9.8 \pm 0.1$ K and $\sigma = 0.51 \pm 0.01$, whereas the ferromagnetic case ($p = 1$) gave $T_{\mathrm{Bm}} = 7.4 \pm 0.2$ K and $\sigma = 0.68 \pm 0.02$ with a much worse quality of the fit.

### *3.3. Ac magnetization data*

Figure 4 shows the in-phase ($\chi'$) and out-of-phase ($\chi''$) components of the ac susceptibility for selected frequencies.

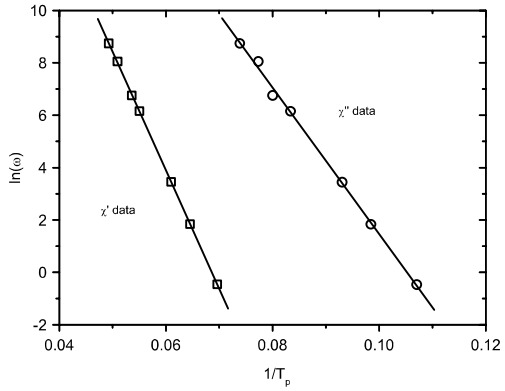


**Figure 5.** Plot of $\ln(\omega)$ versus $1/T_\mathrm{p}$ for $T_\mathrm{p}$ obtained from $\chi'$ and $\chi''$ data. The lines are the results of the linear regression.

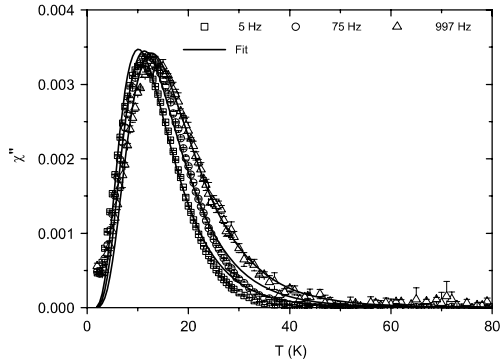


**Figure 6.** $\chi''$ for selected frequencies along with the fit using a single log-normal distribution.

*3.3.1. Peak positions.* A simple and often used way to determine $KV_\mathrm{m}$ and $\tau_0$ is to consider only the positions of the peaks in either the $\chi'$ or the $\chi''$ data. Since $\tau_\mathrm{m} = \tau$ at the blocking temperature, (4) may be rewritten as

$$\ln(\omega) = \ln(1/\tau_0) - \frac{KV_\mathrm{m}}{k_\mathrm{B}}\frac{1}{T_\mathrm{Bm}}. \tag{9}$$

Note that $\tau_\mathrm{m}$ should be compared to the angular frequency $\omega = 2\pi f$ and not the frequency $f$; hence $\tau_\mathrm{m} = 1/\omega$ [25, 26]. Assuming that the observed peak positions $T_\mathrm{p}$ equal $T_\mathrm{Bm}$, estimates of $\tau_0$ and $KV_\mathrm{m}$ may be obtained by plotting $\ln\omega$ versus the reciprocal value of the peak temperatures. Simulations have shown [8], however, that this assumption can lead to erroneous values of $KV_\mathrm{m}$ and $\tau_0$. This will be demonstrated in the following.

Figure 5 shows the result for the peak positions of both $\chi'$ and $\chi''$. We determined the peak positions by fitting the data points close to the maximum using a third-order polynomial. From linear regression we obtained from $\chi'$ (with $r^2 = 0.9999$), $KV_\mathrm{m}/k_\mathrm{B} = 454 \pm 2$ K, $\tau_0 = (3.1 \pm 0.3) \times 10^{-14}$ s, and from $\chi''$ (with $r^2 = 0.9977$), $KV_\mathrm{m}/k_\mathrm{B} = 279 \pm 6$ K, $\tau_0 = (2 \pm 1) \times 10^{-13}$ s. The discrepancy is significant and demonstrates that for antiferromagnetic nanoparticles it is not feasible to estimate $KV_\mathrm{m}$ and $\tau_0$ from the peak positions alone. A reliable estimation requires an analysis of the entire curve.

*3.3.2. Full-curve analysis.* Using the model by Gittleman *et al* [27] one finds for a distribution of particles [8]

$$\chi'(\omega, T) = \frac{\mu_0 M_\mathrm{m}^2}{3K}\int_0^\infty \left(\frac{KV_\mathrm{m}}{k_\mathrm{B}T}\frac{y}{1+(\omega\tau)^2} + \frac{(\omega\tau)^2}{1+(\omega\tau)^2}\right) y^{2p-2} p_\mathrm{V}(y)\,\mathrm{d}y \tag{10}$$

$$\chi''(\omega, T) = \frac{\mu_0 M_\mathrm{m}^2}{3K}\int_0^\infty \left(\frac{\omega\tau}{1+(\omega\tau)^2} - \frac{KV_\mathrm{m}}{k_\mathrm{B}T}\frac{y\omega\tau}{1+(\omega\tau)^2}\right) y^{2p-2} p_\mathrm{V}(y)\,\mathrm{d}y, \tag{11}$$

where $y = V/V_\mathrm{m}$, $p_\mathrm{V}(y)\,\mathrm{d}y$ is the volume-weighted volume distribution (i.e. the relative volume fraction of the sample with volume between $V$ and $V + \mathrm{d}V$ is $p_\mathrm{V}(V/V_\mathrm{m})\,\mathrm{d}(V/V_\mathrm{m})$), and $M_\mathrm{m}$ is the magnetization of a particle having volume $V_\mathrm{m}$ calculated using (2). Note that $\tau$ is also dependent on the temperature, as given by (4).

We have chosen to focus on $\chi''$ as it is insensitive to paramagnetic impurities (since these would be in thermal equilibrium and hence would only show up in the $\chi'$ data). Figure 6 shows the fit using $V_\mathrm{m}$ found from TEM, $c = 2.48 \times 10^{28}$ m$^{-3}$ [21] (as we assumed that the core material is similar to ferrihydrite), $\mu_\mathrm{at} = 5\,\mu_\mathrm{B}$ and a log-normal distribution of volumes. It is emphasized that $M_\mathrm{m}$ was not a free parameter in the fit but was calculated using (2). The parameters obtained were $KV_\mathrm{m}/k_\mathrm{B} = 341 \pm 2$ K, $p = 0.46 \pm 0.01$, $\sigma_\mathrm{V} = 0.50 \pm 0.01$ and $\tau_0 = (2 \pm 1) \times 10^{-13}$ s. These values were used to calculate the expected $\chi'$ data. Figure 7(a) shows a comparison between the calculated and measured $\chi'$ data. Figure 7(b) shows the difference between the two. The difference could be the sign of a paramagnetic impurity; however, it does not fit well with a Curie ($T^{-1}$) law. It could also be related to a diverging energy barrier distribution in ferritin at low energies as observed by St Pierre *et al* [28] and Gorham *et al* [29].

We also tried to fit the $\chi''$ data with $p$ fixed to 1.0 while leaving $M_\mathrm{m}$ as a free parameter. This yielded the parameters $KV_\mathrm{m}/k_\mathrm{B} = 262$ K, $\sigma_\mathrm{V} = 0.50$, and $\tau_0 = 1 \times 10^{-13}$ s. The quality of this fit in terms of $\chi^2$ was identical to that where $p$ was a free parameter.

### *3.4. Mössbauer spectroscopy*

Figure 8 shows Mössbauer spectra of the sample at selected temperatures. Each spectrum is a superposition of a sextet and a doublet, where the doublet is attributed to particles exhibiting fast superparamagnetic relaxation.

If we neglect the effects of a finite sample thickness and assume that the recoil-less fraction $f$ is the same in the blocked and unblocked state, the relative area of the sextet component at each temperature represents the volume fraction of particles still being in the blocked state. As the lines of the sextet are asymmetrically broadened, determining the area fraction is not straightforward. A combination of three different approaches was therefore used: each spectrum was fitted with (a) a single sextet and a single doublet, (b) a distribution of sextets and

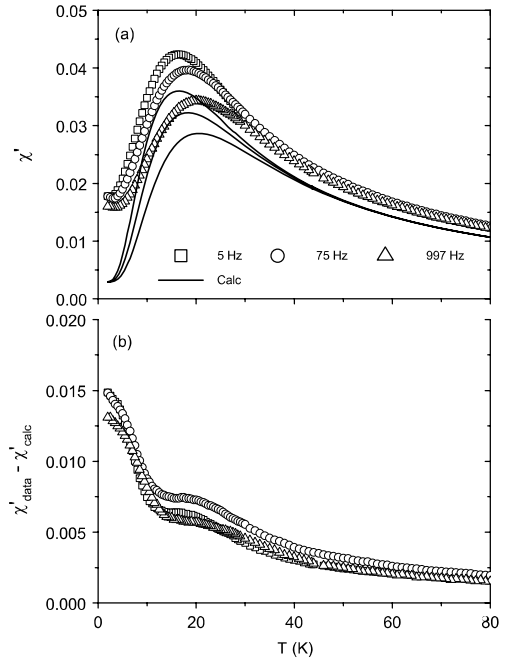


**Figure 7.** (a) $\chi'$ for selected frequencies calculated using the parameters obtained from the fit of the $\chi''$ data. (b) The difference between the calculated and measured $\chi'$ data.

a single doublet, and (c) a distribution of both sextets and doublets. The area fractions obtained differed only little. The area was taken as the average of the three; the differences were used as an estimate of the uncertainty. Figure 9 shows the resulting area ratio as a function of temperature.

The area fraction $A(T)$ of the blocked particles at a given temperature is given as

$$A(T) = A_0 \int_{T_B/T_{Bm}}^{\infty} p_T(y)\,dy, \qquad (12)$$

where $A_0$ is a scale parameter and $p_T(y)\,dy$ is the volume-weighted distribution of blocking temperatures with $y = T/T_{Bm}$. This expression is somewhat similar to (7), except that we do not have to consider the volume dependence of the magnetic moment as this does not enter into the expression. Consequently, the expression should be equally valid for ferromagnetic or ferrimagnetic particles and antiferromagnetic particles.

The area distribution shown in figure 9 was first fitted to (12) with $A_0 = 100\%$, and we obtained $\sigma_V = 0.7$ and $T_{Bm} = 36$ K. This is shown as the 'unscaled' fit in the figure. As one may notice, the fit is not particularly good. We assume when using $A_0 = 100\%$ that at zero temperature $A = 100\%$. To take into consideration that this may not be the case, we have also fitted the data without any restrictions on $A_0$. This gave the much better 'scaled' fit shown in figure 9. For this, we found the parameters $\sigma_V = 0.52 \pm 0.02$, $T_{Bm} = 40.8 \pm 0.5$ K, and $A_0 = 87\%$. This scale parameter corresponds to a doublet with a relative area of 13% at zero temperature. In an earlier Mössbauer study of ferritin it was found that the spectrum at 5 K contained a doublet with a relative area of 7% [28].

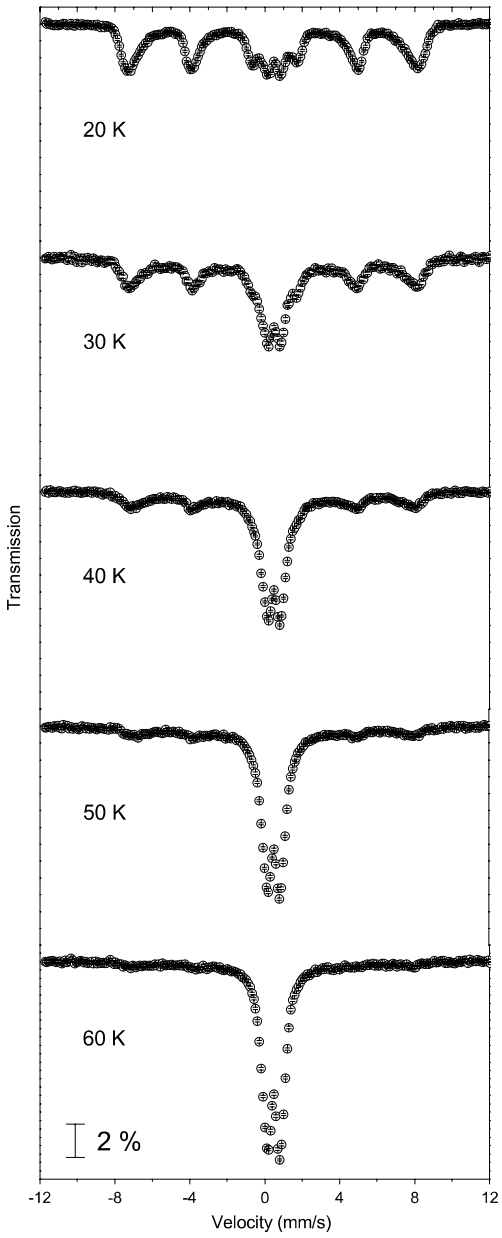


**Figure 8.** Mössbauer spectra of the ferritin sample at selected temperatures. The vertical bar corresponds to a transmission of 2%.

## 4. Discussion

The analysis presented here clearly demonstrates that caution should be exercised when analyzing experimental data for antiferromagnetic nanoparticles. A theoretical study has shown that using simply the peak positions of the ac data for the determination of $KV_m$ and $\tau_0$ is in general not feasible, although $\tau_0$ may be rather accurately determined from the $\chi''$ data [8]. Our present study clearly demonstrates this point, as the same value of $\tau_0$ is found from the $\chi''$ peak data and in the full-curve analysis.

From the ZFC/FC data we obtain directly the distribution of blocking temperatures. However, when considering the

**Table 1.** Parameters obtained with the different methods. [ ] indicates that the parameter was fixed or not part of the fit.

| Method | $KV_m/k_B$ (K) | $\tau_0$ (s) | $\sigma_V$ | $p$ |
|---|---|---|---|---|
| $\chi'$, peak positions | $454 \pm 2$ | $(3.1 \pm 0.3) \times 10^{-14}$ | — | — |
| $\chi''$, peak positions | $279 \pm 6$ | $(2 \pm 1) \times 10^{-13}$ | — | — |
| $\chi''$, full-curve analysis | $341 \pm 2$ | $(2 \pm 1) \times 10^{-13}$ | $0.50 \pm 0.01$ | $0.46 \pm 0.01$ |
| $\chi_{TRM}$ | $332 \pm 3$ | $[2 \times 10^{-13}]$ | $0.51 \pm 0.01$ | [1/2] |
| Mössbauer data | $339 \pm 4$ | $[2 \times 10^{-13}]$ | $0.52 \pm 0.02$ | — |

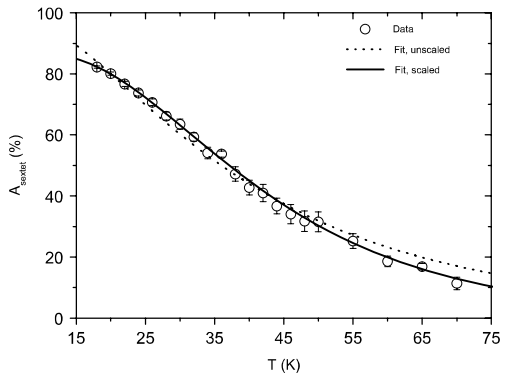


**Figure 9.** Relative area of the sextet component in the Mössbauer spectra as a function of temperature. The lines show the fits described in the text.

distribution obtained with (8) and erroneously using $p = 1$, as shown in figure 3(b), it is clear that the shape of the distribution in the low-temperature region is changed. This should be kept in mind when the distributions obtained are interpreted.

When taking into account a distribution of volumes, good fits of the ac data could be achieved even when the material was just considered to be a ferromagnet (i.e. if $p$ was fixed to 1) *and* if $M_m$ was a free parameter. The value of the median energy barrier, however, differed from that obtained if the material was assumed to be an antiferromagnet with $p = 1/2$. The reason for this is, as shown in the appendix, that if $p(y)$ is a log-normal distribution of volumes, $y^n p(y)$ will also have the shape of a log-normal distribution, although with a different normalization and median value. This demonstrates the danger of disregarding the absolute values of the data and leaving the magnetization or scaling to be a free parameter. Obviously, calculating the magnetization using (1) only is of significance when the absolute value of the susceptibility is considered in appropriate units.

When the volume dependence of the magnetic moment was taken into consideration, consistent values of the various parameters were obtained. It is noteworthy that we find a value of $p$ close to $1/2$ in accordance with previous studies [16–18].

From the analysis of the ac and dc magnetization and Mössbauer spectroscopy measurements almost identical values of $\sigma_V$ were obtained. These values, however, are larger than that obtained from TEM. This could possibly be due to a size dependence of the anisotropy constant. The values of the median energy barriers are not as straightforward to compare, as we obtained from dc magnetization and Mössbauer spectroscopy measurements the median blocking temperature and not the median energy barrier. The median energy barrier may be obtained using (5) with the appropriate value of $\tau_m$. Using that for the dc measurements $\tau_m \approx 100$ s, we find $KV_m/k_B$ as $332 \pm 3$ K (for $p = 1/2$) and $251 \pm 6$ K (with $p = 1$). We see that the result obtained with $p = 1/2$ is in excellent agreement with the value found from the analysis of the ac magnetization data.

For Mössbauer spectroscopy $\tau_m$ is usually assumed to be on the order of $(2-5) \times 10^{-9}$ s, which gives $\ln(\tau_m/\tau_0) \approx 9-10$. This corresponds for the observed blocking temperature to $KV_m/k_B \approx 370-410$ K. Simulations of relaxation Mössbauer spectra, however, have shown that an apparently smaller value of $\tau_m$ may result from a distribution of volumes [8]. For $\tau_0 = 2 \times 10^{-13}$ s, $\sigma_V = 0.5$, and $p = 1/2$, we have found that the superparamagnetic component constitutes half the total area of the Mössbauer spectrum when $KV_m/k_BT \approx 8.3$. This gives an energy barrier of $339 \pm 4$ K, in excellent agreement with the values obtained from the ac and dc magnetization data. Table 1 summarizes the values obtained by the different methods. If we use the value of $KV_m$ obtained from the ac measurements and the value of $V_m$ found from TEM data, we get $K \approx 4.1 \times 10^4$ J m$^{-3}$.

## 5. Summary

We have studied particles of ferritin with ac and dc magnetization measurements, Mössbauer spectroscopy and TEM. The data have been analyzed with different models, some of which take into consideration the antiferromagnetic nature of ferritin. Neglecting the antiferromagnetic nature, in particular the volume dependence of the magnetization, leads to inconsistent and assumedly erroneous results. The antiferromagnetic nature can, in a relatively simply way, be included in the analysis leading to consistent results obtained by the different experimental methods.

## Acknowledgments

The authors would like to thank Jakob Wagner at the Center for Electron Nanoscopy (CEN), DTU, for obtaining the TEM images, and Christian B Koch from the Department of Natural Sciences, Faculty of Life Sciences, University of Copenhagen, for determining the Fe content of our sample. This work was supported by the Danish Research Council for Technology and Production Sciences. We acknowledge funding for the SQUID susceptometer from the Danish Natural Science Research Council (272-06-0128).

## Appendix

If we insert $x_m = \exp(n\sigma^2)x'_m$ in the expression for the log-normal distribution

$$p(x, x_m, \sigma)\,dx = \frac{1}{\sqrt{2\pi}\sigma x}\exp\left(-\frac{(\ln x - \ln x_m)^2}{2\sigma^2}\right)dx, \tag{A.1}$$

where $x_m$ is the median value and $\sigma$ is the width, we obtain

$$p(x, \exp(n\sigma^2)x'_m, \sigma)\,dx = \frac{\exp\left[-n^2\sigma^2/2\right]}{(x'_m)^n}x^n p(x, x'_m, \sigma)\,dx. \tag{A.2}$$

Hence, if $p(x, x_m, \sigma)$ is a log-normal distribution, so $x^n p(x, x_m, \sigma)$ will appear to be, although with a different median value ($x_m e^{n\sigma^2}$) and normalization.

## References


[1] Mørup S, Madsen D E, Frandsen C, Bahl C R H and Hansen M F 2007 *J. Phys.: Condens. Matter* **19** 213202
[2] Barbara B and Chudnovsky E M 1990 *Phys. Lett.* A **145** 205
[3] Néel L 1961 *C.R. Hebd. Seances Acad. Sci.* **252** 4075
[4] Néel L 1962 *Low-Temperature Physics* ed C DeWitt *et al* (New York: Gordon and Breach)
[5] Richardson J T, Yiagas D I, Turk B, Forster K and Twigg M V 1991 *J. Appl. Phys.* **70** 6977
[6] Néel L 1949 *Ann. Geophys.* **5** 99
[7] Brown W F 1963 *Phys. Rev.* **130** 1677
[8] Madsen D E *et al* unpublished
[9] Bahl C R H, Garde J, Lefmann K, Jensen T B S, Lindgård P A, Madsen D E and Mørup S 2008 *Eur. Phys. J.* B **62** 53
[10] Ford G C, Harrison P M, Rice D W, Smith J M A, Treffry A, White J L and Yariv J 1984 *Phil. Trans. R. Soc. Lond.* **304** 551
[11] Theil E C 1987 *Annu. Rev. Biochem.* **56** 289
[12] Blaise A, Chappert J and Girardet J L 1965 *C.R. Hebd. Seances Acad. Sci.* **261** 2310
[13] Schoffa G 1965 *Z. Naturf.* B **20** 167
[14] Bauminger E R and Nowik I 1989 *Hyperfine Interact.* **50** 489
[15] Gilles C, Bonville P, Rakoto H, Broto J M, Wong K K W and Mann S 2002 *J. Magn. Magn. Mater.* **241** 430
[16] Harris J G E, Grimaldi J E, Awschalom D D, Chiolero A and Loss D 1999 *Phys. Rev.* B **60** 3453
[17] Kilcoyne S H and Cywinski R 1995 *J. Magn. Magn. Mater.* **140–144** 1466
[18] Makhlouf S, Parker F T and Berkowitz A E 1997 *Phys. Rev.* B **55** R14717
[19] Mørup S and Frandsen C 2004 *Phys. Rev. Lett.* **92** 217201
[20] Madsen D E and Mørup S 2006 *Phys. Rev.* B **74** 014405
[21] Schwertmann U and Cornell R M 1991 *Iron Oxides in the Laboratory: Preparation and Characterization* (Weinheim: VCH)
[22] Dormann J L, Fiorani D and Tronc E 1997 *Adv. Chem. Phys.* **98** 283
[23] Hansen M F and Mørup S 1999 *J. Magn. Magn. Mater.* **203** 214
[24] Chantrell R W, El-Hilo M and O'Grady K 1991 *IEEE Trans. Magn.* **27** 3570
[25] Lundgren L, Svedlindh P and Beckman O 1981 *J. Magn. Magn. Mater.* **25** 33
[26] Lundgren L, Svedlindh P and Beckman O 1982 *Phys. Rev.* B **26** 3990
[27] Gittleman J I, Abeles B and Bozowski S 1974 *Phys. Rev.* B **9** 3891
[28] St Pierre T G, Gorham N T, Allen P D, Costa-Krämer J L and Rao K V 2001 *Phys. Rev.* B **65** 024436
[29] Gorham N T, St Pierre T G, Chua-Anusorn W and Parkinson G M 2008 *J. Appl. Phys.* **103** 054302

# Paper V

# Neutron study of magnetic excitations in 8-nm $\alpha$-$Fe_2O_3$ nanoparticles

L. Theil Kuhn,* K. Lefmann, C. R. H. Bahl,[†,‡] S. Nyborg Ancona,[§] and P.-A. Lindgård
*Materials Research Department, AFM-228, Risø National Laboratory, DK-4000 Roskilde, Denmark*

C. Frandsen, D. E. Madsen, and S. Mørup
*Department of Physics, Building 307, Technical University of Denmark, DK-2800 Kongens Lyngby, Denmark*
(Received 9 June 2006; revised manuscript received 11 September 2006; published 3 November 2006)

By use of inelastic neutron scattering we have studied magnetic fluctuations in 8-nm particles of antiferromagnetic $\alpha$-$Fe_2O_3$ (hematite) as a function of temperature and applied magnetic fields. The fluctuations are dominated by uniform excitations. Studies have been performed on both coated (noninteracting) and uncoated (interacting) particles. We have estimated the magnetic anisotropy energy and found that the data are in good agreement with the value obtained from Mössbauer spectroscopy. The energy $\varepsilon_0$ of the uniform excitations depends strongly on the uncompensated moment, which is caused by finite-size effects, and we have estimated the size of this moment from the experimental neutron data. The field dependence of $\varepsilon_0$ for the interacting nanoparticles differs strongly from that of the noninteracting nanoparticles, and this is a result of the influence of exchange interaction between the particles.

DOI: 10.1103/PhysRevB.74.184406 PACS number(s): 75.50.Tt, 75.30.Ds, 75.30.Gw, 25.40.Fq

## I. INTRODUCTION

Materials composed of nanoscale magnetic grains are becoming important in technological applications, since they provide the possibility of designing materials with new magnetic properties. This is indeed true for magnetic nanoparticles used in, for example, ferrofluids, biomedicine, hard permanent magnets and magnetic recording media.[1,2] Understanding the fundamental properties of the grains and the influence of magnetic interactions is therefore of great importance.

The magnetic anisotropy of a single nanoparticle is in the first approximation assumed to be uniaxial with the anisotropy energy given by

$$E(\theta) = KV \sin^2 \theta, \tag{1}$$

where $K$ is the magnetic anisotropy constant, $V$ is the particle volume, and $\theta$ is the angle between the (sublattice) magnetization and an easy direction of magnetization. $KV$ is the energy barrier that separates the two minima at $\theta=0$ and $\theta=\pi$. If the thermal energy is comparable to $KV$, superparamagnetic relaxation takes place, i.e., the magnetization vector fluctuates between the easy directions of magnetization.[3] At lower temperatures the magnetization vector fluctuates in directions close to one of the easy axes, i.e., performs collective magnetic excitations.[4,5] These magnetic fluctuations can be described as a uniform precession (a spin wave with wave vector $q=0$) of the magnetization vector around an easy direction of magnetization in combination with transitions between these precession states. Due to finite-size quantization there is a large energy gap in the spin wave spectrum to the spin waves with $q \neq 0$. The spin wave spectrum is discrete[6,7] and excitations of the uniform ($q=0$) mode are therefore predominant.[8]

Interactions between magnetic nanoparticles can have a strong influence on the magnetic properties. For ferromagnetic and ferrimagnetic nanoparticles, the interparticle dipole interaction can have a significant influence on the superparamagnetic relaxation time, see, e.g., Refs. 9–16. Nanoparticles of antiferromagnetic materials have recently attracted much attention because their properties in several ways differ from those of the bulk materials. They have a nonzero magnetic moment, which has been attributed to uncompensated spins,[17,18] but recently it was suggested that it also can have a contribution from so-called thermoinduced magnetization.[19] An anomalous temperature dependence of the magnetic moments, which has been observed in several studies[20–23] seems to support this, but may also be explained by shortcomings in the analysis of magnetization data for antiferromagnetic nanoparticles.[24] Macroscopic quantum tunneling of the magnetization, which is characterized by a temperature-independent relaxation, is expected to be more pronounced in antiferromagnetic nanoparticles than in ferromagnetic and ferrimagnetic nanoparticles.[25] Such a temperature-independent relaxation has been observed in low-temperature studies of, for example, ferritin[26,27] and $\alpha$-$Fe_2O_3$ nanoparticles.[28] Other studies have shown that the magnetic structure of, for example NiO nanoparticles may differ from the bulk magnetic structure.[29] In $\alpha$-$Fe_2O_3$ nanoparticles, the Morin transition is suppressed[30,31] and the spin-flop field decreases with decreasing particle size.[32] In samples of antiferromagnetic nanoparticles the interparticle dipole interactions are negligible, because the magnetic moments of the particles are small,[33] but the exchange coupling between surface atoms of nanoparticles in close contact may be a prominent source of interaction effects.[5,33–37]

In an atomic scale model for the interaction, we assume that the particles are magnetically coupled via exchange interaction between pairs of surface ions. The magnetic interaction energy of a particle $p$ with surface spins $\mathbf{S}_i^p$ may be written

$$E_{\mathrm{ex}} = -\sum_i \mathbf{S}_i^p \cdot \sum_q \sum_j J_{ij}^q \mathbf{S}_j^q, \tag{2}$$

where $\mathbf{S}_j^q$ are the surface spins of the neighboring particles $q$ and $J_{ij}^q$ is the exchange coupling constant related to the inter-

 

action between the surface ions $i$ of the particle $p$ and the surface ions $j$ of the neighboring particles $q$. Neglecting surface spin canting, we may write

$$\sum_j J_{ij}^q \mathbf{S}_j^q = A_q \mathbf{M}_q, \tag{3}$$

where $\mathbf{M}_q$ is the (sublattice) magnetization of the particle $q$ and $A_q$ is an effective interaction constant. Because $\Sigma_i \mathbf{S}_i^p$ is proportional to the (sublattice) magnetization $\mathbf{M}_p$ of the particle $p$, the total energy density may be written[5,33–36]

$$E_i = K_i \sin^2 \theta_i - \mathbf{M}_p \cdot \sum_q J_{pq} \mathbf{M}_q, \tag{4}$$

where $J_{pq}$ is an effective exchange coupling constant.

If the first term in Eq. (4) is predominant, superparamagnetic relaxation of the individual nanoparticle may take place between the easy directions close to $\theta=0$ and $\theta=\pi$. However, if the interactions are significant, the energy at the two minima will differ and the populations will therefore differ. At finite temperatures, the (sublattice) magnetization may then mainly fluctuate around the direction corresponding to the lower energy minimum. The magnetic properties of interacting particles have been calculated by use of a simple mean field model in which the summation in the second term in Eq. (4) is replaced by an average value, which may be considered as an effective interaction field.[33–36]

Interaction effects in samples of magnetic nanoparticles have mainly been studied by ac and dc magnetization measurements and by Mössbauer spectroscopy, which together cover about 10 decades of relaxation times down to $\approx 10^{-10}$ s. It has been demonstrated that inelastic neutron scattering also is a very useful method for investigating spin dynamics in magnetic nanomaterials because the time scale of this technique expands the observable time range down to $10^{-14}$ s.[7,38–43] In the inelastic neutron scattering experiments the energy distribution of the neutrons, which are scattered at momentum transfer corresponding to an antiferromagnetic reflection, is measured. The neutrons can excite or de-excite a $q=0$ spin wave and thereby spin excitations can be probed.

In this paper we present the results of an inelastic neutron scattering study of coated and uncoated nanoparticles of $\alpha$-$Fe_2O_3$ with a mean size of 8 nm. We assume that the coated nanoparticles can be treated as individual, noninteracting, particles, whereas the uncoated nanoparticles interact via exchange interactions within agglomerates. The study shows that interparticle exchange interactions between the $\alpha$-$Fe_2O_3$ nanoparticles can have a strong effect on collective magnetic excitations. We compare the results with data obtained by Mössbauer spectroscopy on the same nanoparticle samples.

## II. SPIN DYNAMICS IN HEMATITE NANOPARTICLES

$\alpha$-$Fe_2O_3$ has the corundum crystal structure, and we describe the structure using the hexagonal unit cell. $\alpha$-$Fe_2O_3$ nanoparticles smaller than about 20 nm in diameter are canted antiferromagnets with the spins in the (001) plane at least down to 5 K.[31] In bulk, the canting angle is approximately 0.07° and the out-of plane magnetocrystalline anisotropy is considerably larger than the in-plane anisotropy.[44] The Néel temperature of bulk $\alpha$-$Fe_2O_3$ is $T_N=955$ K.[44] In nanoparticles, the in-plane anisotropy is larger than in bulk and may become comparable to the out-of-plane anisotropy.[7,31] Here, we will for simplicity assume that the magnetic anisotropy in $\alpha$-$Fe_2O_3$ nanoparticles can be described as an effective uniaxial anisotropy [Eq. (1)] with anisotropy constant $K_{\text{eff}}$.

In noninteracting $\alpha$-$Fe_2O_3$ nanoparticles, the amplitude of the uniform magnetic precession mode with lowest energy lies predominantly in the (001) plane,[39,43] while the second precession mode at higher excitation energy is predominantly perpendicular to the (001) plane.[7] Applied magnetic fields increase the excitation energy and hence suppress the amplitude of collective magnetic excitations. A quantum mechanical description of the details of the relaxation and precession modes can be found in Ref. 45.

In studies of magnetic nanoparticles using inelastic neutron scattering it has been found that superparamagnetic relaxation gives rise to an energy broadening of Lorentzian line shape of the magnetic Bragg reflections.[39,41,43] In the following, this will be termed the quasielastic signal. In inelastic scattering processes, the energy of the scattered neutrons can be changed by an amount $\varepsilon_0$ corresponding to the energy difference between two neighboring uniform precession states.[39–42] This gives rise to inelastic peaks at neutron energy transfers $\pm\varepsilon_0$. In 8-nm $\alpha$-$Fe_2O_3$ nanoparticles, the lowest spin wave excitation with $q\neq 0$ has an energy larger than 10 meV and the antiphase $q=0$ excitation also has high energy.[6,7] Therefore, these transitions were not probed in the present measurements where only neutrons with energy transfer lower than 5 meV were detected.

The broadening of the quasielastic Lorentzian line shape due to superparamagnetic relaxation is given by[39]

$$I(\varepsilon) = D(\varepsilon) \frac{A_{\text{Bragg}}}{\pi} \frac{\Gamma}{\Gamma^2 + \varepsilon^2}, \tag{5}$$

where $D(\varepsilon)=\frac{\varepsilon}{k_b T}\left(\frac{1}{\exp(\varepsilon/k_B T)-1}+1\right)$ is the detailed balance factor, $A_{\text{Bragg}}$ is the integrated intensity (area) of the quasielastic peak coming from the semistatic arrangement of spins, $\Gamma$ is the half width at half maximum (HWHM) and is related to the lifetime of the superparamagnetic relaxation by $\Gamma=\hbar/\tau$.[41]

In previous inelastic neutron studies we have found that the damped harmonic oscillator model gives a good description of the collective magnetic excitations in both antiferromagnetic[7,39,40,43] and in ferrimagnetic nanoparticles.[42] Therefore, we will in this data analysis also apply the damped harmonic oscillator model given by[39,41,43]

$$I(\varepsilon) = D(\varepsilon) \frac{A_{\text{CME}}}{\pi} \frac{2\gamma\varepsilon_0^2}{(\varepsilon^2 - \varepsilon_0^2)^2 + 4\gamma^2\varepsilon^2}. \tag{6}$$

$A_{\text{CME}}$ is the integrated intensity (area) of the peaks, $\gamma$ is the width (HWHM) of the inelastic peaks and $\varepsilon_0$ is the energy difference between the precession modes. At low temperatures ($k_B T \ll K_{\text{eff}} V$) $\varepsilon_0$ can be approximated by[39]

$$\varepsilon_0 \approx g\mu_B\sqrt{2B_AB_E}. \quad (7)$$

$g=2$ is the $g$ factor, $\mu_B$ is the Bohr-magneton, $B_E=900$ T is the exchange field, and $B_A$ is the anisotropy field $B_A=K_{\text{eff}}/M_s$, where $M_s=9\times10^5$ A m$^{-1}$ is the sublattice saturation magnetization of bulk $\alpha$-$Fe_2O_3$.[44] The value of $K_{\text{eff}}$ can be estimated from experimental neutron data.[7,39,41,43]

If the particles are exposed to a magnetic field, $B_{\text{appl}}$, which is large compared to the effective anisotropy field, the energy difference is given by[39]

$$\varepsilon_0 \approx g\mu_B B_{\text{appl}}. \quad (8)$$

In this work we analyze the data from interacting particles by use of the simple model outlined in Sec. I [Eq. (4)], where the influence of interactions is described by an effective interaction field.

The relative area of the inelastic peaks in neutron scattering experiments compared to the total magnetic scattering, also gives information on the magnetic fluctuations. For noninteracting particles with magnetic energy given by Eq. (1) the temperature dependence at low temperatures ($k_BT \ll K_{\text{eff}}V$) is given by[39,43]

$$\frac{A_{\text{CME}}}{A_{\text{Bragg}}+A_{\text{CME}}} = \langle \sin^2\theta\rangle \approx \frac{k_BT}{K_{\text{eff}}V}. \quad (9)$$

In Mössbauer spectroscopy, fast superparamagnetic relaxation results in a collapse of the magnetic hyperfine splitting, and at low temperatures ($k_BT \ll K_{\text{eff}}V$) collective magnetic excitations give rise to a reduction of the observed magnetic hyperfine field $B_{\text{obs}}$ given by[4,5]

$$B_{\text{obs}} = B_0\langle\cos\theta\rangle \approx B_0\left(1-\frac{k_BT}{2K_{\text{eff}}V}\right), \quad (10)$$

where $B_0$ is the magnetic hyperfine field that would be measured in the absence of relaxation phenomena. For strongly interacting magnetic nanoparticles, Eq. (10) may be replaced by[5,33–35]

$$\langle B_{\text{obs}}\rangle \approx B_0\left(1-\frac{k_BT}{2K_{\text{eff}}V+E_{\text{int}}}\right), \quad (11)$$

where $E_{\text{int}}$ is related to the strength of the interactions.

## III. EXPERIMENTAL METHODS

The $\alpha$-$Fe_2O_3$ nanoparticles were prepared by means of a gel-sol method similar to that developed by Sugimoto *et al.*[46] The particles resemble those described in Refs. 36, 37, 47, and 48. Part of the batch was treated with phosphate to produce a sample of particles coated with a layer of nonmagnetic material in order to minimize interparticle interactions.[42,50] For simplicity, the particles in this sample are in the following referred to as the noninteracting particles. Another part of the batch was uncoated and dried such that the particles in this sample were in direct contact. These are referred to as the interacting particles.

Transmission electron microscopy (TEM) images were obtained using a JEOL 3000F microscope, equipped with a Gatan MSC CCD-camera. TEM images are shown in Fig. 1. The particles of both samples are seen to be round with a good crystallinity. The phosphate coating is seen as an amorphous layer around the crystalline particles in Fig. 1(a). The average particle size is approximately 8 nm in accordance with x-ray and neutron powder diffraction data,[47] which also established that each particle consists of a single magnetic domain. In addition, neutron diffraction data confirmed the magnetic Bragg reflections at the scattering vectors $Q=1.37$ and 1.51 Å$^{-1}$ corresponding to the purely antiferromagnetic (003) and (101) reflections, respectively. These data also showed that the nanoparticles are above the Morin transition in the entire measured temperature regime.

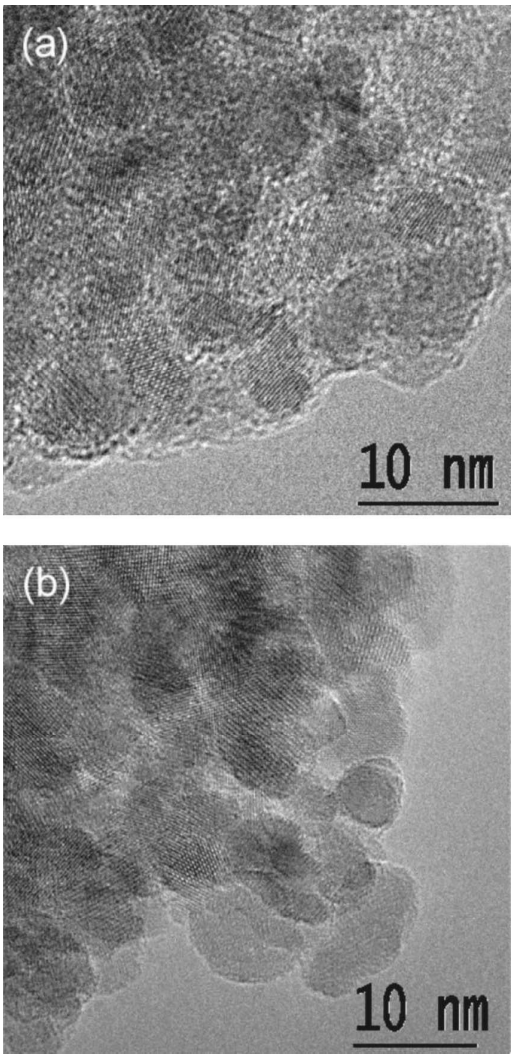


FIG. 1. TEM images of the 8-nm $\alpha$-$Fe_2O_3$ nanoparticles. (a) The noninteracting (coated) particles and (b) the interacting (noncoated) particles. The coating is seen as an amorphous layer around the particles.

The Mössbauer spectra were obtained using constant-acceleration spectrometers with sources of $^{57}$Co in rhodium. Spectra in the temperature range 18–300 K were obtained using a closed cycle helium refrigerator. Spectra at or below

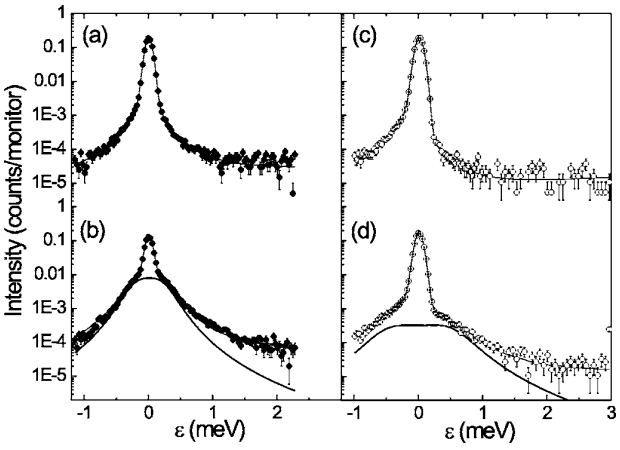


FIG. 2. Inelastic neutron data for 8-nm $\alpha$-$Fe_2O_3$ nanoparticles. (a), (b) Energy scans with $\varepsilon_f$=3.7 meV at constant scattering vector $\tau_{003}$ at 10 and 150 K, respectively, for the noninteracting nanoparticles. Similar data for the interacting nanoparticles are shown in (c) and (d). The thin line represents the fit to the model as explained in the text and the bold line in (b) and (d) shows the contribution from just the collective magnetic excitations. The asymmetric tails is at $\varepsilon < 0.05$ meV are a part of the background, as explained in Sec. III. In each series of measurements, the spectra obtained at the lowest temperatures and zero applied field have been normalized to the same maximum intensity at $\varepsilon_0$=0 meV.

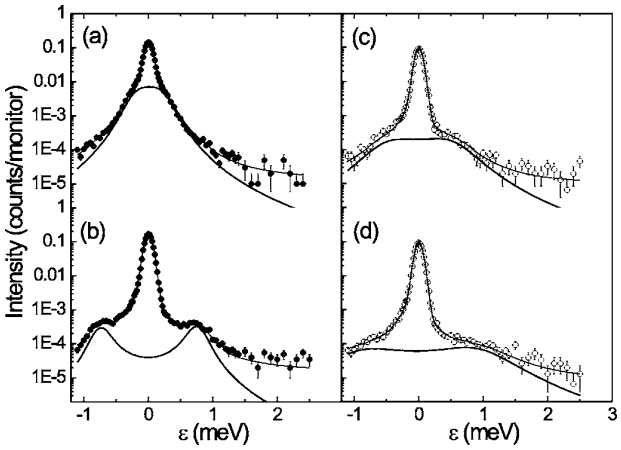


FIG. 3. Inelastic neutron data for the 8-nm $\alpha$-$Fe_2O_3$ nanoparticles. (a), (b) Energy scans with $\varepsilon_f$=3.7 meV at constant scattering vector $\tau_{003}$ at 100 K at an applied magnetic field of 0 and 6 T, respectively, for the noninteracting nanoparticles. Similar data for the interacting nanoparticles are shown in (c) and (d). The thin line represents the fitted model as explained in the text, and the contribution from the just collective magnetic excitations is shown by the bold line.

18 K were obtained in a liquid helium cryostat. The spectrometers were calibrated with a 12.5-$\mu$m-thick $\alpha-$Fe foil at room temperature.

The inelastic neutron scattering experiments were performed at the cold-neutron triple-axis spectrometer RITA-2 at SINQ, Paul Scherrer Institute.[51] The experiments were performed with a 80 ′ collimator after a vertically focusing pyrolythic graphite (002) monochromator, and a radially collimating BeO filter after the sample. The final neutron energy was fixed at $\varepsilon_f$=3.7 meV giving an energy resolution of 80 $\mu$eV. Furthermore, spectra were also obtained for a final neutron energy of $\varepsilon_f$=2.9 meV. The spectrometer was run in the monochromatic point-to-point focusing analyzer mode with a position sensitive detector.[52] Following the same procedure as in Refs. 7, 39, and 43 the data were fitted using the models for superparamagnetic relaxation and collective magnetic excitations as described in Sec. II, Eqs. (5) and (6). First, the resolution function of the setup and the background function were determined from low temperature energy scans, where superparamagnetism and collective magnetic excitations are negligible, and from background energy scans performed at all temperatures at scattering vectors far from the Bragg reflections. The resolution function is composed of a strong Gaussian with FWHM=80 $\mu$eV (pure instrumental resolution) and a weak Lorentzian line with FWHM =2 meV centered at zero energy transfer (caused by incoherent scattering from water adsorbed at the nanoparticles and fluctuations of disordered surface spins[53]). Furthermore, an asymmetry is included for $\varepsilon < 0$ meV, caused by the BeO filter, which blocks elastically scattered (background-causing) neutrons at settings with $\varepsilon > 0.05$ meV. In the fitting procedure the obtained resolution function was convoluted with the expressions for the superparamagnetic relaxation and the collective magnetic excitations [Eqs. (5) and (6)], and a linear background with constant slope was added.

## IV. EXPERIMENTAL RESULTS

### A. Results from inelastic neutron scattering

Figures 2 and 3 show examples of the inelastic neutron scattering data obtained for a constant scattering vector at $Q=\tau_{003}=1.37$ Å$^{-1}$. In all figures the filled circles represent the data for the noninteracting nanoparticles and the open circles represent the interacting nanoparticles. The measurements were performed in the temperature range 5–300 K and in applied magnetic fields up to 10 T perpendicular to the incoming neutron beam and to the neutron scattering vector.

Figures 2(a) and 2(b) show the data for the noninteracting nanoparticles at $T$=10 and 150 K, respectively, including the fit to the model represented by the thin line. At the highest temperature the inelastic peaks have a large intensity indicating an increased population of the uniform magnetic excitations. The related part of the fit is shown by the bold line. Similar data for the interacting nanoparticles are shown in Figs. 2(c) and 2(d) for the temperatures $T$=5 and 150 K, respectively. The inelastic signal is less pronounced and appears considerably broadened as compared to the data for the noninteracting nanoparticles.

Figures 3(b) and 3(d) show the inelastic neutron scattering signal at $T$=100 K when a magnetic field of 6 T has been applied. Figures 3(a) and 3(c) show the corresponding zero field scans. It can be seen that application of a magnetic field increases the excitation energy in both samples. This is quali-

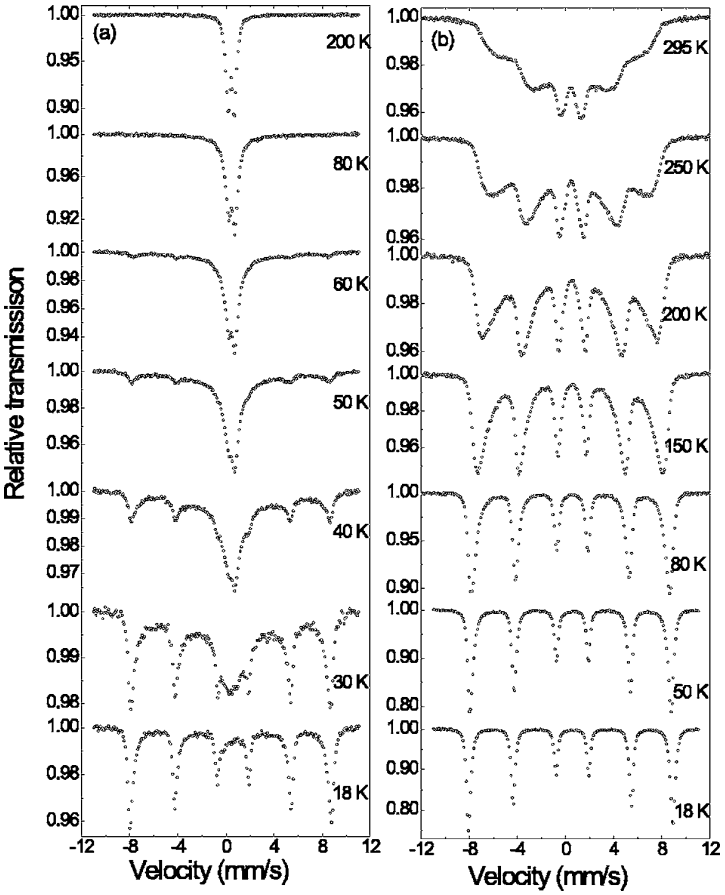


FIG. 4. Mössbauer spectra of the 8-nm $\alpha$ -$Fe_2O_3$ nanoparticles at various temperatures from 18 K to room temperature. (a) Data for the noninteracting particles and (b) data for the interacting particles.

tatively in accordance with Eq. (8). The broad inelastic components associated with the collective magnetic excitations are absent for data taken at nonmagnetic values of the scattering vector (data not shown).

### B. Results from Mössbauer spectroscopy

Mössbauer spectra of the noninteracting and interacting particles, obtained at various temperatures, are shown in Fig. 4. The spectra of the coated nanoparticles [Fig. 4(a)] show a superparamagnetic behavior typical for noninteracting or weakly interacting nanoparticles.[33,35,36] At 18 K the spectrum consists of a sextet with narrow lines, indicating that at this temperature essentially all nanoparticles in the sample have relaxation times longer than the time scale of Mössbauer spectroscopy (i.e., $\gg 5\times 10^{-9}$ s). As the temperature is increased, a doublet appears in the spectra. This doublet is due to nanoparticles with a relaxation time shorter than the time scale of Mössbauer spectroscopy. The relative area of the doublet increases with increasing temperature, and at temperatures above 80 K the contribution from the sextet has disappeared. The spectra show a weak asymmetry of the sextet lines indicating that the coated nanoparticles may actually be weakly interacting.[33,35,36] The spectra of the interacting particles [Fig. 4(b)] show a completely different evolution with increasing temperature. Instead of the appearance of a doublet, the spectra show a substantial asymmetrical broadening of the lines of the sextet at temperatures up to room temperature. This is typical for Mössbauer spectra of interacting magnetic nanoparticles for which the energy is given by Eq. (4) and the relaxation may be described as fluctuations around a direction (mainly defined by the interaction field) rather than fluctuations between two equivalent minima at $\theta=0$ and $\theta=\pi$.[33–36]

## V. DISCUSSION

We have applied the damped harmonic oscillator model to fit the inelastic neutron scattering spectra. Some of the parameters, obtained from the fits, are presented in Figs. 5, 7, and 8.

Around 200 K, the character of the relaxation changes. Well below this temperature, the dynamics can be described as a combination of uniform excitations with small amplitude (which give rise to the inelastic peaks) and superparamagnetic relaxation, i.e., reversal of the sublattice magnetization vectors (which gives rise to a broadening of the quasielastic peak). At temperatures of the order of 200 K, the thermal energy becomes comparable to the anisotropy energy, and then the two types of magnetic dynamics cannot be clearly separated because the sublattice magnetization vectors can fluctuate with similar probabilities in all directions. This isotropic relaxation regime[49] will be discussed

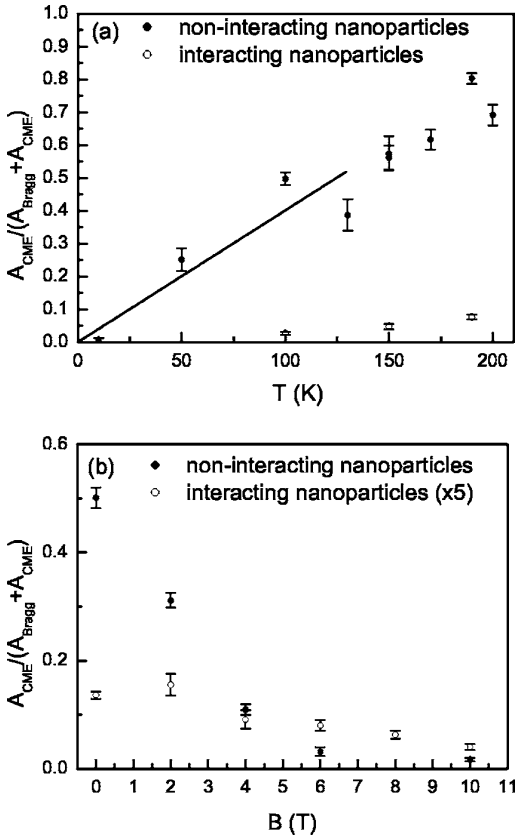


FIG. 5. The area fraction as a function of (a) temperature and (b) field at $T=100$ K. The fit to Eq. (9), which only applies at low temperatures, is shown by the solid line in (a). The data points for the interacting nanoparticles in (b) have been multiplied by 5 for clarity.

elsewhere.[48] Therefore, we will here only discuss the results obtained for $T<200$ K.

We have investigated the influence of a size distribution of the particles by weighting the inelastic neutron intensity with a log-normal size distribution (with standard deviation $\sigma=0.5$) and letting the anisotropy vary with size according to the findings of Ref. 31. For the nanoparticle sizes in this study it only introduces minor modifications, we therefore here present the analysis in which we have assumed monodisperse particles.

### A. The magnetic anisotropy and interaction energies

The relative area of the inelastic peaks as compared to the total magnetic scattering, $A_{\mathrm{CME}}/(A_{\mathrm{Bragg}}+A_{\mathrm{CME}})$, as a function of temperature and applied field is shown in Figs. 5(a) and 5(b), respectively. For both samples, the relative area of the inelastic peaks increases with temperature, but the effect is strongest for the noninteracting particles. We have fitted the low-temperature data for the noninteracting particles with Eq. (9) yielding an estimate of the effective anisotropy of $K_{\mathrm{eff}}V/k_B=250(30)$ K $[K_{\mathrm{eff}}=1.3(2)\times10^4$ J/m$^3]$ for the noninteracting nanoparticles. The data for the interacting particles

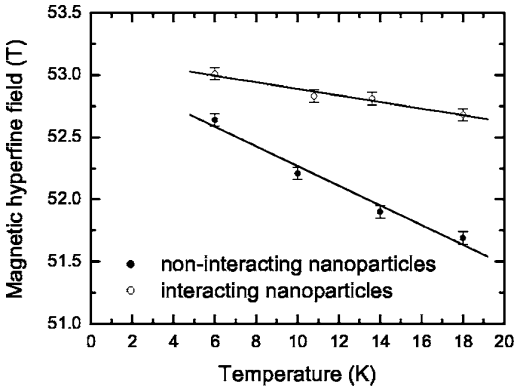


FIG. 6. The average observed hyperfine field $\langle B_{\mathrm{obs}}\rangle$ obtained from the Mössbauer data, as a function of temperature. The lines are linear fits to the data.

show a much smaller relative area of the inelastic peaks than for the noninteracting particles. Application of a magnetic field decreases the inelastic signal from the noninteracting nanoparticles, whereas only magnetic fields larger than about 3 T have a measurable effect on the interacting nanoparticles.

We have fitted the low-temperature Mössbauer spectra to estimate the average hyperfine field $\langle B_{\mathrm{obs}}\rangle$ at temperatures up to 18 K, i.e., in a range where the superparamagnetic relaxation of most particles are blocked, but the spectra are influenced by collective magnetic excitations. The temperature dependence of $\langle B_{\mathrm{obs}}\rangle$ is shown in Fig. 6. From the linear fits we find from Eq. (10) $K_{\mathrm{eff}}V/k_B=335(35)$ K $[K_{\mathrm{eff}}=1.7(2)\times10^4$ J/m$^3]$ for the noninteracting particles, which is in good agreement with the value found from the neutron data. For the interacting particles we find from Eq. (11) $(2K_{\mathrm{eff}}V+E_{\mathrm{int}})/k_B=1330(180)$ K. Assuming $K_{\mathrm{eff}}$V to be the same for the two samples, we obtain $E_{\mathrm{int}}/k_B=660(200)$ K.

In $\alpha$-$Fe_2O_3$ the different superexchange coupling constants are in the range 10–30 K,[44] For $Fe^{3+}$ ions with spin $s=5/2$ this corresponds to an exchange energy per exchange bridge in the range 60–190 K. Therefore only a few (of the order of ten) exchange bridges between neighboring $\alpha$-$Fe_2O_3$ nanoparticles are needed to account for the observed interaction effects. Similar values were estimated from Mössbauer data for interacting 20 nm $\alpha$-$Fe_2O_3$ nanoparticles.[33]

### B. The energy related to the uniform precession states

The measured dynamic behavior of the 8-nm hematite nanoparticles show several interesting effects, which were not observed in previous studies of larger particles.[7,39,43] First we discuss data for the noninteracting nanoparticles. The excitation energy $\varepsilon_0$ shows a weak linear increase with temperature [Fig. 7(a)]. Extrapolating $\varepsilon_0$ to $T=0$ K gives $\varepsilon_{0,T=0}=0.214(5)$ meV. The increase of $\varepsilon_0$ with increasing temperature is surprising since the damped harmonic oscillator model predicts a decreasing $\varepsilon_0$, which was also observed for larger 15-nm $\alpha$-$Fe_2O_3$ nanoparticles.[39,43] Furthermore,

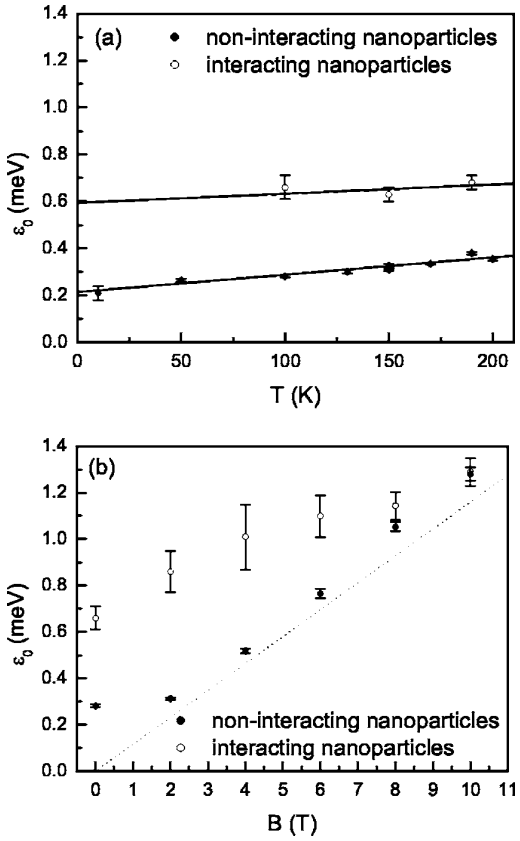


FIG. 7. Position of the inelastic peaks as a function of (a) temperature and (b) field at $T=100$ K. The solid lines in (a) show the linear extrapolation to $T=0$ K and in (b) the dotted line represents Eq. (8).

because the magnetic anisotropy constant of $\alpha$-$Fe_2O_3$ nanoparticles increases with decreasing particle size[31] one would expect an increasing $\varepsilon_{0,T=0}$ with decreasing particle size, and this is also opposite to the present observation (for 15-nm $\alpha$-$Fe_2O_3$ nanoparticles $\varepsilon_{0,T=0}=0.26$ meV).[39]

It is known[17,18] that antiferromagnetic nanoparticles usually have an uncompensated magnetic moment, with a relative size increasing with decreasing particle size. One can show that the equation of motion for the $q=0$ mode in a microscopic model for a particle with different number of spins in two sublattices is equivalent to that of two interacting macrospins.[54] Thus nanoparticles of antiferromagnetic materials should in principle be described as ferrimagnets with a very small difference $\Delta M$ between the sublattice magnetic moments. Even a small uncompensated moment can have a significant influence on the precession frequency of the uniform mode. Introducing the relative uncompensated moment $\zeta=\Delta M/M_s$ in one sublattice, Eq. (7) should be replaced by[55–58]

$$\varepsilon_0^{1,2}=\frac{1}{2}g\mu_B B_E[\sqrt{4\lambda^2+4\lambda(2+\zeta)+\zeta^2}\pm\zeta]. \qquad (12)$$

Here $\lambda=K_{\mathrm{eff}}/(B_E M_s)$. We have assumed that the magnetic anisotropy is uniaxial and given by Eq. (1) and that the spin structure and the precession modes are not influenced by, for example, surface effects in the nanoparticles. In previous work on 15-nm $\alpha$-$Fe_2O_3$ particles[7,39,43] the influence of an uncompensated moment on the precession frequency was not observed. However, in the 8-nm particles studied here, the relative uncompensated moment is expected to be larger and therefore to have a stronger influence on $\varepsilon_0$, and this may explain the small value of $\varepsilon_0$ and its anomalous temperature dependence. Inserting the measured value of $\varepsilon_{0,T=0}=0.214$ meV and using the estimated $K_{\mathrm{eff}}=1.3\times10^4$ J/m$^3$ (obtained in Sec. V A) and assuming that the low-energy mode ($\varepsilon_0^1$) is predominant, we determine an uncompensated moment $\Delta M/M_{s,T=0}\approx1.1\%$. According to Eq. (12), the other mode with higher frequency ($\varepsilon_0^2$) then corresponds to $\varepsilon_{0,T=0}\approx1.7$ meV. We do not resolve the neutron intensity from this mode because it is significantly reduced in comparison to mode $\varepsilon_0^1$.

It should be emphasized that the use of the simple expression Eq. (1) for the magnetic anisotropy energy, which was also used in previous neutron studies of hematite nanoparticles,[39,43] is only a first order approximation. Both in bulk hematite and hematite nanoparticles, the sublattice magnetization is to a large extent confined to the (001) plane because of a large out-of-plane anisotropy with anisotropy constant $K_1$. The smaller in-plane anisotropy, $K_{\mathrm{Bu}}$ has been found to increase with decreasing particle size.[31] In neutron studies of the high-frequency and low-frequency modes in 15 nm particles the values $K_1=5\times10^4$ J/m$^3$ and $K_{\mathrm{Bu}}=0.3\times10^4$ J/m$^3$ were estimated, but from the results above we estimate that $K_{\mathrm{Bu}}$ is larger in the present 8-nm particles. Unfortunately, the value of $K_1$ in 8-nm particles is not known, because we were unable to detect the high-frequency mode, and therefore we are not able to perform a more rigorous data analysis. However, it is likely that $K_1$ and $K_{\mathrm{Bu}}$ are of the same order of magnitude in the 8 nm particles, and therefore Eq. (1) may be a fair approximation to the magnetic anisotropy energy.

Néel[17,18] suggested some simple models for estimating the uncompensated moment. In one model, he assumed that the interior of the nanoparticle is essentially free of defects, but that the surface sites are randomly occupied such that the number of uncompensated spins is of the order of the square root of the number of surface spins. For the present particles this would give a fraction of uncompensated spins of about 0.8% in one sublattice, which is close to the value estimated from the experimental data $\approx1.1\%$.

Mössbauer spectroscopy with large magnetic fields applied to the sample can give information on the relative importance of the magnetic moments due to canting and to uncompensated spins. Such studies of 15-nm hematite particles showed that the moment due to uncompensated spins was small compared to the moment due to canting.[59] We have made similar measurements on the 8-nm particles and found that the two contributions in this case are of the same order of magnitude, i.e., the relative importance of the uncompensated spins is larger in this case.

The nanoparticles with an uncompensated moment may be considered as weak ferrimagnets. However, the dipole interaction energy, even between two particles in contact, is very weak ($\lesssim1$ K).[33] Thus, the interaction effects observed

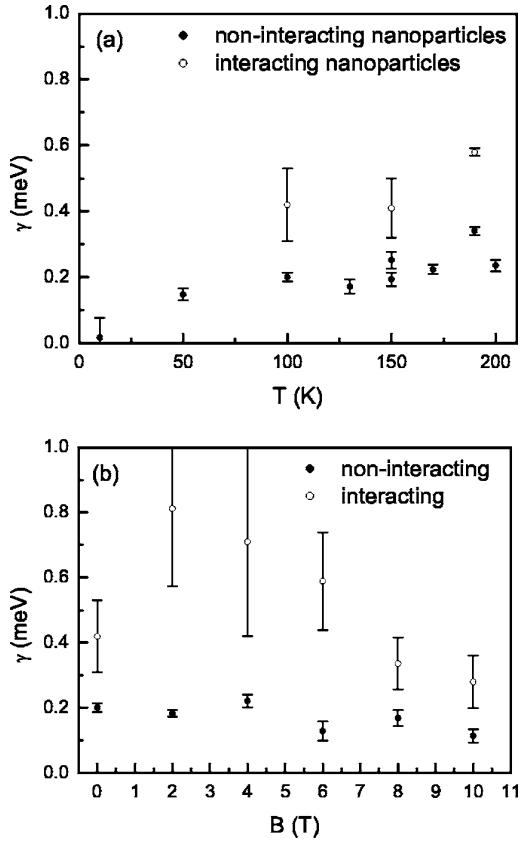


FIG. 8. Width of the inelastic peaks as a function of (a) temperature and (b) field at $T=100$ K.

in the interacting particles must be explained by exchange interactions.

When a magnetic field is applied [Fig. 5(b)] the amplitude of the inelastic peak decreases. This can be explained by the increase of the excitation energy of the precession modes, which results in a decrease of the thermal populations. $\varepsilon_0$ increases for the noninteracting nanoparticles at all fields up to 10 T. At large applied fields $\varepsilon_0(B)$ follows the behavior predicted by Eq. (8), which is shown by the dotted line in Fig. 7(b) (assuming[39] $g=2$).

The width $\gamma$ of the inelastic peak increases with temperature [Fig. 8(a)]. Though the values are comparable, this increase with temperature is opposite to what was seen in previous experiments on 15-nm $\alpha$-$Fe_2O_3$ nanoparticles.[39,43] Theoretically, it has been predicted that the width first decreases with temperature and then at a certain critical temperature starts to increase.[45] This is caused by the balance between the anisotropy energy barrier and the sublattice exchange interaction in $\alpha$-$Fe_2O_3$. For the present experiments the anisotropy energy of the 8-nm $\alpha$-$Fe_2O_3$ nanoparticles may be such that we have entered the regime where an increase in width is possible. For the interacting nanoparticles the width is a factor 2–3 larger indicating that there is a broad range of interaction energies.

Applying a magnetic field [Fig. 8(b)] reduces the width. The magnetic field narrows the range of frequencies and suppresses to some extent the amplitude of the excitations.

Now we discuss the corresponding measurements for the interacting particles. The temperature dependence of $\varepsilon_0$ is similar to that of the noninteracting particles. For the interacting nanoparticles, $\varepsilon_0$ [Fig. 7(b)] starts at a higher value for low magnetic fields $\varepsilon_0(B=0)\approx 0.65$ meV and reaches the value for the noninteracting nanoparticles at 10 T. The field dependence of $\varepsilon_0$ shows a significant deviation from Eq. (8) for fields up to 8 T. Thus the interaction energy is predominant and we estimate that the effective interaction field is of the order of 5 T. On the other hand, $E_{\mathrm{int}}$ can be considered as a product of this interaction field and an effective moment. For $E_{\mathrm{int}}\approx 660$ K one can estimate an effective moment of 130 Bohr magnetons, which would correspond to about 50 iron atoms. The behavior of $\gamma$ for the interacting nanoparticles starts to approach that of the weakly interacting nanoparticles at an applied field of 5 T, in accordance with the previous findings.

## VI. CONCLUSION

Using inelastic neutron scattering we have studied the collective magnetic excitations in noninteracting and interacting 8-nm $\alpha$-$Fe_2O_3$ nanoparticles. The data are well described by the damped harmonic oscillator model. The determined characteristic energy $\varepsilon_0$ suggests that the magnetic properties of the 8-nm $\alpha$-$Fe_2O_3$ nanoparticles are strongly affected by an uncompensated moment in one sublattice of $\Delta M/M_{s,T=0}\approx 1.1\%$, which is present as a finite size effect in the antiferromagnetic nanoparticles. The collective magnetic excitations are strongly influenced by the interparticle exchange interactions, and from Mössbauer spectroscopy data we have estimated the interaction energy $E_{\mathrm{int}}/k_B$ to be approximately 660 K. This energy corresponds to in average a few exchange bridges between the $\alpha$-$Fe_2O_3$ nanoparticles. This is supported by the neutron measurements. We conclude that inelastic neutron scattering besides probing spin dynamics in magnetic nanoparticles also can add important information on uncompensated moments and interparticle interactions.

## ACKNOWLEDGMENTS

We thank F. Bødker for preparing the $\alpha$-$Fe_2O_3$ nanoparticles. We have had many clarifying discussions with B. Lebech for which we are grateful. The work was supported by the Danish Technical Research Council through the framework program on nanomagnetism, and the Danish Natural Science Research Council through the Danish Neutron Scattering Centre, DANSCATT. The electron microscopy was carried out at the Danish TEM Centre, supported by the Danish Natural Science and Technical Research Councils. This work is based on experiments performed at the SINQ neutron source at the Paul Scherrer Institute, Villigen, Switzerland.

*Electronic address: luise.theil.kuhn@risoe.dk
†Author to whom correspondence should be addressed.
‡Electronic address: christian.bahl@risoe.dk
§Present address: Materials Science Div., Argonne National Laboratory, Argonne, IL 60439, USA.

[1] *Fifth International Conference on Fine Particle Magnetism*, edited by Q. Pankhurst, Journal of Physics: Conference Series 17, (2005).
[2] M. P. Morales, S. A. Walton, L. S. Prichard, C. J. Serna, D. P. E. Dickson, and K. O'Grady, J. Magn. Magn. Mater. **190**, 357 (1998).
[3] L. Néel, Ann. Geophys. (C.N.R.S.) **5**, 99 (1949).
[4] S. Mørup and H. Topsøe, Appl. Phys. **11**, 63 (1976).
[5] S. Mørup, J. Magn. Magn. Mater. **37**, 39 (1983).
[6] P. V. Hendriksen, S. Linderoth, and P.-A. Lindgård, Phys. Rev. B **48**, 7259 (1993).
[7] S. N. Klausen, K. Lefmann, P.-A. Lindgård, L. Theil Kuhn, C. R. H. Bahl, C. Frandsen, S. Mørup, B. Roessli, N. Cavadini, and C. Niedermayer, Phys. Rev. B **70**, 214411 (2004).
[8] S. Mørup and B. R. Hansen, Phys. Rev. B **72**, 024418 (2005).
[9] J. L. Dormann, L. Bessais, and D. Fiorani, J. Phys. C **21**, 2015 (1988).
[10] S. Mørup and E. Tronc, Phys. Rev. Lett. **72**, 3278 (1994).
[11] P. E. Jönsson and J. L. García-Palacios, Europhys. Lett. **55**, 418 (2001).
[12] Ò. Iglesias and A. Labarta, Phys. Rev. B **70**, 144401 (2004).
[13] J. Zhang, C. Boyd, and W. Luo, Phys. Rev. Lett. **77**, 390 (1996).
[14] C. Djurberg, P. Svedlindh, P. Nordblad, M. F. Hansen, F. Bødker, and S. Mørup, Phys. Rev. Lett. **79**, 5154 (1997).
[15] H. Mamiya, I. Nakatani, and T. Furubayashi, Phys. Rev. Lett. **80**, 177 (1998).
[16] D. Fiorani, J. L. Dormann, R. Cherkaoui, E. Tronc, F. Lucari, F. D'Orazio, L. Spinu, M. Nogues, A. Garcia, and A. M. Testa, J. Magn. Magn. Mater. **196–197**, 143 (1999).
[17] L. Néel, C. R. Hebd. Seances Acad. Sci. **252**, 4075 (1961).
[18] L. Néel, in *Low Temperature Physics*, edited by C. Dewitt, B. Dreyfus, and P. D. de Gennes (Gordon & Breach, New York, 1962), p. 420.
[19] S. Mørup and C. Frandsen, Phys. Rev. Lett. **92**, 217201 (2004).
[20] M. S. Seehra, V. S. Babu, A. Manivannan, and J. W. Lynn, Phys. Rev. B **61**, 3513 (2000).
[21] J. G. E. Harris, J. E. Grimaldi, D. D. Awschalom, A. Chiolero, and D. Loss, Phys. Rev. B **60**, 3453 (1999).
[22] S. H. Kilcoyne and R. Cywinski, J. Magn. Magn. Mater. **140–144**, 1466 (1995).
[23] S. A. Makhlouf, F. T. Parker, and A. E. Berkowitz, Phys. Rev. B **55**, R14717 (1997).
[24] N. J. O. Silva, V. S. Amaral, and L. D. Carlos, Phys. Rev. B **71**, 184408 (2005).
[25] B. Barbara and E. M. Chudnovsky, Phys. Lett. A **145**, 205 (1990).
[26] J. Tejada and X. X. Zhang, J. Phys.: Condens. Matter **6**, 263 (1994).
[27] M. Duran, E. del Barco, J. M. Hernandez, and J. Tejada Phys. Rev. B **65**, 172401 (2002).
[28] E. del Barco, M. Duran, J. M. Hernandez, J. Tejada, R. D. Zysler, M. Vasquez Mansilla, and D. Fiorani, Phys. Rev. B **65**, 052404 (2002).
[29] R. H. Kodama, S. A. Makhlouf, and A. E. Berkowitz, Phys. Rev. Lett. **79**, 1393 (1997).
[30] W. Kündig, K. J. Ando, G. Constabaris, and R. H. Lindquist, Phys. Rev. **142**, 327 (1966).
[31] F. Bødker and S. Mørup, Europhys. Lett. **52**, 217 (2000).
[32] R. D. Zysler, D. Fiorani, A. M. Testa, L. Suber, E. Agostinelli, and M. Godinho, Phys. Rev. B **68**, 212408 (2003).
[33] M. F. Hansen, C. B. Koch, and S. Mørup, Phys. Rev. B **62**, 1124 (2000).
[34] S. Mørup, M. B. Madsen, J. Franck, J. Villadsen, and C. J. W. Koch, J. Magn. Magn. Mater. **40**, 163 (1983).
[35] S. Mørup, C. Frandsen, F. Bødker, S. N. Klausen, K. Lefmann, P.-A. Lindgård, and M. F. Hansen, Hyperfine Interact. **144/145**, 347 (2002)
[36] C. Frandsen and S. Mørup, J. Magn. Magn. Mater. **266**, 36 (2003).
[37] C. Frandsen and S. Mørup, Phys. Rev. Lett. **94**, 027202 (2005).
[38] F. Gazeau, E. Dubois, M. Hennion, R. Perzynski, and Y. Raikher, Europhys. Lett. **40**, 575 (1997).
[39] M. F. Hansen, F. Bødker, S. Mørup, K. Lefmann, K. N. Clausen, and P.-A. Lindgård, Phys. Rev. Lett. **79**, 4910 (1997).
[40] K. Lefmann, F. Bødker, M. F. Hansen, H. Vázquez, N. B. Christensen, P.-A. Lindgård, K. N. Clausen, and S. Mørup, Eur. Phys. J. D **9**, 491 (1999).
[41] M. F. Hansen, F. Bødker, S. Mørup, K. Lefmann, K. N. Clausen, and P.-A. Lindgård, J. Magn. Magn. Mater. **221**, 10 (2000).
[42] K. Lefmann, F. Bødker, S. N. Klausen, M. F. Hansen, K. N. Clausen, P.-A. Lindgård, and S. Mørup, Europhys. Lett. **54**, 526 (2001).
[43] S. N. Klausen, K. Lefmann, P.-A. Lindgård, K. N. Clausen, M. F. Hansen, F. Bødker, S. Mørup, and M. Telling, J. Magn. Magn. Mater. **266**, 68 (2003).
[44] A. H. Morrish, *Canted Antiferromagnetism: Hematite* (World Scientific, Singapore, 1994).
[45] J. D. Lee, Phys. Rev. B **70**, 174450 (2004).
[46] T. Sugimoto, Y. Wang, H. Itoh, and A. Muramatsu, Colloids Surf., A **134**, 265 (1998).
[47] C. Frandsen, C. R. H. Bahl, B. Lebech, K. Lefmann, L. Theil Kuhn, L. Keller, N. H. Andersen, M. v. Zimmermann, E. Johnson, S. N. Klausen, and S. Mørup, Phys. Rev. B **72**, 214406 (2005).
[48] L. Theil Kuhn, K. Lefmann, C. R. H. Bahl, S. N. Klausen, A. Wischnewski, C. Frandsen, and S. Mørup (unpublished).
[49] A. Würger, Europhys. Lett. **44**, 103 (1998).
[50] E. Tronc and J. P. Jolivet, Hyperfine Interact. **28**, 525 (1986).
[51] S. N. Klausen, K. Lefmann, D. F. McMorrow, F. Altorfer, S. Janssen, and M. Luthy, Appl. Phys. A: Mater. Sci. Process. **74**, S1508 (2002); see also the home page http://sinq.web.psi.ch/sinq/instr/rita2
[52] K. Lefmann, D. F. McMorrow, H. M. Rønnow, K. Nielsen, K. N. Clausen, B. Lake, and G. Aeppli, Physica B **283**, 343 (2000).
[53] L. Theil Kuhn, K. Lefmann, S. N. Klausen, H. M. Rønnow, A. Murani, and R. Stewart, Physica B **350**, e217 (2004).
[54] C. R. H. Bahl, K. Lefmann, T. B. S. Jensen, P.-A. Lindgård, D. E. Madsen, and S. Mørup (unpublished)
[55] A. H. Morrish, *The Physical Principles of Magnetism* (Wiley, New York, 1965).
[56] C. Kittel, Phys. Rev. **82**, 565 (1951).
[57] F. Keffer and C. Kittel, Phys. Rev. **85**, 329 (1952).
[58] R. K. Wangsness, Phys. Rev. **86**, 146 (1952); **91**, 1085 (1953).
[59] F. Bødker, M. F. Hansen, C. B. Koch, K. Lefmann, and S. Mørup, Phys. Rev. B **61**, 6826 (2000).

# Paper VI

# Thermoinduced magnetization and uncompensated spins in antiferromagnetic nanoparticles

Daniel Esmarch Madsen* and Steen Mørup†
*Department of Physics, Bldg. 307, Technical University of Denmark, DK-2800 Kgs. Lyngby, Denmark*
(Received 22 March 2006; revised manuscript received 1 June 2006; published 10 July 2006)

We have investigated the combined effect of an uncompensated moment and the thermoinduced magnetization on the initial susceptibility of nanoparticles of antiferromagnetic materials. We find that for nanoparticles with small values of the anisotropy and exchange fields, the thermoinduced magnetization may be predominant at finite temperatures. In other cases the uncompensated moment may be predominant.

DOI: 10.1103/PhysRevB.74.014405 PACS number(s): 75.75.+a, 75.50.Ee, 75.50.Tt

## I. INTRODUCTION

The magnetic properties of antiferromagnetic nanoparticles have in recent years received much attention. Unlike their bulk counterparts, such nanoparticles possess a finite, albeit small, magnetic moment, originally attributed by Néel[1] to the uncompensated spins present in nanoparticles due to their finite size.

Recently, the existence of another contribution to the magnetic moment of nanoparticles has been suggested.[2,3] This so-called thermoinduced magnetic moment is due to thermally induced spin wave excitations in the form of a uniform precession mode. When this mode is excited, the two sublattices are not strictly antiparallel, and the angle between them increases with increasing excitation energy, leading to a magnetic moment that increases with increasing temperature. Subsequent Monte Carlo simulations of the magnetization of antiferromagnetic nanoparticles support this model.[4]

In several experimental studies of antiferromagnetic nanoparticles, an anomalous increase of the magnetic moment with increasing temperature has in fact been reported and this seems to give experimental support for the existence of thermoinduced magnetization.[2] However, Silva *et al.*[5,6] have pointed out that if the distribution of magnetic moments due to uncompensated spins is disregarded in the analysis of magnetization curves of samples of antiferromagnetic nanoparticles, one may observe an apparent increase of the magnetic moment with temperature, and this may explain the experimental data. It has also been pointed out that the magnetic anisotropy can have a significant influence on magnetization curves of samples of antiferromagnetic nanoparticles.[7,8] Both the moment distribution and the magnetic anisotropy have been neglected in most studies of the magnetization of antiferromagnetic nanoparticles, and therefore, there is not yet unambiguous experimental evidence for thermoinduced magnetization in antiferromagnetic nanoparticles.

In the first derivation of thermoinduced magnetization,[2,3] only perfect antiferromagnetic nanoparticles were considered, i.e., nanoparticles without uncompensated magnetic moments. It has since been debated[9,10] whether the uncompensated magnetic moments in typical antiferromagnetic nanoparticles may be predominant. This would result in a net magnetic moment that decreases with increasing temperature. In order to clarify this, we have extended the previous model for thermoinduced magnetization and calculated the initial susceptibility of antiferromagnetic nanoparticles with a finite uncompensated magnetic moment. We show that the thermoinduced magnetization can be predominant at finite temperatures in particles with relatively small exchange and anisotropy fields and a moderate uncompensated magnetic moment.

## II. MODEL

When considering magnetic nanoparticles, a uniaxial anisotropy is often assumed and the magnetic energy is written as

$$E(\theta) = KV \sin^2 \theta \tag{1}$$

where $K$ is the magnetic anisotropy constant, $V$ is the volume of the particle, and $\theta$ is the angle between the anisotropy axis and the (sublattice) magnetization. At low temperatures, the (sublattice) magnetization will fluctuate around the local energy minima, a process termed collective magnetic excitations.[11] As the temperature is increased, magnetization reversals (i.e., jumps between the two minima at $\theta=0$ and $\theta=\pi$) also take place. This superparamagnetic relaxation can be observed above a critical temperature, known as the blocking temperature ($T_B$), where the time between successive magnetization reversals becomes comparable to the timescale of the experimental method.

The collective magnetic excitations may be thought of as a uniform precession of the spins combined with transitions between precession states with different precession angles. As pointed out previously[3] the uniform precession, which can be considered as a spin wave with wave vector $q=0$, is particularly prominent in nanoparticles. Furthermore, in the antiferromagnetic case it has been shown[12,13] that the two sublattices are not exactly antiparallel during the precession.

In the following we consider a two-sublattice antiferromagnetic nanoparticle, with sublattice magnetic moments $\vec{\mu}_1$ and $\vec{\mu}_2$ (the magnitudes of which are slightly different from the average value $\mu_S$ because of uncompensated spins) as shown in Fig. 1. We here assume that the uncompensated spins are coupled through the ordinary exchange interaction to the other spins, such that their presence is expressed as a difference between $|\vec{\mu}_1|$ and $|\vec{\mu}_2|$, i.e. we write the magnetic moment due to the uncompensated spins, $\mu_u$, as $|\mu_u| = |\mu_1| - |\mu_2|$. For simplicity, we further assume that $\mu_1$ and $\mu_2$ do not depend on temperature, as we are only considering temperatures well below the Nel temperature, i.e., we neglect the

 

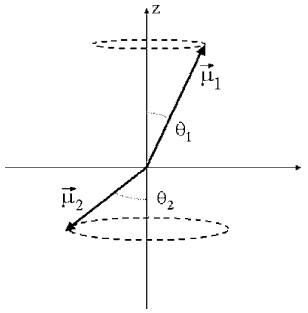


FIG. 1. Coordinate system used in the calculations. The differences in angles and lengths are exaggerated.

influence of spin waves with $q \neq 0$. The precession of the two sublattice magnetic moments around the $z$-axis is described by the angles $\theta_1$ and $\theta_2$, differing slightly from the average value $\theta$. The difference between the two angles is denoted $\theta_\delta = \theta_2 - \theta_1$ such that the resulting magnetic moment in the $z$-direction may be written as

$$\mu_r^z = \mu_1 \cos\theta_1 - \mu_2 \cos\theta_2 \approx \mu_u \cos\theta - \mu_1 \sin\theta \sin\theta_\delta \tag{2}$$

where we have assumed that $\theta_\delta$ is small.

### A. The modes of uniform precession

In order to proceed, one must analyze in some detail the precession modes of such a system. In a perfect antiferromagnetic material the relationship between the precession angles of the two sublattices can be written as[12,13]

$$\frac{\sin\theta_1}{\sin\theta_2} = 1 \pm \delta. \tag{3}$$

Here $\delta \approx \sqrt{2B_a/B_E}$, where $B_E = \mu_0 \lambda_{12} \mu_S / V$ is the exchange field, $\lambda_{12}$ is the exchange constant, and $B_a = KV/\mu_S$ is the anisotropy field.

In order to extend the calculation to a particle with a small uncompensated moment, we treat the system as that of a ferrimagnet, but in the limit where the difference between the sublattice magnetic moments is very small. In such a case, following the derivation by Wangsness[14,15] where the magnetic moments are treated as classical vectors, one may write the equations of motion for each of the two sublattice magnetic moments as

$$\frac{\partial \vec{\mu}_i}{\partial t} = \gamma(\vec{\mu}_i \times \vec{B}_{m,i}), \tag{4}$$

where $i \in (1,2)$, $\gamma$ is the gyromagnetic ratio, and $\vec{B}_{m,i}$ is the field acting on each sublattice. The contributions to this field include the anisotropy field $\vec{B}_a$, the exchange field $\vec{B}_E$, and an applied field, $\vec{B}_{app}$. The anisotropy is assumed to be uniaxial following Eq. (1), the easy axis coinciding with the $z$-axis, along which the external magnetic field is also applied. Further, the particles considered here have a very small net magnetization such that the demagnetization field may be neglected, and in this case the field can be expressed as

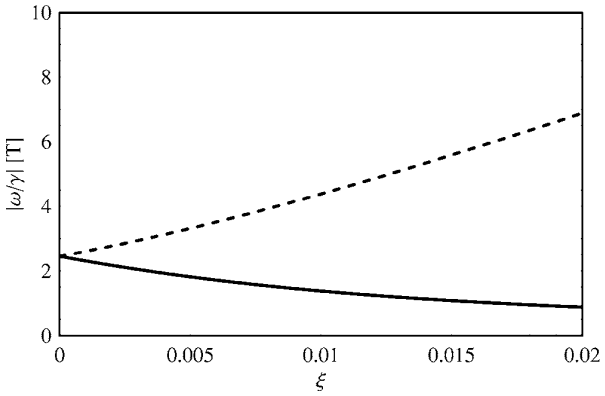


FIG. 2. $|\omega_\pm/\gamma|$ as a function of $\xi$, calculated using Eq. (7), with $B_{app}=0$ T, $B_a=0.01$ T, and $B_E=300$ T. Full line: − mode, dashed line: + mode.

$$\vec{B}_{m,1} = \vec{B}_{app} - \mu_0 \lambda_{12} \frac{\vec{\mu}_2}{V} + \vec{B}_a, \tag{5}$$

$$\vec{B}_{m,2} = \vec{B}_{app} - \mu_0 \lambda_{12} \frac{\vec{\mu}_1}{V} - \vec{B}_a. \tag{6}$$

In the calculation it is assumed that the precession angles are small, i.e., $\cos\theta \approx 1$. Four different modes are found with frequencies pairwise of equal magnitude, i.e., two distinct modes exist (in the following denoted by + and −), and are given by[12]

$$\frac{\omega_\pm}{\gamma} = B_{app} - \frac{\xi B_E}{2} \pm B_E \sqrt{\frac{\delta^4}{4} + \delta^2\left(1 + \frac{\xi}{2}\right) + \frac{\xi^2}{4}}, \tag{7}$$

where $\xi = \mu_r^z / \mu_2^z$. The dependence of $\omega_\pm$ on $\xi$ is illustrated in Fig. 2.

For the precession angles we find in the limit where $\xi \ll \delta$

$$\frac{\mu_1}{\mu_2} \frac{\sin\theta_1}{\sin\theta_2} \approx 1 + \frac{\xi}{2} \pm \delta \tag{8}$$

which, when compared with Eq. (3), shows that the uncompensated moment itself will have an effect on the relative precession angles.

By expressing the angles $\theta_1$ and $\theta_2$ in terms of $\theta$ and $\theta_\delta$ one finds

$$\frac{\sin\theta_1}{\sin\theta_2} \approx 1 + \cot\theta \sin\theta_\delta. \tag{9}$$

When inserting this into Eq. (8) and solving for $\sin\theta_\delta$ one obtains

$$\sin\theta_{\delta_{(\pm)}} \approx \left(\frac{1}{2}\frac{\mu_r^z}{\mu_1 \cos\theta} - \frac{\mu_u}{\mu_1} \pm \delta\frac{\mu_2}{\mu_1}\right)\tan\theta. \tag{10}$$

Inserting this in Eq. (2) gives

$$\mu^{z}_{r(\pm)} \approx \mu_u \left[ \frac{2\cos\theta}{2-\sin^2\theta} \right] \pm 2\delta\mu_2 \left[ \frac{\cos\theta}{2\cot^2\theta+1} \right] \quad (11)$$

after averaging over the fast precessional motion.

### B. The initial susceptibility

Two precession states have been found, and with two possible orientations with respect to $B_{app}$ one is left with four possible combinations. Hence, using Boltzmann statistics one obtains for a particle in thermal equilibrium, i.e., for $T > T_B$

$$\langle \mu \rangle_T = \frac{1}{Z} \sum_\theta P(\theta) \times (\mu_{r+}[e^{-\mu_{r+}B/k_BT} - e^{\mu_{r+}B/k_BT}] + \mu_{r-}[e^{-\mu_{r-}B/k_BT} - e^{\mu_{r-}B/k_BT}]), \quad (12)$$

where $Z$ is the partition function

$$Z = e^{-\mu_{r+}B/k_BT} + e^{\mu_{r+}B/k_BT} + e^{-\mu_{r-}B/k_BT} + e^{\mu_{r-}B/k_BT} \quad (13)$$

and $P(\theta)$ is the probability of finding a precession state with angle $\theta$. In the following we consider the initial susceptibility $\chi_i$ for a single particle, i.e., the limit where $\mu_\pm B_{app} \ll k_BT$. In this case $Z \approx 4$, and we find from Eq. (12)

$$\chi_i = \frac{1}{2} \frac{\mu_0}{Vk_BT} \sum_\theta P(\theta)(\mu^2_{r+} + \mu^2_{r-}), \quad (14)$$

When inserting Eq. (11) in Eq. (14) we obtain

$$\chi_i = \frac{\mu_0}{Vk_BT} \sum_\theta P(\theta) \times \left( \frac{4\mu_u^2 \cos^2\theta}{(2-\sin^2\theta)^2} + \frac{4\delta^2\mu_2^2 \cos\theta}{(2\cot^2\theta+1)^2} \right). \quad (15)$$

Using that $\theta_1 \approx \theta_2 \approx \theta$ we obtain by use of Eq. (1)

$$P(\theta) = \frac{e^{-\alpha \sin^2\theta}}{\sum_\theta e^{-\alpha \sin^2\theta}}, \quad (16)$$

where $\alpha = KV/k_BT$. Inserting this into (15) and assuming that the precession states are close-lying, such that the sums may be turned into integrals, we finally obtain

$$\chi_i = \frac{\mu_0}{V} \left[ \frac{\mu_u^2}{k_BT} \frac{\int_0^{\pi/2} e^{-\alpha \sin^2\theta} [4\cos^2\theta \sin\theta/(2-\sin^2\theta)^2] d\theta}{\int_0^{\pi/2} \sin\theta e^{-\alpha \sin^2\theta} d\theta} + \frac{4\delta^2\mu_2^2}{k_BT} \frac{\int_0^{\pi/2} e^{-\alpha \sin^2\theta} [\cos\theta \sin\theta/(2\cot^2\theta+1)^2] d\theta}{\int_0^{\pi/2} \sin\theta e^{-\alpha \sin^2\theta} d\theta} \right]. \quad (17)$$

If we assume, as in the previous derivations[2,3] that the temperature is low such that only the lowest precession states are occupied, we may write

$$\chi_i \approx \frac{\mu_0}{V} \left[ \frac{\mu_u^2}{k_BT} + \frac{\delta^2\mu_2^2}{k_BT} \frac{\int_0^\infty x^5 e^{-\alpha x^2} dx}{\int_0^\infty x e^{-\alpha x^2} dx} \right] = \frac{\mu_0}{V} \left[ \frac{\mu_u^2}{k_BT} + \frac{2\delta^2\mu_2^2}{(KV)^2} k_BT \right], \quad (18)$$

where the first term is what we would expect from the uncompensated magnetic moment alone, and the second term is due to the thermoinduced moment for a pure antiferromagnet obtained previously.[2,3] Hence, in this approximation, the uncompensated moment simply results in an extra term for the initial susceptibility. By using that $\mu_2 \approx \mu_S$, this may be expressed as

$$\chi_i \approx \frac{\mu_0}{V} \left( \frac{\mu_u^2}{k_BT} + \frac{4k_BT}{B_aB_E} \right). \quad (19)$$

According to Eq. (19) the contribution due to the thermoinduced magnetization will be predominant for $T > \mu_u \sqrt{B_aB_E}/2k_B$. Thus a particle in which the thermoinduced contribution is measurable must have small exchange and anisotropy fields and the uncompensated moment should not be too large. We have simulated the initial susceptibility of nanoparticles by use of Eq. (19). We have used $V = 10^{-24}$ m$^3$, $B_a = 0.01$ T, and $B_E = 300$ T. These values are of the same order of magnitude as those of, for example, ferritin and typical NiO nanoparticles. Magnetization curves for three different values of the uncompensated moment, $\mu_u = 50$, 100, and $200\mu_B$ are shown in Fig. 3. For simplicity, we have assumed that the blocking temperature is a sharp transition. Thus, the contributions from the uncompensated moment are only included at temperatures above the blocking temperature, which here is assumed to be 25 K. Below $T_B$ the contribution from the uncompensated moment to $\chi_i$ is negligible, when the applied field is parallel to the easy axis, but because there is no energy barrier between states with opposite directions of the thermoinduced moment,[2] one should expect it to contribute to the susceptibility even at very low temperatures. At higher temperatures, the assumptions concerning small values of the angles $\theta_1$ and $\theta_2$ may not be fulfilled, and Eqs. (18) and (19) may not be good approximations to the susceptibility. The value of $\langle \cos\theta \rangle$ depends linearly of temperature and is given by[3,11]

$$\langle \cos\theta \rangle \approx 1 - \frac{k_BT}{2KV}. \quad (20)$$

For a particle with sublattice magnetization $M_s = \mu_s/V \approx 10^6$ A m$^{-1}$ one finds that $K = B_aM_s \approx 10^4$ J m$^{-3}$. At 100 K we then find that $\langle \cos\theta \rangle \approx 0.93$, i.e., the condition $\langle \cos\theta \rangle \approx 1$ is reasonably well fulfilled at temperatures up to around 100 K. In Fig. 3, we have therefore only shown data up to 100 K.

## III. DISCUSSION

Most of the previously published magnetization data for antiferromagnetic nanoparticles have been analyzed using a

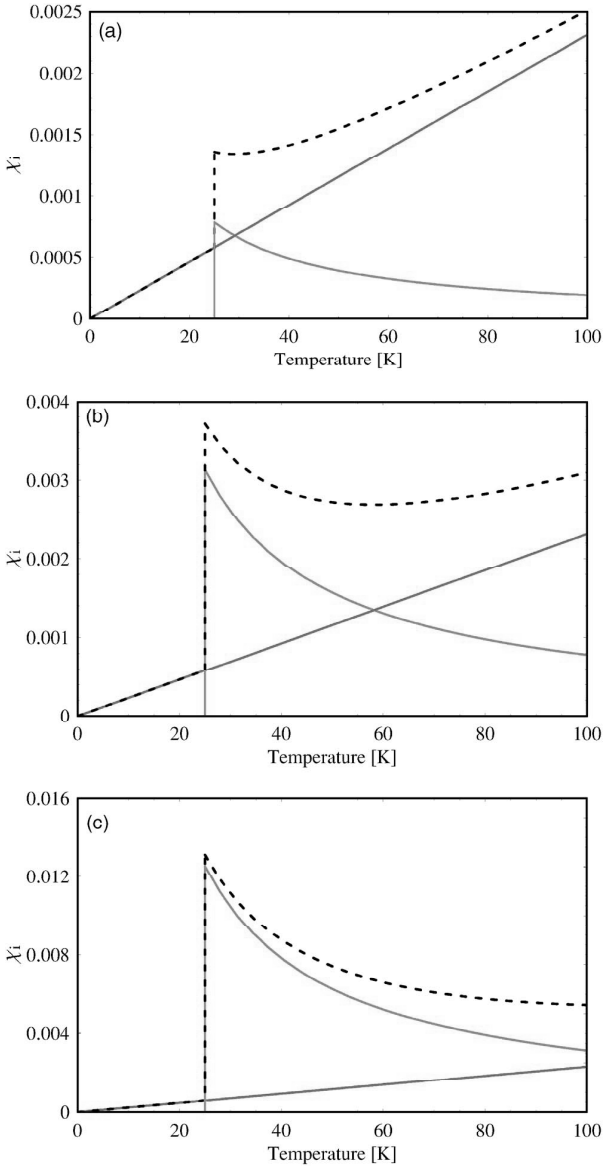


FIG. 3. (Color online) Simulated $\chi_i$ vs temperature curves, with $V=10^{-24}$ m$^3$, $B_a=0.01$ T, $B_E=300$ T, and $\mu_u=$(a) $50\mu_B$, (b) $100\mu_B$, and (c) $200\mu_B$. The dashed line shows the total susceptibility, the increasing full line shows the thermoinduced contribution, while the decreasing full line shows the contribution from the uncompensated spins.

model in which it is assumed that the magnetization is given by the sum of a Langevin function and a linear term. However, as it has been pointed out by Silva *et al.*,[5,6] the inevitable distributions in particle size and particle moments may result in erroneous values of the magnetic moment when this simple model is used. Furthermore, because of the relatively small values of the magnetic moments of antiferromagnetic nanoparticles the magnetic anisotropy plays a relatively larger role in magnetization measurements than in nanoparticles of ferro- and ferrimagnetic nanoparticles, and this can also result in erroneous results when a simple data analysis is used.[7,8] It has been suggested[8,16] that one should focus on the initial susceptibility when analyzing magnetization data for antiferromagnetic nanoparticles, because $\chi_i$ for a sample of randomly oriented nanoparticles does not depend on the anisotropy and the detailed form of the size distribution.

In practice, the distribution in the values of the magnetic moments of the particles will smear the features around 25 K in Fig. 3, and it may not be possible to conclude whether an initial susceptibility, which increases with temperature, is due to the distribution of blocking temperatures or if it is due to thermoinduced magnetization. Furthermore, in a sample of randomly oriented particles at temperatures below $T_B$, the uncompensated magnetic moments give rise to a nonzero, temperature-independent contribution to the susceptibility given by[17]

$$\chi = a\frac{\mu_0\mu_u^2}{|K|V^2}, \tag{21}$$

where $a=\frac{1}{2}\langle\sin^2\beta\rangle$ and $\beta$ is the angle between the applied field and the easy axis. The average is over all particles. In an analysis of the initial susceptibility of antiferromagnetic nanoparticles, it is also necessary to take into account that the antiferromagnetic susceptibility $\chi_{AF}$, which is due to the canting of the sublattice moments in response to the applied field, also contributes to the total susceptibility. This contribution increases with temperature like the contribution from the thermoinduced moment. The value of $\chi_{AF}$ is about $1/\lambda_{12}$ at the Néel temperature.

It should also be realized that surface effects and defects in the interior of a nanoparticle with antiferromagnetic exchange coupling constants can result in localized, noncollinear spin structures, which can contribute to the net magnetic moment.[18,19] The magnitude of this contribution will depend on the particle size, the surface structure, and the concentration of defects. However, normally this contribution to the magnetic moment is expected to be small compared to those discussed above, because only a limited number of spins contribute, and the magnetic moments due to the localized noncollinear spin structures may to a large extent cancel out due to more or less random orientations.

## IV. SUMMARY

We have extended the previous model for thermoinduced magnetization in antiferromagnetic nanoparticles with the effect of an uncompensated moment. We find that the uncompensated moment may contribute significantly, as compared to the thermoinduced moment, to the initial susceptibility of such particles. However, for nanoparticles with values of the exchange field and the anisotropy field that are not too large, the thermoinduced magnetization may give a predominant contribution to the initial susceptibility at finite temperatures.

## ACKNOWLEDGMENTS

The authors would like to thank Cathrine Frandsen and Christian R. H. Bahl for valuable comments and suggestions. This work was supported by the Danish Research Council for Technology and Production Sciences.

*Electronic address: daniel.madsen@fysik.dtu.dk
†Electronic address: morup@fysik.dtu.dk

[1] L. Néel, C. R. Hebd. Seances Acad. Sci. **252**, 4075 (1961).
[2] S. Mørup and C. Frandsen, Phys. Rev. Lett. **92**, 217201 (2004).
[3] S. Mørup and B. R. Hansen, Phys. Rev. B **72**, 024418 (2005).
[4] G. Brown, A. Janotti, M. Eisenbach, and G. M. Stocks, Phys. Rev. B **72**, 140405(R) (2005).
[5] N. J. O. Silva, V. S. Amaral, and L. D. Carlos, Phys. Rev. B **71**, 184408 (2005).
[6] N. J. O. Silva, L. D. Carlos, and V. S. Amaral, Phys. Rev. Lett. **94**, 039707 (2005).
[7] S. Mørup and C. Frandsen, Phys. Rev. Lett. **94**, 039708 (2005).
[8] D. E. Madsen, S. Mørup, and M. F. Hansen, J. Magn. Magn. Mater. **305**, 95 (2006).
[9] A. H. MacDonald and C. M. Canali, Phys. Rev. Lett. **94**, 089701 (2005).
[10] S. Mørup and C. Frandsen, Phys. Rev. Lett. **94**, 089702 (2005).
[11] S. Mørup and H. Topsøe, Appl. Phys. Lett. **11**, 63 (1976).
[12] C. Kittel, Phys. Rev. **82**, 565 (1951).
[13] F. Keffer and C. Kittel, Phys. Rev. **85**, 329 (1952).
[14] R. K. Wangsness, Phys. Rev. **86**, 146 (1952).
[15] R. K. Wangsness, Phys. Rev. **91**, 1085 (1953).
[16] C. R. H. Bahl, M. F. Hansen, T. Pedersen, S. Saadi, K. H. Nielsen, B. Lebech, and S. Mørup, J. Phys.: Condens. Matter **18**, 4161 (2006).
[17] J. I. Gittleman, B. Abeles, and S. Bozowski, Phys. Rev. B **9**, 3891 (1974).
[18] J. M. D. Coey, Can. J. Phys. **65**, 1210 (1987).
[19] S. Mørup, J. Magn. Magn. Mater. **266**, 110 (2003).

# Paper VII

IOP PUBLISHING JOURNAL OF PHYSICS: CONDENSED MATTER

J. Phys.: Condens. Matter **20** (2008) 135215 (6pp) doi:10.1088/0953-8984/20/13/135215

# Interactions between goethite particles subjected to heat treatment

**Daniel E Madsen**[1], **Mikkel F Hansen**[2], **Christian B Koch**[3] **and Steen Mørup**[1]

[1] Department of Physics, Technical University of Denmark, DTU Physics, Bldg. 307, DK-2800 Kongens Lyngby, Denmark
[2] Department of Micro- and Nanotechnology, Technical University of Denmark, DTU Nanotech, Bldg. 345 East, DK-2800 Kongens Lyngby, Denmark
[3] Department of Natural Sciences, Faculty of Life Sciences, University of Copenhagen, DK-1871 Frederiksberg C, Denmark

E-mail: demadsen@fysik.dtu.dk

Received 4 February 2008
Published 12 March 2008
Online at stacks.iop.org/JPhysCM/20/135215

**Abstract**

We have studied the effect of heating on the magnetic properties of particles of nanocrystalline goethite by use of Mössbauer spectroscopy. Heating at 150 °C for 24 h leads to a change in the quadrupole shift in the low-temperature spectra, indicating a rotation of the sublattice magnetization directions. Fitting of quantiles, derived from the asymmetrically broadened spectra between 80 and 300 K, to the superferromagnetism model indicates that this change is due to a stronger magnetic coupling between the particles.

## 1. Introduction

Goethite ($\alpha$-FeOOH) is a common mineral, which is often present as a very fine-grained material in soils and sediments [1, 2]. It controls the geochemistry of plant nutrients and pollutants by coprecipitation and surface reactions and records characteristic components of past environments. For example, the discovery of goethite on the surface of Mars [3] gives credibility to the claim that liquid water was present in the past.

Goethite has an orthorhombic unit cell with space group *Pnma*[4]. It is antiferromagnetic with a Néel temperature of about 400 K [4, 5]. The bulk magnetic structure has been suggested to consist of four sublattices, where the spins are inclined $\pm 13^\circ$ with respect to the [010] direction [6]. The particles are usually found to be elongated along the [010] direction. Mössbauer spectra of fine-grained goethite usually show line broadening, which is attributed to fluctuations of the magnetization directions of the grains.

If heated to temperatures above approximately 200 °C, goethite transforms into hematite ($\alpha$-$Fe_2O_3$). Previous studies of goethite have shown that heating at *lower* temperatures can also affect the magnetic properties. Koch *et al* [7] studied samples of goethite heated in air at temperatures from 60 to 105 °C and the results indicated an increase in the strength of the inter-particle interactions. This was suggested to be due to desorption of water from the surface of the particles, leading to a stronger coupling between the particles. In another study, Mørup *et al* [8] heated a sample at 150 °C for 24 h, and observed that the heating induced rather prominent changes in the Mössbauer spectra as the lines became broader and the hyperfine field decreased. They attributed this to a reduction of the average volume of the particles. These differences in behavior are believed to correlate with the synthesis conditions determining the initial aggregation of the crystallites [9]. Betancur *et al* [10] also studied goethite particles synthesized with different methods, and observed upon heating to 107 °C considerable changes in the Mössbauer spectra. In this case the average hyperfine field was also found to decrease as a result of the heat treatment. The authors suggested a model where the heating leads to additional vacancies due to evaporation of water. They suggested that this may lead to a reduction of the magnetic interactions as the hydroxyl groups are mediators of the exchange coupling between the $Fe^{3+}$ ions. Thus, different samples of goethite seem to be affected differently upon heating.

In this work we have studied particles of goethite subjected to heat treatment, with special focus on low-temperature Mössbauer data and quantitative analysis of the

[4] It should be noted that some authors use the space group *Pnmb* which results in a different indexing of directions and lattice planes.

 

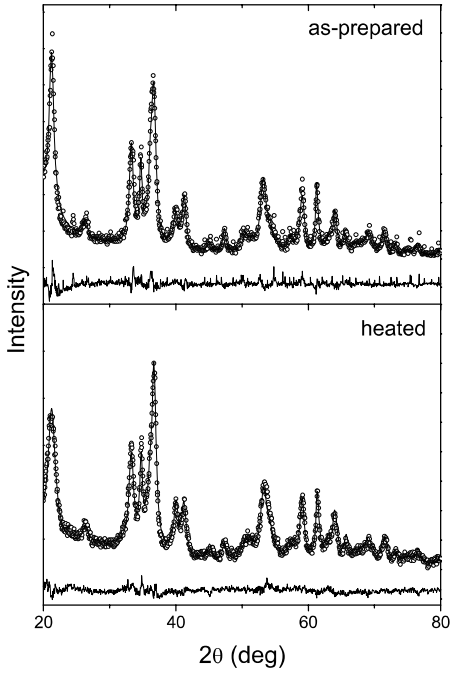


**Figure 1.** XRD data for the as-prepared and heated samples. The fit residue from the Rietveld analysis is shown below each plot.

hyperfine field distributions of the spectra obtained a higher temperatures in order to further elucidate this topic. We find that the magnitude of the quadrupole shift of the heated sample at low temperature is reduced, indicating that the increased degree of inter-particle interactions has led to a rotation of the sublattice magnetization directions. Moreover, when analyzing the individual quantiles of the magnetic hyperfine field distributions of Mössbauer spectra obtained over a range of temperature with the superferromagnetism model [5] we obtain quantitative results for the anisotropy energy barriers and the strength of the inter-particle interactions. These results support the conclusion concerning increased inter-particle interactions after heating.

## 2. Experimental details

Goethite was prepared by acid hydrolysis of an iron nitrate solution. 1.4 mol $Fe(NO_3)_3$ was dissolved in 700 ml 2 M $HNO_3$ and mixed with 2.8 mol NaOH in 2.8 l of water. The mixture was allowed to age at 285 K for approximately 3900 days with periodic stirring. The precipitate was washed in dilute $HNO_3$ three times followed by extensive washing in water. Finally, the sample was dried in air at room temperature. The resulting sample will in the following be referred to as the as-prepared sample.

A sample was heated in air at 150 °C for 24 h and will be referred to as the heated sample. As a bulk reference we used a natural well-crystallized sample from Cornwall, UK (the same as the one used by Mørup *et al* [5]).

The $^{57}$Fe Mössbauer spectra were obtained in a conventional transmission geometry in the constant acceleration mode. The source was $^{57}$Co in Rh. A foil of $\alpha$-Fe was used for calibration at room temperature. Temperatures above 80 K were obtained with a liquid nitrogen cryostat, whereas measurements below 80 K were performed in a closed cycle helium refrigerator. Temperatures above 320 K were obtained in a specially designed oven. Samples were re-measured at 20 K after being measured at elevated temperatures in order to confirm that no changes had been induced during the measurement.

Powder x-ray diffraction (XRD) data were obtained with a Philips PW1820 diffractometer using Cu K$\alpha$ radiation. Rietveld refinements were carried out using the Fullprof software package [11].

Transmission electron microscopy (TEM) images were obtained with a JEOL 3000 FEG microscope equipped with a Gatan 16 Mpix CCD camera. The samples for TEM were ultrasonically dispersed in demineralized water before being transferred (just a few droplets) to a holey carbon film where they were allowed to dry.

**Table 1.** Lattice parameters and particle dimensions (in nm) obtained from the Rietveld analysis of the XRD data. Numbers in parenthesis indicate uncertainty on last digit.

| Sample | $a$ | $b$ | $c$ | $d_{[100]}$ | $d_{[010]}$ | $d_{[001]}$ |
|---|---|---|---|---|---|---|
| As-prepared | 0.947(1) | 0.3026(3) | 0.462(1) | 12(2) | 20(2) | 7(1) |
| Heated | 0.959(1) | 0.3021(3) | 0.461(1) | 9(2) | 16(2) | 3(1) |

## 3. Results

Figure 1 shows XRD data for the two samples. All peaks correspond to those expected for goethite and no other phases are discernible. A Rietveld refinement of the XRD data was carried out to estimate the particles sizes. The refinement was done with the *Pnma* space group, which yielded the lattice parameters listed in table 1. These values are very close to those reported for bulk goethite [12]. In the analysis the shape of the particles was assumed to be ellipsoidal. The resulting dimensions of the crystallites are also reported in table 1.

Figure 2 shows TEM images of the two samples. No significant differences between the two samples could be observed. For both samples, a number of agglomerates are found, each consisting of several smaller rod-like entities bundled together. The dimensions of each rod is approximately 5 nm × 50 nm. It was not possible to determine whether each of these rods constituted a single goethite crystal. It is noteworthy that the sizes obtained from the Rietveld refinement are much different from those found by TEM. This seems to be a common observation for goethite, as it has also be demonstrated in a comparison by Bocquet *et al* [13] between numerous samples of different origin. The discrepancies may be explained by (imperfect) oriented attachment of particles, which is common in goethite samples [14–16], and which can make it difficult to define the crystal size in a unique way.

Figure 3 shows Mössbauer spectra of the two samples obtained at different temperatures. At the lowest temperatures the spectrum consists of a single sextet with narrow lines. As the temperature is increased, these lines become asymmetrically broadened as often observed for nanoparticles of goethite. The development with temperature is similar

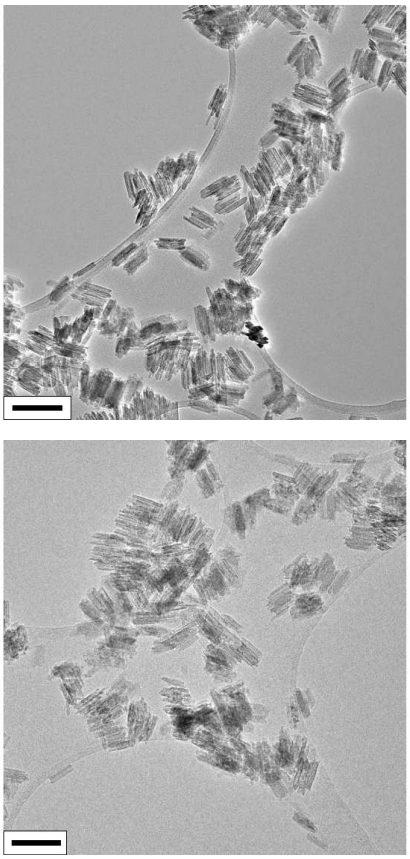

**Figure 2.** TEM images of the as-prepared (top) and heated (bottom) samples. The bar in the lower left corner corresponds to 100 nm.

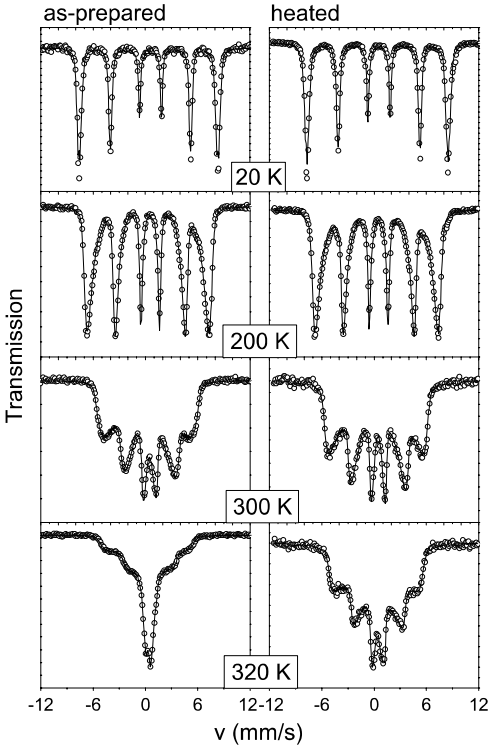


**Figure 3.** Mössbauer spectra of the as-prepared (left) and heated (right) samples. The lines are fits using a distribution of sextets.

for both samples and the differences are only obvious at the highest temperatures. At 320 K the sextet component is most prominent in the spectra of the heated sample. Further spectra were obtained at temperatures up to 368 K. At these temperatures, the spectra of both samples contained a single doublet with narrow lines (data not shown).

## 4. Analysis of the Mössbauer spectra

The low-temperature (20–80 K) Mössbauer spectra could be well fitted with a single sextet with narrow lines. Figure 4 shows the variation of the isomer shift $\delta$, the quadrupole shift $\varepsilon$, and the hyperfine field $B_{\rm hf}$ for the as-prepared and heated samples as a function of temperature. Data for the bulk sample are shown for comparison. Compared to the as-prepared sample, data for the heated sample indicate that the isomer shift is slightly smaller, the absolute value of the quadrupole shift is decreased, and the magnetic hyperfine field remains essentially unaffected.

As the temperature is increased above 80 K, the fits with only a single sextet become increasingly unsatisfactory due to the asymmetrical broadening of the lines. As a consequence we have fitted the spectra with a distribution of sextets, all with the same value of the isomer shift and the quadrupole shift, but with different hyperfine fields [17]. Figure 3 shows the resulting fits. We have for comparison also fitted the 20 K spectra using a distribution. However, as one may observe this does not lead to very satisfactory fits, due to the small number of steps within such a narrow distribution. As a consequence, the analysis presented in this section is only based on data from 80 K and up.

At 368 K, the spectra of both samples could be satisfactory fitted using a single doublet with an quadrupole splitting $\Delta E_{\rm Q}$ of $0.50 \pm 0.01$ mm s$^{-1}$. At this temperature the isomer shifts and quadrupole splittings obtained for the two samples were identical within the experimental uncertainty.

Figure 5 shows the hyperfine field distributions, obtained for the spectra shown in figure 3. At the highest temperatures, the emerging doublet component becomes apparent in the distributions as a sextet component with a small (<5 T) hyperfine field. Based on the hyperfine field distributions, $p[B_{\rm hf}(T)]\,{\rm d}B_{\rm hf}$, we could follow the temperature dependence of certain $f$-quantiles, $B_f(T)$, defined by the relation

$$f = \int_0^{B_f(T)} p\,[B_{\rm hf}(T)]\ {\rm d}B_{\rm hf}. \qquad (1)$$

These temperature dependences were analyzed with the model of 'superferromagnetism' [5, 18, 19]. In this model each particle is assumed to be coupled to its neighbors through ordinary exchange interactions. In the absence of this coupling, each particle is assumed to exhibit fast superparamagnetic relaxation, but the interactions result in an (at least local) ordering of the (sublattice) magnetization directions of the particles below a temperature $T_{\rm p}$.

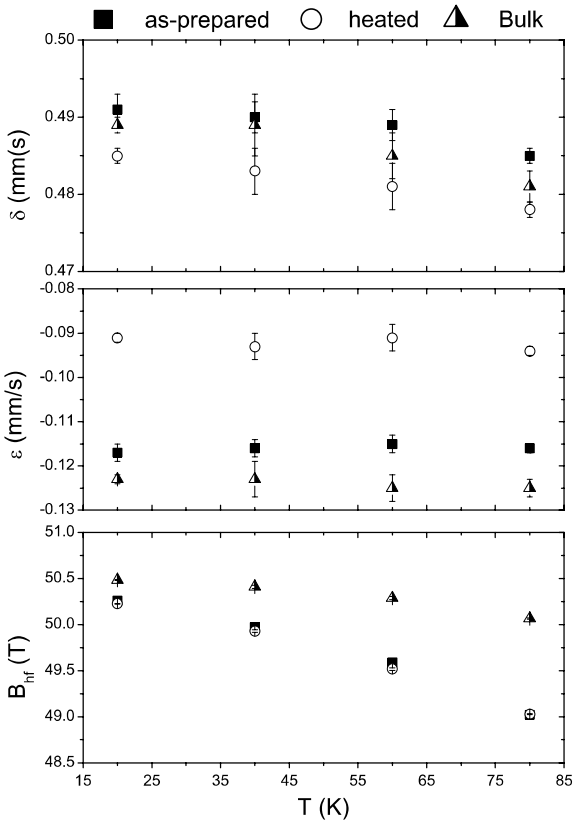


**Figure 4.** Isomer shift ($\delta$), quadrupole shift ($\varepsilon$), and magnetic hyperfine field ($B_{\rm hf}$) as a function of temperature for the as-prepared, heated, and bulk samples.

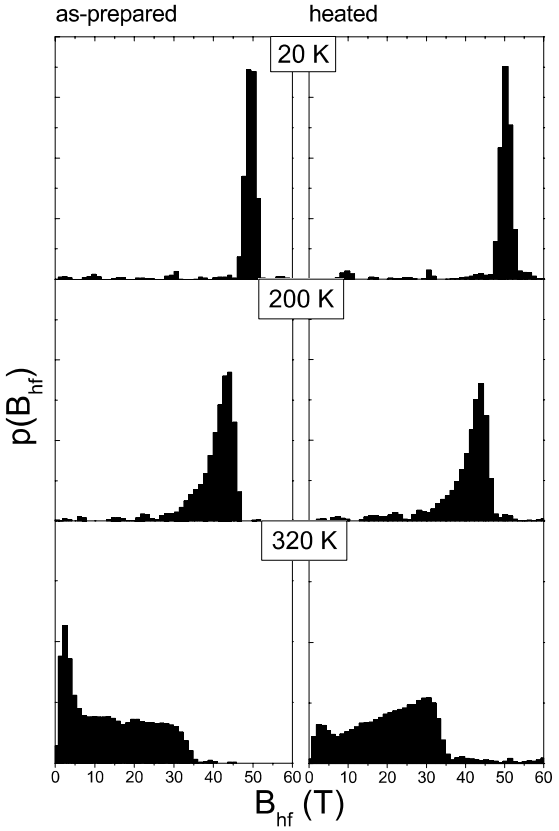


**Figure 5.** Magnetic hyperfine field distributions obtained from fits to a number of the Mössbauer spectra shown in figure 3.

The interaction energy between two crystallites $i$ and $j$ may be written [18]

$$E_{ij} = -\vec{M}_i(T) \cdot K_{\rm ex}^{ij} \vec{M}_j(T), \tag{2}$$

where $K_{\rm ex}$ is an exchange coefficient, which depends on the coupling strength between the two particles. Summing over all neighbors we arrive at

$$E_i = -\vec{M}_i(T) \cdot \sum_j K_{\rm ex}^{ij} \vec{M}_j(T), \tag{3}$$

which in a mean-field approximation reduces to

$$E_i = -K_{\rm m} \vec{M}_i(T) \cdot \langle \vec{M}(T) \rangle, \tag{4}$$

where $K_{\rm m}\langle \vec{M}(T)\rangle$ is the mean field from the all neighboring crystallites, and $K_{\rm m}$ is the effective exchange coefficient.

Introducing the order parameter

$$b(T) \equiv \frac{|\langle \vec{M}(T)\rangle|}{M_0(T)}, \tag{5}$$

where $M_0 = |\vec{M}_i|$ is the saturation value of the (sublattice) magnetization, (4) may be rewritten

$$E_i = -K_{\rm m} M_0^2(T) b(T) \cos\varphi, \tag{6}$$

where $\varphi$ is the angle between $\vec{M}_i$ and $\langle \vec{M}(T)\rangle$. As a result we write the total magnetic energy of crystallite $i$ as

$$E_{\rm tot} = -E_{\rm a} \cos^2\theta - K_{\rm m} M_0^2(T) b(T) \cos\varphi \tag{7}$$

where $E_{\rm a} = KV$ is the anisotropy energy barrier, $K$ is the anisotropy constant, $V$ is the volume of the particle, and $\theta$ is the angle between $M$ and the magnetic easy axis (a uniaxial anisotropy has been assumed).

Nanoparticles in close contact often exhibit oriented attachment, i.e., they are oriented along common crystallographic orientations. This has been observed in studies of $TiO_2$ [20], $\alpha$-$Fe_2O_3$ [21], and goethite [14–16]. In this case, the easy axes of magnetization must be pointing in almost the same direction. As a first approximation one may therefore assume that $\langle \vec{M}(T)\rangle$ is parallel to the easy axis of particle $i$ [19] and the above expression reduces to

$$E_{\rm tot} = -E_{\rm a} \cos^2\theta - K_{\rm m} M_0^2(T) b(T) \cos\theta. \tag{8}$$

The resulting temperature variation is found using Boltzmann statistics as

$$b(T) = \frac{\int_0^\pi \exp(-\beta E_{\rm tot}) \sin\theta \cos\theta \, {\rm d}\theta}{\int_0^\pi \exp(-\beta E_{\rm tot}) \sin\theta \, {\rm d}\theta}, \tag{9}$$

where $\beta = (k_{\rm B}T)^{-1}$. This expression for the temperature dependence of $b(T)$ can be solved numerically. In the absence

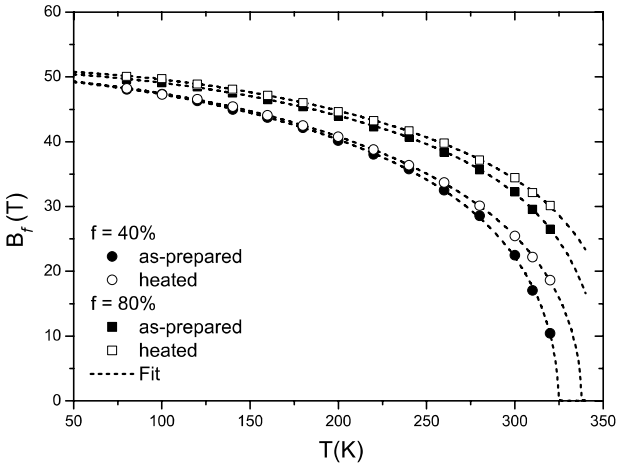


**Figure 6.** $B_f$ versus $T$ for $f = 40$ and 80% extracted from the hyperfine field distributions. The fits to the superferromagnetism model are shown as lines.

of anisotropy, (9) yields

$$b^0(T) = \mathscr{L}\left(\beta K_{\mathrm{m}} M_0^2(T) b^0(T)\right), \tag{10}$$

where $\mathscr{L}(x)$ is the Langevin function. The resulting ordering temperature in the absence of anisotropy may be expressed as [18]

$$T_{\mathrm{p}}^0 = \frac{K_{\mathrm{m}} M_0^2(T_{\mathrm{p}}^0)}{3k_{\mathrm{B}}}. \tag{11}$$

We will in the following report results in terms of $E_{\mathrm{int}} = K_{\mathrm{m}} M_0^2(T_{\mathrm{p}}^0) = 3k_{\mathrm{B}} T_{\mathrm{p}}^0$ and $E_{\mathrm{a}}$. In our case, we fitted (9) to the experimentally found order parameter

$$b_f(T) = \frac{B_f(T)}{B_0(T)}, \tag{12}$$

where $B_0(T)$ is the hyperfine field for the bulk sample, in order to obtain values of the interaction strength and the anisotropy energy barrier for each quantile. In previous studies of goethite particles [5, 7], the *average* hyperfine fields were fitted with the same model, but the estimated magnetic anisotropy was in that case found to be negligible. As discussed by Hansen *et al* [19] the influence of the anisotropy energy may be averaged out if only the average hyperfine field is considered.

Figure 6 shows the fits for selected quantiles. We have only considered quantiles between 40 and 80% as the noise in the derived hyperfine field distributions leads to less reliable quantiles outside this range. The superferromagnetism model is found to fit the data very well.

Figure 7(a) shows the obtained interaction strengths. A slightly larger value (∼60 K on average) of $E_{\mathrm{int}}/k_{\mathrm{B}}$ is observed for the heated sample compared to the as-prepared sample. Figure 7(b) shows the anisotropy energy barriers. The values of $E_{\mathrm{a}}/k_{\mathrm{B}}$ are found to be very similar for the two samples, and all increase with increasing $f$, from close to 400 K at $f = 40\%$ to ≈1600 K at $f = 80\%$.

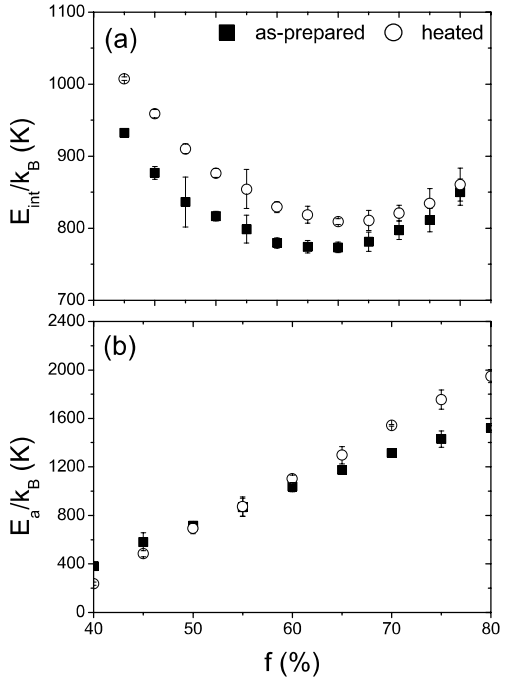


**Figure 7.** (a) Interaction strength ($E_{\mathrm{int}}$) and (b) anisotropy energy barrier ($E_{\mathrm{a}}$) as a function of $f$. Both are shown in units of K.

## 5. Discussion

From the TEM images, we see that in our case the heating has little, if any, effect on the morphology of the particles. The XRD data also confirm the absence of new phases, hence no phase transformation has taken place. This is also indicated by the observation that $\delta$ and $B_{\mathrm{hf}}$ at the lowest temperatures are very similar for the two samples. The finding that almost the same value of the barrier (except for the highest quantiles) is found for the two samples also indicates that the heating has not resulted in a volume change.

The sizes obtained from XRD differ and the particle dimensions seem to be reduced as a result of the heating. However, no such change could be inferred from the TEM images. These differences could be due to the fact that microstrain was not included in our Rietveld refinement of the XRD data.

From figure 4 it can be concluded that the heat treatment results in a change in the quadrupole shift $\varepsilon$. In general, the magnitude of the quadrupole *shift* depends on parameters ($V_{zz}$, $\eta$) pertaining to the electric field gradient (EFG) of the material, and the angles between the principal component of the EFG and the magnetic hyperfine field. On the other hand, the quadrupole *splitting* ($\Delta E_{\mathrm{Q}}$) depends only on $V_{zz}$ and $\eta$. As the quadruple splittings at high temperature were identical, the observed change cannot be attributed to differences in the EFG, but must be related to the angles between the EFG and the hyperfine field. Frandsen and Mørup [22] also observed a similar change in $\varepsilon$ when the interactions between 8 nm particles of hematite ($\alpha$-$Fe_2O_3$) were varied. In the case of hematite, the value of $\varepsilon$ depends on the angle $\phi$ between the

magnetization and the EFG (assuming uniaxial symmetry) as

$$\varepsilon = \varepsilon_0(3\cos^2\phi - 1)/2. \quad (13)$$

It was suggested that the particle interactions result in a rotation of the sublattice magnetization directions. Although the EFG in goethite is more complex [23] we suggest that a similar effect is in play here. The mechanism behind this spin rotation was in the case of hematite suggested to be interactions between particles with non-aligned lattice planes [22]. Because of the exchange coupling between the particles, the sublattice magnetization in each particle is slightly rotated.

The magnetic anisotropy constant of goethite is on the order of $5 \times 10^4$ J m$^{-3}$ [6, 13]. With a particle volume on the order of 500–1000 nm$^3$ (table 1), one finds that $KV \gg k_B T$ at room temperature. Therefore, one should not expect relaxation of the sublattice magnetization directions of a particle as a whole. However, high-resolution TEM (HRTEM) studies of the as-prepared sample have shown that the rod-shaped particles contain many low-angle grain boundaries [24]. The net exchange interaction between neighboring grains may be weak because of the magnetic mismatch in the grain boundary, and therefore the (sublattice) magnetization directions in the grains may fluctuate. This can explain the relaxation effects seen in the Mössbauer spectra. The magnetic mismatch may also result in magnetic frustration and a related spin-canting near a grain boundary. The present Mössbauer data show that the heating results in some suppression of the magnetic fluctuations and also leads to a larger spin rotation. Both effects can be explained by a stronger exchange coupling across the interfaces between the grains, which could be related to, for example, some structural relaxation in the grain boundaries or to evaporation of impurities such as water.

The Néel temperature, $T_N$, of bulk goethite is close to 400 K. In our as-prepared sample, the sextet has almost completely collapsed to a doublet at 320 K. It has been debated whether this collapse should be attributed to fast superparamagnetic relaxation or to a reduction of $T_N$ [25]. If the particles are not superparamagnetic to begin with, the observed changes after heating could also be explained by an increase in $T_N$. As the heating does not seem to cause an increase of the particle volume, such a change in $T_N$ would imply stronger magnetic interactions, possibly through a change in the number of imperfections in the crystal structure. Bocquet and Hill [26] have found such a correlation between $T_N$ and the number of vacancy defects. Although it is plausible that sample heating results in a change in the number of lattice defects, it is observed that, upon heating our sample, the value of $\varepsilon$ moves *away* from the bulk value, rather than approach it as one would expect from such a correlation. We therefore do not find that such a mechanism can explain the effects observed in our current study.

## 6. Summary

We have studied samples of goethite before and after heat treatment. We find that the quadrupole shift at low temperatures is markedly different in the heated sample, indicating a rotation of the sublattice magnetization directions. Using the model of superferromagnetism to analyze the spectra at elevated temperatures, we find that the heating increases the inter-particle interaction, in agreement with previous studies. We conclude that this is the probable cause of the rotation of the sublattice magnetization directions.

## Acknowledgments

The authors would like to thank Flemming Grumsen for help with obtaining the TEM images and Bente Lebech for help with the Rietveld analysis. This work was supported by the Danish Research Council for Technology and Production Sciences.

## References

[1] Schwertmann U and Cornell R M 1991 *Iron Oxides in the Laboratory: Preparation and Characterization* (Weinheim: VCH)
[2] Schwertmann U and Cornell R M 2003 *The Iron Oxides: Structure, Properties, Reactions, Occurrences and Uses* 2nd edn (Weinheim: Wiley–VCH)
[3] Morris R V, Klingelhöfer G, Schröder C, Rodionov D S, Yen A, Ming D W, de Souza P A, Fleischer I, Wdowiak T, Gellert R, Bernhardt B, Evlanov E N, Zubkov B, Foh J, Bonnes U, Kankeleit E, Gütlich P, Renz F, Squyres S W and Arvidson R E 2006 *J. Geophys. Res.-Planet.* **111** E02S13
[4] Forsyth J B, Hedley I G and Johnson C E 1968 *J. Phys. C: Solid State Phys.* **1** 179
[5] Mørup S, Madsen M B, Franck J, Villadsen J and Koch C J W 1983 *J. Magn. Magn. Mater.* **40** 163
[6] Coey J M D, Barry A, Brotto J M, Rakoto H, Brennan S, Mussel W N, Collomb A and Fruchart D 1995 *J. Phys.: Condens. Matter* **7** 759
[7] Koch C J W, Madsen M B, Mørup S, Christiansen G, Gerward L and Villadsen J 1986 *Clay. Clay Miner.* **34** 17
[8] Mørup S, Meaz T M, Koch C B and Hansen H C B 1997 *Z. Phys.* D **40** 167
[9] Koch C J W, Madsen M B and Mørup S 1985 *Surf. Sci.* **156** 249
[10] Betancur J D, Barrero C A, Greneche J M and Goya G F 2004 *J. Alloys Compounds* **369** 247
[11] http://www-llb.cea.fr/fullweb/
[12] Szytula A, Burewicz A, Dimitrij Z, Krasnick S, Rzany H, Todorovi J, Wanic A and Wolski W 1968 *Phys. Status Solidi* **26** 429
[13] Bocquet S, Pollard R J and Cashion J D 1992 *Phys. Rev.* B **46** 11657
[14] Nesterova M, Moreau J and Banfield J F 2003 *Geochim. Cosmochim. Acta* **67** 1177
[15] Burleson D J and Penn R L 2006 *Langmuir* **22** 402
[16] Penn R L, Erbs J J and Gulliver D M 2006 *J. Cryst. Growth* **293** 1
[17] Wivel C and Mørup S 1981 *J. Phys. E: Sci. Instrum.* **14** 605
[18] Mørup S 1983 *J. Magn. Magn. Mater.* **37** 39
[19] Hansen M F, Koch C B and Mørup S 2000 *Phys. Rev.* B **62** 1124
[20] Penn R L and Banfield J F 1999 *Geochim. Cosmochim. Acta* **63** 1549
[21] Frandsen C, Bahl C R H, Lebech B, Lefmann K, Theil Kuhn L, Keller L, Andersen N H, von Zimmermann M, Johnson E, Klausen S N and Mørup S 2005 *Phys. Rev.* B **73** 214406
[22] Frandsen C and Mørup S 2005 *Phys. Rev. Lett.* **94** 027202
[23] Barrero C A, Vandenberghe R E, De Grave E, Morales A L and Perez G 2003 *Hyperfine Interact.* **148** 337
[24] Madsen D E *et al* unpublished
[25] Bocquet S and Kennedy S J 1992 *J. Magn. Magn. Mater.* **109** 260
[26] Bocquet S and Hill A J 1995 *Phys. Chem. Minerals* **22** 524

# Paper VIII

Version 29.05.08

# Magnetic fluctuations in nano-sized goethite (α-FeOOH) grains

D. E. Madsen[1], L. Cervera-Gontard[2], T. Kasama[3], R. E. Dunin-Borkowski[2], C. B. Koch[4], M. F. Hansen[5], C. Frandsen[1] and S. Mørup[1].

[1]Department of Physics, Building 307, Technical University of Denmark, DK-2800 Kongens Lyngby, Denmark

[2]Center for Electron Nanoscopy, Building 307, Technical University of Denmark, DK-2800 Kongens Lyngby, Denmark

[3]Department of Materials Science and Metallurgy, University of Cambridge, Pembroke Street, Cambridge CB2 3QZ, UK

[4]Department of Natural Sciences, Faculty of Life Sciences, University of Copenhagen, Thorvaldsensvej 40, DK-1871 Frederiksberg C, Denmark

[5]Department of Micro- and Nanotechnology, Technical University of Denmark, DTU Nanotech, Building 345 East, DK-2800 Kongens Lyngby, Denmark

***Abstract.***

Mössbauer spectra of antiferromagnetic goethite (α-FeOOH) particles usually show an asymmetric line broadening, which increases with increasing temperature, although the magnetic anisotropy is expected to be so large that magnetic relaxation effects should be negligible. By use of high-resolution transmission electron microscopy (HRTEM) we have studied a sample of goethite particles and have found that the particles contain many defects such as low-angle grain boundaries, in accordance with previous studies of other samples of goethite particles. Such defects can result in a magnetic mismatch at the grain boundaries between nanometer-sized grains, leading to a weakened magnetic coupling between the grains. We show that the Mössbauer data of goethite can be explained by fluctuations of the sublattice magnetization directions in such weakly coupled grains. It is likely that the influence of defects such as low-angle grain boundaries also play a role for the magnetic properties in other antiferromagnetic nanograin systems. We discuss the results in relation to Mössbauer studies of α-$Fe_2O_3$ and α-$Fe_2O_3$/NiO nanoparticles.

PACS numbers: 61.72.Ff; 68.37.Og; 75.50.Tt; 76.80.+y.

Corresponding author: Daniel E. Madsen, Department of Physics, Building. 307, Technical University of Denmark, DK-2800 Kongens Lyngby, Denmark.
E-mail: Daniel.Madsen@fysik.dtu.dk

## 1. Introduction

Crystallographic defects can have a significant influence on the magnetic properties of materials. In ferromagnetic materials, domain walls may be trapped by, for example, dislocations and grain boundaries, and therefore structural defects usually increase the coercivity. However, in nanocrystalline ferromagnets small grain sizes can lead to ultrasoft magnetic properties in accordance with the random anisotropy model [1, 2]. In ferrimagnets, defects such as vacancies, substituted diamagnetic ions and missing neighbor atoms at surfaces can lead to localized spin-canting, which may result in a reduced magnetization [3-5]. The influence of defects in antiferromagnetic materials like goethite ($\alpha$-FeOOH) seems, however, to be less well understood.

Goethite is a common antiferromagnetic mineral in soils and sediments on Earth [6], and it has recently also been found on Mars [7]. Goethite has an orthorhombic unit cell (space group *Pnma*), and a Néel temperature around 400 K [8, 9]. Usually, goethite appears as rod-shaped nanoparticles, both when formed in nature and when synthesized in the laboratory. The sublattice magnetization directions are close to the [010] direction along which the particles are elongated [10]. In addition to cation substitution [6], natural goethite crystals often exhibit dislocations [11]. Mössbauer spectra of goethite particles commonly show an asymmetric line broadening that increases with increasing temperature, and the average hyperfine field decreases much faster with temperature than in well crystallized goethite [9, 12-15]. Usually, Mössbauer spectra of goethite particles do not show the presence of both a doublet and a sextet with a temperature-dependent area ratio over a broad temperature range, as one would expect for superparamagnetic, non-interacting nanoparticles. Instead, the evolution of the spectra with temperature is typical for nanoparticles in which the sublattice magnetization directions fluctuate because of their small size, but the superparamagnetic relaxation is suppressed by interparticle interactions [9, 16-21]. As the magnetic anisotropy constant of goethite is relatively large [10, 12, 22, 23], one would not expect relaxation effects for particles that are larger than about 10 nm. However, substantial line broadening has been seen even in particles that are larger than 100 nm [12, 13]. The unusual magnetic properties of goethite have lead to much debate in the literature [9-16, 23, 24].

In this paper, we present studies of goethite particles by Mössbauer spectroscopy and high-resolution transmission electron microscopy (HRTEM). We show that defects, such as low-angle grain boundaries between small grains within larger, rod-shaped particles, may result in a

substantial weakening of exchange coupling, such that the sublattice magnetization directions of the grains can fluctuate. We also discuss some puzzling observations obtained from samples of interacting nanoparticles of $\alpha$-$Fe_2O_3$ [25] and of interacting $\alpha$-$Fe_2O_3$ and NiO nanoparticles [17], which can be explained by a related weakening of the interface exchange interaction.

## 2. Experimental

Goethite particles were prepared by the acid hydrolysis of an iron nitrate solution. 1.4 mol $Fe(NO_3)_3$ was dissolved in 700 mL 2M $HNO_3$ and mixed with 2.8 L 1M NaOH. The mixture was aged at 285 K for approximately 3900 days with periodic stirring. The precipitate was washed 3 times in dilute $HNO_3$ followed by extensive washing in water, and the sample was dried in air at room temperature. Below, this sample is referred to as the as-prepared sample. In an attempt to physically separate the particles and diminish their size, we also applied low energy ball-milling to the as-prepared sample (1 g) together with nano-sized NaCl (5 g) as a dispersion medium [26] for 48 hours, after which the NaCl was washed out. The ball-milling was performed in a Retsch planetary ball mill with agate vial and balls and a rotation speed of approximately 200 rpm. As a bulk reference, we used a natural, well-crystallized sample from Cornwall, UK [9].

HRTEM, high-angle annular dark field (HAADF) and dark-field (DF) imaging were carried out at 200 kV using JEM-2200FS and FEI Tecnai F20 field emission gun (FEG) TEMs. Lattice images were analyzed using geometrical phase analysis (GPA), a technique that allows the quantitative measurement and mapping of displacement and strain fields by masking and inverse Fourier transforming individual Bragg spots in Fourier transforms of HRTEM images. The phase of each resulting complex image can be related to the displacement field distorting the fringes with respect to a reference lattice with high precision (up to 0.03 Å [27]).

Powder X-ray diffraction (XRD) data were obtained at ambient conditions with a Philips PW 1820 diffractometer using Cu K$\alpha$ radiation. XRD data acquired from the as-prepared and the ball-milled samples showed the presence of goethite only. A Rietveld refinement of the data using the FullProf software [29] was used to determine the average crystallite sizes, which are given in Table 1.

$^{57}$Fe Mössbauer spectra were obtained with conventional Mössbauer spectrometers in the constant acceleration mode. The sources were $^{57}$Co in Rh and a foil of $\alpha$-Fe was used for calibration of the

spectrometer at room temperature. Spectra obtained at temperatures between 80 K and room temperature were recorded in a liquid nitrogen cryostat. Spectra obtained between 20 K and 80 K were recorded in a closed cycle helium refrigerator. A spectrum obtained in an applied field of 6 T was recorded in a liquid helium cryostat with a superconducting coil.

## 3. Results

### *3.1. Morphology and crystallography of goethite particles*

Figure 1(a) shows a representative HRTEM image of the as-prepared sample. Figure 1(b) shows an image of the same agglomerate acquired using the HAADF detector of the microscope in scanning TEM (STEM) mode. In Fig. 1(b), the intensity is approximately proportional to the density and the thickness of the sample, and provides evidence that the crystals are far from perfect and contain many voids. The images show rods that are stacked with parallel [010] orientations. The dimensions of the rods, as estimated from HRTEM images, are given in Table 1. The graph in Fig. 1(c), which was obtained using GPA, shows the change in orientation of the lattice planes between points 1 and 2 in the particle shown in Fig. 1(a). It shows that the (010) planes have variations in their orientation of 1-2 degrees. The data in Fig. 1(d) was obtained using HAADF tomography [28], a technique that allows the three-dimensional shapes and distributions of materials to be measured with nanometer spatial resolution. Fig. 1(d) shows the three-dimensional shape and internal structure of a stack of goethite crystals, which are representative of the sample studied here. Figure 1(e) shows a cut-away visualization of the same crystals revealing the presence of internal voids, which form a network that seemingly interpenetrates between the different crystals of the stack. Figure 2 shows a similar distortion in another crystal. The main cause of the change of orientation between the lower and upper parts of the crystal seems to be a grain boundary. Interpretation of the curves shown in figures 1 and 2 requires some caution because local changes in crystal thickness may affect the local values of the geometrical phase. Also, the limited size of the mask used when Fourier filtering the image degrades the resolution of the geometrical phase image and the local values of the curves correspond to averaged values over several pixels along each profile. The curves in figures 1 and 2 were obtained by integrating several profiles measured over a width of 10 pixels, and although high-frequency information is not directly interpretable, the curves can still be used to measure low-frequency variations in the orientation of the crystal planes, by measuring changes between minima and maxima of the profile.

Figure 3 shows an HRTEM image of part of a goethite rod, acquired using a microscope equipped with a spherical aberration corrector. The improved interpretability and resolution of this image is noticeable at the edges of the particles. Lattice fringes parallel to the long direction of the rod (the [010] direction) are visible. Closer inspection of the image reveals the presence of dislocations, and the particle is seen to consist of several grains with more or less perfect oriented attachment. Moreover, there are indications of Moiré fringes, suggesting a slight relative rotation between grains in the particle.

Figures 4(a) and 4(b) show DF TEM images of the as-prepared and ball-milled samples, respectively. Figure 4(a) shows significant variations in contrast within the individual rods, indicating variations in crystallographic orientation. This observation is in accordance with the presence of low-angle grain boundaries and voids shown in Figs. 1 and 2. Figure 4(b) shows that the ball-milled sample is dominated by agglomerates of irregularly-shaped particles with an average size of approximately 9 nm.

Other recent studies of the synthesis and morphology of goethite particles have shown that they can form from precursor nanoparticles of ferrihydrite, which have diameters of a few nanometers [30-34]. The ferrihydrite particles transform to goethite, followed by (often imperfect) oriented attachment to form nanorods. Each goethite rod may be formed by the attachment of more than 100 precursor particles [34]. Inspection of HRTEM images of such rods has revealed the presence of low-angle grain boundaries [30, 32, 33], with some rod-shaped goethite particles consisting of grains with dimensions of 5-8 nm [34]. Thus, defects such as low-angle grain boundaries seem to be common in goethite samples prepared in different ways. Positron annihilation studies have also revealed a high concentration of defects in goethite [35], with a correlation between defect concentration and magnetic properties. Goethite particles usually contain more water and/or $OH^-$ than predicted by the theoretical formula, and this also has an influence on the magnetic properties [15].

The dimensions of the goethite rods in the as-prepared sample, as estimated from TEM, differ considerably from the crystallite sizes estimated from XRD (Table 1). The length of the rods along the [010] direction is considerably larger when measured using TEM than the [010] crystallite dimension obtained from XRD. This discrepancy suggests that the rods are not perfect single

crystals, in accordance with the HRTEM observations of defects, including voids and grain boundaries, within the rods. In contrast, along the [100] direction, the dimension found using XRD is larger than that from HRTEM. This difference may be associated with oriented attachment of adjacent rods, such that the crystallographic order continues to some extent across grain boundaries [36]. Similar results were found by Bocquet *et al*. [12], who compared sizes estimated from TEM and XRD for a number of synthetic and natural goethite samples. For most of the samples, the particle length estimated from TEM was considerably larger than any dimensions estimated from XRD, whereas the width of the rods, estimated from TEM, was often smaller than any of the dimensions obtained from XRD. Similar observations were also reported in a study of goethite particles with length exceeded 1000 nm [13]. Thus, the occurrence of more or less perfect oriented attachment in goethite samples appears to make it difficult to define and measure the sizes of goethite particles in a unique way. Discrepancies between particle sizes obtained from TEM and XRD have also been found in studies of Pt nanoparticles [37].

*3.2. Mössbauer spectroscopy*

Mössbauer spectra acquired from both the as-prepared and the ball-milled goethite samples are shown in Fig. 5. At low temperatures, the spectra consist of sextets with relatively narrow lines. At temperatures above approximately 100 K, the lines become asymmetrically broadened in a manner that is typical for goethite. Spectra acquired from the as-prepared sample show no clearly visible doublet component due to particles with fast superparamagnetic relaxation up to 300 K. In contrast, the ball-milled sample shows an intense doublet at 300 K, which is also visible at 260 K. The spectra were fitted with a distribution of sextets with different hyperfine fields, as described earlier [16, 38].

Mössbauer spectra of the as-prepared sample at 350 K in zero magnetic field and in an applied field of 6 T are shown in Fig. 6. The zero-field spectrum is dominated by a doublet, indicating that most of the particles are superparamagnetic or paramagnetic at this temperature. The 6-T spectrum shows a substantial broadening of the doublet, indicating that the majority of the atoms have hyperfine fields larger than 10 T. This observation indicates that the particles are not paramagnetic, but superparamagnetic at 350 K, in contrast to the suggestion of Bocquet *et al*. [12], who interpreted the transition of goethite Mössbauer spectra from a sextet to a doublet as a Néel temperature.

## 4. Discussion

### *4.1. The superferromagnetism model*

In earlier work on interacting nanoparticles, the temperature dependence of the magnetic hyperfine fields was analyzed with the "superferromagnetism" model [9, 16, 39, 40]. In samples of antiferromagnetic nanoparticles, the dipole interaction is negligible, but there may be a strong exchange coupling between particles in close proximity [16 - 20]. In the model, it is assumed that the magnetic energy of a particle with volume *V* and magnetic anisotropy constant *K*, and which interacts with neighboring particles, can be written in the form

$$E = KV\sin^2\theta - \sum_{i,j} J_{ij}\vec{S}_i \cdot \vec{S}_j, \qquad (1)$$

where $\theta$ is the angle between the easy magnetization direction and the sublattice magnetization vector. $\vec{S}_i$ and $\vec{S}_j$ represent the surface spins belonging to the particle and to the neighboring particles, respectively, and $J_{ij}$ is the exchange coupling constant. *K* is assumed to be independent of temperature and surface effects are neglected. It should be emphasized that in general the inter-particle interaction should not be treated as an extra contribution to the uniaxial anisotropy, although this is often assumed in the literature. The interactions should rather be treated in terms of a unidirectional interaction field in accordance with the fact that low-temperature hysteresis loops of field cooled samples of interacting nanoparticles show a horizontal shift (exchange bias) and not only an enhanced coercivity as one would expect if the interactions only resulted in an enhanced uniaxial anisotropy.

The influence of inter-particle interactions may be described by a mean field model, in which the summation in the last term in Eq. (1) is replaced by an effective interaction field acting on the sublattice magnetization of the particle [9, 16, 39, 40]:

$$E = KV\sin^2\theta - J_{eff}\vec{M}(T)\cdot\left\langle\vec{M}(T)\right\rangle. \qquad (2)$$

$\vec{M}(T)$ represents the sublattice magnetization vector of the particle at temperature *T* and $J_{eff}$ is an effective exchange coupling constant, such that $J_{eff}\left\langle\vec{M}(T)\right\rangle$ is the effective interaction field acting

on $\vec{M}(T)$. In a study of interacting hematite nanoparticles [16], the data indicated that there was a tendency for the interaction field to be parallel to the easy direction of magnetization, in accordance with the tendency for oriented attachment of hematite nanoparticles [18]. As discussed in Sec. 3.1, there is usually (nearly) oriented attachment of grains in samples of goethite particles. Therefore, it is reasonable to assume that the interaction field is approximately parallel to the easy direction of magnetization in the present study. Eq. (2) can then be written in the form [16]

$$E(\theta) \approx KV \sin^2 \theta - J_{eff} M_0^2(T) b(T) \cos\theta , \tag{3}$$

where $M_0(T)$ is the sublattice magnetization in the absence of magnetic fluctuations, which can be assumed equal to the bulk value, and

$$b(T) = \frac{\left| \left\langle \vec{M}(T) \right\rangle \right|}{M_0(T)} \tag{4}$$

is the order parameter. Assuming thermal equilibrium, the order parameter can be calculated by the use of Boltzmann statistics to take the form

$$b(T) = \frac{\int_0^{\pi} \exp(-E(\theta)/k_B T) \sin\theta \cos\theta d\theta}{\int_0^{\pi} \exp(-E(\theta)/k_B T) \sin\theta d\theta} \quad . \tag{5}$$

With $E(\theta)$ given by Eq. (3), Eq. (5) can be solved numerically to find the order parameter *b*(*T*), which decreases with increasing temperature and vanishes above a critical temperature, $T_p$ [9, 16].

The influence of magnetic fluctuations on Mössbauer spectra depends crucially on the relaxation times in relation to the time scale of Mössbauer spectroscopy, $\tau_M$, which is on the order of a few nanoseconds. It must be realized that in general there are different types of relaxation processes in nanoparticles, namely relaxation across an energy barrier with relaxation time, $\tau$ and relaxation between states in one of the energy wells. For a ferromagnetic particle exposed to a small (applied

or interaction) field along the easy direction, the relaxation times for superparamagnetic relaxation, i.e., relaxation between the two energy minima at $\theta = 0$ and $\theta = \pi$ is given by [41]

$$\tau_{\pm} \cong \tau_0 (1-\varepsilon^2)(1\pm\varepsilon)\exp\left[\frac{KV}{k_B T}(1\pm\varepsilon)^2\right], \qquad (6)$$

where $\tau_+$ and $\tau_-$ are the relaxation times for relaxation processes with initial states in the lower and the upper minimum, respectively. $\tau_0$ is in the range $10^{-13}$ to $10^{-9}$ s and $\varepsilon = B_i / B_a$ where $B_i$ is an applied magnetic field (or an interaction field) and $B_a$ is the anisotropy field. When $\tau << \tau_M$, the magnetic splitting of the spectra is expected to be proportional to the average magnetization, i.e., the magnetic splitting vanishes in non-interacting particles in zero field, but if the particles are exposed to an applied field or an interaction field, a non-zero magnetic hyperfine splitting will be observed. If $\tau >> \tau_M$, the Mössbauer spectra are magnetically split, but the magnetic splitting may be reduced compared to the bulk value, because of fluctuations of the magnetization vector close to the energy minima (collective magnetic excitations) [39, 42].

The magnetic fluctuations can be described by a multi-level model [42, 43, 44] in which a ferromagnetic particle is considered as a quantum mechanical macrospin, $S^M$. Thus, the particle has $2S^M + 1$ states with *z*-components of the spin given by $S^M$, $S^M$-1, $S^M$-2, ·····, $-S^M$. The characteristic times for magnetic relaxation between states within the same energy well is on the order of $\tau_0$ or smaller [43, 44]. Therefore, if $\tau_0 \lesssim 10^{-10}$ s it is a good approximation to assume that relaxation within an energy well is fast compared to the time scale of Mössbauer spectroscopy such that the magnetic hyperfine splitting is proportional to the average magnetization with the average taken over fluctuations within an energy well [39, 42]. If $\tau_0$ is on the order of $10^{-10}$ s, the relaxation between the states within an energy well may result in a slight line broadening of the Mössbauer spectra. In antiferromagnetic nanoparticles the value of $\tau_0$ is usually much smaller than $10^{-10}$ s [20] and then the relaxation between states within an energy well will be fast compared to $\tau_M$. Although the magnetic fluctuations in antiferromagnetic nanoparticles are more complex, the relaxation can be described by a similar multi-level model [42].

For interacting nanoparticles the relative size of the two terms in Eq. (3) is important. If the interaction energy is predominant, there will only be one energy minimum, and the relaxation will then take place between states in this energy well and is expected to be fast, as discussed above. The magnetic hyperfine splitting can therefore be considered to be proportional to $\left|\left\langle \vec{M}(T)\right\rangle\right| = M_0(T)b(T)$. If the anisotropy energy is predominant or comparable to the interaction energy, there will be two (non-equivalent) energy minima, which are separated by an energy barrier. The transition probability per unit time for transitions across the energy barrier will be given by an expression similar to Eq. (6). At low temperatures, the relaxation across the energy barrier may therefore be slow compared to the time scale of Mössbauer spectroscopy, but relaxation between states within an energy well is still expected to be fast. The magnetic hyperfine splitting is then proportional to the sublattice magnetization, averaged over the fluctuations within a minimum, rather than being proportional to $\left|\left\langle \vec{M}(T)\right\rangle\right|$ [39, 42]. The magnetic hyperfine splitting will in general be different for the two non-equivalent minima. Because of the interaction field, the thermal population of the two minima will be temperature dependent. When the thermal energy is low compared to the interaction energy, the population of the upper minimum will be negligible. In this case, the observed hyperfine field will approximately be given by the thermal equilibrium value, taken over fluctuations within the lower minimum, and it will essentially be proportional to $\left|\left\langle \vec{M}(T)\right\rangle\right|$.

The distribution of anisotropy energies and interaction energies in a sample will result in a distribution of magnetic hyperfine fields at finite temperatures. Fits of the temperature dependence of the *average* hyperfine field of interacting hematite [16] and goethite [9] nanoparticles to the superferromagnetism model gave negligible values of the magnetic anisotropy energy, presumably because the influence of anisotropy is averaged out if only the average hyperfine field is fitted [16]. However, in the study of hematite nanoparticles, it was found that the temperature dependence of quantiles in the hyperfine field distribution $p\left(B_{hf}(T)\right)$ gave finite values of the magnetic anisotropy energies, which were in accordance with those found for the non-interacting particles. This strongly supports the validity of the model. The quantile, *f*, is defined as

$$f = \int_0^{B_f(T)} p\left(B_{hf}(T)\right) dB_{hf} \quad . \tag{7}$$

In the superferromagnetism model, the values of the anisotropy energy, $KV$ and the interaction energy parameter $T_p^0$ are free parameters for each quantile. $T_p^0$ is defined as the ordering temperature for a sample with zero anisotropy ($KV$ = 0) and is given by the expression [9, 39]

$$T_p^0 = \frac{J_{eff} M (T_p^0)^2}{3k_B} \ . \qquad (8)$$

The interaction energy, $E_i(T) = J_{eff} M_0(T)^2 b(T)$, depends on temperature because both $b(T)$ and $M_0^2(T)$ are temperature dependent. As an approximate measure of the interaction energy well below $T_p$ we use the value $E_{\text{int}} = 3k_B T_p^0$.

*4.2. The as-prepared sample*

Magnetization [10] and Mössbauer spectroscopy [12, 22] studies of goethite samples with relatively large particle size and in large applied magnetic fields showed that the magnetic anisotropy constant is relatively large, $K \approx 5\times10^4$ Jm$^{-3}$, and the estimated values for three different samples were similar. In a high-field Mössbauer study of a single crystal of goethite, a lower limit of $K = 6\times10^4$ Jm$^{-3}$ was estimated [23]. Previous studies have shown that the magnetic anisotropy constant of magnetic nanoparticles generally increases with decreasing particle size, especially for particle dimensions below 10 nm [45-47], presumably because of the influence of surface anisotropy. In the following, we assume that $K \gtrsim 5\times10^4$ Jm$^{-3}$ for our goethite particles.

Let us consider non-interacting particles with superparamagnetic relaxation time given by Eq. (6), $\varepsilon = 0$, $\tau_0 \approx 10^{-11}$ s, $K \gtrsim 5\times10^4$ Jm$^{-3}$ and a volume of $V$ ~1800 nm$^3$, corresponding to one of the rods seen in the TEM images of the as-prepared sample. Such particles have a superparamagnetic relaxation time, $\tau >> \tau_M$ at $T$ < 350 K, and the influence of collective magnetic excitations will be almost negligible. Interactions between rod-shaped particles in close proximity may also contribute to a suppression of the relaxation. Thus, magnetic fluctuations of the spin structure of the rods as a whole cannot explain the line shapes of the Mössbauer spectra in Fig.5.

The Mössbauer spectra have similarities to those of interacting hematite nanoparticles, which have been successfully analyzed by use of the superferromagnetism model [16]. In studies of hematite nanoparticles, it was possible to control the strength of the interparticle interactions. If the particles are coated with, for example, oleic acid the interactions are negligible, but if a suspension of uncoated particles is dried, there may be strong inter-particle interactions due to exchange interactions between surface atoms of neighboring particles [16, 17, 40]. Gentle grinding of interacting particles can significantly reduce the interaction [48], and it has been shown that the aggregation processes are reversible [19]. Similar results have been found for $^{57}$Fe-doped NiO nanoparticles [21]. Mössbauer spectra of non-interacting or weakly interacting hematite nanoparticles typically consist of a superposition of a sextet and a doublet with relatively narrow lines due to particles with relaxation times that are very long or very short compared to $\tau_M$, respectively. The relative areas of the two components depend on temperature. Due to the exponential dependence of the relaxation time on the volume, there is a very broad distribution of relaxation times, and only a small fraction of the particles have relaxation times close to $\tau_M$. The evolution with temperature of the spectra of interacting hematite nanoparticles is quite different. Instead of the appearance of a doublet at finite temperatures, the lines of the sextet broaden, and the average hyperfine field decreases much faster with increasing temperature than the bulk hyperfine field. The distributions of magnetic anisotropy energies and of the interaction energies will result in a distribution of hyperfine fields, which leads to asymmetric line broadening in the Mössbauer spectra [9, 16-21]. The influence of interactions on the spectral shape is similar to that of an applied magnetic field [16, 40], in accordance with Eq. (2).

We have analysed the temperature dependence of the magnetic hyperfine fields of the goethite sample by using the superferromagnetism model. For each quantile, *f*, in the hyperfine field distribution, the temperature dependence of the magnetic hyperfine field $B_f(T)$, was fitted to

$$B_f(T) = B_0(T) b_f(T), \tag{9}$$

where $B_0(T)$ is the bulk hyperfine field (which is assumed to be proportional to $M_0(T)$). Data for the 40%, 60% and 80 % quantiles are shown in Fig. 7 together with the bulk hyperfine field.The critical temperatures, $T_p$, above which the particles are superparamagnetic, are of the order of 325-

350 K. Therefore, the zero-field spectrum at 350 K (Fig. 6) contains an intense doublet. Figure 8 shows the estimated values for the anisotropy energy $KV/k_B$ and the interaction energy $E_{\mathrm{int}}/k_B$ as a function of the quantile, *f*. The anisotropy energy, $KV/k_B$ varies from around 400 K to 1400 K, whereas $E_{\mathrm{int}}/k_B$ is on the order of 800 K and varies only little as a function of the quantile. For the largest values of *KV*, there will be two minima of the magnetic energy. However, with $E_{\mathrm{int}}/k_B \approx$ 800 K the population of the upper minimum will be well below 1% even at 300 K and is therefore negligible. Thus, it seems to be a good approximation to assume thermal equilibrium and analyze the data using the order parameter $b_f(T)$, calculated by use of Eq. (5).

Using the data for the anisotropy energy *KV* in Fig. 8 and $K \gtrsim 5\times10^4$ Jm$^{-3}$, we find that the effective volumes of the relaxing and interacting grains are $V_g \lesssim$ 100-400 nm$^3$, corresponding to grain dimensions around 5-8 nm or smaller. These volumes are much smaller than the overall sizes of the rods estimated from TEM, but similar to the typical sizes of the grains separated by defects, including voids and low-angle grain boundaries. This suggests that the magnetic fluctuations are governed not by relaxation of the sublattice magnetizations of the entire rod-shaped particles as a whole, but rather by magnetic fluctuations in smaller grains within them. Thus, the rod-shaped particles seem to consist of small grains with relatively weak inter-grain interactions.

It may seem surprising that defects such as low-angle grain boundaries in the rod-shaped particles can result in a substantial weakening of the magnetic interaction between neighboring grains. Some low-angle grain boundaries may be described in terms of dislocations. As illustrated schematically in Fig. 9, a simple defect such as an edge dislocation with an extra plane with a single layer of magnetic atoms, which would have negligible influence on the magnetic properties of a ferromagnet, may have a significant effect on the properties of an antiferromagnetic material. For the dislocation shown in Fig. 9, the sublattice magnetization direction of the extra plane cannot be antiparallel to the magnetization direction in both of the neighboring planes and will therefore cause magnetic frustration. If we neglect spin-canting, and calculate the magnetic interaction energy (the summation in Eq.(1)) along the dotted line in Fig. 9, assuming that all exchange coupling constants are equal, we find that the eight contributions to the interaction energy cancel. In practice, one would expect that the magnetic frustration around a dislocation will give rise to spin canting, but in any case, such a dislocation will result in a significant weakening of the magnetic coupling. A small

relative rotation of grains in a particle, as suggested by the Moiré fringes in Fig. 3, will also result in magnetic mismatch, which will weaken the coupling across the interface. Thus, although there are many atoms in close contact at an interface, the effective magnetic exchange coupling between grains (the last term in Eq. (1)) may be small in an antiferromagnetic material. Voids in the particles, as seen in Fig. 1, as well as excess water and/or $OH^-$ [15], may also contribute to weakening of the coupling between grains. The weak coupling between grains can explain why the sublattice magnetization directions of the grains can fluctuate. Heating of goethite nanoparticles may result in stronger interactions between the grains [49, 50], indicating that some of the defects have disappeared.

*4.3. The ball-milled sample*

The presence of a doublet in the room temperature spectrum of the ball-milled sample indicates that fast superparamagnetic relaxation takes place in this sample. In the ball-milled sample, the particle volume, determined by both XRD and TEM, is around 300-400 $nm^3$ and the interaction between the particles may be small because the particles are not stacked regularly as in the as-prepared sample. We then estimate that the superparamagnetic relaxation time at 300 K for relaxation of the spin structure of a particle as a whole may be less than 1 ns if $\tau_0 \approx 10^{-11} s$ and $K \approx 5 \cdot 10^4 \, Jm^{-3}$, in accordance with the presence of a doublet in the Mössbauer spectrum at 300 K.

The temperature dependence of the hyperfine fields for different quantiles and the parameters $KV$ and $E_{int}$, as estimated from fits to the superferromagnetism model, are shown in Figs. 7 and 8, respectively, together with the data for the as-prepared sample. It is remarkable that the values of $KV$ and $E_{int}$ are similar for the as-prepared and ball-milled samples, although the overall particle sizes differ. This agreement supports the interpretation of the data in terms of magnetic fluctuations in much smaller grains, which have similar sizes in the two samples.

It appears that there are two types of relaxation in the ball-milled goethite particles, namely magnetic fluctuations of the small, interacting grains within the rod-shaped particles and superparamagnetic relaxation of the spin structure of the whole particles at the highest temperatures. Below the superparamagnetic blocking temperature, such a particle will be influenced by fluctuations of the average sublattice magnetization directions of the particle as a whole (collective

magnetic excitations), which result in a small reduction in the measured hyperfine field according to the expression [39, 42]

$$B_f^{obs}(T) \cong B_f(T)\left[1-\frac{k_B T}{2KV_{part}}\right] \qquad (10)$$

where $V_{part}$ is the volume of the whole particle. Thus, the hyperfine fields of the ball-milled sample should be reduced slightly compared to the as-prepared sample because of this effect. This can explain the slightly lower values of $KV/k_B$ in Fig. 8. If we assume that $B_f(T)$ is the same for the two samples and that the slightly smaller hyperfine fields in the ball milled sample is due to collective magnetic excitations, we find that $K \approx 10^5$-$10^6$ Jm$^{-3}$, i.e. somewhat larger than the values found in magnetization and high-field Mössbauer studies [10, 12, 22, 23] of larger goethite particles. The difference may be due to a larger contribution from surface anisotropy in our particles.

*4.4. α-$Fe_2O_3$ and NiO nanoparticles*

On the basis of the interpretation of the goethite data, discussed above, it is relevant to discuss the Mössbauer data obtained from interacting of α-$Fe_2O_3$ [25] and from interacting α-$Fe_2O_3$ and NiO nanoparticles [17]. Interaction between randomly aggregated α-$Fe_2O_3$ nanoparticles leads to Mössbauer spectra with a reduced absolute value of the quadrupole shift at low temperatures, indicating a rotation of the sublattice magnetization directions [25]. The effective interaction field presumably makes a finite angle with the anisotropy field of these particles, and it is likely that this leads to the observed spin rotation [25]. Interaction with NiO nanoparticles was found to result in faster superparamagnetic relaxation of the α-$Fe_2O_3$ nanoparticles, as compared to a similarly prepared sample with only α-$Fe_2O_3$ nanoparticles [17]. This observation indicates that the inter-particle interaction between α-$Fe_2O_3$ and NiO is weaker than the interaction between α-$Fe_2O_3$ nanoparticles. However, in the samples containing both α-$Fe_2O_3$ and NiO, a more significant spin rotation in the α-$Fe_2O_3$ particles was observed, suggesting a strong exchange interaction across the α-$Fe_2O_3$/NiO interfaces [17]. We are currently investigating the attachment of α-$Fe_2O_3$ and NiO nanoparticles [51]. In case of the effective exchange field making a finite angle with the anisotropy field of the particles, the origin of spin rotation seems similar to that observed in pure α-$Fe_2O_3$

nanoparticle systems [25]. Additionally, if there are mismatches in the crystallographic and/or magnetic structures at the interface, then the surface spins cannot be oriented in such a way that the exchange energy is minimized for all interacting neighboring spins, leading to magnetic frustration. Such mismatches may both reduce the interparticle interaction as in goethite and result in spin canting, which may lead to a rotation of the sublattice magnetization directions.

## 5. Conclusions

By use of Mössbauer spectroscopy we have studied goethite particles that show the commonly observed asymmetric line broadening in the spectra, which has been debated in the literature for decades. We have studied goethite particles before and after ball milling and analyzed the temperature dependence of different quantiles in the magnetic hyperfine field distribution. The data were in accordance with the superferromagnetism model, with similar anisotropy energy and interaction energy for the two samples in spite of different particle sizes. The data suggest that the temperature dependence of the spectra is due to fluctuations of the magnetization directions in grains that are much smaller than the overall particle size. The presence of such grains is supported by HRTEM studies. Magnetic mismatch at the interfaces leads to a weakened magnetic coupling between the antiferromagnetic grains such that the sublattice magnetization directions can fluctuate. Similar phenomena may occur in other antiferromagnetic nanograin systems, and we have discussed the results obtained for goethite in relation to Mössbauer studies of $\alpha$-$Fe_2O_3$ nanoparticles and of $\alpha$-$Fe_2O_3$/NiO nanoparticle composites.

## Acknowledgements

The work was supported by the Danish Research Council for Technology and Production Sciences. Thanks are due to P. A. Midgley at the University of Cambridge and A. I. Kirkland at the University of Oxford for access to their electron microscopy facilities under the ESTEEM project (no 026019) for transnational access. We are grateful to Bente Lebech for help with the Rietveld analysis and to Mihaly Posfai for providing supporting electron microscopy observations.

**References**


1. G. Herzer, Scripta Metallurgica et Materialia, **33** 1741 (1995)
2. G. Herzer, J. Magn. Magn. Mater. **157** 133 (1996)
3. J.M.D. Coey, Phys. Rev. Lett. **27** 1140 (1971)
4. A. H. Morrish and K. Haneda, J. Magn. Magn. Mater. **35** 105 (1983)
5. S. Mørup, J. Magn. Magn. Mater. **266** 110 (2003)
6. U. Schwertmann and R.M. Cornell, *The Iron Oxides: Structure, Properties, Reactions, Occurrences and Uses*, Wiley-VCH., 2. edition, 2003
7. R.V. Morris *et al*. J. Geophys. Res.-Planet, E02S13 (2006)
8. J.B. Forsyth, I.G. Hadley and C.E. Johnson, J. Phys. C (Proc. Phys. Soc.) Ser. 2, Vol 1, p. 179 (1968).
9. S. Mørup, M.B. Madsen, J. Franck, J. Villadsen and C.J.W. Koch, J. Magn. Magn. Mater. **40** 163 (1983)
10. J.M.D. Coey, A. Barry, J-M. Brotto, H. Rakoto, S. Brennan, W.N. Mussel, A. Collomb, and D. Fruchart, J. Phys.: Condens. Matter **7** 759 (1995)
11. N. Taitel-Goldman, C. B. Koch and A. Singer, Clays  Clay Minerals **52**, 115 (2004)
12. S. Bocquet, R.J. Pollard and J.D. Cashion, Phys. Rev. B **46** 11657 (1992)
13. C.J.W. Koch, M.B. Madsen and S. Mørup, Surf. Sci. **156** 249 (1985)
14. E. Murad, Amer. Miner. **67** 1007 (1982)
15. C.A. Barrero, J.D. Betancur, J.M. Greneche, G.F. Goya and T.S. Berquó, Geophys. J. Int. **164** 331 (2006)
16. M.F. Hansen, C.B. Koch and S. Mørup, Phys. Rev. B **62** 1124 (2000)
17. C. Frandsen and S. Mørup, J. Magn. Magn. Mater. **266** 36 (2003)
18. C. Frandsen, C.R.H. Bahl, B. Lebech, K. Lefmann, L.T. Kuhn, L. Keller, N.H. Andersen, M. v. Zimmermann, E. Johnson, S.N. Klausen and S. Mørup, Phys. Rev. B **72** 214406 (2005)
19. C. Frandsen and S. Mørup, J. Phys. Condens. Matter **18** 7079 (2006)
20. S. Mørup, D.E. Madsen, C. Frandsen, C.R.H. Bahl and M.F. Hansen, J. Phys.: Condens. Matter **19** 213202 (2007)
21. C.R.H. Bahl and S. Mørup, Nanotechnology **17** 2835 (2006)
22. Q.A. Pankhurst and R.J. Pollard, J. Phys.: Condens. Matter **2** 7329 (1990)
23. A. Meagher, Q.A. Pankhurst and D.P.E. Dickson, Hyperfine Interact. **28** 533 (1986)

24. S. Bocquet, J. Phys.: Condens. Matter **8** 111 (1996)
25. C. Frandsen and S. Mørup, Phys. Rev. Lett. **94** 0027202 (2005)
26. J. Ding, Y. Shi, L.F. Chen, C.R. Deng, S.H. Fuh and Y. Li, J. Magn. Magn. Mater. **247**, 249 (2002)
27. M.J. Hÿtch, J.L. Putaux and J.M. Pénisson, Nature **423** 270 (2003)
28. P.A. Midgley, E.P.W. Ward, A.B. Hungría and J.M. Thomas, Chem. Soc. Rev. **36** 1477 (2007)
29. http://www-llb.cea.fr/fullweb/
30. J.F. Banfield, S.A. Welch, H. Zhang, T.T. Ebert and R.L. Penn, Science **289** 751 (2000)
31. Y. Guyodo, A. Mostrom, R.L Penn and S.K. Banerjee, Geophys. Res. Lett. **30** 1512 (2003)
32. M. Nesterova, J. Moreau and J.F. Banfield, Geochim. Cosmochim. Acta **67** 1177 (2003)
33. D.J. Burleson and R.L. Penn, Langmuir **22** 402 (2006)
34. R.L. Penn, J.J. Erbs and D.M. Gulliver, J. Cryst. Growth **293** 1 (2006)
35. S. Bocquet and A.J. Hill, Phys. Chem. Minerals **22** 524 (1995)
36. R.M. Cornell, S. Mann and A.J. Skarnulis, J. Chem. Soc., Faraday Trans. I, **79**, 2679 (1983)
37. L.C. Gontard, R.E. Dunin-Borkowski, D. Ozkaya, T. Hyde, P.A. Midgley and P. Ash, J. Phys.: Conf. Ser. **26**, 367 (2006)
38. C. Wivel and S. Mørup, J. Phys. E. Sci. Instrum. **14** 605 (1981)
39. S. Mørup, J. Magn. Magn. Mater. **37**, 39 (1983)
40. L.T. Kuhn, K. Lefmann, C.R.H. Bahl, S.N. Ancona, P.-A. Lindgård, C. Frandsen, D.E. Madsen and S. Mørup, Phys. Rev. B **74** 184406 (2006)
41. W.F. Brown, Phys. Rev. **130** 1677 (1963)
42. S. Mørup and B.R. Hansen, Phys. Rev. B **72** 024418 (2005)
43. D.H. Jones and K.K.P. Srivastava, Phys. Rev. B **34** 7542 (1986)
44. J. van Lierop and D.H. Ryan, Phys. Rev. B **63** 064406 (2001)
45. F. Bødker, S. Mørup and S. Linderoth, Phys. Rev. Lett. **72** 282 (1994)
46. F. Bødker and S. Mørup, Europhys. Lett. **52** 217 (2000)
47. E. Tronc, Nuovo Cimento D **18** 163 (1996)
48. M. Xu, C.R.H. Bahl, C. Frandsen and S. Mørup, J. Colloid Interface Sci. **279** 132 (2004).
49. C.J.W. Koch, M.B. Madsen, S. Mørup, G. Christiansen, L. Gerward and J. Villadsen, Clays Clay Miner. **34** 17 (1986).
50. D.E. Madsen, M.F. Hansen, C.B. Koch, S. Mørup, J. Phys.: Condens. Matter **20** (2008) 135215
51. C. Frandsen et al. (unpublished).

| Sample | *d*[100] | *d*[010] | *d*[001] |
|---|---|---|---|
| As-prepared | | | |
| XRD | 12 | 20 | 7 |
| TEM | 3-5 | 40-70 | 5-20 |
| Ball-milled | | | |
| XRD | 7 | 9 | 5 |
| TEM | ~ 9 | ~ 9 | ~ 9 |

.

Table 1: Sizes of goethite particles in nm, obtained from Rietveld refinement of XRD data and from TEM images.

**Figure captions.**

**Figure 1.** (a) HRTEM image of the as-prepared sample acquired in a Tecnai F20 TEM operated at 200 kV. (b) The same area imaged in HAADF STEM mode, showing evidence of the presence of voids. (c) shows changes in the orientation of the prominent lattice planes shown in (a) measured using GPA (see text for details). The profile goes from point 1 to point 2 along the line drawn in (a). Although the graph is noisy, it clearly indicates low frequency distortions of the crystal. (d) Three-dimensional isosurface visualization of a stack of goethite crystals obtained using HAADF STEM tomography. (e) Internal structure of the same crystals revealing the presence of an interpenetrating network of voids.

**Figure 2.** (a) HRTEM image of a representative crystal in the as-prepared goethite sample. (b) False-color map showing angles of the prominent lattice planes in (a) measured using GPA. (c) Line profile obtained from (b) along the line marked in (a), indicating an accumulated change of direction by approximately 2 degrees between points 1 and 3 and a noisy signal at the grain boundary of point 2.

**Figure 3.** HRTEM image acquired in a JEM 2200 FS electron microscope operated at 200 kV with the coefficient of spherical aberration adjusted to approximately -2 μm. The image shows overlapping crystals of goethite, between which slight misorientations resulting in the presence of Moiré fringes. The arrows show the indications of Moiré fringes.

**Figure 4**. Single beam DF TEM images showing crystalline domains in goethite crystals in (a) the as-prepared sample and (b) the ball-milled sample.

**Figure 5.** Mössbauer spectra of both the as-prepared and the ball-milled goethite samples obtained at the indicated temperatures.

**Figure 6**. Mössbauer spectra of the as-prepared sample at 350 K, (a) in zero field and (b) in an applied field of 6 T.

**Figure 7**. Temperature dependence of the magnetic hyperfine fields for the 40%, 60% and 80% quantiles for the two samples. Data for the reference (bulk) sample are shown for comparison.

**Figure 8.** Values of $E_{\mathrm{int}} / k_B$ and $KV / k_B$ as a function of the quantile parameter *f*.

**Figure 9**. Schematic illustration of the magnetic structure around a dislocation in an antiferromagnetic material. Possible spin-canting is not taken into account.

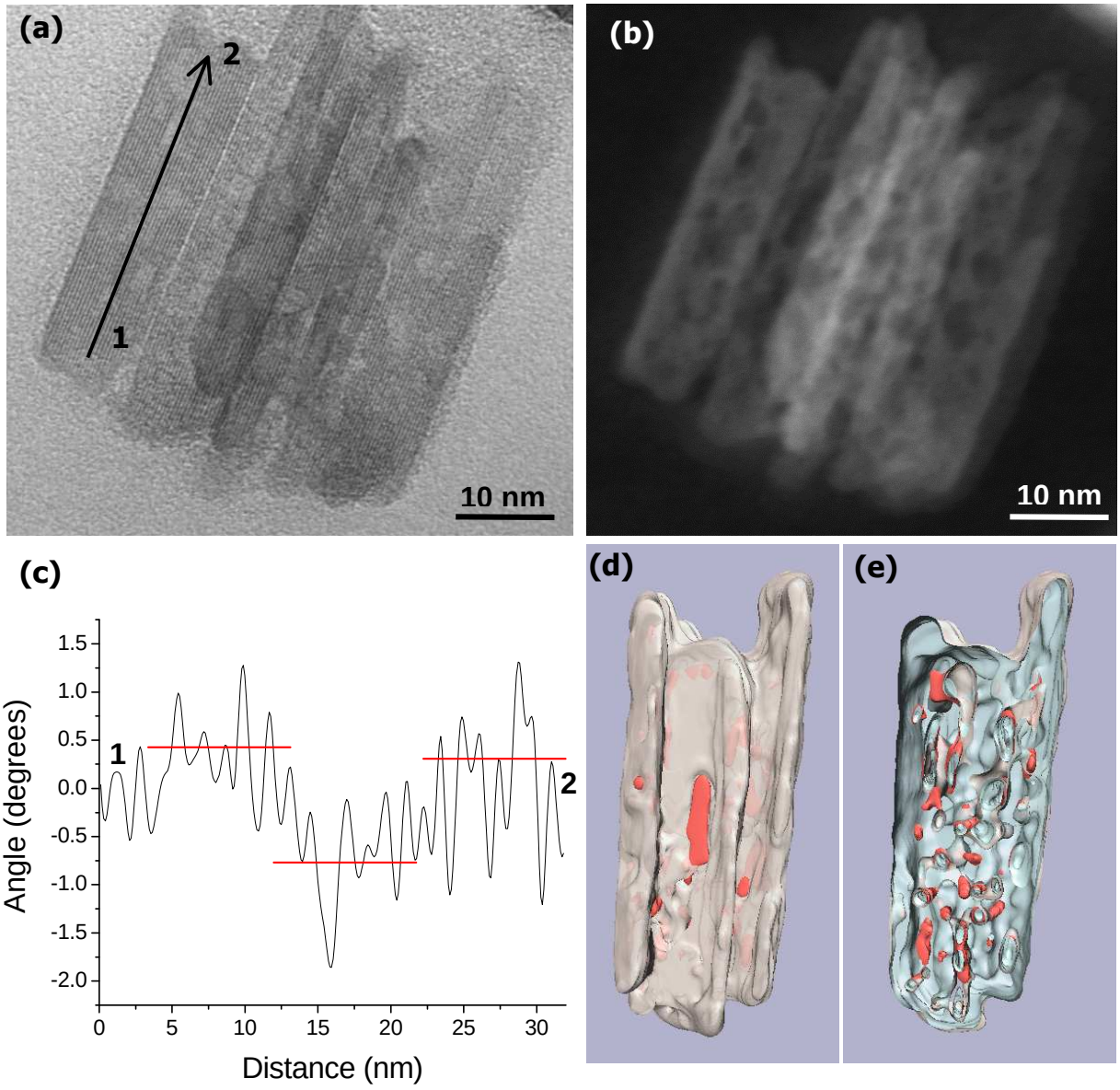
(a)
2
1
10 nm
(b)
10 nm
(c)
Angle (degrees)
1.5
1.0
0.5
0.0
-0.5
-1.0
-1.5
-2.0
1
2
0
5
10
15
20
25
30
Distance (nm)
(d)
(e)

**Figure 1**

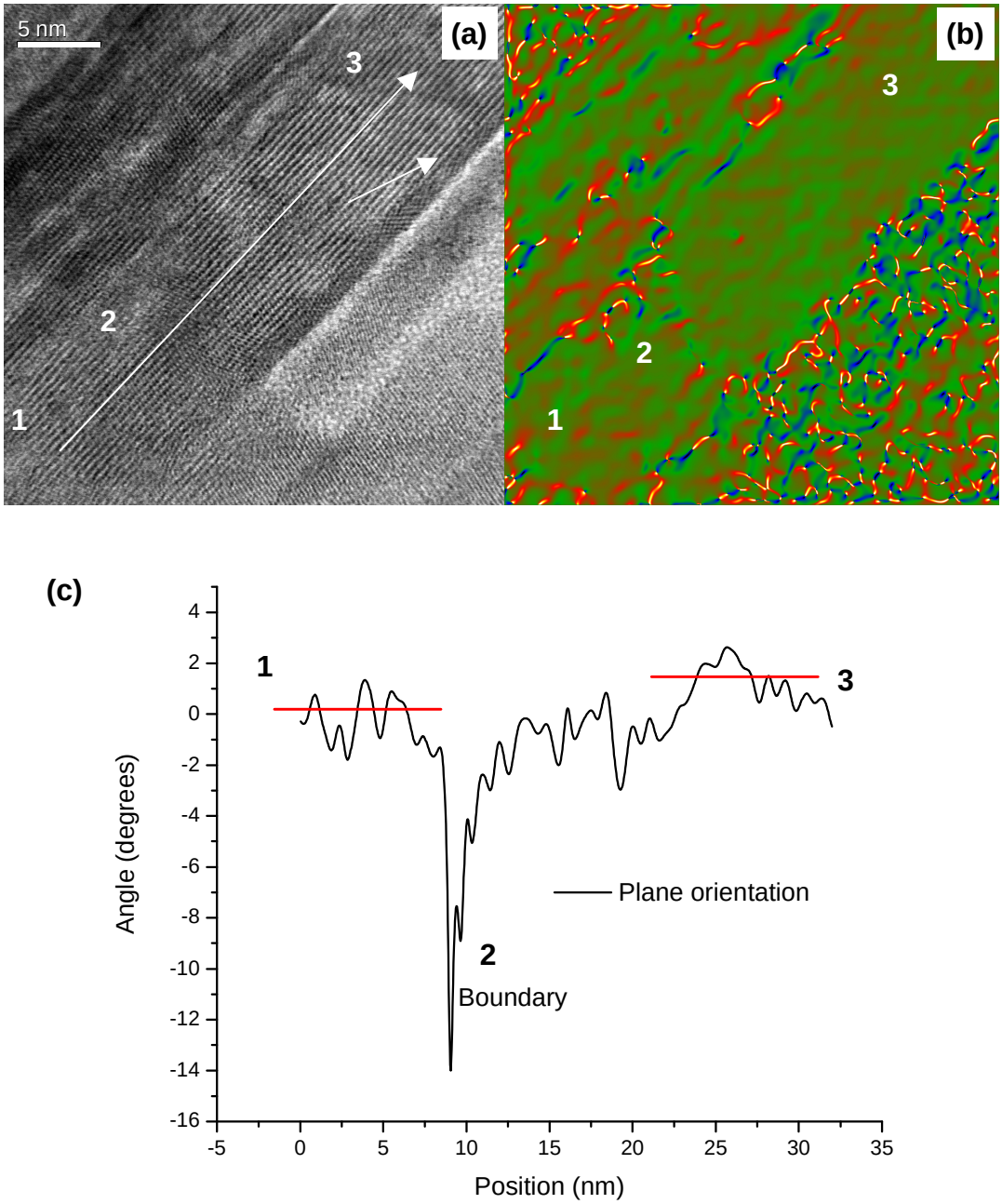
5 nm
(a)
(b)
1
2
3
(c)
Angle (degrees)
Position (nm)
Plane orientation
Boundary

**Figure 2**

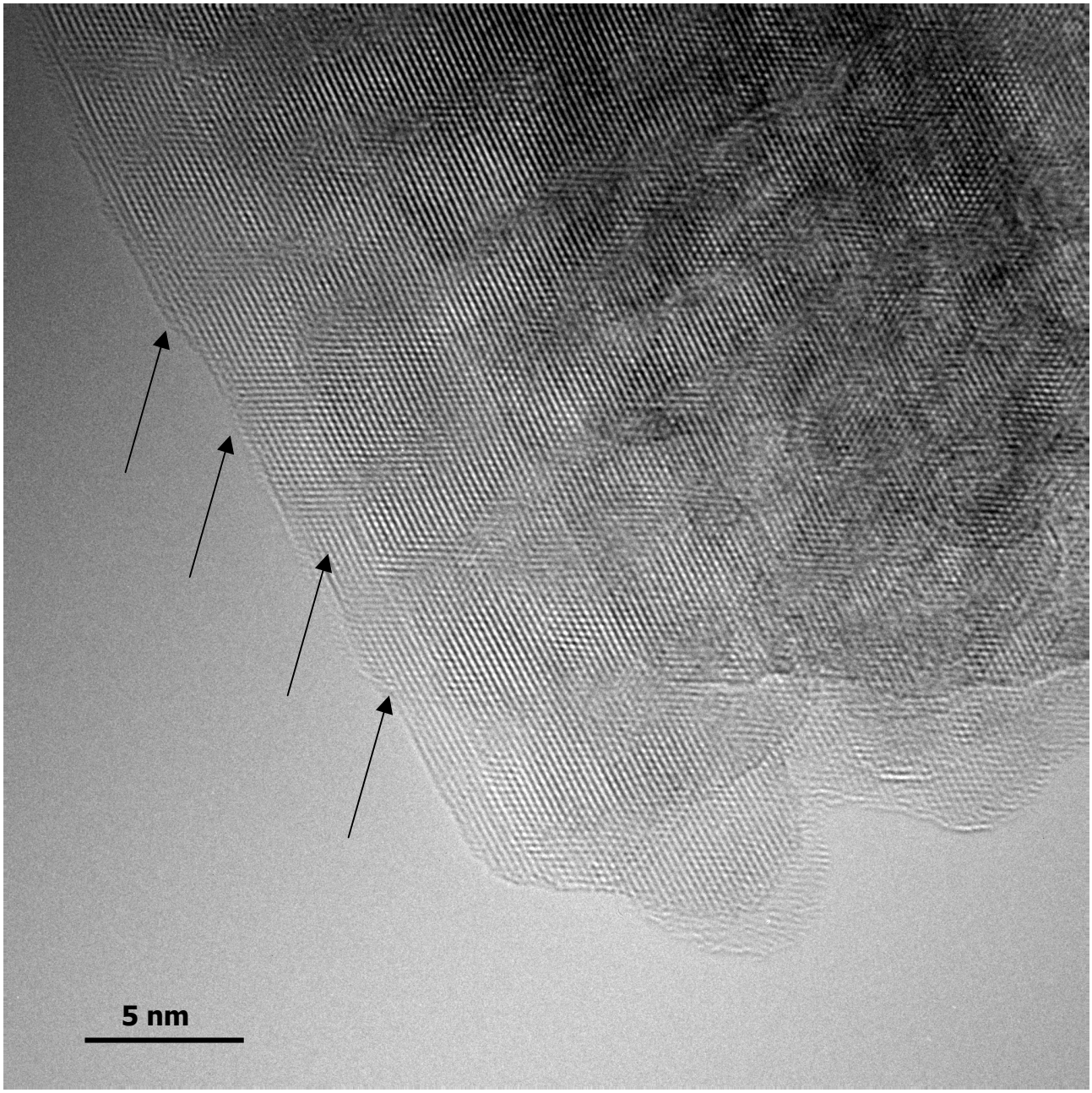


**Figure 3**

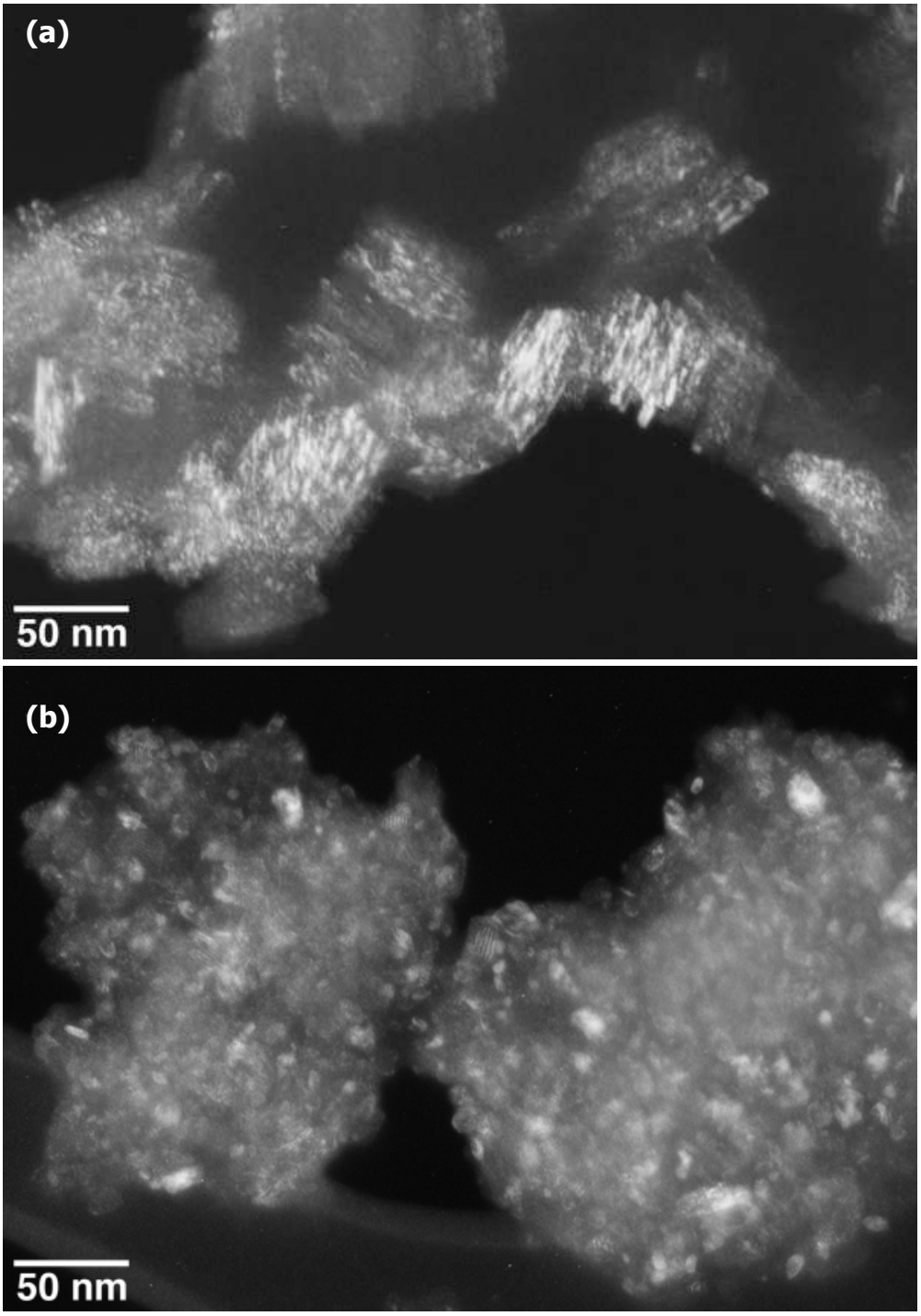
(a)
50 nm
(b)
50 nm

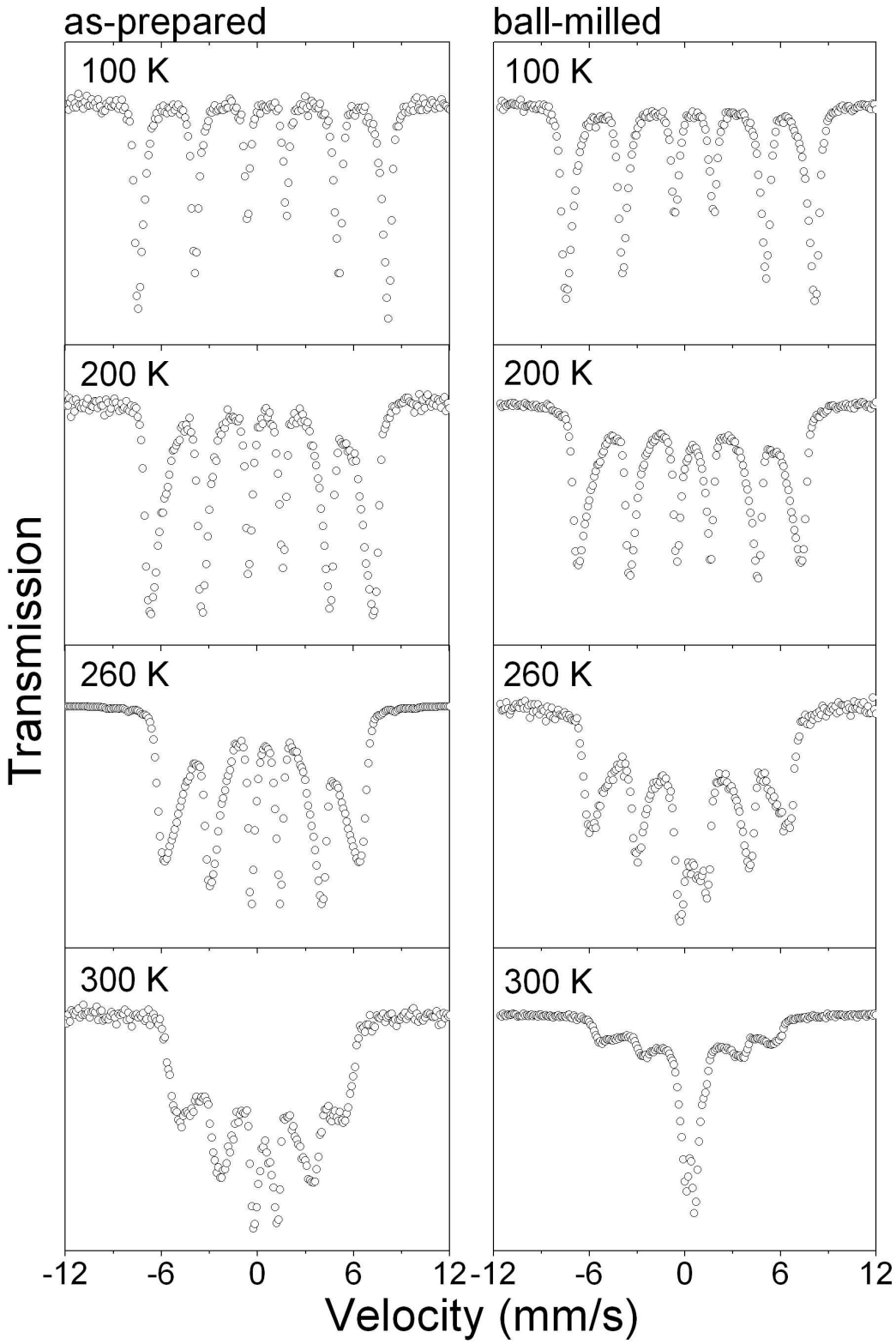
as-prepared
ball-milled
100 K
200 K
260 K
300 K
Transmission
-12
-6
0
6
12
Velocity (mm/s)

**Figure 5**

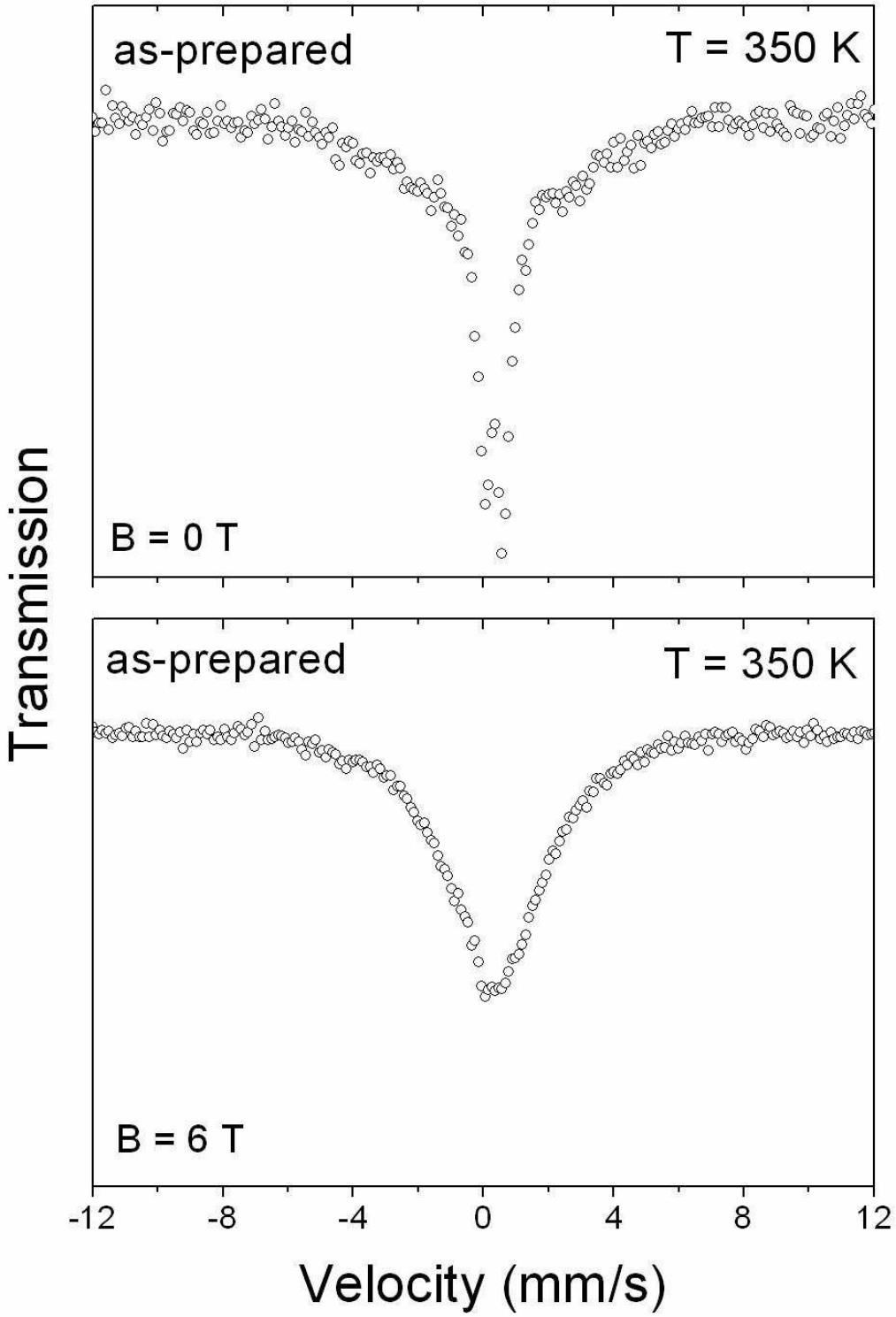
as-prepared
T = 350 K
B = 0 T
as-prepared
T = 350 K
B = 6 T
Transmission
-12
-8
-4
0
4
8
12
Velocity (mm/s)

**Figure 6**

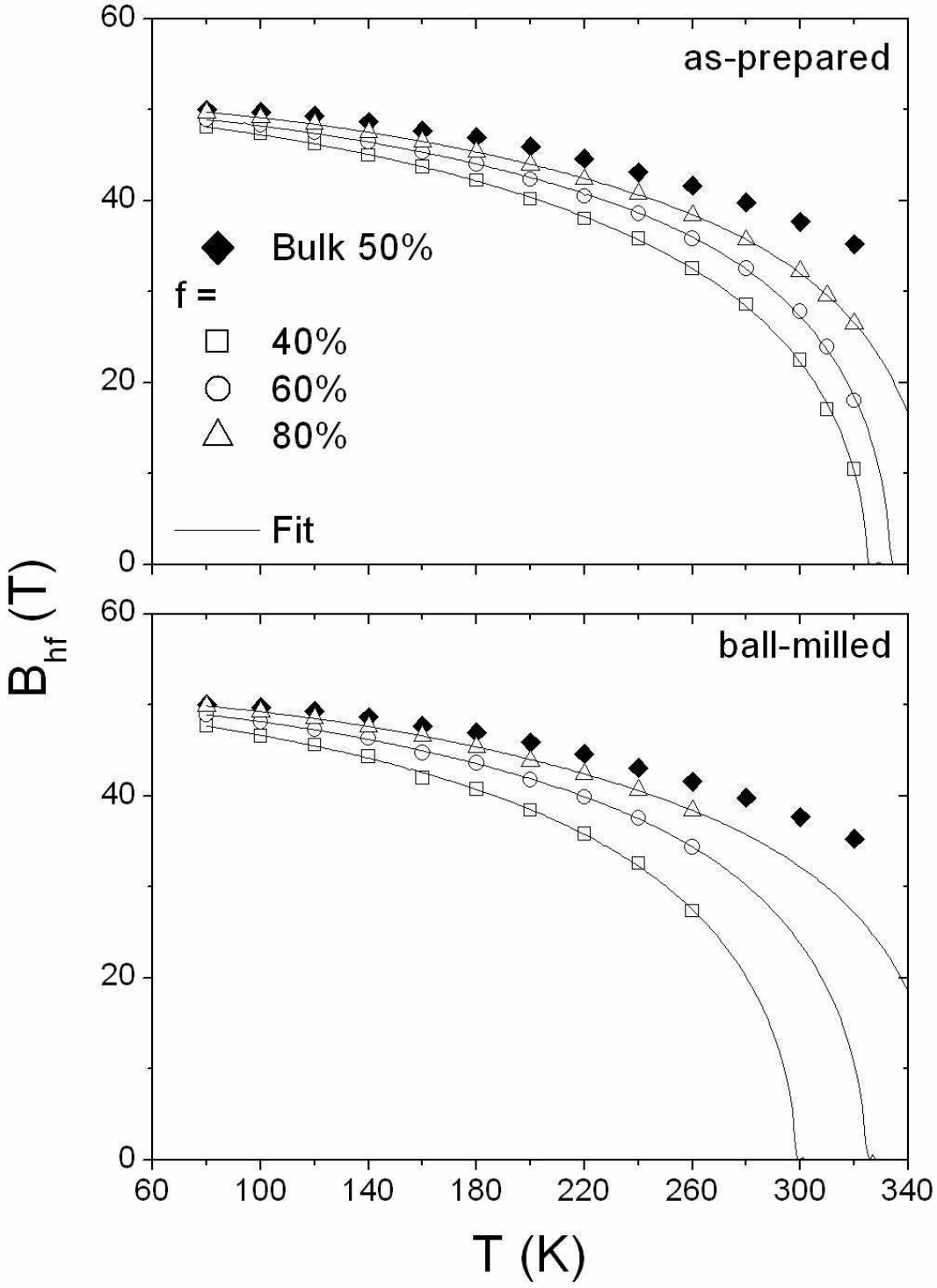
as-prepared
Bulk 50%
f =
40%
60%
80%
Fit
ball-milled
$B_{hf}$ (T)
T (K)
0
20
40
60
60
100
140
180
220
260
300
340

**Figure 7**

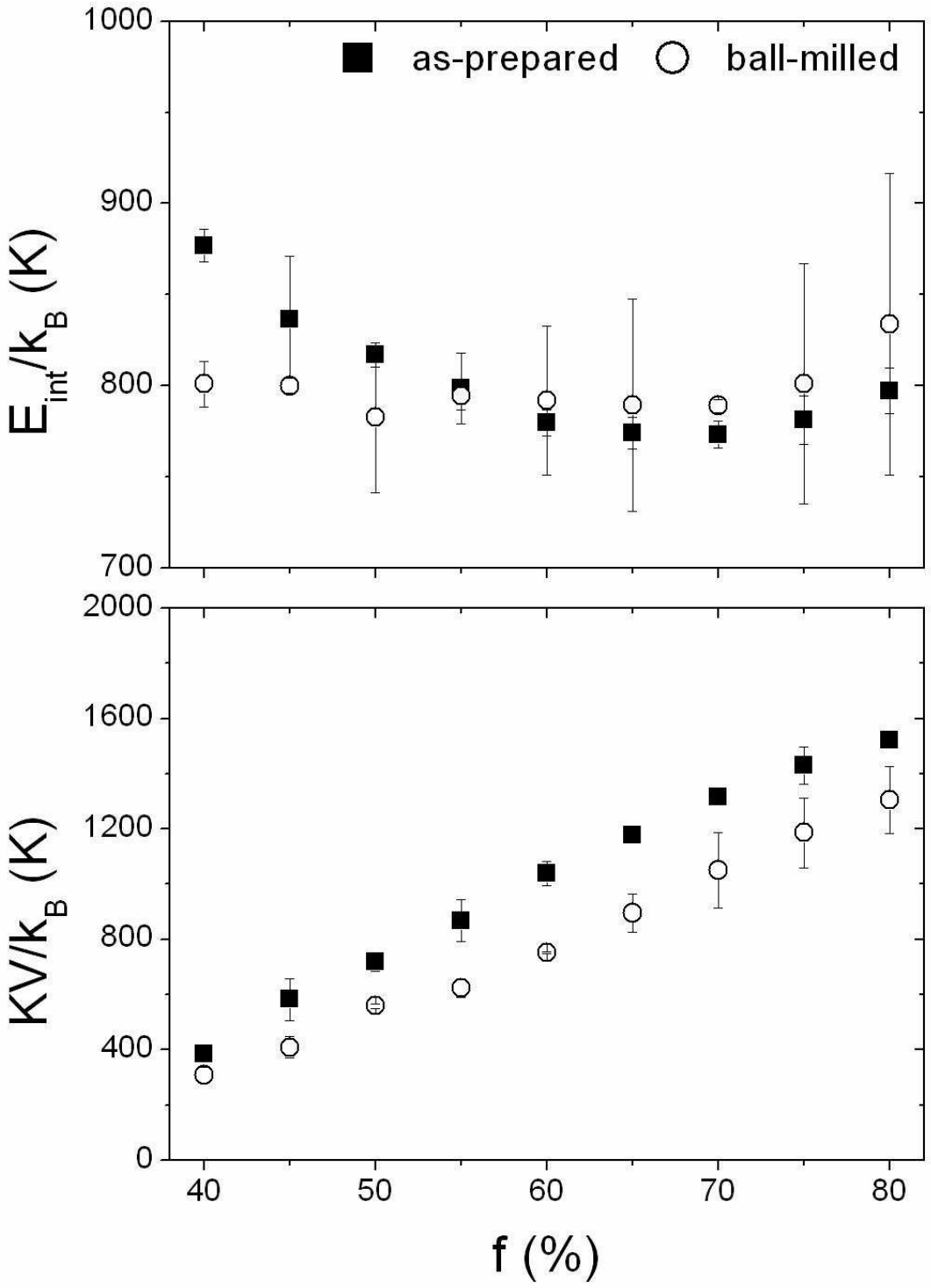
as-prepared
ball-milled
$E_{int}/k_B$ (K)
$KV/k_B$ (K)
f (%)
1000
900
800
700
2000
1600
1200
800
400
0
40
50
60
70
80

**Figure 8**

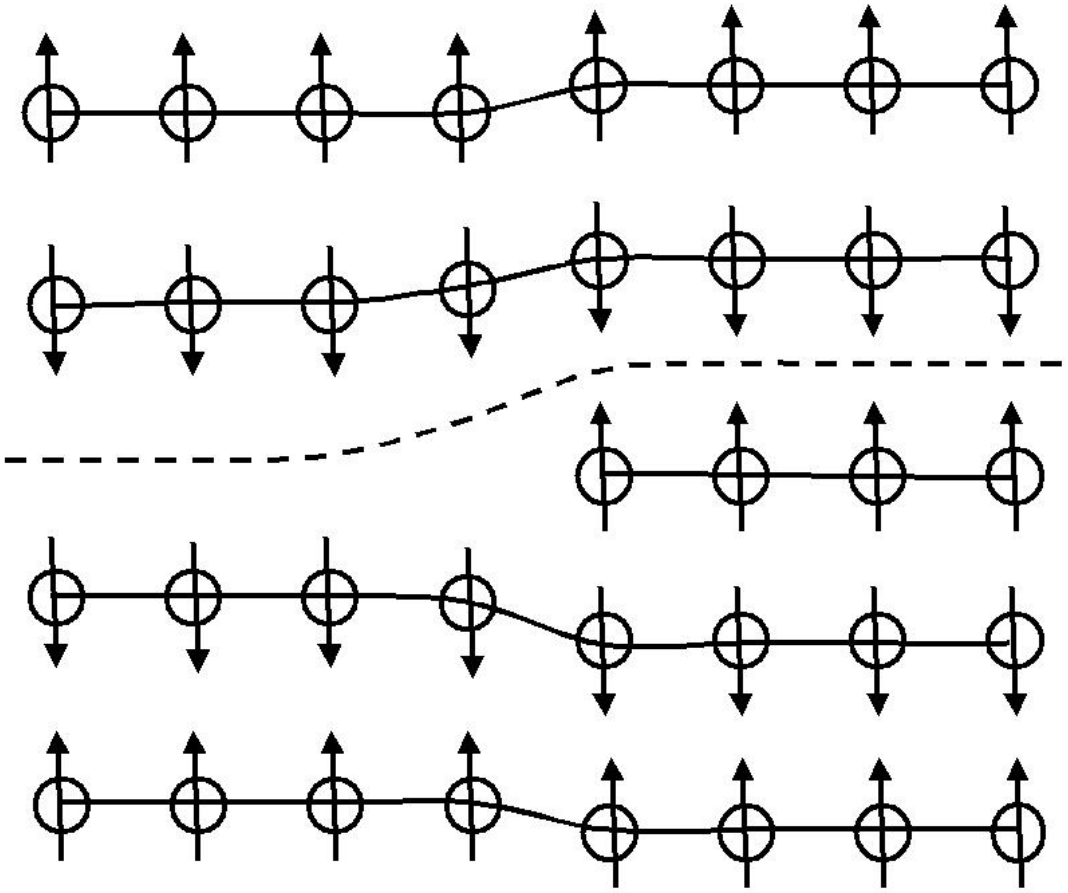

**Figure 9**